DEUTSCHES ELEKTRONEN–SYNCHROTRON

DESY-PRC 00/04
October 2000

HERA – B

Report on Status and Prospects
October 2000

The HERA – B Collaboration

HERA – B

Report on Status and Prospects

Department of Physics, University of Texas, Austin, TX 78712, USA

University of Barcelona, Dept.E.C.M., Facultat de Fisica(U.B.), E-08028 Barcelona, Spain

Institute for High Energy Physics, Beijing, P.R. China

Institute of Engineering Physics, Tsinghua University, Beijing 100084, P.R. China

Institut für Physik, Humboldt-Universität zu Berlin, Germany

Dipartimento di Fisica, Università di Bologna and INFN, Bologna, Italy

Physics Dept., University of Cincinnati, Cincinnati, Ohio 45221, USA

LIP Coimbra and Lisboa, Portugal

Wayne State University, Dept. of Physics and Astronomy, Detroit, MI 48202, USA

Institut für Physik, Universität Dortmund, Germany

Northwestern University, Evanston, Il 60208, USA

DESY, Hamburg, Germany

II. Institut für Experimentalphysik, Universität Hamburg, Germany

Max-Planck-Institut für Kernphysik, Heidelberg, Germany

Physikalisches Institut, Universität Heidelberg, Germany

Physics Department, University of Houston, Houston, TX77204, USA

Institute for Nuclear Research, Ukrainian Academy of Science, Kiev, Ukraine

Niels Bohr Institutet, DK 2100 København, Danmark

Institut J. Stefan and Oddelek za fiziko, Univerza v Ljubljani, Ljubljana, Slovenia

University of California, Los Angeles, CA 90024, USA

Lehrstuhl für Informatik V, Universität Mannheim, Germany

Institute of Theoretical and Experimental Physics, Moscow, Russia

Joint Institute for Nuclear Research Dubna, Moscow, Russia

Moscow Physical Engineering Institute, Moscow, Russia

Max-Planck-Institut für Physik, Werner-Heisenberg-Institut, München, Germany

Dept. of Physics, University of Oslo, Oslo, Norway

Universität Rostock,Fachbereich Physik, Germany

Institut für Physik, Universität Siegen, Germany

Universiteit Utrecht/NIKHEF Amsterdam, 3584 CB Utrecht, The Netherlands

DESY – Institut für Hochenergiephysik, Zeuthen, Germany

Physikalisches Institut der Universität Zürich, Zürich, Switzerland

Contents

1 Executive Summary **1**

1.1 Introduction 1

1.2 Detector Status and Plans 2

1.2.1 Introduction 2

1.2.2 Inner Tracker 3

1.2.3 Outer Tracker 4

1.2.4 High-p_T Chambers 6

1.2.5 Muon 8

1.3 Trigger Status and Plans 9

1.3.1 Calorimeter Pretrigger 9

1.3.2 Muon Pretrigger 9

1.3.3 High-Pt Pretrigger 10

1.3.4 Optical Links 11

1.3.5 First Level Trigger 11

1.3.6 Trigger Efficiency Estimates 12

1.3.7 FLT Track Finding Efficiency Estimate (OTR) 12

1.3.8 Trigger Efficiency for $J/\psi \to e^+e^-$ 14

1.3.9 Trigger Efficiency for $J/\psi \to \mu^+\mu^-$ 15

1.4 Run 2000 17

1.5 Physics Prospects 19

1.5.1 CP Violation in $B^0 \to J/\psi\, K^0_S$ Decays 23

1.5.2 The FCNC Decay $B^0 \to \mu^+\mu^- K^{*0}$ 25

1.5.3 B^0_s–$\overline{B^0_s}$ Mixing 27

1.6 Conclusions 30

2 Detector Status and Plans for the Shutdown 2000/2001 **33**

2.1 Target 33

2.1.1 Requirements, Setup and Basic Rationale of the HERA – B Target 33

2.1.2 Status and Run Experience 37

2.1.3 HERA and Beam Related Topics 45

2.1.4 Shutdown Plans: Hardware Upgrades & Repairs 49
2.1.5 Shutdown Plans: Software Setup 51
2.1.6 Target Setup & Commissioning Plans for the Year 2001 51
2.2 Beam-Pipe 53
2.2.1 Introduction 53
2.2.2 Previous Upgrade Plans 54
2.2.3 Plans for the Shut-down 56
2.3 Vertex Detector System 58
2.3.1 Status 59
2.3.2 Performance 59
2.3.3 Radiation Damage 65
2.3.4 Material Budget 66
2.3.5 Improvements 66
2.3.6 Module Production and Installation Plan for the Year 2001 68
2.4 Inner Tracking 69
2.4.1 Status of Installation and Subsystems 69
2.4.2 Detector Operation 71
2.4.3 Tracking 71
2.4.4 Trigger Signals 74
2.4.5 Improvements of the Inner Tracking Detector during Shutdown 75
2.4.6 Summary 75
2.5 Outer Tracker 76
2.5.1 Hardware Status 76
2.5.2 Track Reconstruction Software 84
2.5.3 Detector Performance 87
2.5.4 Repairs and Upgrades During the Shutdown 92
2.5.5 Outer Tracker Summary 95
2.6 Status of the High-p_T Trigger 97
2.6.1 Overview 97
2.6.2 Performance of Inner Chambers during the 2000 Run 98
2.6.3 Status of Outer Chambers during the 2000 Run 105

2.6.4 Status of Pretrigger Electronics 105
2.7 The HERA – B RICH 109
2.7.1 Expected Performance 109
2.7.2 Measured Single-photon Angular Resolution 110
2.7.3 Measured Photon Yield 110
2.7.4 Stability of Operation 111
2.7.5 Tracking Capabilities 111
2.7.6 Particle Identification Capabilities 114
2.7.7 Plans for the Shut-down 118
2.8 Transition Radiation Detector 124
2.8.1 Status 124
2.8.2 Detector Performance 125
2.8.3 Shutdown Plans 2000-2001 126
2.9 Electromagnetic Calorimeter 128
2.9.1 General Remarks 128
2.9.2 Radiation Hardness 128
2.9.3 Noise Problem 129
2.9.4 Readout Electronics 129
2.9.5 Slow Control 130
2.9.6 Calibration 130
2.9.7 Monitoring 131
2.9.8 Performance 131
2.9.9 Upgrade/Repair Plans 132
2.10 Muon System 137
2.10.1 Status of Muon System Hardware 137
2.10.2 Performance and Running Experience 138
2.10.3 Chamber Aging Studies 143
2.10.4 Shutdown Plans 144

3 The Trigger System: Status and Prospects **147**

3.1 The First Level Trigger 147

3.1.1 Introduction . . . 147
3.1.2 Operation . . . 149
3.1.3 Performance . . . 162
3.1.4 Conclusions . . . 173
3.2 The ECAL Pretrigger system . . . 176
3.2.1 Technical Description . . . 177
3.2.2 Present Status and Performances . . . 179
3.2.3 Future Plans . . . 183
3.3 The Muon Pretrigger System . . . 184
3.3.1 Requirements and Coincidence Algorithm . . . 184
3.3.2 System Overview and Latency . . . 184
3.3.3 Efficiency Measurements . . . 188
3.3.4 Software and Monitoring . . . 188
3.3.5 Future Improvements . . . 190
3.4 High-P_T Pretrigger . . . 191
3.4.1 Introduction . . . 191
3.4.2 Pretrigger Logic . . . 191
3.4.3 Electronics Overview . . . 192
3.4.4 The Link Board . . . 192
3.4.5 The Pretrigger Board . . . 193
3.4.6 The Message Generator . . . 193
3.4.7 Status . . . 193
3.4.8 Plan for Luminosity Shutdown . . . 194
3.5 Second Level Trigger . . . 195
3.5.1 Introduction . . . 195
3.5.2 SLT hardware . . . 195
3.5.3 SLT Algorithm . . . 197
3.5.4 The Use of SLT in 1998–2000 . . . 198
3.5.5 The SLT Performance in August 2000 . . . 200
3.6 Third Level Trigger . . . 205
3.6.1 Changes since the Technical Design Report . . . 205

3.6.2 System Status . . . 205
3.6.3 Monte Carlo Studies for a TLT using the VDS . . . 205
3.6.4 Plans for the Luminosity Shutdown . . . 206
3.7 Farm . . . 208
3.7.1 Introduction . . . 208
3.7.2 Concept . . . 208
3.7.3 Implementation . . . 209
3.7.4 Status in 2000 . . . 210
3.7.5 Data Handling . . . 211
3.7.6 Perspectives . . . 212
3.8 Data Acquisition System . . . 215
3.8.1 Introduction . . . 215
3.8.2 The SHARC Cluster Board . . . 215
3.8.3 Second Level Trigger Switch and Data Buffering . . . 215
3.8.4 Logging . . . 216
3.8.5 Status and Performance . . . 217
3.8.6 Event Building . . . 217
3.8.7 Prospects . . . 219
3.9 Online Calibration and Alignment (CnA) . . . 221
3.9.1 Description and Implementation . . . 221
3.9.2 Status and Performance . . . 221

4 Achievements of the Physics Run 2000 223

4.1 Introduction . . . 223
4.2 Minimum Bias Triggers . . . 223
4.2.1 Luminosity Monitoring . . . 223
4.2.2 Single Particle Inclusive Distributions . . . 225
4.2.3 Strangeness Production . . . 229
4.2.4 Multiplicities . . . 230
4.2.5 Particle Fractions . . . 231
4.3 Double Lepton Triggers . . . 232

4.3.1 Electron Triggers . . . 233
4.3.2 Muon Triggers . . . 235
4.4 Single High-p_T Lepton Triggers . . . 237
4.5 Summary . . . 239

5 HERA-B Physics Beyond the Shutdown 241

5.1 Physics of Proton-Nucleus Interactions . . . 244
5.1.1 Normal Inelastic Proton-Nucleus Interactions . . . 244
5.1.2 High p_T Physics and QCD Tests . . . 250
5.2 Physics of High Mass Lepton Pair Triggers . . . 259
5.2.1 Drell-Yan Pair Production . . . 259
5.2.2 Heavy Quarkonium Production . . . 260
5.2.3 Beauty Production Cross Section in Proton Nucleus Interactions . . . 266
5.2.4 CP Violation in $B^0 \to J/\psi\, K^0_S$ Decays . . . 270
5.2.5 CP Violation in $B^0_s \to J/\psi\, \Phi$ Decays . . . 272
5.2.6 Exclusive Lifetimes of Beauty Hadrons . . . 274
5.2.7 Measurement of $\Delta\Gamma_s$ from $B^0_s \to J/\psi\Phi$ Decays . . . 276
5.2.8 Rare Decays $B^0 \to \ell^+\ell^-(X_s)$ . . . 277
5.3 Physics of Triggers Based on High p_T Leptons . . . 285
5.3.1 $B^0 - \overline{B^0}$ Mixing . . . 285
5.3.2 $D^0 - \overline{D^0}$ Mixing . . . 285
5.3.3 Measurement of $\Delta\Gamma_s$ from Semi-Leptonic Decays . . . 291
5.3.4 Charm Physics . . . 292
5.4 Physics of Triggers Using High p_T Hadrons . . . 294
5.4.1 High p_T Hadron Production and QCD . . . 294
5.4.2 $B^0_s - \overline{B^0_s}$ Mixing . . . 294
5.4.3 Measurement of CKM Angles α and γ . . . 302
5.4.4 Hadronic Rare B Decays . . . 315

References 320

1 Executive Summary

1.1 Introduction

HERA – B was approved in February, 1995 to carry out a study of the physics of B meson production and decay. According the Design Report, "HERA – B is an experiment designed primarily to search for CP violation in decays of B mesons into the "gold plated" decay mode $B^0 \to J/\psi\, K^0_S$".

The ambitious schedule, calling for completion of the detector by the beginning of 1998, was not to be met. The proposed technologies for the main tracker were proven to fail quickly when confronted with the high radiation environment required for HERA – B operation. Vigorous R&D programs for both the inner and outer trackers were launched and eventually solutions were found. The detector was finally completed [1] only in February, 2000 – a two year delay.

The schedule established to build and commission the sophisticated First Level Trigger system of HERA – B also proved to be seriously over-optimistic. Production finished in 1999 and installation was largely completed by January 2000. System-level commissioning began in 1999 and continued through to the end of this year's run in late August. The trigger system is now able to find tracks starting from pretrigger seeds and map them through the tracker stations behind the magnet, as designed, but is not yet fully commissioned. There is, however, good reason to hope that the remaining problems can be solved during the present shutdown.

In the meantime, the new e^+e^-machines at KEK and SLAC have held to their (also ambitious) schedules and the associated detectors, BELLE and BABAR have reported first physics results this summer, including preliminary measurements of CP violation in the $B^0 \to J/\psi\, K^0_S$ decay mode: our primary goal according to the Design Report.

It is therefore necessary to ask if HERA – B can be reasonably expected to contribute in a meaningful way to the physics topics for which it was designed and if it is possible to use what is arguably the most sophisticated fixed-target multiparticle spectrometer and trigger system ever built for other, perhaps more mundane, physics topics. To answer these questions we must first summarize the state of the detector and estimate the efficiencies and sensitivities we can hope to achieve. Next, a survey of potential physics topics and HERA – B's competitiveness must be estimated.

The collaboration has produced a lengthy report ($\approx$ 300 pages) which attempts the answer to these questions on a rather short time scale, particularly given that the primary goal during most of this period had to be to make best of the available beam-time before the start of the long HERA upgrade shutdown. We apologize in advance for any omissions, inconsistencies and rough edges still present in the report.

This summary will first review the status of the detector and triggering systems, with emphasis on problem areas. We will then give a brief description of the data taken during the year 2000 run and finally summarize the studies of potential physics topics.

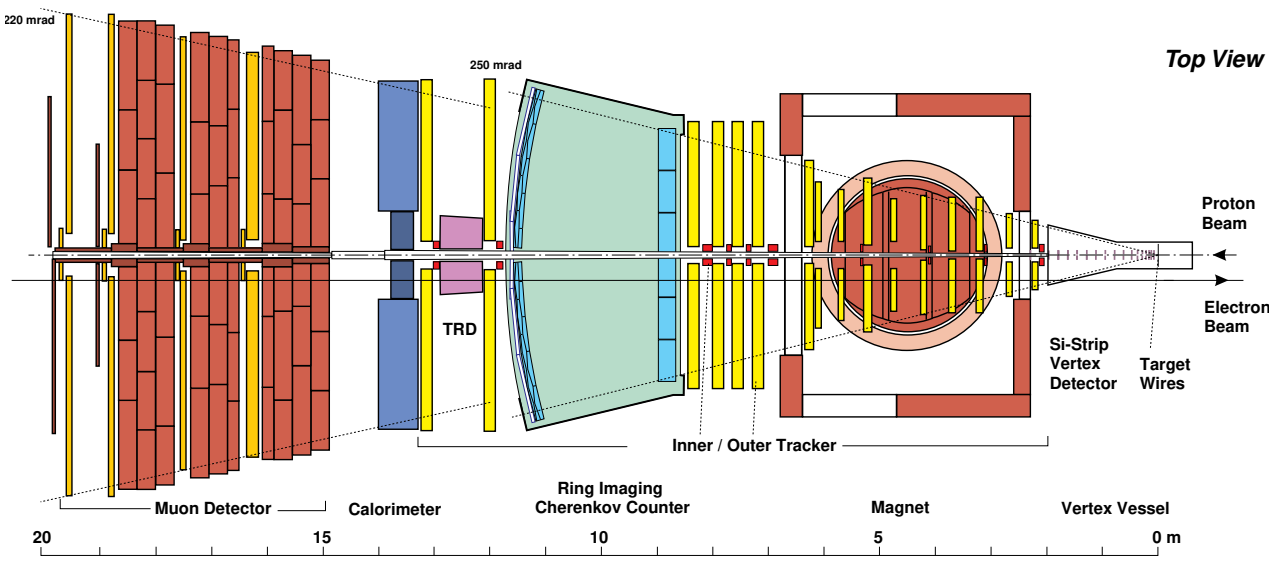

Figure 1: *The HERA – B spectrometer*

1.2 Detector Status and Plans

1.2.1 Introduction

The HERA – B spectrometer is shown in Fig. 1. We start with a very brief summary of the subsystems. Those systems in need of a more detailed status report are deferred to the following sections.

- **Target and beam:** The target has been operating regularly already since 1997. In 2000, the target was in operation during 94% of HERA luminosity periods, usually at rates between 5 and 10 MHz. Beam conditions were for the most part acceptable. Remaining problems include a large contribution to the interaction rate from unbunched beam when operating with outer and above wires and rate instability at high interaction rates. Both of these problems are being addressed together with the machine group.

- **Vertex Detector System:** The vertex detector installation was largely completed in December, 1999 (and fully completed in March 2000 with the installation of the remaining 8 modules outside the vacuum vessel). The detectors were positioned close to the beam for the majority of luminosity time during the 2000 run. The performance is as designed with signal/noise ratios of $15 - 25$ (p-side, n-side), overall efficiencies >97%. Secondary vertex resolution is about a factor of two worse than expected (630 μm vs. 300 μm). This discrepancy is under study.

- **Inner Tracker:** See Section 1.2.2.

- **Outer Tracker:** See Section 1.2.3.

- **High-Pt system:** See Section 1.2.4.

- **RICH:** Installation of the RICH was completed in Spring, 1998. Since then, the system has been in stable operation. Studies show that the RICH has fully reached design specifications.

[1] With the exception of the "High-pt" system, two inner tracker stations and the TRD.

- **Transition Radiation Detector:** The TRD was installed in summer 1999 but has yet to be equipped with more than a few channels of readout electronics for budgetary reasons. The detector was powered to full high-voltage for most of the running period and operated stably. We plan to complete the installation and commissioning of this device in 2001.
- **Electromagnetic Calorimeter:** The calorimeter installation was completed in the Winter shutdown of 1997/1998. Production and installation of readout electronics lagged behind due to problems in the production and testing. By the end of the run, inner and middle regions had been equipped and the installation of electronics for the outer region had begun. The system is now complete. Energy and spatial resolutions are close to design values.
- **Muon Detector:** See Section 1.2.5.
- **First Level Trigger:** See Section 1.3.
- **DAQ and Second Level Trigger:** The hardware and software of the DAQ and the SLT are intimately intertwined since both systems use the second level buffer system, the switch and the second level processing nodes. These systems are fully installed and operating stably. A major activity of the DAQ group was growing the system as channels were added and digging out subtle bugs exposed by this growth. The DAQ/SLT system has been shown to be capable of stable operation for periods of many hours at input event rates up to 22 kHz. The second level trigger algorithm was used as a stand-in for the incomplete First Level Trigger. By the end of the run, the algorithm was close to that envisaged in the design. Suppressions and timing depend sensitively on input.
- **Fourth Level:** The 4th level hardware is complete. The farm was used for event reconstruction in the latter part of run 2000. The reconstruction time depends sensitively on interaction rate and trigger conditions. For triggered runs at 5 MHz, an average time of 4s/event was achieved. The data rates from the second level and to the computer center exceed design specifications.

1.2.2 Inner Tracker

The inner tracking system provides coverage in the area around the beam pipe up to distances of 25 cm. It provides tracking at small radii, for about 40% of all tracks from B-decays and provides input for the First Level Trigger. The Inner Tracker uses a total of 184 MSGC/GEM detectors, each with 768 anode strips organized into 10 tracking stations.

All but two (the furthest downstream) of the stations were installed and commissioned in the course of run 2000. Because of problems with the trigger outputs which precluded use in the First Level Trigger and because they are of little use for pattern recognition, the final two were not installed.

In general, the chambers and ancillary systems have run for several months and worked well, apart from some problems with the low voltage power supplies which we are investigating, together with the manufacturer. During operation, a few problems appeared which affected $\approx 2\%$ of installed chambers. All broken detectors will be repaired or replaced during the shutdown. At this point, remaining problems will be limited to defective anodes at the level of 1%.

The efficiencies of the chambers in the first inner tracking station (MS01) were determined using vertex detector tracks. The results for 7 detectors are shown in Fig. 2 as a function of GEM voltage. After individual adjustment of GEM voltages, efficiencies in the range .91 – .98 were achieved. We have recently learned that the gain variations between GEM foils (leading to the spread in efficiencies)

is most likely due to a mismatch between electrodes on the two sides of the foil. An efficiency study for the entire system awaits tuning of the alignment and general track-finding code.

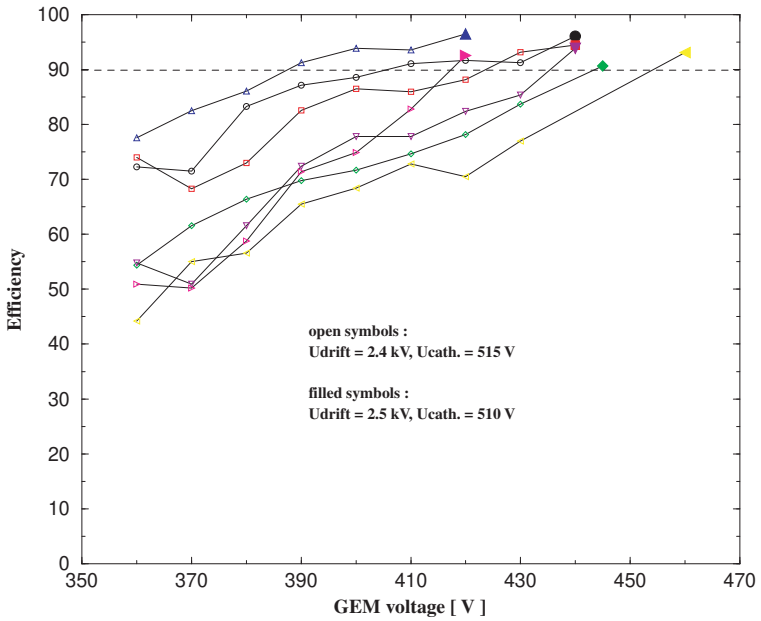

Figure 2: *Efficiency of 7 detectors of station MS01 versus GEM voltage for fixed cathode and drift voltages. The filled symbols show the efficiencies for the current voltage settings after individual gain adjustments.*

Four of the tracking stations behind the magnet will have to provide hit information for the First Level Trigger. To guarantee high efficiency, each of these stations has two layers per view whose trigger outputs are ORed in the front-end electronics. Hit information comes from discriminating the analog signal for each strip and subsequent ORing of 4 neighbors. Each readout chip delivers 32 hit/no-hit signals for each event.

The present trigger installation cycles correctly but, because the discriminator threshold had to be raised to prevent oscillation, it does not give adequate efficiency. By reducing the voltage swing of the trigger output drivers and reworking the grounding scheme, the oscillation could be overcome. Three double trigger layers were installed and operated in August. The measured efficiency is at least 90% and compatible with 100%.

During the shutdown, all detectors will be taken out of the experiment. Broken ones will be repaired or replaced. All front end cards for trigger layers will receive a new version of the readout chip to correct an error with the analog pipeline length. New trigger driver boards will be installed and the path to the First Level Trigger will be commissioned during the shutdown. By the end of the shutdown, the system will be fully installed, including the remaining two trigger stations.

1.2.3 Outer Tracker

The Outer Tracker provides coverage starting from about 25 cm from the beam pipe up to the full aperture of the spectrometer (220 $\times$ 160 mrad). The Outer Tracker is organized into 13 super-layers extending from the vertex vessel to the calorimeter. Each super-layer is logically segmented into 12 sectors of varying dimensions. The Outer Tracker is built from honey-comb drift cells with a wire

pitch of either 5 mm or 10 mm, depending on sector. Four of the super-layers behind the magnet are used in the First Level Trigger. The trigger layers are doubled for high efficiency.

The installation of the Outer Tracker was completed in January 2000. Since then, the system has been available >90% of the time. The high voltage and gas systems are operational and fully integrated with the global HERA – B slow control.

Apart from a potentially serious problem with high voltage stability (described below), only relatively minor and solvable problems were encountered:

- On two occasions, the system was out of operation due to leaks in the gas system. Finding the leaks proved to be a difficult and time consuming operation, resulting in a total downtime of about two weeks. The failure modes have been identified: dirt in bellows of pumps and loosening of gas fittings and measures have been taken to eliminate them.
- 138 (of 7200) readout boards were not giving signals. Most of these failures probably occurred at assembly (cables coming loose). Improvements in assembly procedures are expected to reduce this problem to a negligible level.
- The thresholds of the four super-layers used in the First Level Trigger had to be raised because of additional noise induced by connections between the TDC boards and trigger electronics. We are studying ways to reduce or eliminate this additional noise.

From the beginning of Outer Tracker operation in July 1999, high voltage groups[2] started to fail. The average failure rate was one group per 5 hours of operation. By the end of the run, 6.9% of high voltage groups had failed.

The failure rate was particularly high in the first assembled super-layer. It was suspected that the reason for the failures was mechanical instability since the modules of this super-layer had not been reinforced with carbon fiber stiffener rods. This super-layer was removed and overhauled in December 1999, then reinstalled. Since the repair, the failure rate decreased by a factor of 10, one of the lowest rates in the system.

Several initial tests and observations indicated that discharges and mechanical module imperfections might have been responsible. After the end of the run in September 2000, inspection of damaged modules revealed a completely unexpected source of failure. Of the modules inspected, 39 of the 49 "shorts" were caused by burnt-in carbon traces of varying resistance in residue left over from the soldering process across either of two capacitors on the bottom side of the high-voltage board responsible for distribution to a 16-wire group. A total of 17 capacitors are mounted on this board, 15 on the top and 2 on the bottom. Failures were seen only in connection with the 2 capacitors mounted on the bottom. This systematic difference is most likely due to differing mounting techniques.

While it is clear that shorts across the capacitors are implicated in the vast majority of the failures, we are concerned about remaining failure modes which might by a first indication of future problems. We are currently working to understand the experimental findings and making tests to try to reproduce the failures on a test bench.

During the shutdown, all bottom-side capacitors will be exchanged using a clean soldering technique. Also all modules which have not yet already received carbon fiber stiffeners will be reinforced

[2] A high voltage group consists of 16 channels.

(mainly 2 half super-layers). All modules will be subjected to a rigorous high voltage test to identify short and hot wires, while mechanically exercising them. Improved assembly and test procedures should reduce the number of unplugged readout boards to nearly zero.

We have determined the Outer Tracker cell efficiency for data taken at various times throughout the run. As an example, Fig. 3(a) shows the efficiency of cells in one 5 mm module of one sector of one super-layer, near the end of the run. From the fitted curve, the efficiency in the plateau was determined to be 0.93. The region has a radius of about 2 mm around the wire. Outside the plateau region, (near the edges of the hexagonal cell), the efficiency drops to zero[3]. The efficiencies of the 128 cells of the same module sector are mainly above 0.90, as shown in Fig. 3(b).

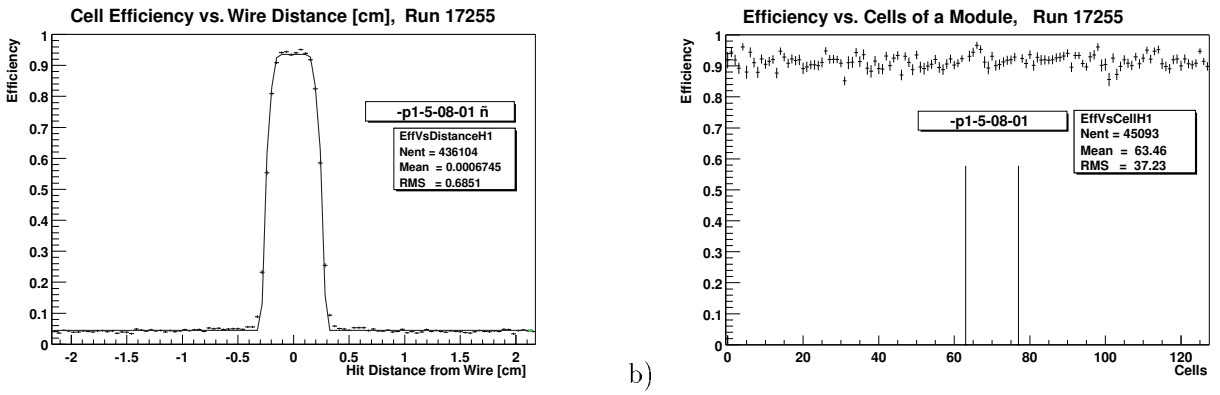

Figure 3: *a) Dependence of the cell efficiency on the distance from the anode wire (5 mm cell) for module 8 in sector 1 in stereo layer 5 of super-layer PC1–. b) Efficiency of the 128 cells of the same module.*

The results of the same analysis applied to 8 super-layer halves in the main tracker behind the magnet for two runs are shown in Fig. 4, as a function of the discriminator threshold setting averaged over the super-layer half. A clear threshold dependence is seen. The runs 17255 and 17254 were taken nearby in time and differ only in high voltage settings and therefore gain. Most of the data taken during year 2000 run was taken with settings similar to those of run 17255 because of the high-voltage stability problem described above. It now seems likely that we will be able to run with the increased gain settings of run 17254 and thus benefit from the increased efficiency.

Two methods were used to check the resolution of the chambers. One method estimated a "local" resolution by comparing the hit positions of hits on adjacent double layers. The method has the advantage of being insensitive to alignment effects and extrapolation errors. A resolution of 240 μm – 300 μm was found, compared to a value of 500 μm – 700 μm, estimated using found tracks. The discrepancy is most likely due to our still preliminary alignment.

1.2.4 High-p_T Chambers

The concept of the high-p_T trigger is as follows: tracking chambers with a pad-type readout are placed within the spectrometer magnet. Pad hits are input to dedicated processors, and high-p_T tracks are selected based on the hit patterns. Such tracks tend to bend little or make larger angles with respect to the beam, and their hit-patterns are distinct from those caused by minimum bias tracks.

[3]By construction, the neighboring cell overlaps sufficiently to ensure negligible efficiency drop in the edge region.

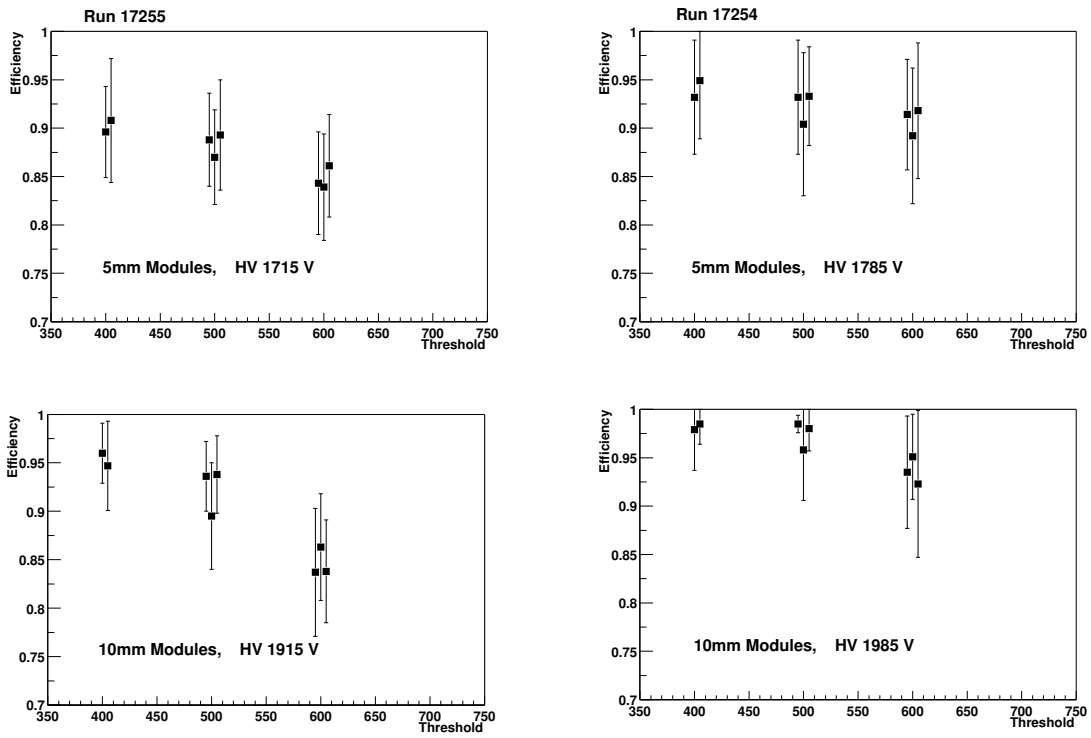

Figure 4: *Average efficiency of the PC super-layer halves for runs 17255 and 17254 taken under identical conditions, except the high voltage. The corresponding gains are 1.17 and 1.46. The horizontal axis is the preamplifier threshold voltage in millivolts.*

The tracking chambers with pad readout come in two types: gas-pixel chambers for the region nearest the beam, and straw-tube chambers with "pickup-pads" for the larger outer region.

The gas-pixel chambers use short anode wires oriented parallel to the beam. The tracks going from the main vertex to the inner high-p_T chambers are almost parallel to the wires resulting in large primary ionization and sharp rise times.

The straw tube chambers utilize straw tubes against which are positioned printed circuits consisting of a pad pattern. These pads are positioned very close to, or in contact with, the outer surface of the straw tubes. A gas avalanche occurring at an anode wire then induces an image charge on the pad directly above the avalanche.

There are a total of 12 chamber halves organized into 3 super-layers: six gas-pixel chambers for the inner region and six straw tube chambers for the outer region.

Status of Inner Chambers: All inner chambers were installed during the 2000 running period and were operational at a voltage setting at least 50 V above the value corresponding to the beginning of the efficiency plateau. During the last month of data taking, the chambers were operated routinely along with the rest of the HERA – B detector. The number of dead channels is relatively small: out of 11 960 channels, 18 are dead due to missing wires or disconnected cables and 12 have lost one wire (of two in the cell) resulting in an efficiency loss of about 30%.

The single-cell efficiency was determined using tracks defined by matching VDS, ECAL, and RICH segments and two of the three high-p_T stations (e.g., PT1 and PT3). All known dead and hot

channels were excluded. The efficiencies obtained for different chambers and cell sizes are shown in Fig. 5.

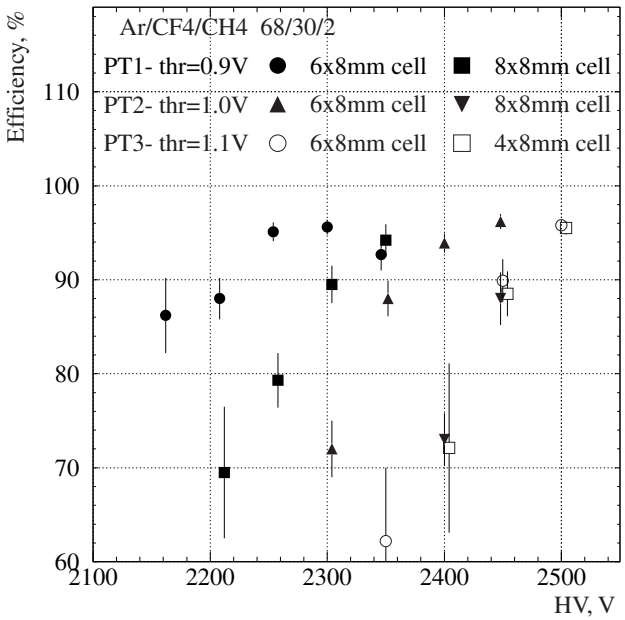

Figure 5: *Efficiencies measured for inner high-p_T chambers during the 2000 run using VDS-ECAL-RICH tracks.*

The efficiency measured reaches a plateau of about 96% and does not increase further. This could indicate that some fraction of the reference tracks are ghosts; alternatively, there may exist a timing problem or an electronics inefficiency with large signals. Previous tests at the ITEP synchrotron yielded a single-cell efficiency higher than 99% for fluxes up to about 5×10^5 particles/cm^2-s. These measurements, however, were performed without a magnetic field.

Status of Outer Chambers: During the 2000 running period, four of six outer high-p_T chambers were installed and run regularly at nominal high voltage. All but two of 1488 straw tubes were active. The very limited access to the detector precluded installation of the remaining two chambers, they will be installed during the present shutdown.

The installed chambers were partially instrumented with front-end cards and read out. Substantial intermittent noise and oscillations were seen on the front-end ASD-8 cards which prevented us from measuring chamber efficiencies or inputting meaningful signals to the pretrigger electronics. During the present shutdown, we will attempt to trace the sources and eliminate the oscillations.

1.2.5 Muon

The muon system provides a pretrigger signal for the First Level Trigger and is used for muon identification in the offline analysis. It consists of a muon filter and four super-layers of muon chambers. Each super-layer has pixel chambers covering the area near the beam pipe. The outer regions are covered by a combination of tube and pad chambers. The outer regions of the first two super-layers consist of three layers of muon tube chambers with 0^o and $\pm 20^o$ views. The outer

regions of the third and fourth super-layers consist of one 0^o layer with both anode and pad readout. The pads (and pixels) of these layers are used in the muon pretrigger. The First Level Trigger also relies on the tube chambers of the first, third and fourth layers for tracking.

All 342 tube chambers, 132 pad chambers and 16 pixel chambers are installed and running. Chamber operation has been smooth and reliable.

The major cause for concern in the muon system is the efficiency of the pad chambers. The measured efficiencies for the MU3 and MU4 pads are 75% and 68% respectively. Since one pad from each chamber is required in the muon pretrigger, the efficiency per track is just 51% and since most triggers require two tracks, the pretrigger efficiency is just 26%. Studies are underway to understand how to improve on this. Foreseen improvements including a better grounding scheme, installation of additional filter capacitors, a modified termination scheme, repair of high-voltage problems and broken readout channels, and operation at higher chamber bias (high voltage) are expected to improve the efficiency to $\approx$90%, resulting in an overall 2-track pretrigger efficiency of 66%. Improvements beyond this will almost certainly require replacement of the front-end amplifier board (ASD-8). The ASD-8 amplifier has a shaping time of 6 ns which is a poor match to the 25 ns rise time of the pad pulses. We are looking into the feasibility of designing, producing and installing new amplifier cards in the present shutdown.

The efficiency of the tube chambers is also somewhat uncertain. A tube efficiency of $> 99\%$ was measured in a test beam, however a measurement in situ shows efficiencies in a range from 96.6% – 98.3%, depending on super-layer, despite the fact that we are running the chambers well above the knee of the plateau curve. The discrepancy between the test beam result and the in situ measurement has not been fully tracked down however it is due in part to some residual broken channels ($\approx$ 1%) which we expect to repair during the shutdown. We also suspect that the sample of reference tracks includes some ghosts.

1.3 Trigger Status and Plans

We first briefly review the status of the pretrigger systems and the First Level Trigger. An extended discussion of the trigger efficiency of the pretrigger/FLT system follows.

1.3.1 Calorimeter Pretrigger

The calorimeter pretrigger system has been in operation since the beginning of the 1999 run, providing a high-E_T trigger which allowed detection of the J/ψ in its e^+e^-decay mode. During the course of the 1999, 2000 runs, the system grew and was finally completed near the end of run 2000. By Summer 2000, the majority of the system ($\approx$ 80% by end July) was fully integrated with the DAQ and running reliably. The intrinsic efficiency of the system was determined by comparing clusters found in the offline analysis with those generated by the pretrigger system and inserted into the event stream via the FLT electronics. The average efficiency for working cells is 95%.

1.3.2 Muon Pretrigger

The muon pretrigger has been in operation and supplying pretriggers since July of this year. Coverage of the muon pad chambers is complete. The efficiency of the system was measured using a technique similar to that used to measure calorimeter pretrigger efficiency. Half of the system was found to

have an efficiency >99% while 28% showed efficiencies between 95% and 99% and 7% have efficiencies between 80% and 95%. The remaining channels suffered from hardware failures in the readout chain. A major reason for the inefficiencies has been traced to bit errors in the pretrigger messages. The errors most likely occur in a single FLT module in the transmission chain. (If this turns out to be the case, this module will be repaired or replaced.) The electronics needed to cover the pixel chambers exists and has been tested. The installation will be completed during the shutdown.

1.3.3 High-Pt Pretrigger

A small test setup consisting of six link boards and four pretrigger boards was installed in the experiment and, after considerable effort to tune the optical links, worked essentially error-free during periods without target operation. During data taking, bit errors occurred occasionally, presumably due to the larger number of hits in the data streams. This may imply that the DC offset for the optical receivers should be increased at higher interaction rates. The problem is under study (see Sect 1.3.4.

Using data from the inner chambers collected during minimum bias runs at various interaction rates, we have estimated the pretrigger rate. This rate as a function of interaction rate is shown in Fig. 6 (for inner chambers only). All channels with occupancy larger than 20% have been masked out. The average number of pretriggers is 0.18/BX at an interaction rate of 5 MHz, about 60% larger than the Monte Carlo prediction of 0.11/BX. The contributions from the $+x$ and $-x$ sides are equal. The pretrigger rate drops if one makes more stringent cuts on noisy channels. The pretrigger rate is 1.06/BX at an interaction rate of 20 MHz, again somewhat larger than the Monte Carlo prediction of 0.61/BX. The rate of the high-p_T pretriggers in coincidence with the electron (FLT-SLT trigger with $p_t > 1.5\,(1.0)$ GeV/c is 0.82/BX at 2 MHz. This is a factor of two larger than the Monte Carlo prediction.

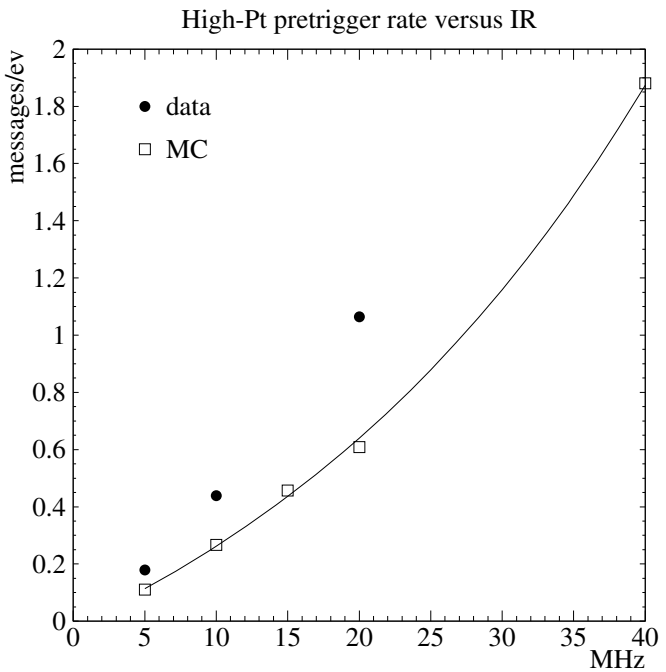

Figure 6: *High-p_T system pretrigger rate as a function of interaction rate.*

1.3.4 Optical Links

Optical links are used for transmitting hit data from the trackers to the pretrigger systems and the TFUs. A serious concern is whether the present optical links can provide the required stability over an extended period of time. In the present scheme, offset and modulation currents are adjusted with potentiometers. Because of different attenuation for the different optical fibers, temperature drifts and other effects, the pre-adjusted values have often proven to be outside the dynamic range of the receiver. The potentiometers are not accessible once the boards are installed. Hence any adjustment requires removal of the board which is a delicate and lengthy procedure. Thus we are considering adding the capability to adjust the offset and bias currents remotely. A new optical transmitter piggy-back is being designed and the feasibility of producing and replacing some or all of the links installed in the experiment is being evaluated.

1.3.5 First Level Trigger

The FLT attempts to find tracks in the tracking super-layers behind the magnet starting from seeds defined by the pretrigger systems (4 main-tracker super-layers and, for the muons, also 3 muon super-layers). It is capable of making cuts on kinematical properties of tracks, of requiring any number of tracks from combinations of pretrigger sources and of combining tracks pair-wise, and imposing cuts on the pair mass.

The track finding is done in an array of 82 interconnected purpose-built processors (called Track Finding Units). Each processor takes input from one section of one super-layer. Messages containing track parameters pass from pretrigger systems to TFUs and then from TFU to TFU and finally (for accepted tracks) into Track Parameter Units which calculate and cut on kinematical parameters, passing on accepted tracks to the Trigger Decision Unit which is responsible for the final trigger decision.

By the beginning of 2000, the FLT electronics had been largely installed and was undergoing system tests. Many problems were yet to be solved, among them:

- The optical links were not working properly and had to be hand-tuned. Eventually most optical links (96%) were made to work and those with significant error rates ($> 10^{-6}$) were set "on" meaning that all channels serviced by that link showed hits for all events.
- Other system level hardware problems had to be corrected to stabilize the system, such as cooling in the TFU crates and unstable "repeater boards" between TFUs.
- The Outer Tracker was not behaving at performance levels: many channels were being lost due to high voltage problems. The resulting inefficiencies were large enough to kill any hope of using the FLT as a trigger until a way had been found to mask ON the dead areas.
- The cell spacing of the Outer Tracker was found to be less uniform than expected, due to the modular construction. A new software tool had to be written to minimize the resulting inefficiencies.
- Links between pretriggers and the track-finding units were flaky and had to be stabilized.
- Many of the tools needed to control, monitor and simulate the FLT were found to be either missing or inadequate and had to be either written or rewritten.

Nonetheless, by the end of the run, the system was working at the level of finding tracks with fair efficiency (see below) and producing messages containing lists of triggered tracks and their coordinates for the second level trigger. The FLT was also used as a trigger in the last days of the run, with mixed success. This is further discussed in the next section.

1.3.6 Trigger Efficiency Estimates

In the remainder of Section 1.3, we go into quite some detail to explain our present understanding of the trigger efficiency of the complete triggering chain based on data taken during the year 2000 run and our expectations for startup in 2001. Readers not interested in the details are invited to skip to tables 2 and 4.

1.3.7 FLT Track Finding Efficiency Estimate (OTR)

Table 1: *Efficiency factors needed to calculate the track finding efficiency of the First Level Trigger. Row 13 is the calculated efficiency based on the given figures. The upper limit of the range given in the last line under "present" has been increased to accommodate a measurement not consistent with the model of 74% (see text).*

		Efficiency model	
		Present	**Potential**
1	Working-cell efficiency	0.90	0.95
2	Dead single cells	0.08	0.015
3	Dead double cells	0.08	0
4	Masking efficiency	0.8	1
5	Partially working optical links	0.04	0
6	Efficiency TDC-TLB links	1.00	1
7	Efficiency optical links TLB-TFU	1.00	1
8	Hit efficiency	0.968	0.997
9	All trigger layers hit, 1 track	0.68	0.96
10	Lookup table coding problems	0.97	>0.97
11	Understood geometrical effects	0.95	>0.95
12	Other geometrical effects	0.92	>0.92
13	Tracking efficiency (model)	0.58	>0.81
14	Adjusted track efficiency	0.58 - 0.74	0.81 - 0.96

In this subsection we summarize our present understanding of the FLT tracking efficiency in the four Outer Tracker super-layers. There are several ways to arrive at efficiency estimates using data sets taken under different conditions, using simulation and paper models based on known efficiencies. We find inconsistencies when comparing the various estimates which we are working to resolve.

We start with a paper model. The input numbers are given in the column labeled "Present" of Table 1. Row 1 of this table is the measured single-cell plateau efficiency (see the Outer Tracker section). Most dead single cells (row 2) are due to disconnected high voltage groups. Dead double cells (row 3) are mainly due to malfunctions of ASD8 preamplifier cards or misplugged cables from chamber to preamplifers.

As described in the paragraph entitled "Optical link performance tests" of the FLT report, a comparison was made of occupancy distributions as seen in the wire memory of the TFUs and in the offline analysis. Discrepancies at the level of 1.5% are seen. Most of these errors can be attributed to failures in the masking technique. If we assume that the entire 1.5% is due to such failures, the fraction of successfully masked channels must be 0.8 (row 4) since the total number of dead double layers is 8.0%.

At run startup, the optical links connecting the detector to the TFUs are checked and if a significant bit error rate is found ($> 10^{-6}$), the corresponding cells are switched on (i.e. the TFU sees a hit for each cell). Typically, 4% of the links were switched on (row 5). Since they were on, no inefficiency is incurred (we list them in the table for completeness). The remainder of the links were 100% effective (rows 6,7).

To first order, the hit efficiency is:

$$P_{hit} = P_3 \cdot P_4 + (1 - P_3) \cdot (P_2 \cdot P_1 + (1 - P_2) \cdot P_1 \cdot (2 - P_1))$$

The numbers refer to the rows in Table 1. Plugging those numbers into the formula yields a hit efficiency of 96.8%. Thus the probability that all hits needed to find a track are present is $P_{hit}^{12} = 68\%$, since 12 hits are required.

Next, we turn to the results of a simulation. The simulator does a "bit-wise" identical emulation of the FLT hardware and can take input from either Monte Carlo or data, in this case we use Monte Carlo. The Monte Carlo takes into account the Outer Tracker single-cell efficiency as well as the complete map of dead and hot channels. The simulator also uses the dead/hot channel map to turn on dead channels but assumes 100% masking efficiency in place of the 80% given in the table. The simulator result of 80% for percentage of tracks with all hits becomes 67% after a global correction for the non-masked (1.5%) channels is applied, in good agreement with row 9.

The next factor to consider is the track-finding efficiency of the FLT itself, given that the hits are present. The simulator shows a total drop in efficiency of 15% from "algorithmic" effects. We separate these effects into 3 factors in the table:

- Lookup table coding problems: The algorithm used to generate the lookup tables uses an oversimplified geometrical model of the detector. Most of this inefficiency can be recovered with a more realistic model.
- Understood geometrical effects: These are mainly due to irregularities in the cell spacing of the Outer Tracker arising from its modular structure. It is in principle possible to recover most of this ineffeciency by treating the position of each wire individually when generating the lookup tables.
- Other geometrical effects: These effects are not yet understood.

When these effects are taken into account, an overall tracking efficiency of 58% is found. This can be compared with measured values derived from other studies:

- Data was taken while triggering on the calorimeter. The FLT was in "transparent" mode, i.e. found tracks were recorded but the FLT decision did not actually produce triggers. Reference tracks were defined using reconstructed ECAL-RICH-VDS matches. The reference tracks were matched to tracks in the FLT output record 74% of the time.
- Compare the same set of reference tracks with the simulator output (rather than the recorded FLT record) on an event by event basis. The measured efficiency is found to be 59%.

- Run the simulator on the sample of J/$\psi \to \mu^+\mu^-$ events accumulated over the summer. The result is 59%. (Additional inefficiencies in the muon tracking are not included in this estimate.) The estimate is clearly somewhat biased by the trigger selection which should, if anything, lead to an overestimate.

The discrepancy between these values is not understood. Until the inconsistency is resolved, we use the lowest and highest measured values to indicate the range: 58% – 74% (line 14).

We also list in Table 1 the numbers we expect to achieve by the end of the present shutdown. Improvements in the Outer Tracker's single-cell efficiency and dead channel count will result in a findable track (i.e. all hits present) efficiency of 96%. After losses in the FLT algorithm are taken into account, this will be reduced to between 81% and 96%. Finally, we adjust the lower end of the range to the lower limit of the present range multiplied by the ratio of the values given in line 9. We hope to reduce the errors on this estimate in the near future.

1.3.8 Trigger Efficiency for J/$\psi \to e^+e^-$

Table 2: *Efficiency for J/$\psi \to e^+e^-$. All rows are event level efficiencies.*

		Model		Design
		Present	**Potential**	
1	Geo., ktrig 500, m > 2 GeV	0.34*	0.34*	0.45
2	Missing low angle coverage	0.44*	1	1
3	ECAL pretrig eff. (incl coverage)	0.62	0.95	1
4	Tracking efficiency (2 tracks)	0.34 - 0.55	0.66 - 0.92	1
5	Frontend pipeline overflows	1	1	1
6	Total efficiency	0.032 - 0.051	0.21 - 0.30	0.45
7	Ratio to design	0.07 - 0.11	0.47 - 0.67	1
Triggered rates (5 MHz)				
8	direct J/$\psi \to e^+e^-$ / hour	1000 - 1700	7000 - 10000	15000
9	B $\to$ J/$\psi \to e + e-$ / hour	.7 - 1.2	5 - 7	10

* to be verified

In Table 2 we summarize our understanding of the geometrical and trigger efficiency for J/$\psi \to e^+e^-$ as seen near the end of Run 2000, what we expect to achieve and a comparison of these to the values given in the Design Report. Rows 1 and 2 of the table come from the FLT simulation[4]. Row 3, the pretrigger efficiency was, at the time of this estimate (end July), dominated by missing calorimeter readout and pretrigger coverage but also includes an intrinsic inefficiency of 5% when compared to the offline calorimeter reconstruction (hence the 95% in the "Potential" column). Row 4 is explained in section 1.3.7.

Row 5 gives that the efficiency factor due to the loss of triggers which arrive after the event data has left the frontend pipelines is zero. Since the trigger decision is made in the required time when the processor network is unloaded, the number can always be adjusted to 1 by adjusting the

[4]We believe these numbers to be correct, however we were unable to dispel all doubts before the deadline for publication.

interaction rate. The issue then is the maximum interaction rate imposed by congestion in the processor network. By design, the processor network is intended to cope with interaction rates up to 40 MHz. A conclusive measurement has not yet been made.

Over the lumi upgrade shutdown we expect to complete the low angle coverage by introducing the Inner Tracker into the trigger, utilize the complete calorimeter coverage, improve the Outer Tracker and work to better understand and improve the FLT efficiency. Row 7 shows that we expect the final efficiency to lie between a third and two thirds of the design value. Much of the difference between the Design Report and present estimates comes from the geometric and kinematical factors shown in row 1. The number given in the Proposal (32%) is much closer to the presently accepted value. The figure given in the Design Report is clearly over-optimistic.

Note that, as in the Design Report, we have not included SLT efficiency in this table since it is highly correlated with reconstruction efficiency. The estimates of reconstruction efficiency given throughout the document include SLT efficiency, except when specifically itemized. A discussion of the observed and simulated SLT efficiency can be found in the SLT report.

1.3.9 Trigger Efficiency for $\mathbf{J/\psi \to \mu^+\mu^-}$

Table 3 shows factors entering into the calculation of the muon pretrigger efficiency for a single muon as well as additional factors needed to determine tracking efficiency in the muon system. The numbers in the 2nd column refer to the present setup, those in the 3rd to the setup at startup in 2001.

The pad and pixel chambers (super-layers 3 and 4) are used to define pretrigger candidates and three of the four muon tube chambers (super-layers 1,3,4) are used to define track seeds in preparation for tracking through the tracker super-layers. At present, only the pad chambers have been used in the pretrigger. The average pad efficiency is 71%, implying a coincidence efficiency of 51% (row 1). Some losses are measured in the pretrigger and peripheral electronics (row 3). The overall per-track efficiency of the pretrigger system is given in row 4.

Pretrigger candidates initiate track-finding in the FLT processors dedicated to muon tracking. The tracks are followed through 3 of the 4 muon super-layers before being passed into the main Outer Tracker processors, thus the efficiency of the muon tube chambers also affects the trigger efficiency. Since 5 tracking layers are used, the effective hit efficiency is raised to the fifth power, leading to an overall probability that all hits needed to find a track are present of between 86% and 95%. (row 10).

The factors pertaining to intrinsic FLT efficiencies (rows 11 - 13) are closely related to the corresponding factors in Table 1. See Section 1.3.7 for explanations.

The full tracking efficiency (including Outer Tracker) is obtained by multiplying the values from row 14 of Table 1 for tracking in the Outer Tracker: 39% to 56%. This can be compared to two other efficiency estimates:

- A data set was accumulated using a trigger which required a single track at the first level. The second level then looked for two tracks using the same algorithm used for the bulk of the muon-triggered running. A (somewhat biased) tracking efficiency can be derived by comparing the rate of J/ψs found in this data with that seen with the SLT-only runs taken nearby in time. The resulting efficiency is 19% per track.

Table 3: *Efficiency factors needed to calculate the muon pretrigger efficiency and track finding efficiency in the muon system. Row 15 is the calculated track-finding efficiency in the muon chambers, based on the given figures. The values given in line 16 refer to the full efficiency for finding a track in both the muon and outer tracker chambers. Line 16 has been adjusted to accommodate all of the measurements.*

		Efficiency Model	
		Present	**Potential**
1	MU3 · MU4 pad efficiency	0.51	> 0.90
2	Dead/hot channels (muon pads)	0.01	0.01
3	Pretrigger system efficiency	0.92	1
4	Overall pretrigger efficiency/trk	0.46	0.90 - 0.98
5	Tube efficiency (working cells)	0.85 - 0.90	0.85 - 0.90
6	Double layer tube efficiency	0.97 - 0.99	0.97 - 0.99
7	Dead/hot muon tubes (single layer)	0.06	0.02
8	Link efficiency	1.00	1
9	Effective hit efficiency	0.97 - 0.99	0.97 - 0.99
10	Hits in all tube chambers/trk	0.86 - 0.95	0.86 - 0.95
11	Lookup table coding problems	0.94	>0.94
12	Understood geometrical effects	0.95	>0.95
13	Other geometrical effects	0.89	>0.89
14	Muon system tracking	0.68 - 0.76	0.68 - 0.95
15	Complete Muon + OTR tracking	0.39 - 0.56	0.55 - 0.91
16	Adjusted complete tracking	0.19 - 0.56	0.27 - 0.91
17	Pretrigger & tracking(adjusted)	0.09 - 0.26	0.24 - 0.89

- A data set with a 2-track FLT trigger and 2-track SLT trigger was accumulated in the last days of the run. No J/ψ was seen so no efficiency can be derived. However an upper limit of 28% efficiency per track can be inferred by comparing with SLT-triggered runs taken nearby in time.

The first of these measurements is not consistent with the range given on line 15. We are therefore, once again, forced to adjust the range to accommodate this lower value (line 16). Finally, we multiply in the pretrigger efficiency given on line 4 and obtain our final estimate of pretrigger + FLT efficiency for a single track of $9\% - 26\%$ for the current setup.

The efficiency estimates for $J/\psi \to \mu^+\mu^-$ are given in Table 4. The uncertainties in both the muon tracking and the main tracker tracking lead to a large uncertainty in the total J/ψ efficiency. In the present setup, the maximum efficiency estimate is 2.7% of the design value. Foreseeable improvements should bring the efficiency up to near 79% of the design value. Most of the uncertainty lies in the "algorithmic" problems of the First Level Trigger and inconsistencies between the various efficiency measures. We are working on narrowing down the errors on these estimates with high priority.

Some losses are seen due to triggers arriving too late (row 5) even at an interaction rate of 5 MHz, implying an upper limit on the interaction rate somewhat less than 5 MHz for the present setup. Foreseen improvements will reduce these losses to at most 8% at 5 MHz interaction rate. At least part of the reason for the present high latency is congestion in the FLT network stemming from the large number of switched on channels. We expect improvements after the number of masked

Table 4: *Efficiency for $J/\psi \to \mu^+\mu^-$. All rows are event level efficiencies (i.e. 2 tracks).*

		Model		Design
		Present	**Potential**	
1	Geometry, p > 5 GeV	0.62	0.62	0.62
2	Missing low angle coverage	0.44*	1	1
3	Pretrig, tracking efficiency (2 tks)	0.008 - 0.07	0.06 - 0.79	1
4	Frontend pipeline overflows	0.77 - 0.88	0.92 - 1	1
5	Total efficiency	0.002 - 0.017	0.03 - 0.49	0.62
6	Ratio to design	0.003 - 0.027	0.06 - 0.79	1
Triggered rates (5 MHz)				
7	direct $J/\psi \to \mu^+\mu^-$ / hour	70 - 560	1000 - 16000	21000
8	$B \to J/\psi \to \mu^+\mu^-$ / hour	0 - 0.4	0.7 - 12	15

* to be verified

channels is reduced to the number given in line 2 of Table 1 and the the 4% of non-working optical links are repaired. Further ways to decrease the trigger latency are under study (e.g. using 2 rather than 3 muon super-layers in the track propagation).

1.4 Run 2000

A summary of the major data sets taken since April of this year is given in Table 5. The FLT tracking was under intense development during the run and was not available for taking production data, except at the very end. We therefore triggered using calorimeter and muon pretriggers and the Second Level Trigger. The Trigger Decision Unit of the FLT received the pretrigger messages and issued a trigger if a required number (one or two) of pretrigger candidates were seen. The second level made further cuts on p_T and possibly mass then attempted to find tracks associated with the pretrigger candidates.

After a short run with a minimum bias trigger, we concentrated on developing the Di-lepton trigger. At first, we triggered with the electron pretriggers and the SLT. During this period, the SLT projected pretrigger candidates directly into the vertex detector, with no intermediate tracking in the OTR. The bulk of the data of the year 2000 sample was taken with these conditions. When the Outer Tracker stabilized and an alignment became available in mid-June, the second-level algorithm for tracking behind the magnet was commissioned. At the end of June, we introduced muon pretriggers and ran simultaneously with both electron and muon pretriggers. Finally, in the last two weeks of the run, we turned on tracking at the first level and took data with both single and double track conditions at the FLT and both single and double track requirements at the SLT. Most of the di-lepton data was taken with an interaction rate of 5 MHz. The single lepton data was taken with a 2 MHz interaction rate. Higher rate running (up to 40 Mhz) was tested on a weekly basis.

The invariant cross section per event, as derived from the minimum bias sample, is shown in Fig. 7 together with the reconstructed Monte Carlo. The Monte Carlo agrees with the data to about 20% except for the high p_T region where the measured spectra are somewhat harder. For the charge ratio shown in the bottom of the figure, most acceptance corrections cancel and, for $p_T > 0.5$ GeV/c, the data and Monte Carlo are in good agreement. The relative deficit of low-p_T positive particles in

Table 5: *The major data sets taken during the year 2000 run. The active pretriggers (E = ECAL, μ = Muon) are shown in the "pre" column. The "FLT" column distinguishes between runs with no tracking requirements and a requirement of 1 track or 2 tracks. The "SLT" column gives the SLT requirements: 1 $\Rightarrow$ 1 track, 2 $\Rightarrow$ 2 tracks, V $\Rightarrow$ Vertex detector tracking, O $\Rightarrow$ Outer tracker tracking.*

Type	Start	Stop	Trigger			Events	Time(min)	
			Pre	FLT	SLT	$\cdot 10^{-6}$	total	live
Min Bias	10 Apr	14 Apr	-	-	-	2	2000	-
Di-lepton	29 Apr	13 Jun	E	-	V,2	12	10387	7508
Di-lepton	15 Jun	27 Jun	E	-	OV,2	1	1385	953
Di-lepton	28 Jun	16 Aug	Eμ	-	OV,2	3.7	9363	4853
Hard γ	17 Aug	17 Aug	E	-	-	0.6	390	375
Single lepton	17 Aug	18 Aug	μ	1	OV,1	1.4	362	116
Di-lepton	18 Aug	18 Aug	Eμ	2	OV,2	0.4	470	390
Di-lepton	18 Aug	22 Aug	Eμ	1	OV,2	1.0	1297	995
Single lepton	24 Aug	25 Aug	Eμ	1	OV,1	3.1	831	465

the data is not yet understood.

The left hand side of Fig. 8 shows the e^+e^-invariant mass spectrum from a preliminary analysis of a subsample of 2 million events of the electron-triggered di-lepton sample. The analysis defines tracks by matching calorimeter clusters with track segments in the vertex detector. To eliminate background, each electron candidate is required to have an associated bremsstrahlung cluster in the calorimeter from radiation in front of the magnet. The analysis yields a preliminary value for the J/ψ production cross section of 270 ± 128 nb/nucleon. The error is currently dominated by the simulation of calorimeter acceptance which was still evolving while the data was being accumulated in April and May. Analysis of the full sample is underway.

The right hand plot in Fig. 8 shows the $\mu^+\mu^-$ mass spectrum from $\approx 80\%$ of the di-muon sample. The peak is some 30 MeV lower than the accepted value of the J/ψ and has a width of 75 MeV, compared to a Monte Carlo value of 60 MeV. The total J/ψ sample of 3000 events is being used to tune vertex packages. The final goal of the analysis is to detect displaced vertices which can then be used to determine the $b\overline{b}$ cross section.

The left hand plot in Fig. 9 shows the distribution of the z difference between primary vertex and $\mu^+\mu^-$ vertex for selected $\mu^+\mu^-$ pairs in the J/ψ region. The right hand plot in Fig. 9 shows the same distribution but with the additional requirement that at least one extra track is consistent with having originated at the $\mu^+\mu^-$ vertex. Despite the low statistics, the plots demonstrate the capacity to reconstruct detached vertices. A $b\overline{b}$ cross section of 12 nbarn would contribute about two $\mu^+\mu^-$ pairs. We expect that ongoing optimization of software tools and alignment will further decrease the background on these plots in the near future.

It is evident that a measurement of the $b\overline{b}$ cross section can only come from an analysis of the full J/ψ sample collected with the electron trigger. We estimate that the sample contains about 30,000 reconstructible J/ψ's without bremsstrahlung cut, about 20 of which come from b decay. The bremsstrahlung cut would reduce this to 3000 J/ψ's, not enough for a cross section measurement. However, other combinations of cuts, including a secondary vertex cut may allow a signal to emerge. The analysis is in progress.

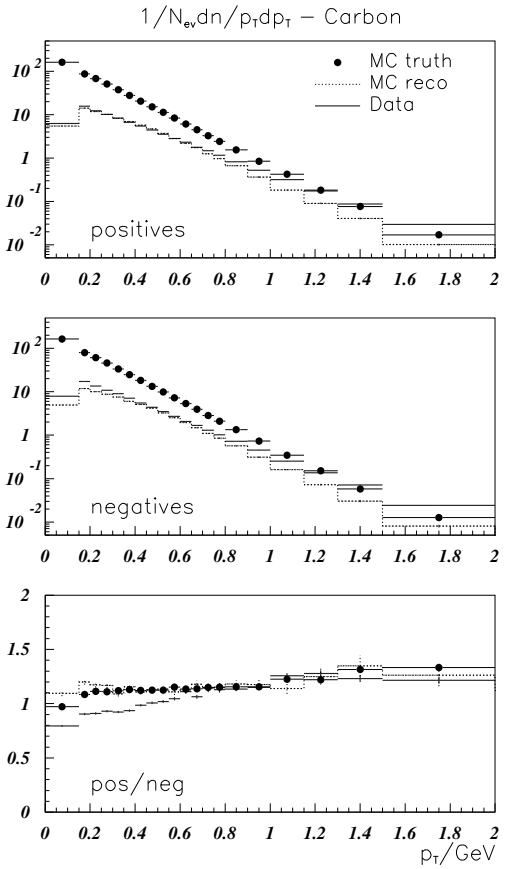

Figure 7: *Transverse momentum spectra for inelastic interactions in proton-carbon scattering. The data for positives and negatives are compared to Monte Carlo predictions after reconstruction and on the generator level ("truth"). Also shown is the ratio of positives to negatives.*

Finally, in Fig. 10, we show the $\pi^{\pm}K^{\mp}$ mass spectrum from the 1.2 million event sample collected with a single muon high-p_T ($p_T > 1.2\,\mathrm{GeV}$) trigger requirement run of Aug. 17. The $\pi^{\pm}K^{\mp}$ candidates were required to have a vertex separation of at least 2 mm. The candidates were required to have a RICH identification consistent with a pion hypothesis and the kaon candidates were required to be both consistent with a kaon hypothesis and inconsistent with a pion hypothesis. A D^0 signal is also seen in all of the hard-triggered (single lepton and di-lepton) data samples.

1.5 Physics Prospects

The chapter entitled "HERA – B Physics Beyond the Shutdown" is a compilation of 16 contributions by 20 authors. Each section evaluates the HERA – B potential to contribute to particular physics topics. The topics fall into 3 main categories: B physics, charm physics and QCD studies. The level of simulation ranges from the generator level through to complete detector simulation and reconstruction using the standard reconstruction software.

We have chosen to delve into three topics in the field of B physics in more detail in this summary:

- CP Violation in $B^0 \to J/\psi\, K^0_S$ Decays: It now appears unlikely that HERA – B will contribute

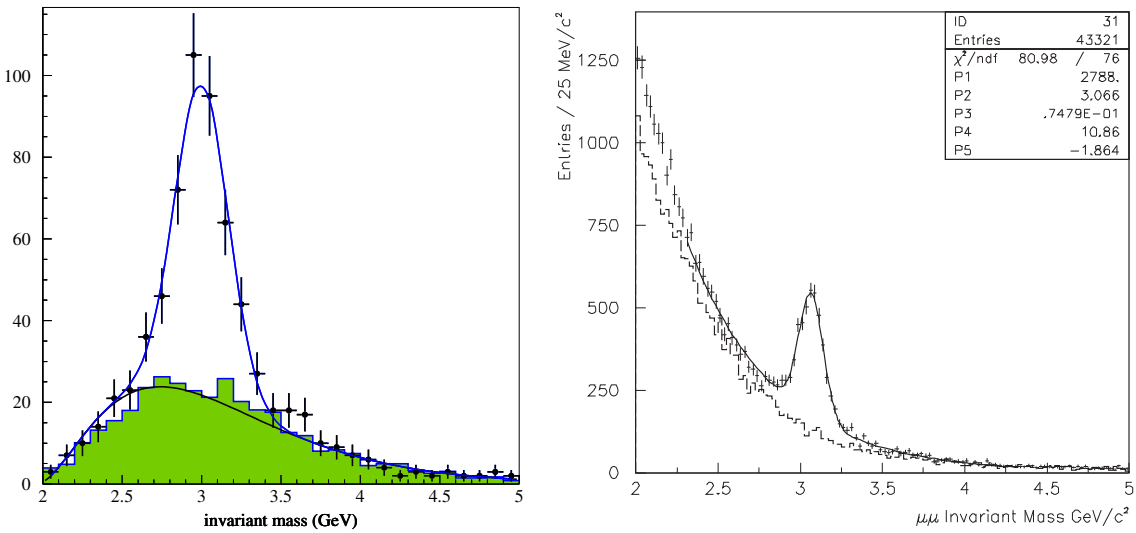

Figure 8: *The left hand plot shows the* e^+e^- *invariant mass spectrum from 10% of the electron-triggered data. The right hand plot shows the* $\mu^+\mu^-$ *and* $\mu^\pm\mu^\pm$ *(histogram) invariant mass spectra from 80% of the muon triggered data.*

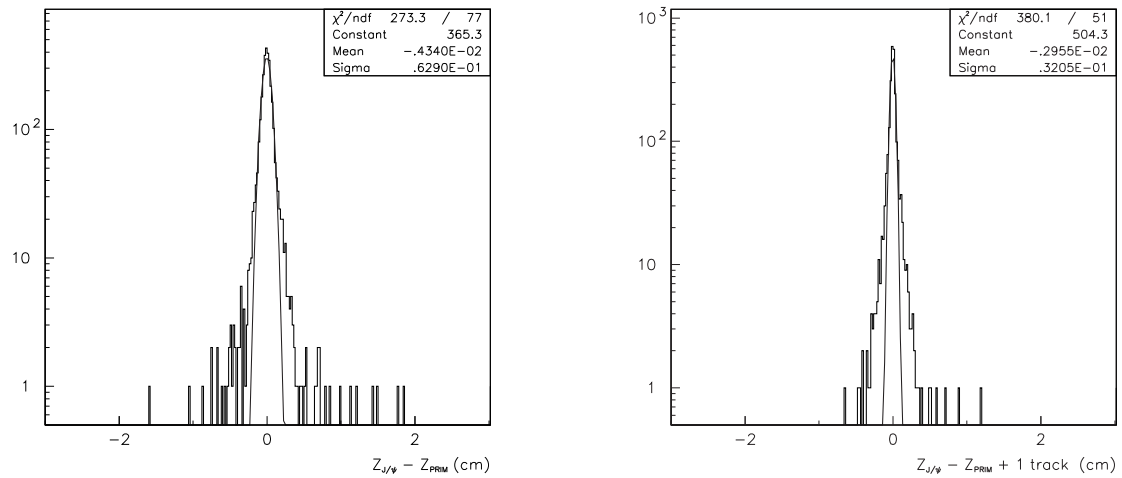

Figure 9: *The left hand plot shows the distribution of the z difference between primary vertex and* $\mu^+\mu^-$ *vertex for selected* $\mu^+\mu^-$ *pairs in the* J/ψ *region. The right hand plot shows the same distribution but with the additional requirement that at least one extra track is consistent with having originated at the* $\mu^+\mu^-$ *vertex.*

to this measurement at a level comparable to the e^+e^-experiments. Nonetheless, a significant measurement is still possible. Furthermore, a new visit to this topic gives the opportunity to update sensitivity estimates made at the time of the proposal in the light of a much more detailed simulation and full reconstruction.

- The flavor changing neutral current decay: $B^0 \to \mu^+\mu^- K^{*0}$. The Standard Model offers testable predictions for the decay rate of this process which is highly sensitive to new physics, such as charged Higgs bosons or heavy supersymmetric particles. HERA – B has the potential to compete

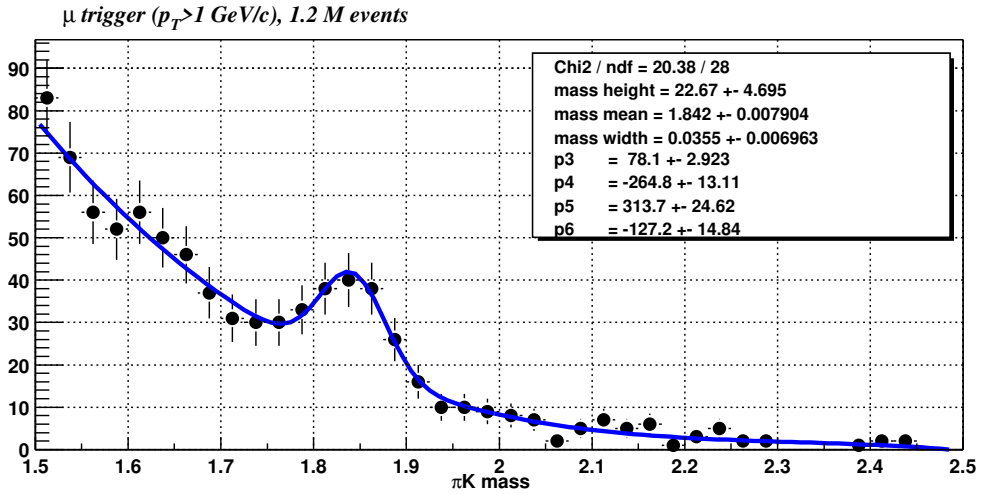

Figure 10: *Invariant mass spectrum of $\pi^{\pm}K^{\mp}$ candidates from a run taken with a trigger requiring a single high-p_T muon with $p_T > 1.2$ GeV.*

in this field with both e^+e^-machines and the TEV II experiments. $B^0 \to \mu^+\mu^- K^{*0}$ is but one of several exclusive final states relevant for FCNC studies.

- $B_s^0 - \overline{B_s^0}$ Mixing: This very challenging measurement can provide important constraints on parameters of the CKM matrix.

Before turning to these topics, we first comment in general on HERA – B potential for the topics studied. For most of the B physics measurements considered here, our most serious potential competition comes from the Tevatron RUN II program, depending on how quickly the Tevatron and the collider experiments reach design performance. Since we are unable to judge this, we offer two evaluations. The first, in Table 6, compares HERA – B's physics reach to existing measurements and extrapolations of existing experiments. The second, in Table 7 assumes that the TEV II experiments quickly reach design performance. Most likely, the situation by mid-2002 will be somewhere in between the scenarios.

In both tables, we indicate competitiveness for a baseline scenario which assumes a 20 MHz interaction rate, a single-track reconstruction efficiency of 80%, full trigger functionality and a $b\overline{b}$ cross section of 12 nb. We also indicate what would happen if the rate of accepted $b\overline{b}$ events falls below the baseline by a factor of 10. Once again, reality will most likely lie between these limits.

In the scenario of Table 6, it can be seen that, even for relatively modest assumptions on the performance of HERA – B, much of the field of heavy flavor physics is open to us. Even with optimistic assumptions on the capabilities of competing experiments, Table 7 shows that HERA – B can produce competitive or at least interesting and significant results in some areas of heavy flavor physics, but only if the baseline scenario is reached.

The interesting topics in the field of charm physics require a relaxation of trigger thresholds (invariant masses, transverse momenta etc.) and therefore greater demands are placed on the second and higher trigger levels. The feasibility is yet to be evaluated. Most likely a charm physics program can not be carried out in parallel with a B physics program in a transparent way.

It is noteworthy that the very preliminary study of measuring CP violation in $B^0 \to \pi^+\pi^-$ decays in this report shows promise. Assuming the branching fraction recently measured by the BABAR

Table 6: *Summary of requirements and performances of HERA – B for the main physics topics, measured against the presently available experimental results and extrapolations of existing experiments (excluding the TEV II experiments). Needed triggers are indicated by a cross. A double-cross indicates that the trigger must be operated at reduced thresholds (invariant masses, transverse momenta etc.). The assessment of competitiveness is made for a baseline scenario which assumes an interaction rate of* 20 MHz*, a conservative single-track reconstruction efficiency of* 80%*, and the full trigger functionality. A second scenario is included which assumes that the reconstructed* $b\overline{b}$ *rate is 10% of the baseline. The* $b\overline{b}$ *production cross section is assumed to be* 12 nb *per nucleon for the baseline scenario (more precisely, a* $b\overline{b}$ *production rate of* 18 Hz *is assumed), a value which is at the lower end of the range allowed by existing measurements. This cross section could be larger by up to a factor* 5*.*

Topic	Trigger Requirements μ	e	hpt	FLT	Competition	Potential (% of baseline) 100%	10%
B physics							
$\sigma_{b\overline{b}}$	$\times$	$\times$	–	$\times$	-	***	***
$\sin(2\beta)$	$\times$	$\times$	–	$\times$	e^+e^-,TEV I	*	–
$CP(B_s^0 \to J/\psi\Phi)$	$\times$	$\times$	–	$\times$	LEP,SLC,TEV I	*	–
b lifetimes	$\times$	$\times$	–	$\times$	LEP,SLC,TEV I	***	**
$\Delta\Gamma_s$	$\times$	$\times$	–	$\times$	LEP,SLC,TEV I	***	*
$B_s^0 \to \mu^+\mu^-$	$\times$	–	–	$\times$	CLEO,TEV I	***	**
$B^0 \to K^{*0}\mu^+\mu^-$	$\times$	–	–	$\times$	e^+e^-,TEV I	***	**
$B^0 - \overline{B^0}$ Mixing	$\times$	$\times$	–	$\times$	e^+e^-,TEV I	*	–
$B_s^0 - \overline{B_s^0}$ Mixing	$\times$	$\times$	$\times$	$\times$	LEP,SLC,TEV I	***	–
α, γ	$\times$	$\times$	$\times$	$\times$	e^+e^-	*** (?)	–
rare B $\to$ hadrons	$\times$	$\times$	$\times$	$\times$	e^+e^-,TEV I	*** (?)	–
Charm physics							
$D^0 - \overline{D^0}$ Mixing	$\times$	–	–	$\times\times$	e^+e^-	**	*
$D^0 \to \mu^+\mu^-$	$\times$	–	–	$\times\times$	E771,e^+e^-	***	**
$D^0 \to e\mu$	$\times$	$(\times)$	–	$\times\times$	E789,e^+e^-	***	**
QCD physics							
Drell-Yan	$\times$	$\times$	–	$\times$	E866	***	**
Quarkonia	$\times$	$\times$	–	$\times$	E866	***	**
soft pN	–	–	–	–	-	***	***
hard pN	–	$\times$	$(\times)$	$(\times)$	-	***	***

*** Possible to perform the first or best measurement.

** Sensitivity worse than extrapolated values of competition but still interesting.

* Sensitivity comparable to existing measurements attainable.

experiment and that the FLT is operational with an overall trigger efficiency of 0.6, we obtain a surprisingly favorable result. Obviously this would be an important measurement and we are now investigating this possibility more carefully with a full simulation of the detector performance. It is worth noting that this measurement depends critically on K - π separation, as $B^0 \to \pi^+\pi^-$ decays must be distinguished from more copious $B^0 \to K^+\pi^-$. Such K - π separation is expected to be substantially better at HERA-B than at, e.g., CDF.

Table 7: *Assessment of the HERA – B physics potential as in Tab. 6, however measured against the full design performance of present and future competition, including the TEV II program.*

Topic	Trigger Requirements				Competition	Potential (% of baseline)	
	μ	e	hpt	FLT		100%	10%
B physics							
$\sigma_{b\bar{b}}$	×	×	–	×	-	***	***
$\sin(2\beta)$	×	×	–	×	e^+e^-,TEV II	*	–
$CP(B_s^0 \to J/\psi\Phi)$	×	×	–	×	TEVII	*	–
b lifetimes	×	×	–	×	TEVII	**	*
$\Delta\Gamma_s$	×	×	–	×	TEVII	**	–
$B_s^0 \to \mu^+\mu^-$	×	–	–	×	TEVII	**	–
$B^0 \to K^{*0}\mu^+\mu^-$	×	–	–	×	e^+e^-,TEV II	***	–
$B^0 - \overline{B^0}$ Mixing	×	×	–	×	e^+e^-,TEV II	*	–
$B_s^0 - \overline{B_s^0}$ Mixing	×	×	×	×	TEVII	**	–
α, γ	×	×	×	×	e^+e^-,TEV II	** (?)	–
rare $B \to$ hadrons	×	×	×	×	e^+e^-,TEV II	** (?)	–
Charm physics							
$D^0 - \overline{D^0}$ Mixing	×	–	–	××	e^+e^-	**	*
$D^0 \to \mu^+\mu^-$	×	–	–	××	E771,e^+e^-	***	**
$D^0 \to e\mu$	×	(×)	–	××	E789,e^+e^-	***	**
QCD physics							
Drell-Yan	×	×	–	×	E866	***	**
Quarkonia	×	×	–	×	E866	***	**
soft pN	–	–	–	–	-	***	***
hard pN	–	×	(×)	(×)	-	***	***

*** Possible to perform the first or best measurement.
** Sensitivity worse than extrapolated values of competition but still interesting.
* Sensitivity comparable to existing measurements attainable.

For completeness, we note that HERA – B can make significant contributions in the areas of heavy quarkonium production and spectroscopy, and of the physics of soft and hard proton-nucleus interactions even in the most pessimistic scenario.

1.5.1 CP Violation in $B^0 \to J/\psi\ K_S^0$ Decays

The HERA – B detector was designed to reconstruct the final states $\mu^+\mu^-\,\pi^+\pi^-$ and $e^+e^-\,\pi^+\pi^-$ of the golden decay mode $B^0 \to J/\psi\ K_S^0$. At the time of the Design Report [1] many idealistic assumptions had to be made to estimate the reconstruction efficiencies for these decay modes. Since then software became available for track reconstruction and trigger simulation. Several studies have been performed using these programs [2, 3, 4]. The numbers presented here are based on the most recent ones [5].

Tab. 8 lists the current estimates of the reconstruction efficiencies for the muon and the electron channel in comparison to the Design Report. The L1 trigger efficiencies are the upper limit efficiencies

given in Tables 2 and 4. The reconstruction efficiencies are smaller now for various reasons. The actual mechanical constraints in the fabrication of the Outer Tracker and the compensation coil of the electron beam pipe lead to holes in the acceptance and to an increase in multiple scattering. The lifetime cut was increased in ref. [5] to improve background suppression. This reduces the efficiency by 18% but has practically no impact on the measurement error of $\sin(2\beta)$ since the CP asymmetry only builds up during the mean lifetime of the B meson and can hence anyway not be measured at very small decay times. The geometrical acceptance for pions from K^0_S decays is smaller due to fewer Inner and Outer Tracker super-layers in the magnet.

Table 8: *Reconstruction efficiencies for the golden decay mode in comparison to the Design Report. The* K^0_S *reconstruction in ref. [5] is too small due to a bug in the Monte Carlo simulation which was found recently [6]. The number listed here is the corrected one.*

	$B^0 \to J/\psi\ K^0_S \to \mu^+\mu^-\ \pi^+\pi^-$		$B^0 \to J/\psi\ K^0_S \to e^+e^-\ \pi^+\pi^-$	
	Design	ref. [5]	Design	ref. [5]
L1 trigger efficiency*	62%	49%	45%	30%
lepton tracking in PC	89%	87%	89%	87%
J/ψ vertex+mass	99%	91%	99%	92%
pion tracks (geometry, reconstr.)	63%	50%	63%	55%
K^0_S vertex+mass	97%	93%	97%	93%
B^0 vertex+mass	94%	88%	73%	56%
main vertex	-	92%	-	87%
vertex detector tracking	-	90%	-	90%
lepton particle ID	94%	94%	85%	85%
decay kinematics	80%	-	80%	-
lifetime cut	69%	57%	69%	71%
total	16%	7.1%	8.3%	3.3%

* The numbers in columns 3 and 5 are the upper efficiency bounds from Tables 2 and 4.

For the measurement of CP violation the flavor of the B meson at production time has to be determined (tagged). Several tagging methods have been developed by other experiments and their applicability in HERA – B has been studied repeatedly [4, 7, 8].

Every method has a certain efficiency ϵ for finding a tag and a probability χ of correctly measuring the b quark charge. Hence the measured asymmetry is smaller by the dilution factor $D = 2\chi - 1$ and the error on $\sin(2\beta)$ scales with the tagging power $P = D\sqrt{\epsilon}$. All studies yield similar results of $P \simeq 0.3$.

The "same side tagging" method has successfully been used by CDF [9] and was a powerful tag in their analysis of the golden decay mode [10]. So far this method was not studied by HERA – B. Hence it is conceivable that the achievable tagging power can be increased.

Tab. 9 lists the expected statistical error on $\sin(2\beta)$ for one and four years of running (10^7 s per year) for different scenarios: for the nominal detector at an interaction rate of 20 MHz, and for a 20% reduced single track reconstruction efficiency. The assumed $b\overline{b}$ production cross section is 12 nb/nucleon. Note that this number is at the lower end of the expectations from measurements [11, 12] ranging from 8 nb/nucleon to about 60 nb/nucleon when scaled to 920 GeV/c proton beam energy.

In the worst case the achievable error on $\sin(2\beta)$ is 0.22 for four years of nominal running of

Table 9: *The CP reach of HERA – B , assuming a 20 MHz interaction rate and efficiencies as given in Table 8 (nominal) and when an additional factor of 0.80 per track is applied to the efficiency estimates given in Table 8.*

	nominal	80% tracking eff.
$b\bar{b}$/year	1.8×10^8	1.8×10^8
$B^0 + \overline{B^0}$	1.5×10^8	1.5×10^8
golden decays	74000	74000
produced $\mu^+\mu^- \pi^+\pi^-$ evts	3060	3060
produced $e^+e^- \pi^+\pi^-$ evts	3060	3060
reconstr. $\mu^+\mu^- \pi^+\pi^-$ evts	220	90
reconstr. $e^+e^- \pi^+\pi^-$ evts	100	40
backgr. fraction in $\mu^+\mu^-$ channel	0	0
backgr. fraction in e^+e^- channel	0.1	0.1
tagging power	0.3	.28
error on $\sin(2\beta)$ after 1 year	0.24	0.40
error on $\sin(2\beta)$ after 4 years	0.13	0.22

HERA – B. In comparison BABAR, Belle and CDF plan to achieve an error around 0.11 for one year [13, 14, 15]. Even though the situation is less favorable for HERA – B our result will still be valuable. The value of $\sin(2\beta)$ is a fundamental number of the SM and several measurements obtained with different experimental techniques are obligatory, especially if the current central values of CDF on one hand ($\sin(2\beta) = 0.79 \pm 0.44$ [10]) and preliminary results from BABAR ($\sin(2\beta) = 0.12 \pm 0.35$ [16]) and Belle ($\sin(2\beta) = 0.45 \pm 0.45$ [17]) on the other hand sustain with increased statistics. An additional measurement even with lower precision could become important.

It has to be realized, of course, that the above projections assume a First Level Trigger running near the upper limit of the range allowed by the present understanding of the trigger efficiency. Should the trigger performance stay much below design, HERA – B will not be able to make a significant measurement in this field.

1.5.2 The FCNC Decay $B^0 \to \mu^+\mu^- K^{*0}$

One of the dominant mechanisms in the $B^0 \to \mu^+\mu^- + X_s$ decay is a flavor changing neutral current (FCNC) penguin diagram with an intermediate top quark $b \to t \to s$, and a W-boson loop. Because of the heavy intermediate particles the process is very sensitive to the presence of new physics. From the theoretical point of view, a measurement of the fully inclusive non-resonant FCNC decay $B^0 \to \mu^+\mu^- + X_s$ represents an ideal testing ground for the standard model due to the absence of uncertainties from the hadronic final state.

The exclusive decay channel $B^0 \to \mu^+\mu^- K^{*0}$, chosen to characterize the HERA – B potential in searching for FCNC decays, is theoretically more difficult to treat but has a very clean experimental signature, giving powerful handles for background suppression. The decay has a large predicted branching fraction[5][18, 19]: $(2.0 \pm 0.7) \cdot 10^{-6}$) compared to $(5.7 \pm 0.7) \cdot 10^{-6}$ for $B^0 \to \mu^+\mu^- + X$.

[5]This more recent estimate of the branching fraction is somewhat larger than that ($1.5 \cdot 10^{-6}$) given later in this report. See also [20]

An important observable in this decay is the di-muon invariant mass spectrum or equivalently the differential decay rate as a function of s, the squared invariant mass of the di-muon system. The SM prediction, as well as the predictions for two other models, for the differential decay rate is shown in Fig. 11 (for details refer to [21]).

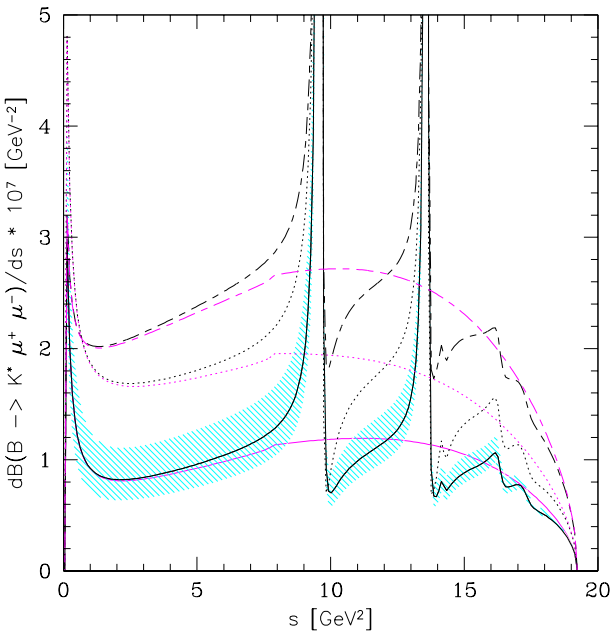

Figure 11: *The dilepton invariant mass distribution in* $B^0 \to \mu^+\mu^- K^{*0}$ *decays[21], using the form factors from LCSR as a function of s. The solid lines represents the SM and the shaded area depicts the form factor related uncertainties. The dotted lines corresponds to the SUGRA model. The long-short dashed lines correspond to an allowed point in the parameter space of the MIA-SUSY model. The corresponding pure SD spectra are shown as the lower curves in each case.*

Estimates for HERA – B acceptance and reconstruction efficiency for $B^0 \to \mu^+\mu^- K^{*0}$ are derived from an estimate of $B^0 \to J/\psi K^{*0}$ efficiency, based on a GEANT simulation and reconstruction using existing software packages. The trigger will be less efficient for $B^0 \to \mu^+\mu^- K^{*0}$ compared to $B^0 \to J/\psi K^{*0}$ because of p_T and mass cuts. Based on Fig. 11, we estimate that a 2 GeV mass cut will cut an additional 25% of the signal after p_T cuts.

The efficiency estimates are summarized in Tab. 10, assuming a (reduced) total interaction rate of 20 MHz and a conservative reconstruction efficiency of 80% per track. The First Level Trigger efficiency is the upper limit efficiency given in Table 4. Combining all factors, the total efficiency for detection and reconstruction of the FCNC decay $B^0 \to K^{*0}\mu^+\mu^- \to K^+\pi^-\mu^+\mu^-$ is about 6% corresponding to about 13 observed events per year. At the same time, roughly 1000 examples of the $B^0 \to J/\psi K^{*0}$ would be collected.

The decay $B^0 \to K^{*0}\mu^+\mu^-$ has been studied extensively by the BABAR collaboration (cf. [22] and references therein). BABAR expects a final statistics of 8 events[23] in a full year run with a nominal integrated luminosity of $30\,\mathrm{fb}^{-1}$. The CDF collaboration quotes a similar sensitivity, down to a branching fraction of 2×10^{-7} (corresponding to roughly 10 events) with the expected integrated luminosity of $2\,\mathrm{fb}^{-1}$ for Tevatron RUN II [24]. To gain enough statistics to measure the mass spectrum and a predicted forward-backward asymmetry in the $\mu^+\mu^-$system[18, 19], however, an integrated luminosity of $\mathcal{O}(10\ \mathrm{fb}^{-1})$ would be needed [25]. Any potential of HERA – B to measure

Table 10: *Estimate of HERA – B sensitivity for the non-resonant FCNC decay* $B^0 \to K^{*0}\mu^+\mu^- \to K^+\pi^-\mu^+\mu^-$ *for one year of running at a (reduced) interaction rate of* 20 MHz *and an assumed conservative single track reconstruction efficiency of* 80%. *The total trigger efficiency is denoted by* ϵ_{trig}.

Production per Year:	
$b\overline{b}$ per year	1.8×10^8
$B^0 + \overline{B^0}$ per year	1.5×10^8
$B^0 \to K^{*0}\mu^+\mu^- \to K^+\pi^-\mu^+\mu^-$	210
Acquisition and Reconstruction:	
FLT efficiency (incl. Geo, p,p_T cuts, tracking)(Table 4)	49%
FLT mass cut	75%
reconstruction efficiency $\mu^+\mu^-$	64%
geometrical acceptance $K^{*0} \to K^+\pi^-$	84%
reconstruction efficiency $K^{*0} \to K^+\pi^-$	64%
Background Cleaning:	
Jψ, ψ' mass cuts ($\pm$ 150 MeV)	75%
decay vertex cut ($\Delta z > 5$ mm)	62%
total efficiency	0.06
$B^0 \to K^{*0}\mu^+\mu^- \to K^+\pi^-\mu^+\mu^-$ per year	12.6

this FCNC process is therefore important in order to increase the world statistics necessary for sensitive tests of the standard model.

In conclusion, HERA – B has a chance to contribute in a significant way to the world statistics expected for the next years, provided that the di-muon trigger is running close to the upper limit of the range given in Table 4. So far, study of the HERA – B capability to measure this decay mode has been limited to efficiency estimates. An in depth analysis of possible background sources is beginning. HERA – B's excellent vertex detection and particle identification capabilities are powerful tools for background suppression which may also allow study of the inclusive process $B^0 \to \mu^+\mu^- + X_s$. It is perhaps also worth pointing out that many of the final states in the "X_s" system will also be reconstructible, such as $B^0 \to K^{*0}\pi^+\pi^-\mu^+\mu^-$, as well as decays of the charged B mesons: $B^+ \to K^+\pi^+\pi^-\mu^+\mu^-$. Channels such as $B^0 \to K^{*0}\pi^0\mu^+\mu^-$ may also be accessible.

1.5.3 B_s^0–$\overline{B_s^0}$ Mixing

The measurement of the B_s^0 oscillation frequency, Δm_s, provides important constraints on parameters described by the unitarity triangle. Present lower limits on Δm_s are set by LEP experiments, SLD and CDF, all using semi-leptonic B_s^0 decays. Because of the missing neutrino, the proper time resolution for B_s^0 decays in these experiments is not sufficient to discern the very rapid oscillations that are expected. To improve the Δm_s reach, one needs fully reconstructed B_s^0 decays. Among the most promising decay modes are $B_s^0 \to D_s^-\pi^+$ and $B_s^0 \to D_s^-\pi^+\pi^+\pi^-$. These final states have relatively large branching ratios and low multiplicities. The CDF group realized the importance of these decays and is constructing a special all-hadronic trigger for RUN II in order to accept them. These decays can also be detected at HERA – B.

B_s^0 decays to $D_s^-\pi^+$ and $D_s^-\pi^+\pi^+\pi^-$ can be accepted by a hadron-lepton trigger [1]. The requirements we consider at the first-level of the HERA – B trigger are a high-p_T charged track

($p_T > 1.5\,\mathrm{GeV/c}$) and a high-$p_T$ lepton ($p_T > 1.0\,\mathrm{GeV/c}$ for muons and $p_T > 1.4\,\mathrm{GeV/c}$ for electrons). The high-p_T lepton is produced in the semi-leptonic decay of the second B hadron present in the event. The charge of the lepton track provides a high quality tag.

Using data taken in the year 2000 run and Monte Carlo, we estimate a combined suppression from pretriggers and FLT of 3000 for electron/high-p_T triggers and 290 for muon/high-p_T triggers, corresponding in an SLT input rate of 35 kHz. This is somewhat lower than the SLT design input rate of 50 kHz. The SLT suppression from tracking, an impact parameter cut on the pion and lepton identification is estimated to be a factor of 100. This leads to an output rate of 350 Hz. At the third level, the presence of a second B meson in the event can be used to further suppress background. This is under study.

As shown in Table 11, we plan to reconstruct B_s^0 mesons in 9 decay modes, most of which were reconstructed by LEP experiments. We expect that the excellent vertex resolution and kaon identification at HERA – B will allow sufficient suppression of combinatorial background also in high multiplicity modes.

The result of efficiency studies are summarized in Table 11. The high-p_T pretrigger efficiency was estimated using a full Monte Carlo simulation. The efficiencies of the muon and ECAL pretriggers as well as the FLT are provisionally assumed to be 1 (more below). SLT efficiencies are based on currently achieved values. The reconstruction efficiency is based on performance studies of the tracking algorithms for $1 + 4$ interactions. In addition, the 17% of tracks which interact in the material of the spectrometer are assumed to be lost. The number of events reconstructed with this standard technique are listed in Table 11.

The efficiency can be improved considerably if one starts reconstruction in the vertex detector and does not require that the track passes the full tracking system. Moreover, if the track direction is determined in the vertex detector, its momentum can be obtained from kinematical constraints. Such a procedure does not deteriorate the proper time resolution significantly. The numbers of events reconstructed with this method are shown in Tab. 11.

The tagging power is larger than the $P \approx .3$ (see Sec. 1.5.1) derived in other HERA – B studies because the triggering lepton is used for a tag. The tagging efficiency is therefore 1 and the high-p_T lepton requirement assures a high quality. We estimate a tagging power $P \approx 0.6$.

Two background sources were studied: inelastic events where the tagging lepton is fake and both reconstructed D_s^- and B_s^0 are fake, and $c\bar{c}$ events where the tagging lepton is real while the reconstructed D_s^- meson is either real or fake and the reconstructed B_s^0 meson is fake. The estimated signal-to-background ratio (S/B) from these sources is about 20.

The B_s^0 proper time resolution is dominated by vertex resolution which we estimate at $\sigma_z = 356\,\mu$m for the $D_s^-\pi^+$ and $\sigma_z = 338\,\mu$m for $D_s^-\pi^+\pi^+\pi^-$. Using the target wire constraint, the primary vertex resolution is $150\,\mu$m. The resulting proper time resolution is $\sigma_t = 0.060\,$ps and $\sigma_t = 0.057\,$ps for the $D_s^-\pi^+$ and the $D_s^-\pi^+\pi^+\pi^-$ decay modes, respectively.

In addition to the events listed in Table 11, we expect to collect 56 (22) reconstructed $B_s^0 \to D_s^{*-}\pi^+(\pi^+\pi^-)$ decays in the same period of time. The B_s^0 invariant mass distribution for the D_s^{*-} modes with a missing photon is estimated to be five times wider than that for the fully reconstructed D_s^- modes and the background is expected to be correspondingly larger, but still we expect a large signal-to-background ratio. In addition we expect to collect 34 (20) $B_s^0 \to D_s^{*-}\pi^+(\pi^+\pi^-)$ decays with kinematically determined momentum of one of the tracks reconstructed in the VDS only.

Fig. 12 shows the expected significance of our measurement of B_s^0 oscillations, using both the

Table 11: *Expected fraction of signal events per inelastic (minimum bias) event.*

	$B_s^0 \to D_s^- \pi^+$	$B_s^0 \to D_s^- \pi^+ \pi^+ \pi^-$
Physics:		
$\sigma_{bb}/\sigma_{inel.}$	10^{-6}	10^{-6}
$b\overline{b} \to B_s^0$ (or $\overline{B_s^0}$)	0.16	0.16
$B_s^0 \to D_s^- \pi^+ (\pi^+ \pi^-)$	3.0×10^{-3}	8.0×10^{-3}
$D_s^+ \to \phi\pi^+ \to K^+K^-\pi^+$	0.018	0.018
$K^+\overline{K^{*0}} \to K^+K^-\pi^+$	0.022	0.022
$(K^+K^-\pi^+)_{nonres.}$	0.009	—
$K^+\pi^-\pi^+$	0.010	—
$\pi^+\pi^+\pi^-$	0.010	—
$K^{*+}\overline{K^{*0}} \to K_S^0\pi^+K^-\pi^+$	0.009	—
$\phi\pi^+\pi^+\pi^- \to K^+K^-\pi^+\pi^+\pi^-$	0.006	—
Total D_s^+ branching fraction	0.084	0.040
Trigger:		
Geometry, $p_T(\mu) > 1.0$ or $p_T(e) > 1.4$ GeV/c	0.095	0.095
Pretrigger, $p_T(had) > 1.5$ GeV/c	0.70	0.38
μ Pretrigger	1.0	1.0
e Pretrigger	1.0	1.0
FLT	1.0	1.0
SLT Slicer/Refit	0.9	0.9
Lepton ID	0.95	0.95
Geometrical acceptance	0.68	0.51
Track reconstruction (0.965×0.83 per track)	0.41	0.30
Main vertex	0.94	0.94
B_s^0 and D_s^- vertices	0.81	0.81
$VX(B_s^0) > 3.0$ mm	0.66	0.66
$VX(D_s^-) > 4.5$ mm	0.95	0.95
Summary	3.0×10^{-13}	1.1×10^{-13}
$B_s^0 \to D_s^- \pi^+ (\pi^+ \pi^-)$:		
#events/year	61	23
#events/year, 1 track reconstr. in VDS only	37	21
$B_s^0 \to D_s^{*-} \pi^+ (\pi^+ \pi^-)$:		
#events/year	56	22
#events/year, 1 track reconstr. in VDS only	34	20
Total number of events	188	86

$D_s^{(*)-}\pi^+$ and the $D_s^{(*)-}\pi^+\pi^+\pi^-$ decay modes modes, as a function of the oscillation parameter $x_s = \Delta m_s \cdot \Gamma_s$. Using the fully reconstructed $B_s^0 \to D_s^{(*)-}\pi^+(\pi^+\pi^-)$ decays, x_s values up to 24 can be measured at a $3\,\sigma$ level within one year of operation at 20 MHz interaction rate. We expect that we will find handles against the larger backgrounds[20] in the partially reconstructed decays. This would allow HERA – B to cover the complete range allowed by the Standard Model, assuming full pretrigger and FLT performance.

This conclusion is not significantly modified when the upper-limit trigger and pretrigger efficiencies arrived at in Sect. 1.3 are taken into account. The upper-limit efficiency for triggering on a

single muon (electron) and tracking it with the FLT algorithm is 89% (91%). Track-finding of the pion from the high-p_T pretrigger contributes another factor of 96% for a total efficiency of 86%. The statistical significance scales as the square root of the number of events, implying a loss of significance of just 7%.

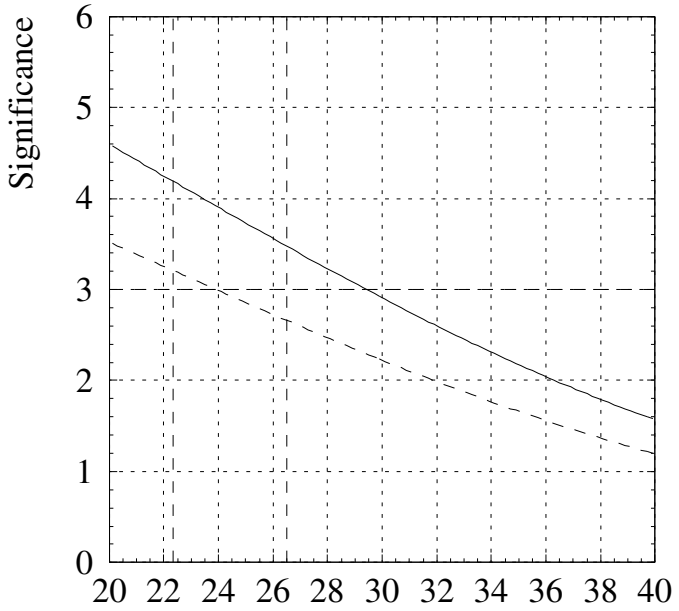

Figure 12: *Significance of* B_s^0 *oscillation measurements as function of* x_s*, expected to be achieved after one year of operation at an interaction rate of* 20 MHz*, using the* $D_s^{(*)-}\pi^+(\pi^+\pi^-)$ *decay modes (dashed line). The solid line shows the expected significance, if a kinematical reconstruction for the momentum of one of the tracks is also used. The present experimental lower limit and the upper limit from Standard Model fits are also indicated by vertical dashed lines.*

1.6 Conclusions

The HERA – B detector was completed in February of this year and has, for the most part, behaved stably. With some exceptions, the subsystems are either operating close to design or can be reasonably expected to approach design specifications with improvements already underway. Still, some work has yet to be finished and some concerns remain:

- The Outer Tracker was losing high-voltage channels at a high rate during the year 2000 run. The causes of this are believed to be understood and a remedy has been found. Investigations continue to determine if any of the observed failure modes are indicative of possible future problems.
- The efficiency of the muon system's pad chambers is low. Steps are being taken to improve it but full efficiency can probably only be reached if the preamplifiers are replaced. We are looking into the feasibility of doing so during the present shutdown.
- The optical links connecting chamber output to FLT are probably not sufficiently stable. A new link is being designed and the feasibility of replacing all or part of the system is under study.

- The readout electronics of outer chambers of the high-p_T system suffer from induced oscillations and noise pickup from an unknown source. This is not likely to be fatal since several similar systems have been made to work in the experimental hall but some additional experience with beam will most likely be necessary to fully debug the system.
- The capabilities of the FLT are not well known. Many tests have been performed but the results are not fully consistent. We expect that additional study of the data taken and of the simulation code will allow a clear picture to emerge on a time scale of several weeks. Until then, we cannot guarantee that the system will work close to design specifications.
- The ultimate rate capability of HERA – B is not yet known. The design calls for 40 MHz. To be more conservative, we have made the sensitivity estimates for this study assuming a 20 MHz interaction rate. It is not yet established that the trigger can operate without deadtime at even this rate.
- One item totally beyond our control but nonetheless relevant is the value of the $b\overline{b}$ cross section at 920 GeV which is still uncertain by nearly a factor of 8. (Our estimates assume a value of 12 nb, close to the low end (8 nb) of this range.

Many uncertainties remain but we have not found any fundamental flaw which would prevent HERA – B from working near to design.

The year 2000 run was used for commissioning the detector and triggering system. Data samples were accumulated with a combination of pretriggers and second level trigger. The data is under analysis and may be of sufficient quality to allow determination of the $b\overline{b}$ cross section. While the J/ψ signal in the $\mu^+\mu^-$mode is fairly clean, the signal can only be seen in the $e^+e^-$when inefficient particle id cuts are applied. We are looking into more efficient ways of reducing background (RICH cuts, improved E/p) but if none are found the utility of the e^+e^-decay mode for B studies will be limited.

Studies were performed to evaluate the potential of HERA – B to contribute to several areas of B-physics as well as charm-physics and QCD studies. The results are summarized in Tables 6 and 7. The general conclusion is that HERA – B can still be competitive in some areas such as a measurement of the $B^0 \to \mu^+\mu^- K^{*0}$ provided we succeed in operating close to design potential. Given the uncertainties listed above, this must be regarded as an "optimistic" scenario. In any case, there remains a good chance that HERA – B can provide meaningful and solid data in the area of B-physics, possibly charm physics and certainly QCD studies.

2 Detector Status and Plans for the Shutdown 2000/2001

2.1 Target

The HERA – B target is designed to produce the required large number of B-mesons for the HERA – B experiment in proton nucleon interactions. It is realized as a multi-wire fixed target which operates in the halo of the 920 GeV HERA proton beam in parallel to the usual HERA e-p luminosity operation.

This section describing the HERA – B target is structured as follows. After a brief review of the basic requirements and rationales in section 2.1.1 the status and achievements obtained by the end of the last run period in August 2000 are summarized in section 2.1.2. Beam related topics are briefly reviewed and discussed in section 2.1.3. The shutdown plans which include upgrades, repairs, maintenance work, improvements and modifications of the setup etc. are divided into two subsections: foreseen hardware upgrades are discussed in 2.1.4 and software related improvements are considered in 2.1.5. Finally the anticipated target setup and configuration together with the (re-)commissioning plans during the HERA and HERA – B start-up phase in the autumn of the year 2001 are sketched in section 2.1.6.

2.1.1 Requirements, Setup and Basic Rationale of the HERA – B Target

Fig. 13 shows a simplified sketch of the HERA – B halo target. The main idea is rather simple: protons leaving the beam core interact on the wires before getting lost on any aperture limitation. In the following section the most important design requests are summarized and the basic construction, layout and functionality is described.

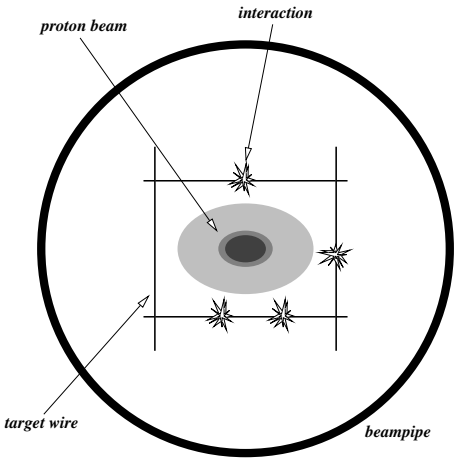

Figure 13: *Sketch showing the basic idea of a halo target. Protons leaving the beam core interact on the target (typical interaction points are indicated by stars) before getting lost on aperture limitations.*

Rates, Luminosity & Target Efficiency

An interaction rate R_{ia} of around 40 MHz is required to achieve the HERA – B physics goals [26]. For a titanium target with an inelastic cross section per nucleon of $\sigma_{nucl}(Ti) \approx 13.3\,\mathrm{mb}$ [27] one gets therefore the following produced luminosity[6] $\mathcal{L}$ per second:

$$\mathcal{L}/\mathrm{s} = \frac{R_{ia}}{\sigma_{nucl}(Ti)} = \frac{4 \cdot 10^7/\mathrm{s}}{13.3\,\mathrm{mb}} = \frac{3.0}{\mathrm{nb\,s}} = 3.0 \cdot 10^{33}\mathrm{cm}^{-2}\mathrm{s}^{-1} \qquad (1)$$

[6]The luminosity is given per nucleon. For comparison: the value corresponds exactly to the PEP/BaBar design luminosity.

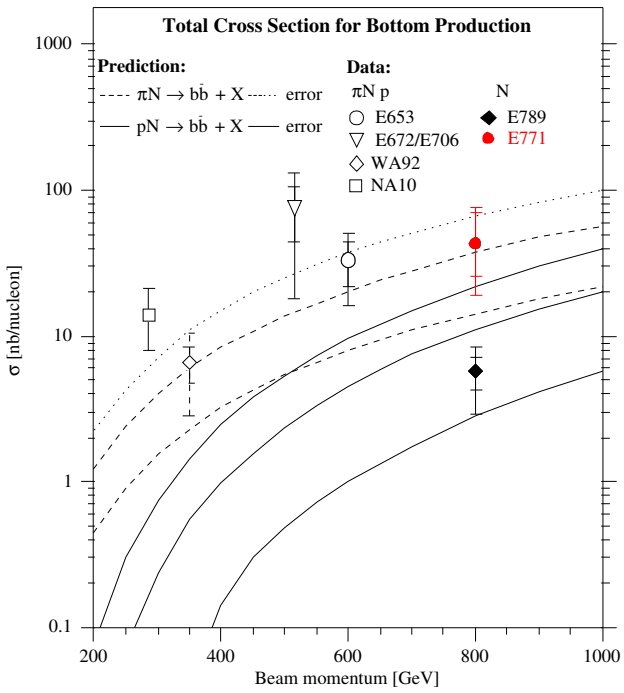

Figure 14: *QCD prediction for the $b\bar{b}$ cross section and experimental results[11].*

The 920 GeV HERA protons hitting a fixed target leads to a center of mass energy $\sqrt{s} \approx 40\,\mathrm{GeV}$, here the $b\bar{b}$ cross section is suppressed by six orders of magnitudes compared to the inelastic cross section. Figure 14 shows the result of QCD calculations up to α_s^3 [28]; they predict for 920 GeV protons a cross section $\sigma_{b\bar{b}} \approx 17$ nb but with large uncertainties. Also shown are experimental data on $b\bar{b}$ production. The results of the two Fermilab experiments E771 [11] and E789[12] which are obtained at an energy range very similar to the HERA – B target differ by nearly one order of magnitude - but they are still consistent within their large errors.

Assuming the QCD predictions for the $b\bar{b}$ cross section one gets at design luminosity the following number of produced $b\bar{b}$ pairs at the HERA – B target:

$$N_{b\bar{b}}/\mathrm{s} = \sigma_{b\bar{b}} \cdot \mathcal{L}/\mathrm{s} \approx 17\,\mathrm{nb} \cdot \frac{3.0}{\mathrm{nb\,s}} \approx 50\mathrm{Hz}\,. \tag{2}$$

This leads to a yield of around 40 B_0 or $\bar{B}_0$ mesons per seconds. The b-yield depends slightly on the choice of the target material [26].

The target efficiency ϵ_T is a very important number to judge on the performance of the target operation, especially at high rates. It describes the ratio between the number of protons interacting with the HERA – B target and the total number of protons which are lost inside the complete HERA p-ring:

$$\epsilon_T = \frac{\text{Interaction Rate}}{\text{Proton Loss Rate}} = \frac{\tau_p}{N_p} \cdot R_{ia} \tag{3}$$

The proton loss rate is determined by the number of protons N_p or the proton current and the proton lifetime τ_p, e.g. a proton beam with a current of $I_p = 100$ mA and a still acceptable lifetime $\tau_p = 50$ h has a loss rate of roughly 72 MHz. This example demonstrates that it is quite important to catch up the main fraction of protons inside the target, before they get lost anywhere else. To limit the impact on the proton lifetime to an acceptable level it is therefore quite important to achieve a target efficiency $\epsilon_T > 50\%$, particular if the target is operated at higher rates.

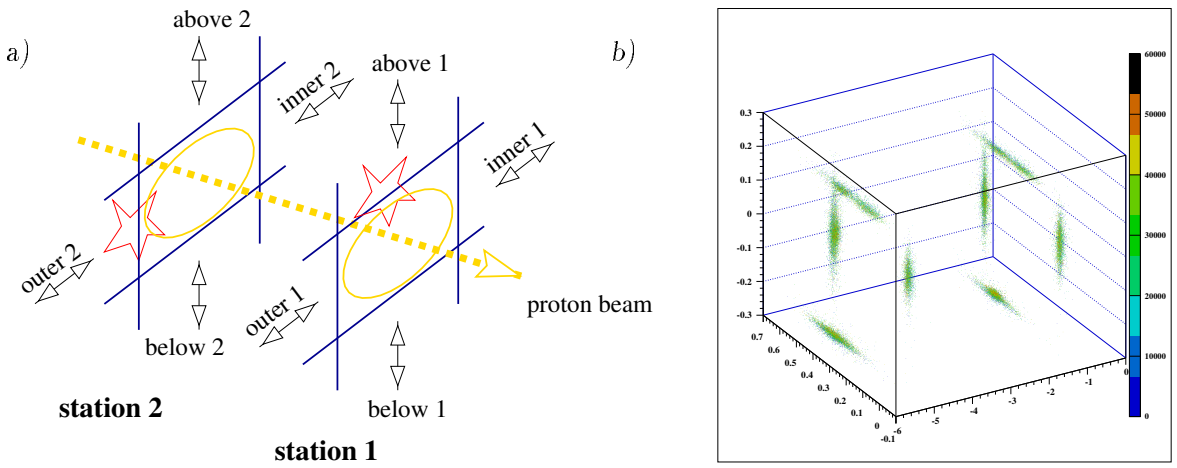

Figure 15: *a) Schematic drawing of the eight target wires surrounding the HERA proton beam. b) Reconstructed vertices while all eight target wires are operated simultaneously at the beam.*

Continuous Operation

A reliable and regular target operation is required to accumulate the necessary statistics for the HERA – B experiment. An operation time of around 10^7 seconds per year is anticipated, something what has to be achieved in parallel to the HERA *e-p* luminosity operation. This requires a continuous and very efficient target operation which uses more than 90% of the HERA *e-p* luminosity time. On the one side this demands a save, reliable and easy procedure to operate the HERA – B target. On the other side the interference with the *e-p* luminosity operation has to be small, something what is strongly correlated with the HERA operation and here mainly to the settings of the proton collimator system and the beam orbit. The HERA proton collimator system was extended during the shutdown in the year 1996 to minimize the impact of target induced background on the other HERA experiments [29]. Since that time the system has proven that a reasonable optimized working point can be established which allows the operation of the HERA – B target at design rate without interfering seriously with the other experiments [30].

Multiple Interactions, Separated Vertices & Target Geometry

The bunch crossing rate of the filled HERA proton bunches is approximately 8.5 MHz[7]. This leads to multiple interactions which are in first order distributed according to the Poisson statistics:

$$P_\mu(n) = \frac{\mu^n}{n!}\exp(-\mu), \quad n = 0, 1, 2, 3, ... \tag{4}$$

where $P_\mu(n)$ describes the probability to get n interactions during one bunch crossing (bx) if the mean number of interactions per bx is μ. The variance of the Poisson distribution is equal to its mean value μ, i.e. one gets a broad distribution.
To simplify and improve the reconstruction of the events it is necessary to obtain a reasonable spatial separation of these multiple simultaneous interactions. Therefore HERA – B uses a multi-wire setup with eight target wires (see Fig. 15)[8]. They are mounted and operated in two stations separated by approximately 4 cm along the beam axis. The typical operation point in radial direction is between 3 to 6 beam sigma, with a typical beam sigma of around 400 μm.

[7] 180 out of 220 buckets are filled - the bunch distance is 96 ns: $f_{bx-filled} = 180/220 * (1/96\text{ns}) \approx 8.5\,\text{MHz}$.

[8] The naming convention (inner, outer, above, below) was chosen with respect to the HERA storage ring. The 1.station is closer to the HERA – B VDS (Vertex Detector System).

Until now the target wires are usually small ribbons with a thickness of 500 μm along the beam axis and a radial width of 50 μm. These dimensions are chosen in such a way that the geometrical defined location[9] of the main interaction vertex on the target is smaller than the expected vertex resolution[10] of the HERA – B detector. The dimensions of the target wires have been not yet decreased further to have a reasonable large amount of material close to the beam in order to be on the safe side with respect to the required large target efficiency. Protons with a betatron amplitude large enough to reach the target usually hit the target each $\mathcal{O}(100)$ turns [39]. Before the protons interact they have to pass in the mean one interaction length λ_{int} of target material (see Table 12), i.e. with the actually used geometrical setup several ten thousand up to a few hundred thousand turns are required. This time scales with the geometrical target dimensions. Hence using smaller target wires the required time increases - and with time also the probability that the proton gets lost somewhere else, e.g. due to diffusion or other scattering processes[11].

Table 12: *Atomic number Z, mass A, interaction length λ_{int}, radiation length X_{rad} and mean angular smearing Θ_{sc} at 920 GeV for various target materials.*

Material	C	Al	Ti	Fe	Cu	W
Z	6	13	22	26	29	74
A	12.	27.	47.9	55.9	63.6	184.9
λ_{int}/cm	38.1	39.4	27.5	16.8	15.1	9.6
X_{rad}/cm	18.8	8.9	3.56	1.76	1.43	0.35
Θ_{sc}/μrad	23.	34.	45.	49.	52.	80.

Stable Rates & Target Steering

To achieve an efficient triggering and an effective data taking and reconstruction with the HERA – B detector[12] it is necessary to provide a reasonable stable interaction rate equally distributed among the various wires in use. This is the task of the target control system (TaCoS). All target wires can be moved in radial direction by stepping motors. The main steering loop operates with a frequency of around 10 Hz and a minimal step-size of 50 nm to stabilize the interaction rate. It retracts the wires in case the actual measured interaction rate is too large or moves them closer to the beam in case the rate is too low. The interaction rate is measured with a hodoscope, which consists of four pairs of scintillating counters. These are equipped with fast electronics, allowing a dead-time less rate measurement. A measurement of the interaction rate on the individual wires is performed by means of integrating the charge produced by δ electron generation inside the target wires [31]. This provides the information for a proper wire selection in a multi-wire operation mode.

Rate Performance & Beam Properties

An efficient triggering and data taking demands that several additional conditions have to be met by the produced target interactions. They are closely related or even defined by the HERA beam properties. The following list summarizes briefly the main topics, which are then discussed in more details in section 2.1.3:

[9] dimension divided by $\sqrt{12}$.

[10] $\approx$ 25 μm in transversal direction and $\approx$ 500 μm in longitudinal direction.

[11] Due to the high intrinsic proton lifetime and the positive experience with a thin test wire we intend to use in the future thinner wires - as discussed in section 2.1.6.

[12] The HERA – B detector with its trigger and reconstruction is basically occupancy limited.

1. The timing of interactions should be within 1 ns out of the 96 ns between two consecutive bunches. Observed problems are coasting beam and side-bunch contributions.

2. One is aiming for a uniform bunch structure, i.e. all filled proton bunches should contribute equally to the interaction rate.

3. The global rate stability also depends on HERA. It is correlated with the settings (e.g. collimators) and stability (e.g. beam orbit) of the machine and HERA has measures to increase the beam halo population which improves the HERA – B rate stability.

2.1.2 Status and Run Experience

First tests of a halo target operation at the HERA proton ring have been performed already in the year 1992. The basic layout, requirements and general principles of operation are discussed in the HERA – B proposal [26] and the HERA – B Design Report [1]. A target test experiment with a reduced and simplified setup was operated in the HERA west right straight section[13] until the year 1995[32]. During that time period the main operation and steering concepts for the target have been developed and the basic properties of the target have been studied. During the shutdown in the year 1996 the final target mechanics was installed at their final position in the HERA – B experiment[14]. Four target mechanics stations are mounted from four sides on the HERA – B VDS vessel, each containing two wire targets which are separated along the beam axis by 40 mm. Since the year 1997 the HERA – B target is in regular and nearly continuous operation. Details of the target commissioning are documented e.g. in [30, 33, 34] and in several Diploma & PHD theses [35, 36, 37, 38, 39, 40, 41, 42, 43, 44, 45].

The target environment is handled regularly by the HERA – B shift crew and worked very stable, reliable and secure. Therefore the maintenance effort could be kept on a reasonable low level since 1998. Most of the basic requirements are obtained regular and a high level in understanding the rationale and the main impacts on the performance and the various dependencies has been achieved so far. In the following section the most important achievements and the performance of the target operation are summarized together with considerations of remaining problems and open questions.

Run Statistic & Reliability of the Target System

Fig. 16 shows the target operation statistics for the last two years. The total number of produced interactions within the years 1999 and 2000 are around $N_{int} \approx 33{,}000\,\mathrm{MHz\,h} \approx 1.2 \cdot 10^{14}$. In some months the target operation time is even slightly higher than the HERA *e-p* luminosity time due to the fact that the target was sometimes operated during periods without *e-p* luminosity (no positrons available, HERMES 12 GeV running, ...).

- The target operation time in the year 1999 was 84 % and in the year 2000 94 % compared to the HERA *e-p* luminosity time. The main losses are caused by waiting for the permission from the other HERA experiments to insert the target. In the year 2000 this was mainly the time until the HERMES detector was switched on. The lower run efficiency in the year 1999 was mainly caused by the interferences with the ZEUS-LPS [46] detector and the correlated intensive task force studies (details are discussed in section2.1.3).

[13] at WR118 - i.e. in the **W**est **R**ight HERA octant, 118 m upstream of the center of the HERA West Hall.

[14] The location is approximately at z=0 m in the HERA – B coordinate system, which corresponds to WR009 in the HERA coordinate system.

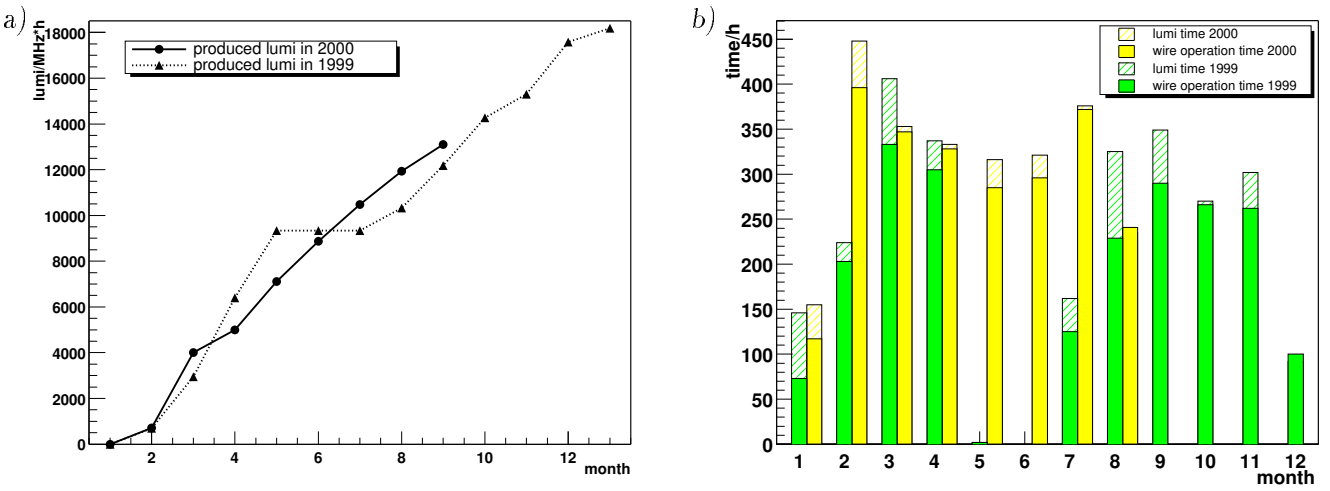

Figure 16: *Target operation statistics for the years 1999 and 2000: a) Number of interactions produced at the HERA – B target in the years 1999 and 2000. b) HERA luminosity time and target operation time for each month in the years 1999 and 2000.*

- Losses due to technical problems account for $\mathcal{O}(< 1\,\%)$. They have been mainly due to: crashes of the target database server, failure of the HV or stepping motor controller, break of electronics components, ...
- Problems to insert wires or a very unstable and non proper target operation also accounts to losses of $\mathcal{O}(1\,\%)$. They are usually correlated with bad beam conditions, e.g. high and spiky background. Therefore this behavior should be considered more as a feature than a bug. Nevertheless serious considerations has started to adopt inside the target control more automated to unstable beam conditions.
- The reliable and smooth operation allowed to schedule on call target experts for periods of two week. Their main effort during these 14 day periods went into:
  - visiting meetings and coordination tasks (HERA and dedicated target studies)
  - $\approx$ 2 working days to provide run overviews, including the handling and accounting of data base files and the preparation of summary pictures
  - the communication with the shift crews, give them instructions and advice. This accounts for less than one day.
  - fixing technical problems demands usually less than 10 % of their time

Target Operation in the Year 2000: Wires, Rates & Operation Point

Fig. 17 shows how often the individual wires have been used and at which rate the target was operated during the run period in the year 2000. The running was dominated by the operation of the single wire *Inner2* at a rate of 4 or 5 MHz. During 26.7 % of the runtime a multi-wire configuration was used. This was typically a two-wire setup (14 %). Four wires have been operated during 8.1 % and more than four wires just during 0.13 % of the run time.

As shown in Fig. 18a) the various target wires operate usually at a distance of $3 - 5$ rms beam width[15] from the center of the beam. One observes systematic differences between the various

[15] The typical beam size of the HERA proton beam at the target wires is $\sigma_x \approx \sigma_y \approx 400\,\mu$m.

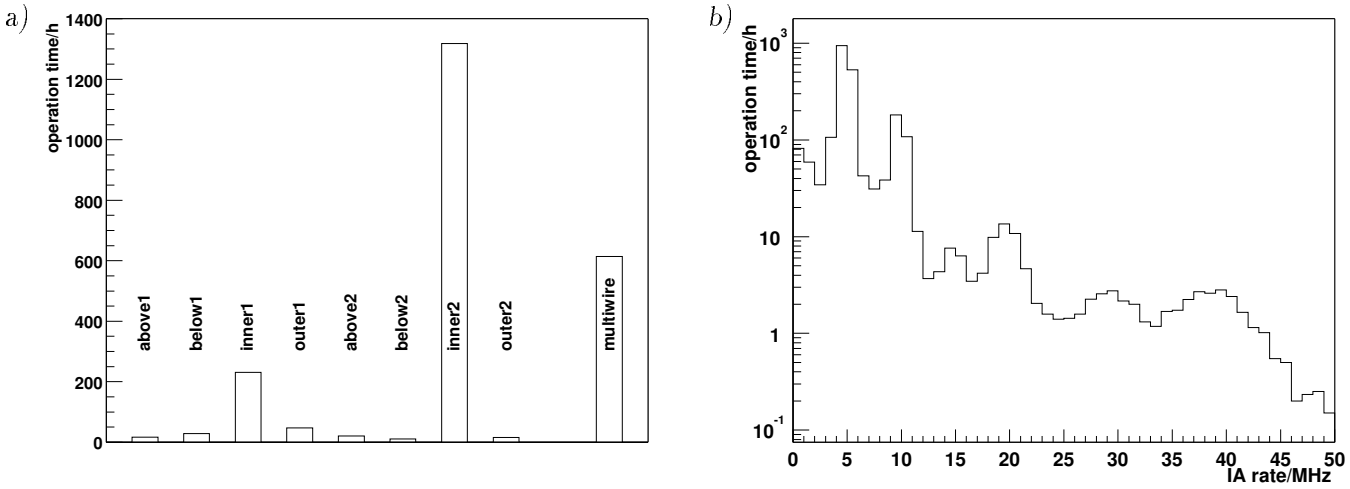

Figure 17: *Overview about the usage of the individual wires (a) and the target rate (b) during the run period in the year 2000.*

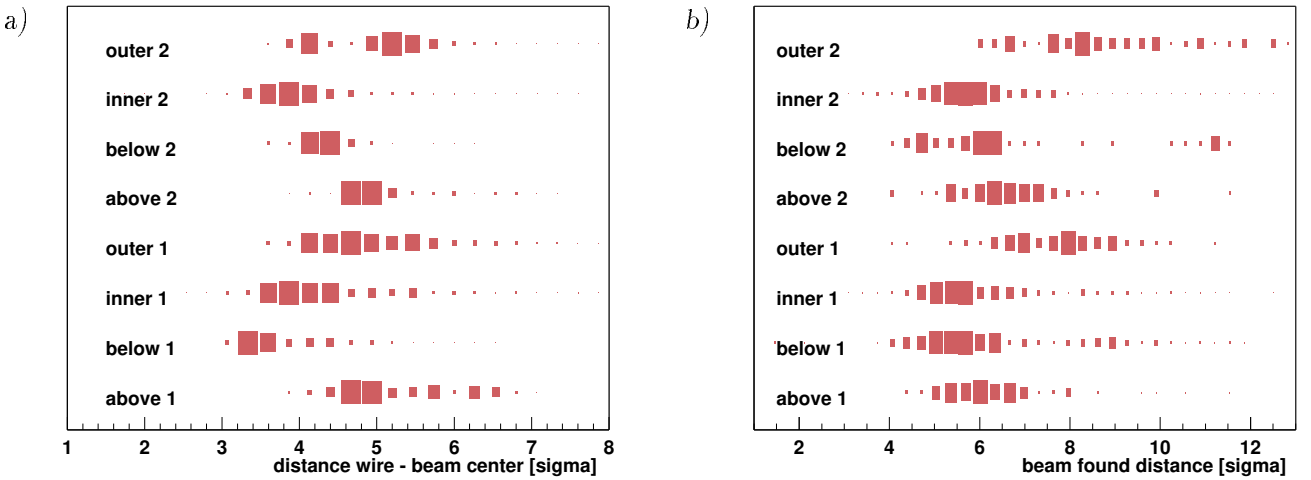

Figure 18: *a) Distance of the various used target wires from the beam center during rate operation in the year 2000. b) Distance δ_{bf} of the various wires when they "found" the beam (cp. text).*

wires. The most obvious and dominating impact arises from coasting beam protons which causes due to the dispersion $D_{x/y}$ in the target area broad transverse tail on the outer and above side (see section 2.1.3). Other reasons for the differences are e.g. due to varying values for the beam sigma, influenced by the operation conditions (collimators, rates, new or old fill, statistics) or due to errors in the alignment or the measurement of the target and the beam position. Fig. 18b) shows the distance from the beam center at which the target wires reached the beam halo. This *beam found position* δ_{bf} is calculated by the first significant increase of the target rate and is determined by the aperture limitation A which is mainly defined by the HERA p collimator-system. One gets rather tight settings[16]: the mean value of δ_{bf} is around $6.5\,\sigma$ and the most probable value around $5.5\,\sigma$. Transverse coasting beam tails are again the main source for systematic deviations; these tails are very distinct on the outer side and causes there the high values of δ_{bf}. Evaluating the collimator settings one gets similar close aperture limitations for the HERA proton beam. Such tight aperture

[16]Values larger than $10\,\sigma$ are usually unreasonable and should be neglected. They are mainly due to measurement errors e.g. unstable background rates which makes it difficult to define in an automated way the beam found position.

limitations causes a problem for the target operation[17], it reduces the target efficiency and leads to less stable rate as discussed in the next sections.

Under the actual HERA operation conditions with a very high intrinsic proton lifetime the impact of diffusion processes on the target efficiency ϵ_T is small. ϵ_T is dominated by the multiple scattering inside the target which is described by the mean scattering angle Θ_{sc} within one interaction length λ_{int} of target material (cp. Tab. 12):

$$\Theta_{sc}^2 \approx \left(\frac{14\,\mathrm{MeV}}{p}\right)^2 \cdot \frac{\lambda_{int}}{X_{rad}} \tag{5}$$

with p the momentum of the protons hitting the target. The scattering angle is large compared to the beam divergence $\sigma_{x'/y'} = \sqrt{\epsilon/\beta} \approx 10\mu$rad at the target. This angular smearing leads therefore to a significant broadening of the betatron amplitude of these protons and to their potential loss on collimator jaws or other aperture limitations. Very tight proton collimator settings results therefore in a small target efficiency ϵ_T. The distance between the target position and the aperture should be at least two sigmas to achieve the requested target efficiency of more than 50 %. Actually the mean distance is just around $1.5\,\sigma$. The better understanding of coasting beam properties at HERA-p also improved the understanding of its impact to the target efficiency. Depending on the used wire configuration one has to distinguish between bunched and non bunched loss rates. Unbunched coasting protons are shifted due to the dispersion in the target area mainly to the outer side. If one operates just a target wire on the inner side then these protons have nearly no possibility to interact with the target wire. The analysis of rate scan data allows here to distinguish between two loss rates, a bunched beam loss rate which generates the target interactions and an independent coasting beam loss rate. One gets then even with the actual tight collimator settings a mean value for the target efficiency of around 45% with respect to the bunched loss rate. The estimated coasting beam loss rates are typically $\mathcal{O}$(10 MHz).

Rate Stability

All kind of rate fluctuations[18] leads to a frequency distribution of the number of produced interactions which is broader than the optimal Poisson distribution. One gets therefore an enhanced probability for events with less and events with more interactions than aspired. The low multiplicity events reduce directly the available statistics and the high multiplicity events are usually rejected within the trigger or reconstruction chain[19]. The measurement of rate fluctuations depends on the chosen frequency or time range, details can be found in [42, 45]. Most of the pictures and numbers quoted within this section uses the important short term rate fluctuations σ_s which are evaluated by means of the normalized difference between two consecutive measured hodoscope rates; they are measured approximately every 100 ms[20]. Fig. 19 shows these short term fluctuations for the complete run period in the years 1999 and 2000 as a function of the time within a week. One obtains a mean value for the rate fluctuations of approximately 8 % with a very pronounced structure. The target rate gets much more unstable during usual working hours, i.e. Monday to Friday between 7h and 16h, revealing a strong impact of civic noise on the target performance. The overall rate stability is reasonable good[21], but there are time periods with larger fluctuations which leads to an efficiency loss for the HERA – B experiment.

[17] The usual conditions are now significant tighter than the initially requested and assumed $\geq 3\sigma$ free space between target and collimator position.

[18] Also the later on discussed bunch to bunch variations.

[19] The trigger system even selects dominantly high multiplicity events, which might then even spoil up the system.

[20] The short term fluctuations here are obtained by calculating the sigma per each half hour of stable target operation.

[21] Fluctuations smaller than 10 % are considered as good.

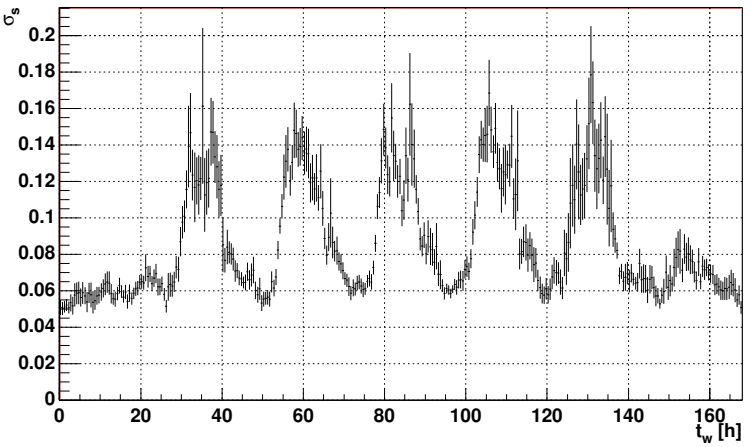

Figure 19: *Short term rate fluctuations σ_s during the run period in the years 1999 and 2000 plotted versus the time in hours of a week (starting on Sunday 0h up to Saturday 24h).*

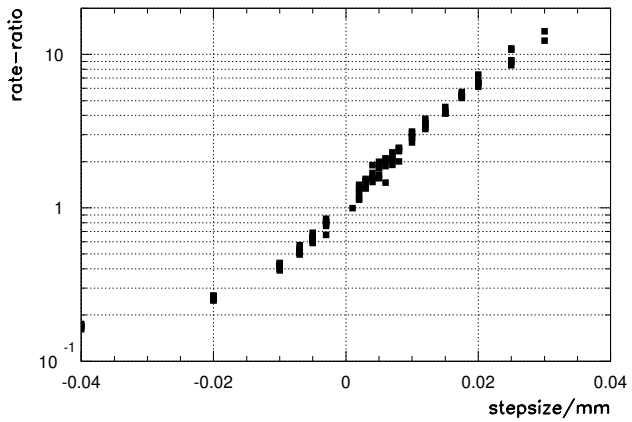

Figure 20: *Step functions measurement: ratio of the interaction rate as function of the applied step size.*

One important investigation in the understanding of rate fluctuations is the analysis of step function measurements. Such a measurement is shown in Fig. 20: it indicates the ratio between the obtained interaction rate after and before the target was moved with a well defined step size. These measurements reveals typically a rate sensitivity of a factor two per 10 μm. This indicates that the target rate stability is sensitive to beam orbit fluctuations. Fig. 21 shows the fluctuations of the beam orbit close to the HERA – B target for the run period during the years 1999 and 2000 also as a function of the time within a week. They show the same systematic increase during usual working hours as the rate fluctuations in Fig. 19. Assuming the rate sensitivity obtained from step function measurements then the level of the observed rate fluctuations is compatible with what one expects from these beam orbit fluctuations [45]. During the run-period in the end of the year 1998 and in the beginning of the year 1999 several extreme examples have been observed which emphasizes the close correlation between civic noise and rate stability. During this time period an ongoing heavy ground work in the Volkspark stadion close to DESY took place which spoiled up sometimes the target operation completely. This was strongly correlated with an increased ground motion[34, 42].

Other important systematic impacts to the rate stability are shown in Fig. 22:
(a) - tighter apertures leads to increased fluctuation
(b) - a low ϵ_T is correlated with tight apertures and results in larger fluctuations.
Fig. 23 shows the obtained rate fluctuations for all eight target wires during the run period in the year 2000. One observes several systematic dependencies:

Target Orientation: Wires moving in vertical direction deliver a more unstable rate than the wires in the horizontal direction. This is correlated with the larger beam fluctuations in the y direction (cp. Fig. 21).

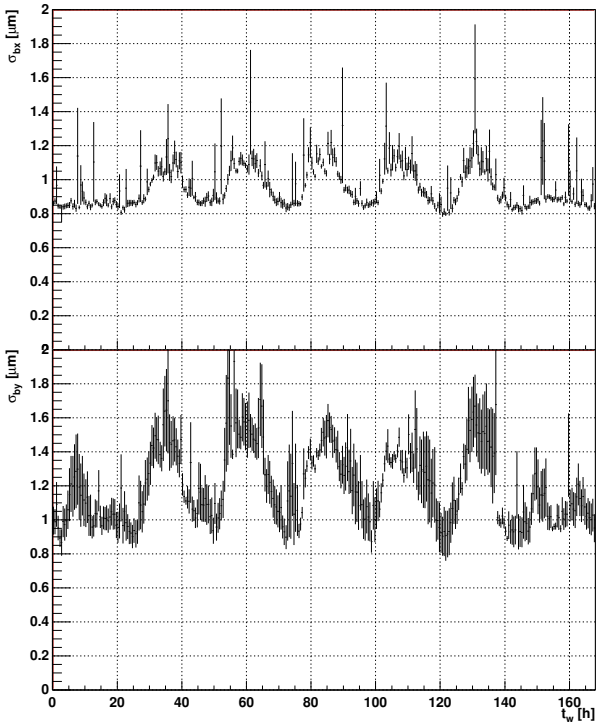

Figure 21: *Short term beam orbit fluctuations in horizontal (σ_{bx}) and vertical (σ_{by}) direction for the run period in the years 1999 and 2000 plotted versus the time in hours of a week (starting on Sunday 0h up to Saturday 24h).*

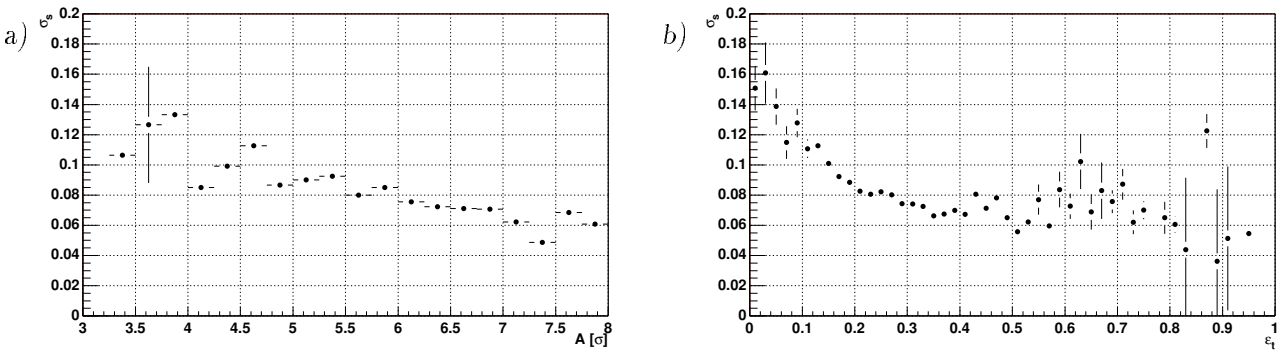

Figure 22: *Short term rate fluctuations σ_s as a function of the measured aperture A (which corresponds to the beam found position δ_{bf}) (a) and the target efficiency ϵ_T (b).*

Target Material: The tungsten wire at the position Below-2 ($n_w = 5$) gives the largest rate fluctuations. This is presumably due to the large scattering inside the heavy target material (cp. Tab. 12 and Eq. 5) which leads to a low target efficiency ϵ_T. This target ribbon has in addition a nearly "perfect" geometrical shape without small edges and roughness of the surface. Even if this target moves just by a small step towards the beam a large amount of even heavy material arises where the protons scatters. One assumes that targets consisting of lighter material and with non perfect geometrical properties or with a round shape enables a smoother "beam scraping" (cp. section 2.1.3).

Outer Wires: Their operation is dominated by coasting beam properties which results usually in very unstable rate while one scrapes off transversal coasting beam tails (which accounts for a considerable fraction of the operation time for the Outer-1 target) and rather stable rates after that at the bunched beam (presumably due to the larger transversal "diffusion" rate).

Target Shape: For the Outer-2 target ($n_w = 7$) a 50 μm round wire was used. This target shows the smallest fluctuations.

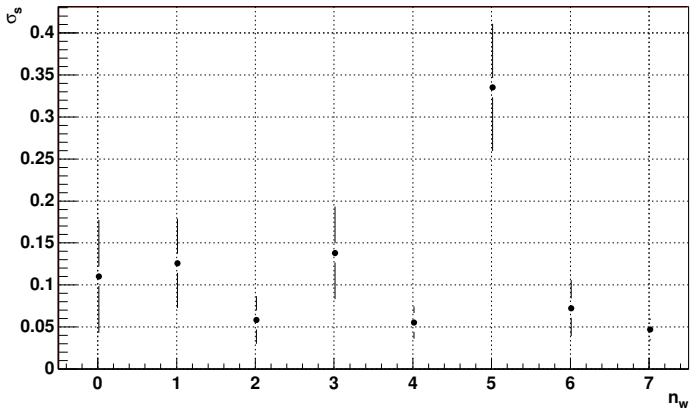

Figure 23: *Short term rate fluctuations σ_s for the different target wires. The wire number n_w from 0 to 7 corresponds to the above, below, inner and outer targets of the 1. station (0 to 3) then of the 2. station (4 to 7).*

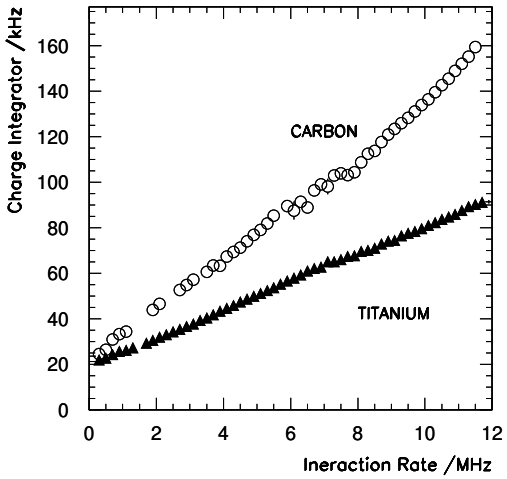

Figure 24: *Example of two calibration curves for the charge integrators connected to the target wires Inner-1 (Ti) and Inner-2 (C).*

Multi-wire Operation

A big improvement in the hardware setup for multi-wire operation has been achieved in the last run period. During the Xmas shutdown 1999/2000 the charge integrator electronics was completely replaced[22]. The sensitivity of the electronics is increased by more than two orders of magnitude[23], it works very reliable and gives an improved stability and linearity. Fig. 24 shows an example of the correlation between the interaction rates measured with the hodoscopes and the values obtained by the charge integrator measurement. With this setup one obtains a very reasonable multi-wire operation performance. The main cross check comes from the analysis of vertex detector data. Fig. 15b) shows the reconstructed vertices for a run where all eight target wires have been operated simultaneously and contribute rather equally to the interaction rate[24]. A more quantitative event by event based analysis is summarized in Fig. 25. It shows for a four wire operation the correlation between the number of wires on which a vertex was found and the total number of reconstructed vertices for real data and Monte-Carlo data. The agreement is remarkable good and indicates a very homogeneous illumination of the four used wires.

[22]Thanks to the common effort of the MPI Heidelberg and KINR Kiev.

[23]compared to the previous used first generation of electronics.

[24]this describes the time integrated properties. The more often tested four wire operation leads to a contribution of $\approx 25 \pm 3\%$ for each individual targets.

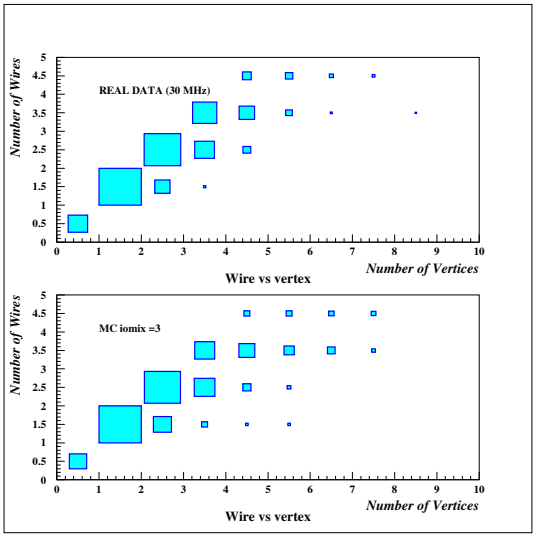

Figure 25: *Four wire operation: number of wires on which a vertex was found as function of the total number of reconstructed vertices for real data and MC data. The left lowermost point corresponds to (0,0), the neighboring point (1,1) has the highest probability.*

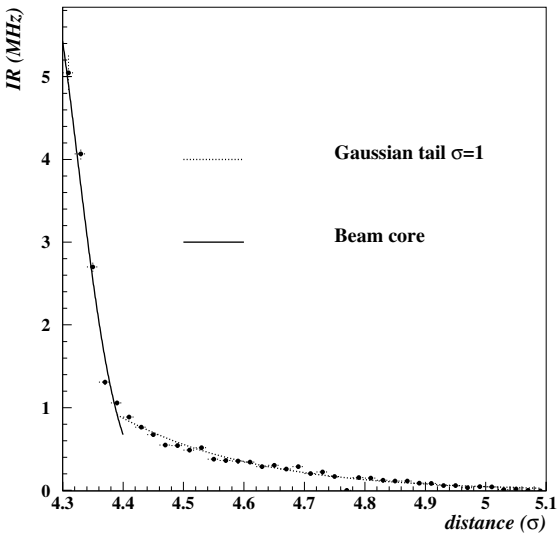

Figure 26: *Interaction rate produced on the Below-1 target as a function of the distance to the beam core during a two wire operation at a constant total rate of 10 MHz.*

Several studies have been carried out to investigate the impacts and to reveal the sensitivity of the multi-wire operation. One example where two target wires (Inner-1 and Below-1) have been in operation is shown in Fig. 26. The Below-1 target was retracted and reinserted (typically using 10 μm steps) while the total interaction rate was kept constant at 10 MHz[25]. During the first few retraction steps the contribution of the Below-1 wires drops steeply. Already after four steps the relative rate contribution decreased from the initial 50 % to roughly 10 %. This reveals a similar sensitivity as the step function measurements shown in Fig. 20. The further decrease can be well described by a Gaussian distribution with the sigma of the proton beam.

Even if the general multi-wire operation performance looks quite promising some problems have been observed. The baseline of the charge integrator electronics[26] is not very stable. Variations are observed which correspond to an interaction rate of several hundred kHz (or even more). This makes the calibration difficult and might lead especially at lower rates to non equal contribution of the various wires. These base line variations are most likely caused by the RF field of the charged p-beam[27] and cross talk between the different channels. Therefore several potential improvements

[25] The Inner-1 target was moved by the automatic slightly ($< 0.1\,\sigma$) closer to the beam.
[26] Defined by a calibration current.
[27] mirror currents, pickup or wake fields - that's not yet finally understood.

for the next run period are under considerations. The charge integrator cabling including the various connections, grounding and shielding will be improved. A more complicated tube wire configuration[28] is as test setup for one single wire under discussion. Additional improvements might come from the online analysis of the vertex detector data. The number of vertices per wire found in the second or third level trigger could be used as a feedback to readjust the calibration constants.

Another problem was occasionally observed at the operation at higher rates, the rate stability got worse and screwed up the multi-wire performance. The main improvement here has to come from measures applied by HERA (as discussed in the next section) to increase the rate stability. The long term multi-wire operation, especially at higher interaction rates, is not yet finally commissioned. That is mainly due to the fact that the target operation during the last two run periods have been dominated by a low rate single wire operation.

2.1.3 HERA and Beam Related Topics

The performance of the target operation and the quality of the produced interaction rate are closely related to the HERA operation and the properties of the p-beam.

Background and Interference with other Experiments

During the last years the potential interference of the HERA – B target operation with the other HERA experiments was seriously considered. Protons scattered elastically at larger angles inside the target might cause increased backgrounds at the other experiments. In addition it was realized that a second important background source at HERA arises from coasting beam protons. This lead to more complicated conditions, because this coasting beam background shows a different behavior: it develops with time during a fill and depend very strongly on the used wire configuration; here the target operation can even improve significantly the background situation.

In the beginning of the run period which started in July 1999 the ZEUS LPS[29]-detector[46] suffered under serious background problems which were partially correlated to the target operation. This lead to the formation of a task force group which investigated the overall background situation and finally managed to establish good running conditions for all HERA experiments [48]:

- A key point is the understanding of aperture limitations and the operation point of detectors or devices which are moved close to the beam[30].
- The main background reduction has to come from the collimator system. The system is able to fulfill this task, but this requires optimized settings. E.g. the jaws should not be set too close to the beam, because this reduces the target efficiency ϵ_T and increases therefore the number of scattered protons which get lost without interacting in the target.
- The smooth operation of all experiments with their various requirements relies on an optimized and very stable and reproducible operation of HERA.
- Any measure to reduce the coasting beam content at HERA helps to improve the background situation.

[28] target wire with thin insulator surface and one additional shielding surface - which would be connected to a second voltage to increase the gain further.

[29] Leading Proton Spectrometer

[30] e.g. it was initially tried to operate the LPS detector too close to the beam [48].

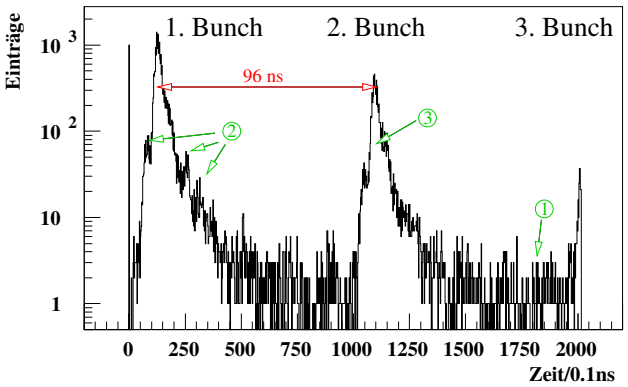

Figure 27: *TDC measurement of the interaction rate: (1) - coasting beam contributions, (2) - side bunch contributions and (3) contributions from the main bunch.*

After that optimization the usual HERA – B low rate running was performed without any serious interferences. Even during the several shorter test operations at our design rate no critical background problems has been observed. H1 observed sometimes a non critical increase of several rates inside their central detector. Due to the fact that the HERA – B detector and trigger commissioning required a low rate operation no systematic studies and attempts to improve the situation further has been performed.

Timing of the Interactions & Coasting Beam

The generated interactions in the HERA – B target should be due to protons in a narrow time window of approximately 1 ns length around the main bunch. Fig. 27 shows a TDC measurement of the interaction rate over two consecutive bunch crossing, which reveals this requirements together with the observed deviations. Two problems are obvious, which are observed on a regular basis:

Side Bunch Contributions: a significant amount of interactions are coming out of the ± 5 ns side bunches. These buckets are generated by the 208 MHz RF-system and filled with protons from the main bunch. Their existence is well known since long time and they are regularly observed e.g. inside the LOPEZ monitor measurements[47]. Different HERA – B measurements reveals side bunch contributions in the 10...20% level[31] [43]. All potential measures to reduce the side bunch population relies on HERA, it depends on details of the timing, synchronization and the RF system operation during the HERA filling procedure. The problem could be reduced if it would be possible to provide shorter bunches, but there exists serious limitation inside the HERA pre accelerator chain. The side bunch population is presumably correlated with the coasting beam generation inside HERA.

Coasting Beam: especially on the outer and above targets a significant amount of unbunched coasting beam contributions to the interaction rate are observed. Typical values are between a few MHz up to more than 10 MHz. Details concerning coasting beam are discussed e.g. in[33, 38, 44, 49]. Protons with an energy deviation $|\Delta E/E| > 2...3 \cdot 10^{-4}$ start to cross the separatrix in the longitudinal phase space and travel now freely (unbunched) around the proton ring. At HERA one usually just observes protons with negative energy deviation, the main reason for that are presumably the energy losses due to synchrotron radiation which accounts for approximately 10 eV/turn. Due to the dispersion $D_{x/y}$ in the target area these protons are displaced in the horizontal phase space to the outer and above side: $\Delta x/y = D_{x/y} \cdot \Delta E/E$. The production

[31] target hodoscopes, RICH and OTR. There are some uncertainties e.g. with the time resolution properties of the counters - thats one reason to build a new set of scintillator counters.

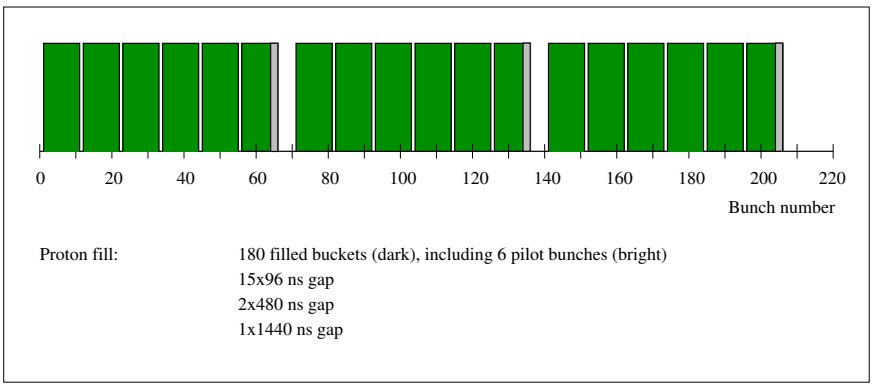

Figure 28: *Bunch scheme of the HERA proton ring.*

mechanism, which forces the protons to cross the separatrix, is not yet finally understood, several potential reasons are under discussions:

- **Intra Beam Scattering:** is most likely the main reason for the observed longitudinal lengthening of the main bunch
- **RF settings:** tests which has been performed during the summer of the year 2000 indicates that the production depends e.g. on the amplitude of the 52 MHz system.
- **RF noise:** noise in the RF system is supposed to generate chaotic behavior and to increase the longitudinal instability. Until yet it is not verified whether the actual low level of noise in the HERA RF-system leads to any significant impact.
- **Energy loss inside the target:** from all actual considerations and observations one concludes that the energy loss of protons inside the target is not the main source [33].

To reduce the impact of the coasting beam HERA has invented a system which excites the coasting beam protons transversally inside the dump gap with the intention to kick them effectively out of the proton ring [44]. In Fig. 28 the bunch scheme of HERA is presented, the last 1440 ns long gap is required to ensure a save dump of the protons. The coasting beam kicker was in nearly regular operation during the last run period. It helped to keep the coasting beam related background under control and to reduce slightly the level of coasting beam target interactions on the outer and above side[32]. Unfortunately it causes other problems, the excitation of several filled bunches, which lead to nonuniform contributing bunches. This is discussed in the next section.

Equal Contributions of all Bunches

A measurement how regular all $N = 180$ filled proton bunches contribute to the interaction rate is performed by calculating the RMS from the distribution of the relative contributions λ_i of the 180 filled bunches [38, 44]:

$$\sigma^2_{bx,rel} = \sigma^2_{bx}/\bar{\lambda}^2 = 1/\bar{\lambda}^2 \cdot \frac{1}{N}\sum_{i=1}^{N}(\lambda_i^2 - \bar{\lambda}^2) \ . \tag{6}$$

The RMS value is directly correlated to the number of effectively contributing bunches n_{eff}:

$$n_{eff} = \frac{(\sum_{i=1}^{N}\lambda_i)^2}{\sum_{i=1}^{N}\lambda_i^2} = \frac{180}{1+\sigma^2_{bx,rel}} \tag{7}$$

[32]Due to the rare operation of these wires it is difficult to judge quantitatively about the achievements. An analysis of the data is underway.

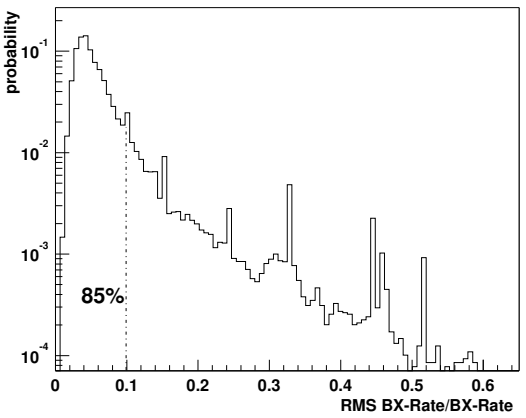

Figure 29: *Measured bunch to bunch variation $\sigma_{bx,rel}$ for the year 2000.*

In Fig. 29 the measured bunch to bunch variations for the run period in the year 2000 are plotted. During 85 % of the time the variations are smaller than 10 %, a value which is considered as limit for good running condition. More non uniform contributions are usually due to one of the following reasons:

- Reflections of the coasting beam kicker leads sometimes to a characteristic excitation of several bunches within the first 20 filled bunches. This problem can be usually significantly reduced by separating the HERA tunes from the kicker frequency.
- The tune control on a certain positron bunch increases usually the contribution of the corresponding proton bunch due to beam beam interaction drastically. Switching off the tune control is the measure which improves or even cures the situation[33]. The important impact of the beam beam interaction on the halo population of the proton bunches is also in other examples obvious, e.g. the six non colliding proton pilot bunches contribute usually much less to the interaction rate compared to the other bunches and quite often differences in the positron bunch currents are reflected in the bunch contribution to the HERA – B interaction rate [49].
- Another source for non-homogeneous bunch contributions arises sometimes from timing problems during the injection.

Rate Stability and Beam Tail Shaping

Also the global rate stability depends on HERA. Due to the intrinsic high proton lifetime of several hundred up to a few thousand hours there are not enough protons diffusing into the beam halo for the target operation. Therefore the target has to scrape away protons from the beam tails. This leads to a large sensitivity of the rate stability to all kind of beam fluctuations as shown e.g. in Fig. 19 and Fig. 21.

Several proposals to broaden the beam tails and to increase the halo population without disturbing the emittance of the beam core[34] has been discussed and tested during the last years. These measures to improve the HERA – B rate stability are called "beam tail shaping". A very promising attempt is the application of a tune modulation. First successful tests has been performed by HERA in December 1999 [49]. After solving several safety relevant hardware problems inside the setup a commissioning of the system has started in July 2000. The system is not yet finally commissioned but has already demonstrated that it can improve the rate stability significantly.

[33] another measure would be to scrape away a significant fraction of the affected proton bunch.
[34] which is important to obtain a high specific e-p collision luminosity.

Further Plans and Prospects

The effort to understand and improve the beam related problems of the target operation will continue during the luminosity upgrade shutdown period with the main emphasize on coasting beam and rate stability related topics. This includes the detailed analysis of the data taken during the last years and the further development of target-beam simulations. In addition the theoretical modeling and calculations from the machine physicists are required. The hope is that the comparison and discussion if the result leads to an improved understanding. The further fruitful and constructive cooperation with the HERA machine physicists is here essential for all progress and improvements in the future.

2.1.4 Shutdown Plans: Hardware Upgrades & Repairs

The two main hardware building blocks of the HERA – B target are the target mechanics including stepping motors and controllers and the counters including the required electronics. For both parts major upgrades are foreseen during the shutdown 2000/2001.

Target Mechanics

The actual target mechanics is already since five years in nearly continuous operation. The fact that no spare units are available and that we observed indications of aging and wear out[40] led to the decision to rebuild the mechanics. Several weak points have been located in the old construction. Therefore it was decided to redesign the complete target mechanics.

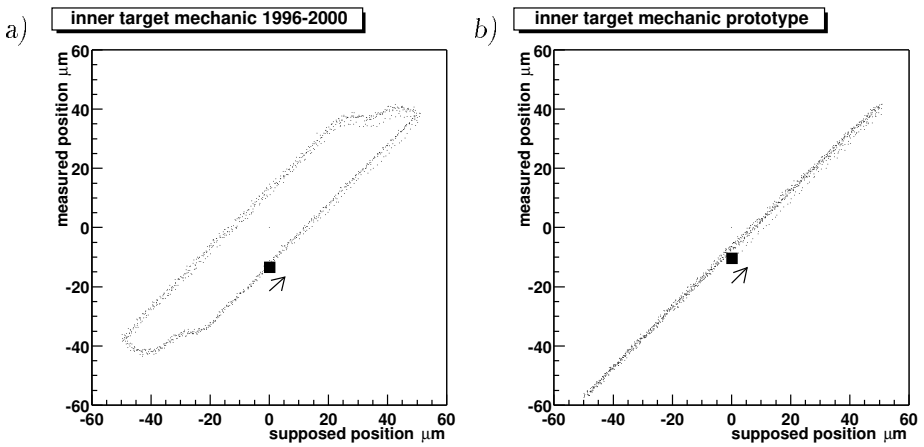

Figure 30: *Measured hysteresis of the actual (a) and the new (b) target mechanics.*

Based on the old design, the experience of the survey and picking up ideas from the VDS manipulator design a very nice solution was found which leads to an improved mechanical accuracy. Fig. 30 shows the measured hysteresis for one axis of the actual setup and of a prototype for the new mechanics. Whereas the old setup shows a significant hysteresis of around 20 μm this problem is completely vanished in the new design. A sketch of the new target mechanics is shown in Fig. 31. The main design criteria was to build something what is rather simple and solid to obtain a precise and robust device. One other key design criteria was the modularity of the system. The most important changes compared to the actual mechanics are:

- A rigid x-y table for the lateral adjustment connected with a large bellow to the VDS vessel.

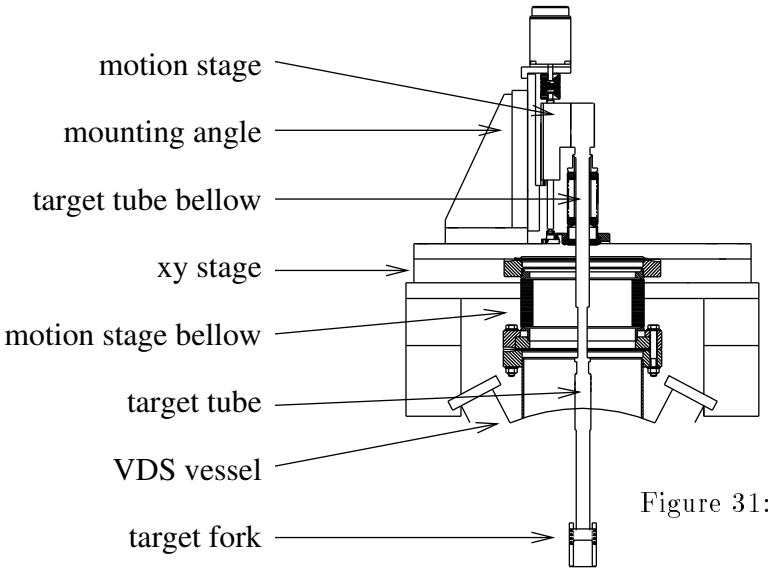

Figure 31: *Scheme of the new target mechanics.*

- Separate small bellows for the transversal movement of the targets mounted on top of the x-y table.
- The target "tube" which goes into vacuum and on which the target forks are mounted is now milled from one block of metal.
- Planar surfaces milled with high precision together with high precision mounting guidance are used for all mounting points at which different parts are screwed together.

Two prototypes have been build in the last year. The old mechanics station on the above side was replaced during the Xmas shutdown 1999 by a prototype mechanics, which has been operated successfully since that time. The second prototype was used for several survey measurements and as starting point for various smaller improvements. In the beginning of September 2000 the revision of the design will be finished followed by the ordering of components and the manufacturing of the new target mechanics. The mechanics is expected to be ready in January 2001 and after some tests it will be installed in May 2001.

The final fork design is actually under consideration. The baseline design foresees a smaller fork width with an opening of 24 mm, this allows a much simpler exchange of single target forks through the round opening for the small bellow on the x-y table[35]. Open issues are e.g. details concerning the cabling of the forks and the mounting of the wires and end-switches. A final design is anticipated after some tests which are scheduled for November 2000.

This rebuild of the target mechanics does not affect the infrastructure. I.e. all parts like cables, end-switches and end-switch box, stepping motor controllers and power amplifier, the target control software etc. can be reused. Some mechanical alignment and intensive survey tests are foreseen but the final alignment has to come from VDS data. The expected costs of around 100 kDM are covered by the University of Dortmund.

Counters & Electronics

The target steering, the HERA – B luminosity determination and the monitoring of beam related rate properties relies mainly on a set of scintillating counters. The actually used hodoscope counters

[35] An optional reuse of the actual target forks is foreseen.

are since five years in continuous operation, there exist no spares and we observed indication of a decreased performance, esp. in the time resolution. This lead to the decision to build one additional set of hodoscope counters, again consisting out of four pairs of scintillating counters. Basic design requests are to obtain a better time resolution (≤ 300 ps) and to cover a larger acceptance (factor four compared to actual counters). The expected costs of around 30 kDM are covered by the University of Dortmund.

For the electronics some maintenance work, an inspection of the modules and a revision of the cabling is foreseen. In addition a few improvements of the setup are under consideration, e.g. to order spares for important components (HV-system), provide additional signals (gated rates and coincidences) and the installation of a multi-hit TDC system.

2.1.5 Shutdown Plans: Software Setup

The considerations on software related developments and improvements have started. For some improvements it is most likely more efficient to perform them during the startup and commissioning phase in the autumn 2001.

TaCoS: A global revision of the target control system (TaCoS) is foreseen. There exists detailed plans, proposals and wish lists. Topics under consideration are e.g. to fix known bugs, a more flexible reconfiguration, the beam finding part, improved online monitoring, the distribution of target info etc.

System Aspects: The structure of the complete setup after the shutdown in the year 2001 is under discussions. The questions here are mainly related to the handling of the database servers and files, the analysis platform and the online monitoring. The anticipated goal thereby is to obtain an even more powerful and reliable system with a simpler setup which reduces the maintenance effort further.

DQM and SCS: A further integration of target diagnostic into the data quality monitoring (DQM) and of control processes into the common slow control system (SCS) is foreseen.

HERA information: The software for the data exchange between the HERA experiments (Netmex) has to be revised. Obsolete info should be removed, new desired data should be added and the programs should be included into the SCS.

2.1.6 Target Setup & Commissioning Plans for the Year 2001

Besides the modifications discussed in the previous section we intend to modify the wire geometry. The proposal is to use as default 50 μm round Ti wires. The actual run experience with such a wire looks very promising and one expects an improvement in the rate stability. Before taking the final decision there are a few questions related to the impact on coasting beam and the target efficiency which has to be studied in more detail. Whether also other target materials should be installed depends strongly on the HERA – B run plans and physics goals for the run period in the year 2001. In case of a strong wish to have different materials to study e.g. A dependencies we propose to consider following options:

- W: wire 50 μm
- Al: wire 50...100 μm or a ribbon with 50 μm $*$ 500 μm thickness

- Fe: wire 50 μm
- C: ribbon with 100 μm $*$ 1000 μm thickness

A first reasonable opportunity to exchange target wires might be during the Xmas shutdown 2001.

The improved target environment should be available from the beginning of August 2001, a stable operation of HERA which allows the operation of the detectors and a physics data taking is not expected before September 2001. The general intention is to provide again a stable, reliable and fully operational device which is able to achieve the desired performance. A couple of commissioning steps are required during the startup phase in the year 2001. Special emphasize requires here the operation of the new hardware components (mechanics and counters) and the modified target control system. Here one really has to ensure a very high level of reliability and safety. The commissioning requests have to be included into the general HERA – B run plans for the year 2001 and depend in addition strongly on the progress of the HERA commissioning after the luminosity upgrade shutdown. For the target operation no serious problems are expected, the main concerns are related to the HERA operation and the beam quality (coasting beam, rate stability, backgrounds, side-bunches and uniform bunch contributions).

Basic Functionality: experience shows that its feasible to establish the basic functionality within a few fills even after a long shutdown. One has to check:

- all wires are reaching the beam and produce rate
- the acceptance of the counters and therefore the rate known within 50 %
- first judgment on beam related topics: background, rate stability, bunch variations, coasting beam
- safety features

In case there occurs no unexpected serious problems the target operation after that first step can be handled over to the usual shift crew

First Calibration & Alignment: this requires a working and reasonable calibrated ECAL and an aligned VDS. One should expect at least a period of one month from the first data taking until one achieves a rate calibration better than 10% and a target alignment with a precision below 10 μm. This accuracy should be sufficient for most commissioning steps of the HERA – B detector. Further improvements depends on the progress of the ECAL and VDS detector. After the first month one should have also a clear picture concerning the calibration and stability of the charge integrators.

Beam Related Studies: all plans and progress on beam related topics like coasting beam and beam tail shaping depends strongly on the HERA performance and their plans. But one should foresee reasonable time slots in the schedule to perform here some measurements.

Long Term High Rate Multi-wire Operation: the final commission makes most likely just sense at a point when HERA – B intends to operate for a longer contiguous time period with these settings. Before that period several tests are necessary to judge already early on the performance and to discuss and develop potential measures to improve it.

2.2 Beam-Pipe

2.2.1 Introduction

Within the HERA – B experiment, the proton beam-pipe is divided in two major sections:

- A thin-walled 12 m long pipe which starts at the exit window of the vertex vessel and extends downstream to the beginning of the muon absorber.
- A 7 - 14 cm diameter stainless steel pipe (5,2 m long) traversing the Muon system.

The second section is a conventional steel pipe, which does not need any optimization with respect to the thickness of the wall. In contrast to this, the first section has to be designed very carefully in order to reduce the interaction of tracks coming from the vertex to a minimum.

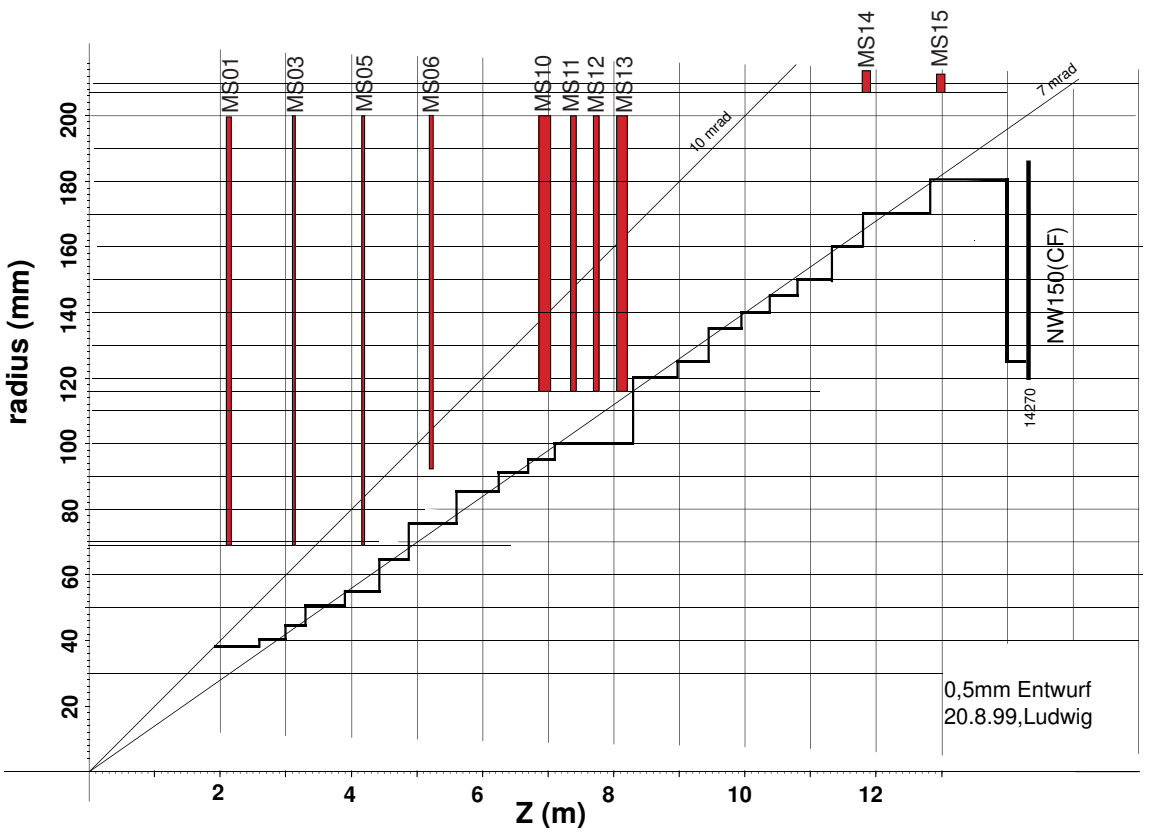

Figure 32: *Sketch of the actual HERA – B proton pipe. The inner tracker chambers are indicated schematically.*

For the time being, this pipe is made of 25 Aluminum cylinders with a wall thickness of 0,5 mm. The inner diameter is increasing from 38 mm at the vertex vessel to 180 mm at the end (within this chapter, this beam-pipe will be called "version A"). The pipe has been designed such that its shape follows a cone with a half-angle of 7 mrad (see Fig. 32). The average length of the cylinders is 47 cm. Due to the fact, that the complete pipe has a constant wall thickness, the required stability has to be obtained by increasing the number of stiffener rings (see Fig. 35) from zero at the beginning to eight for the thickest cylinder. An additional consideration was a clearance of at least 5 mm with respect to the inner tracker chambers.

In order to determine the contribution of the beam-pipe to the occupancy of the detector, the interaction of minimum bias events has been studied with a full GEANT simulation of the complete detector, with and without the beam-pipe. From these two simulations the contribution of the beam-pipe can be calculated. As a figure of merit the fraction of hits in the various detector components being due to tracks generated by interactions in the beam-pipe are plotted in Fig. 33a. The beam-pipe starts at a z-coordinate of about 200 cm. Chambers installed in the dipole magnet of the spectrometer (230 cm $<$ Z $<$ 640 cm) are severely affected by interactions taking place in the beam-pipe.

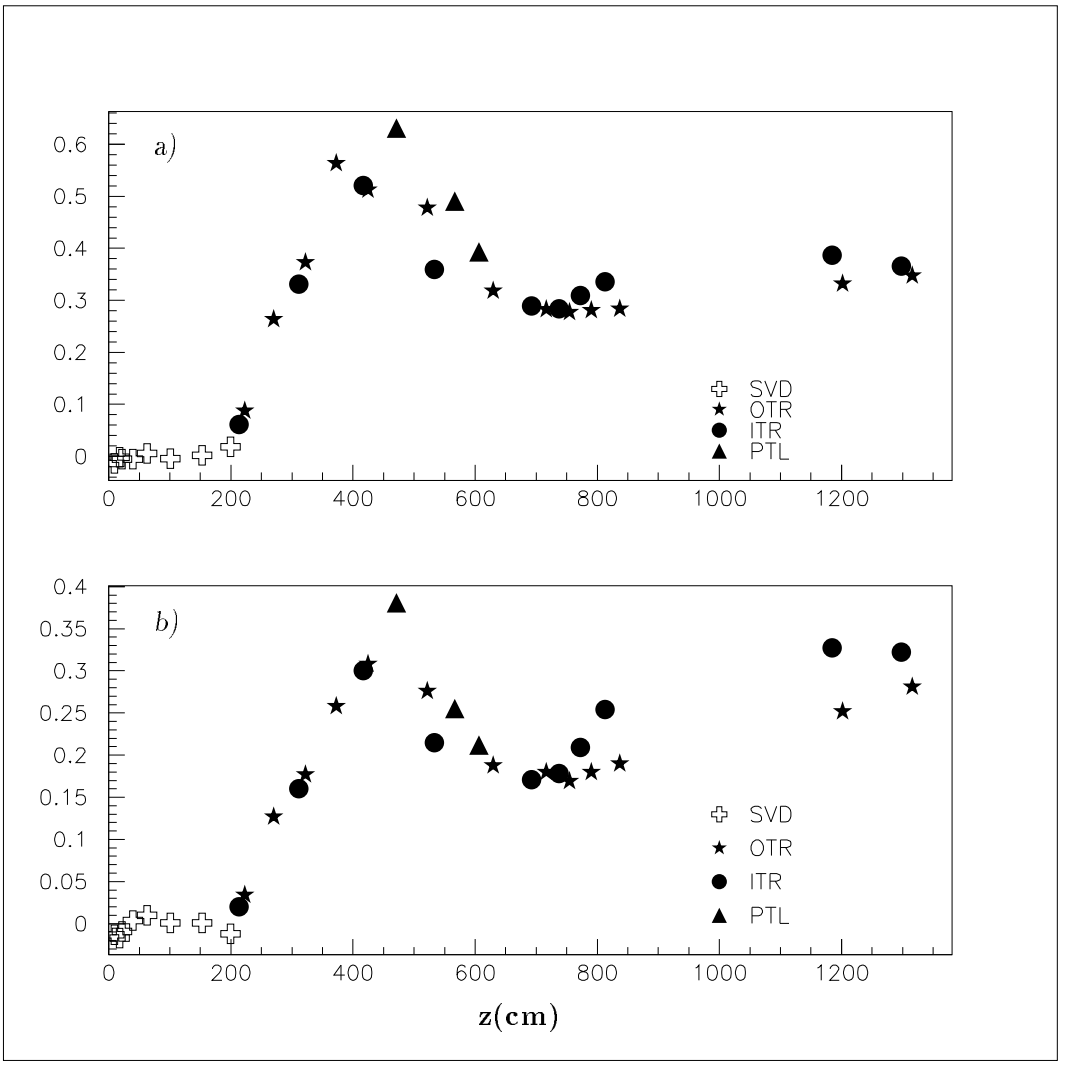

Figure 33: *Fraction of hits due to the beam-pipe plotted vs. the z-coordinate. a) The actually installed version (version A); b) version B.*

2.2.2 Previous Upgrade Plans

Design considerations:

Since three years there are ideas to improve the beam-pipe by reducing its wall thickness. A design

proposed in 1997 is described in Table 13. At that time, no experience concerning the installation

Table 13: *Comparison of the different beam-pipe designs.*

z-coordinate (cm)	wall thickness (mm)			stiffener rings per cylinder		
pipe version	A	B	C	A	B	C
$193 < z < 715$	0,5	0,3	0,3	0 - 2	0 - 3	0 - 3
$715 < z < 832$	0,5	0,57	0,35	2 - 4	0	2
$832 < z < 1342$	0,5	0,5	0,4 - 0,53	4 - 8	1	1 - 3

of the inner tracker chambers and with the required clearance with respect to the beam-pipe was available. Therefore the segment of the beam-pipe between magnet and RICH, where four ITR layers (see Fig. 32) have to be installed very close to the pipe, was designed without any stiffener rings. The results of the Monte Carlo simulation are shown in Fig. 33b). A direct comparison of this design (called "version B") with the pipe presently installed (version A) (see Fig. 34) reveals the pros and cons.

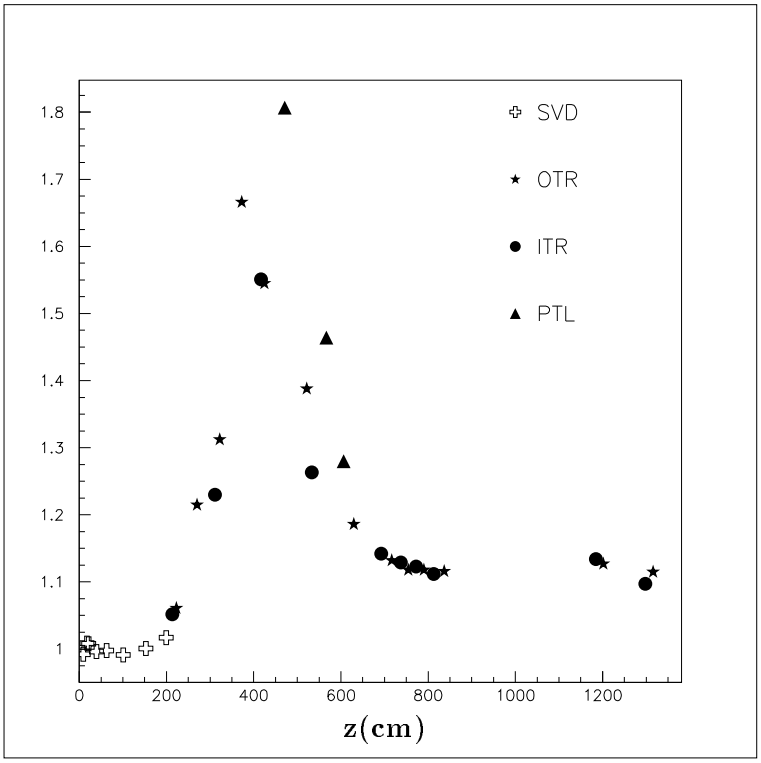

Figure 34: *Ratio of hits of version A and version B plotted vs. the z-coordinate.*

As expected, the largest improvement is obtained for the chambers installed in the magnet. For the rest of the detector only a small reduction in the contribution of the beam-pipe to the occupancy has been achieved. This can be explained by two different reasons:
1) After the magnet the occupancy in the tracking chambers is dominated by background tracks produced in the chambers themselves and their support structure (see Fig. 33a).
2) For pipe version B a substantial reduction in material was achieved only for the first section of the pipe (see Table 13).

Technical realization:

The basic idea was to produce Al cylinders with a wall thickness of 1.3 mm, reduce the thickness down to 0.3 mm by chemical milling and then press-form the resulting pipe in order to obtain the required stability. The press forming is expected to increase the stability of the pipe by about a factor of three. To give you an example: A pipe with flat surface which stands a pressure of 0,9 bar after evacuation should stand a pressure of 2,7 bar after the press folding. However, the factor of three can be obtained only when the pipe shows no deviations from perfect symmetry. Following these ideas, the first test cylinders have been produced. However, the first try to produce a complete pipe failed for two reasons.

a) When applying the technique of chemical milling to a larger amount of pipes, we realized that this process is very unreliable. Some etched cylinders looked very nice, others had a very uneven surface or even holes. However, all of them were treated in exactly the same way in the same chemical bath. The only explanation we found was that the failures must be due to different intrinsic properties of the Al rods themselves. As a consequence, this production technique was given up.

b) A more careful examination of the press formed cylinders with a new, very precise thickness-gauge revealed that they were slightly out of shape. Both flanges at the end of the pipe were distorted and showed some deviations from being a perfect circle. As expected, when pressure testing these pipes, they collapsed at a too small pressure.

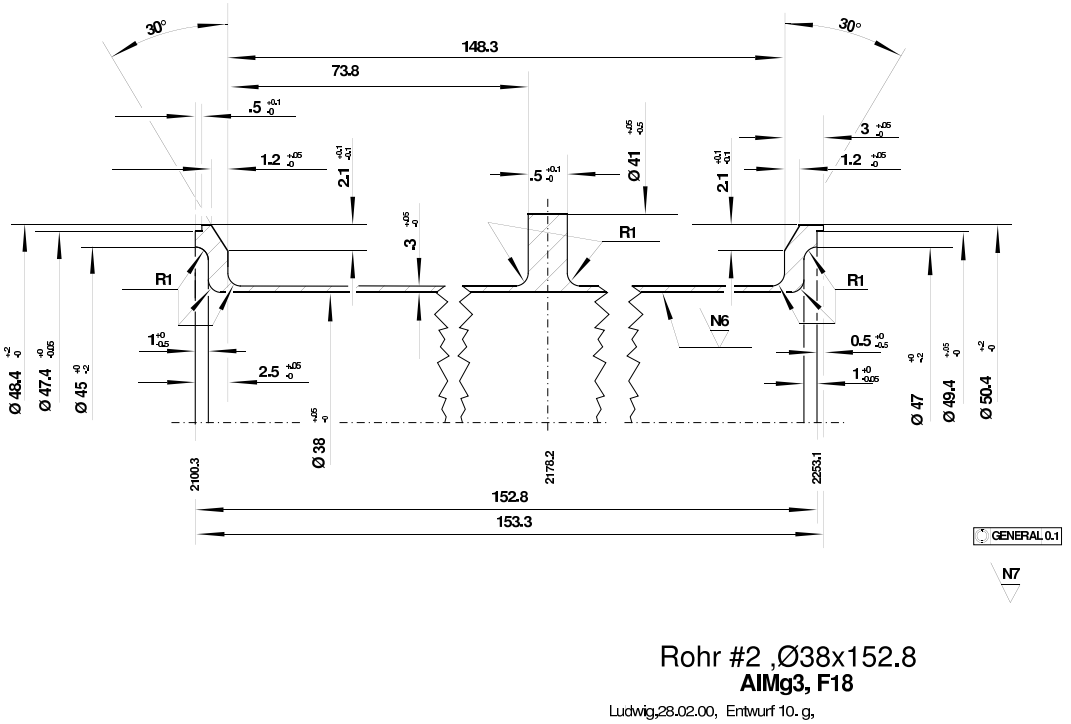

Figure 35: *Technical drawing of one of the cylinders.*

2.2.3 Plans for the Shut-down

Design and stability calculations:

In order to improve the design "version B", it was decided, based on the very positive experience with the installation of the inner tracker chambers, to reduce the wall thickness of the middle section and allow for some stiffener rings. In close collaboration with the DESY design group the stability calculations which fix the amount and cross section of the stiffener rings per cylinder were redone. These are the relevant numbers determining the stability of the pipe when diameter and wall thickness are given. As an example, one of the cylinders is depicted in Fig. 35. Based on our experience, this new version (called "version C") seems to be the optimum which can be achieved. The Monte Carlo calculations are just in preparation. The goal for the shut-down is to solve all remaining problem with the mass production of version C, manufacture all pipes and install the new pipe by the end of the shut-down.

Milling of cylinders:

Since the chemical milling was given up, the question had to be solved how to clamp the cylinder during the milling process. Several techniques were studied. Clamping tools were found which would allow to mill the cylinders in one step down to the final thickness of 0.3 mm with very small tolerances. However, this solution had to be excluded due to its high price. After several experiments a new recipe came up. Very precise steel cylinders will be produced which just fit into the Al pipes when these have been heated up. This trick results in a very precise support for the Al-pipes allowing the milling with very small tolerances (0,01 mm). After the milling both the steel cylinder and the Al-pipe are heated up again and the Al-pipe can be removed. This procedure has been tested successfully with some prototypes. We are just negotiating with different workshops how to ensure the timely milling of all 33 cylinders which have to be available by beginning of next year.

Press forming of cylinders:

The above-mentioned problems during the press forming process could be solved in the following way. In order to avoid the distortions of the welding flanges, some special clamps were designed which enclose the flanges during the press forming process. In addition, a reinforcing crease has been applied to both ends of the cylinder adjacent to the welding joints. Applying these new ideas to two cylinders during the press-forming yielded very nice results. These prototypes didn't show any substantial deformations and they fulfilled our stability requests. After that, the whole procedure was repeated again with several new test cylinders to test the reproducibility. Now we are confident that the time-schedule can be met.

Time schedule:

Milling of all cylinders	15/01/2001
Press-forming	15/02/2001
Welding	30/04/2001
Installation of complete pipe	15/05/2001

2.3 Vertex Detector System

The HERA-B Vertex Detector System (VDS) has the task of providing the track coordinates for the reconstruction of the B meson decay vertices and the impact parameters of the tagging particles. The required vertex resolution amounts to about 5% of the average B decay length (10 mm), and 20 to 30 μm in transverse direction. Even better resolution is desirable for a measurement of the much faster B_s mixing. The VDS information is already used at the second trigger level for background suppression.

The VDS consists of 64 double-sided silicon microstrip detectors which are arranged in eight superlayers (SL) of four quadrants around the proton beam axis, covering an angular range from 10 to 250 mrad (see Fig. 36).

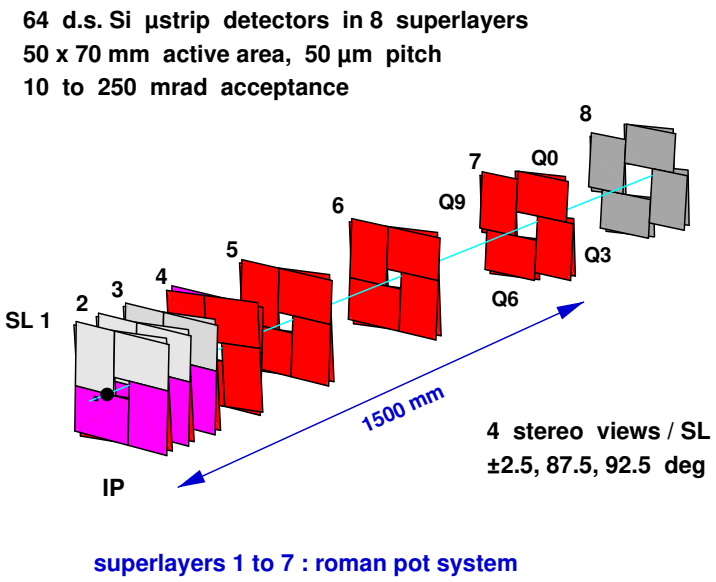

Figure 36: *Isometric view of the arrangement of detector wafers in the VDS. The dark shaded wafers in superlayers 1 to 7 are installed since June 1999; the system is complete since March 2000.*

To minimize mutliple scattering, the first seven SLs are realized as a Roman pot system, that is - together with the target wire stations - contained in a 2.6 m long stainless steel vessel. The eighth SL is mounted 2 m from the targets, immediately behind the 3 mm thick aluminium exit window.

The VDS operation requires an extensive infrastructure, which includes e.g. 16 remotely controllable manipulators for the precise positioning of 20 Roman pots, and adequate cooling for detectors and readout chips which are operated in vacuum. Since the VDS is an integral part of the HERA proton storage ring, three of its auxiliary systems have to perform with the utmost reliability: (i) the moveable RF shield inside the vertex vessel, (ii) the pumping system providing specified pressures for the primary (ring) and secondary (Roman pot) vacuum systems, and (iii) the leak-free water cooling system within the Roman pots; failure of any one of these systems could immediately stop the operation of HERA.

2.3.1 Status

The VDS has been operated routinely with partial instrumentation for several years at interaction rates up to 40 MHz. A brief history of the system is given in Table 14. Reports on the status over recent years have been published elsewhere [50, 51].

Table 14: *A short history of the Vertex Detector System.*

Date	Milestone
Nov 1995	ultra high vacuum vessel for vertex detector system delivered
Mar 1996	vessel with six manipulators and preliminary infrastructure installed
Apr 1996	test installation of 3 detector modules with preliminary mechanics and electronics
Jan 1997	3 detector modules with improved mechanics installed for first J/Ψ search.
May 1998	final infrastructure and 17 modules with final mechanics and Helix2.1 readout installed for system commissioning
May 1999	44 final detector modules with Helix2.2 readout installed for physics running
Dec 1999	vessel completely instrumented with 56 detector modules
Mar 2000	system completed with 8 modules outside the vessel.

Since March 2000, the system is completely installed. The system is also largely commissioned and the data produced are well understood.

As the demands on the VDS have not yet warrented operation at the full radiation load, the modules have so far been positioned at a slightly larger distance to the beam (15 mm) than design (10 mm). In addition, only 3 out of 4 stereo views were implemented for the first three superlayers.

In parallel to the hardware implementation, extensive software [52, 53, 54] has been developed and tuned. It includes packages for raw data processing like cluster finding and sparsification, for track reconstruction and vertexing, for the alignment of the 32 individual pairs of detector wafers, for the monitoring of data quality, and, last but not least, for the general slow control and interlock system. All this code is designed to run on-line and allows the use of the VDS in a stand-alone analysis as well as in conjunction with other subsystems.

2.3.2 Performance

The overall performance of the VDS is as expected. At the moment, the performance is generally evaluated in stand-alone mode.

Signal to Noise

Fig. 37 shows the cluster signal (S) to noise (N) ratios S/N for each chip of a typical double-sided detector module. For the n-side, the values are all well above 25; for the p-side, they vary systematically reflecting the increased and varying capacitive loads for the chips which are due to the (unavoidable) longer and varied traces on the Kapton cable connecting chips and detector.

An extensive study of the width of the S/N distributions has been done. As an example, Fig. 38 shows how different cluster sizes contribute to the overall S/N distribution. The figure also demonstrates how well signal and noise are separated, even on the p-side.

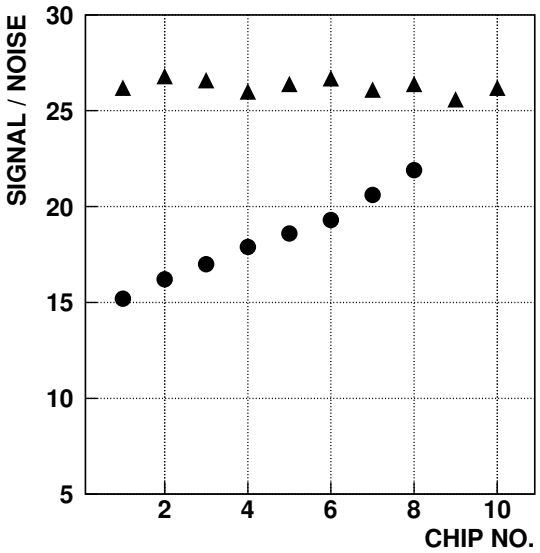

Figure 37: *Chipwise S/N ratios for the p-side (dots) and the n-side (triangles) of a double-sided detector module.*

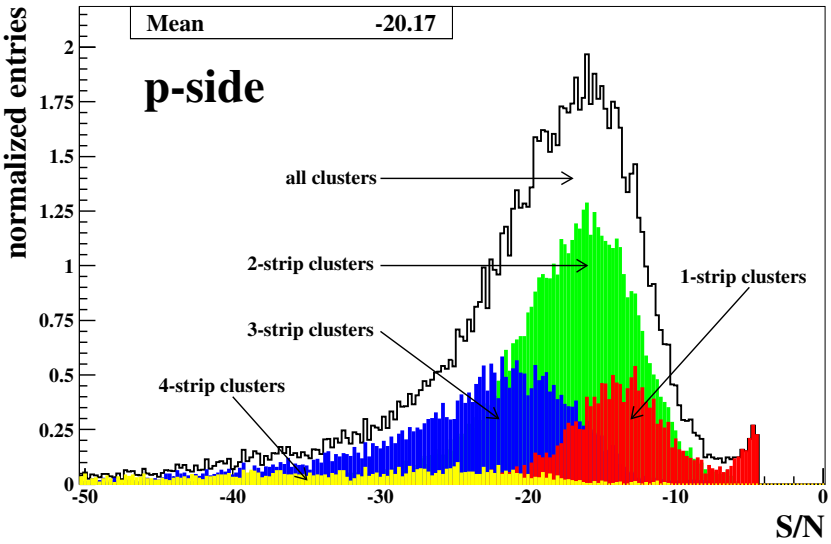

Figure 38: *Distributions of the signal-to-noise ratios (S/N) on the p-side of a silicon detector module; the contributions of various cluster sizes are indicated.*

Hit Efficiency

The hit efficiency is determined by ignoring during track reconstruction both planes of the detector under study and using reconstructed tracks with at least 10 hits in the VDS as well as an associated primary vertex. These tracks are used to predict hits on the two detector sides under study. The predictions have to fall into an area which starts 1000 μm inside the sensitive area. Only track predictions which have no other track crossing within 400 μm are used. If there is no hit within 200 μm of the predicted position an inefficiency is assumed.

The efficiencies obtained are thus detector efficiencies weighted with the track densities in our detector. The large search windows eliminate possible problems due to misalignments.

Table 15 shows the results obtained from run 14577 for superlayers 1 to 8, respectively. More than 80% of all detector planes exhibit efficiencies that are better than 97%. The lower efficiencies of the remaining planes can be traced to isolated bad readout chips. There are in average about 20 such chips, some intermittently, in the system. At the end of the 2000 run period, this number had increased to about 40 chips due to the (avoidable) loss of two planes in superlayer 8.

Table 15: *Efficiencies of the detector planes in superlayers (SL) 1 to 8 as measured in run 14577. The quadrants (Q) of the first three SLs are instrumented with a single- and a double-sided detector and so have only 3 planes (L1, L3, L4).*

SL	Number of detector planes with efficiencies			
	≥99%	≥98%	≥97%	< 97%
1	7	7	7	5 : Q1L3(68%), Q2L3&4(dead), Q3L3(55%), Q4L3(83%)
2	5	7	8	4 : Q1L3(76%), Q2L3,4(93,73%), Q4L3(82%)
3	3	8	10	2 : Q1L3(75%), Q4L3(92%)
4	10	14	15	1 : Q2L1(92%)
5	9	13	14	2 : Q2L2(90%), Q3L2(93%)
6	9	13	15	1 : Q2L3(96%)
7	12	13	14	2 : Q3L1(93%), Q4L1(83%)
8	11	14	14	2 : Q2L3(96%), Q3L3(75%)
sum	66	89	97	19 : Q1,2,3,4: (3,8,4,4), L1,2,3,4: (3,2,12,2)

Tracking Efficiency

The results presented here have been obtained with a tracking package based on cellular automata using space points; a detailed description of the algorithm and the performance studies can be found in [53]. Another VDS tracking package [52] yields similar results using a Kalman filter approach. The tracking efficiency was studied with Monte Carlo (MC) events. In Table 16, results from a study using events with 4 Poisson distributed interactions are given. We do not simulate noise as the observed noise level is significantly below 0.1%.

Table 16: *Results of a tracking efficiency study using events with 4 Poisson distributed interactions generated in a Monte Carlo simulation for three different detector efficiencies.*

Hit eff.	Refset	Allset	Clones	Ghosts	Time
100%	96.5%	85.5%	3.2%	14.3%	33 ms
95%	95.3%	83.6%	3.0%	15.2%	34 ms
90%	93.8%	81.0%	2.5%	16.7%	35 ms

As reference tracks (Refset) we take tracks that hit three superlayers of the VDS and have a momentum above 1 GeV. The set of tracks labeled "Allset" also contains tracks which hit only two superlayers. No momentum cut is applied. These tracks are used in order to study the performance of the code in the case of relaxed track requirements. Obviously, the implementation of - in general - four views per superlayer is providing enough redundancy so that even a low hit efficiency of 90%

does not lead to a significant loss in tracking efficiency.

Primary Vertex Resolution

The primary vertex resolution is studied in MC and in data. Fig. 39 gives the results of a MC study with events where 4 interactions are mixed according to a Poisson distribution.

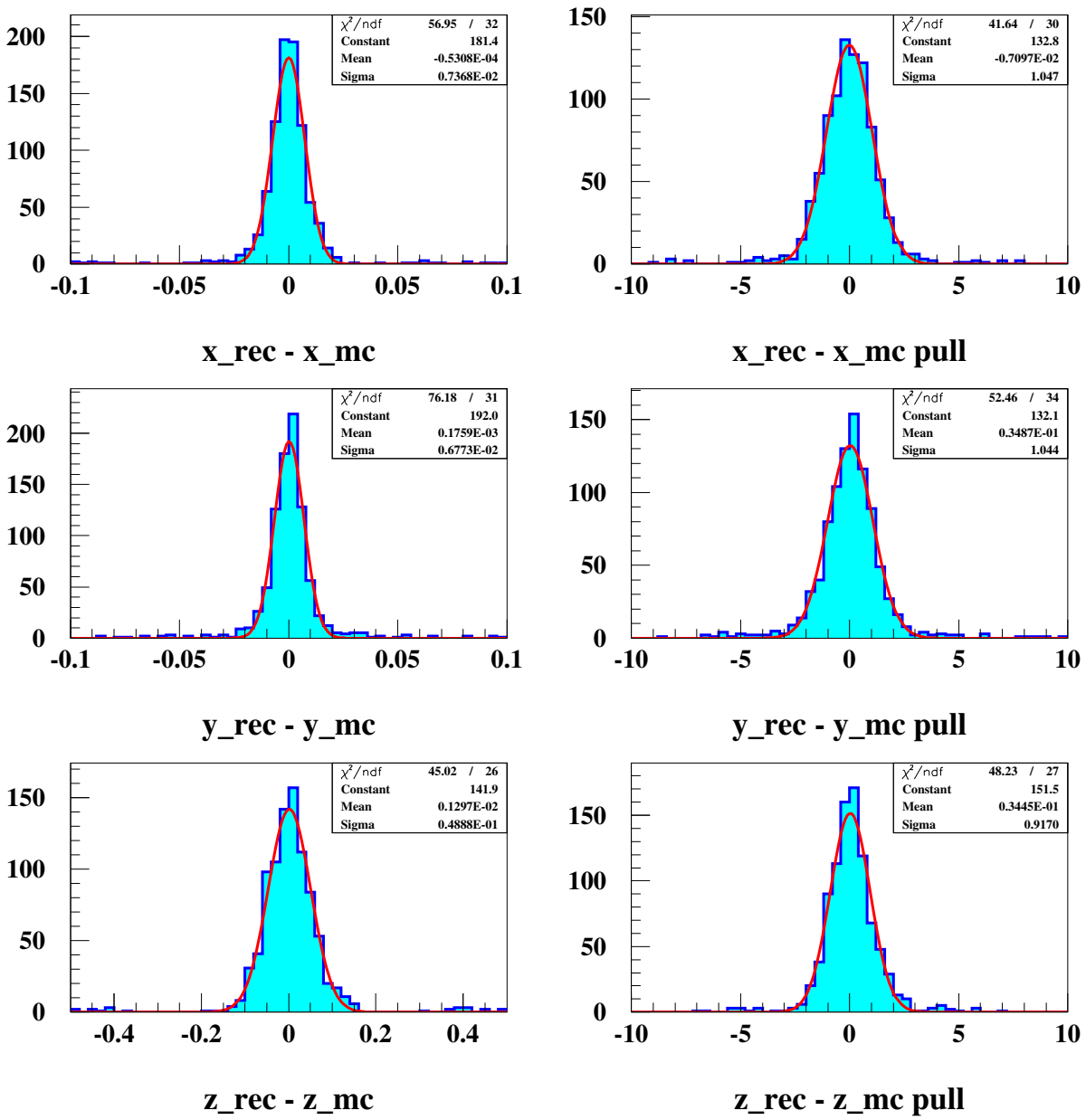

Figure 39: *Resolutions for primary vertices and pull distributions for the two transversal (x, y) and the longitudinal (z) coordinates (units in cm). The pull distributions do not have the width 1 due to the inaccurate momentum estimate in this VDS stand-alone analysis.*

Studies in real data using the known position of the wires confirm the resolutions of about 70 μm transversally and 500 μm longitudinally. These resolutions are obtained with VDS information only. Thus the momentum estimate which is done purely geometrically is crude. This limits the resolution as can also be seen in the pull distributions which do not have a width of unity.

The efficiency of the primary vertex finder is for minimum bias events 94% $\pm$ 1%. This is basically independent of the interaction rate. However, at higher interaction-rates a substantial amount of vertices are split or merged. Table 17 gives an overview about the quality of reconstructed vertices. Fig. 40 shows as example an event taken at 40 MHz interaction rate in which five primary vertices have been reconstructed on four target wires.

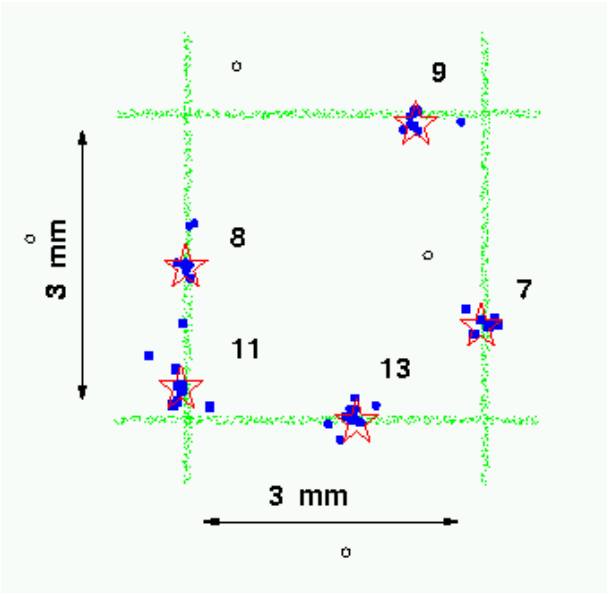

Figure 40: *Impact points of tracks in the target plane and reconstructed vertices for an event with 5 primary vertices. The total number of reconstructed tracks is 65; the numbers of tracks contributing to each vertex as well as the positions of the four target wires are indicated.*

Table 17: *Results of a MC study to determine the significance of reconstructed vertices. Good vertices are vertices that can be attached to a MC vertex. Clone vertices are vertices where the MC vertex was split. Mixed vertices are vertices which can be associated with more than 1 MC vertex: to first order two vertices cannot be resolved and are merged. Ghost vertices are vertices that cannot be associated with a primary MC vertex. The numbers are given for exactly 1 interaction and and for 4 interactions Poisson distributed over 8 wires. All numbers are* $\pm$ *1%.*

#int.	good	clone	mixed	ghost
1	95%	2%	-	3%
<4>	59%	31%	6%	4%

Secondary Vertex resolution

The work to fully exploit the VDS to study secondary vertices is still in progress. We present here results from MC studies where the momentum was smeared by 1%, which is roughly twice the

resolution specified in the Design Report. The results do not change significantly if we assume a momentum resolution of 2%, which seems realistic so far as indicated by the present mass resolution of the $J/\Psi \to \mu^+\mu^-$ peak. Table 18 shows spatial resolutions for 2-, 3-, and 4-track vertices of the decay $B_s \to J/\Psi\Phi \to e^+e^-K^+K^-$.

Table 18: *Spatial resolution for the longitudinal (z) and the two transverse (x,y) coordinates of multitrack secondary vertices as determined in a MC study of the decay* $B_s \to J/\Psi\Phi \to e^+e^-K^+K^-$.

#tracks in vertex	mass constraint	σ_z / μm	$\sigma_{x,y}$ / μm
4	no	280 ± 10	21 ± 1
4	yes	280 ± 10	21 ± 1
3	no	300 ± 10	24 ± 1
2	no	375 ± 10	25 ± 1
2	yes	325 ± 10	26 ± 1

For four and two track vertices, a B or J/Ψ mass constraint was either applied or not. According to these results, the VDS meets the specifications of the Design Report.

Having so far no sample of b-hadrons selected from our data, we extracted distributions for selected direct $J/\Psi \to \mu^+\mu^-$ candidates.

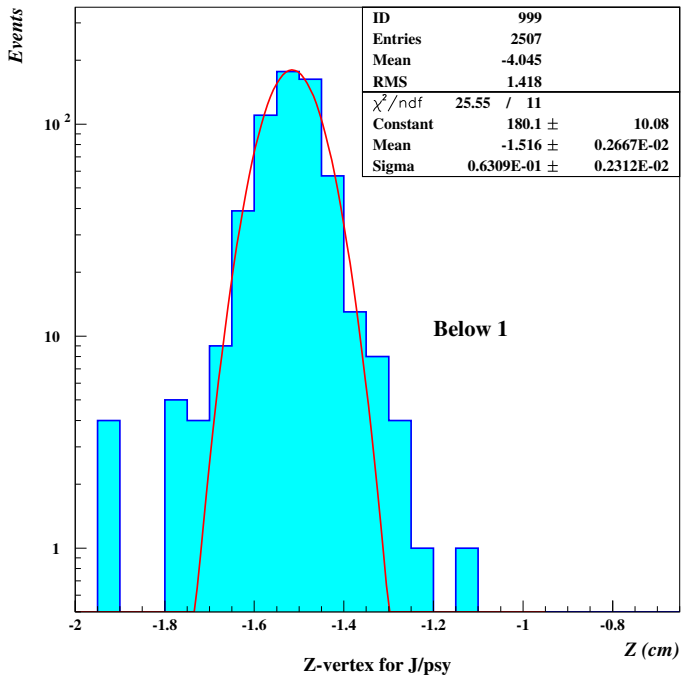

Figure 41: *Longitudinal distribution of* $J/\Psi \to \mu^+\mu^-$ *candidates from the "below-1" titanium wire*

Fig 41 shows the longitudinal vertex distribution for the wire 'below-1' (Ti); similar results have been obtained for the 'inner-2' carbon wire. The events are selected using a χ^2 per degree of freedom (dof) cut of 10 after a constrained fit to the J/Ψ mass. The widths of the distributions are different

for the 0.5 mm thick titanium and 1 mm thick carbon wire - 630 μm and 750 μm, respectively. In both cases, the total width of the distribution shows extra contributions in the order of 510 μm and 610 μm respectively. This is under study. Expected contributions are from misalignments in the detector, incorrect MC description and from combinatoric background. If a χ^2/dof cut of 1 is applied, which reduces the sample by a factor of about 4, the widths of the distributions go down to 600 μm and 670 μm respectively. This indicates that combinatorial background contributes significantly, as contributions to width of about 190 μm and 340 μm are eliminated.

Alignment

The quality of the alignment can be studied much in the same way the efficiency of the modules is studied.

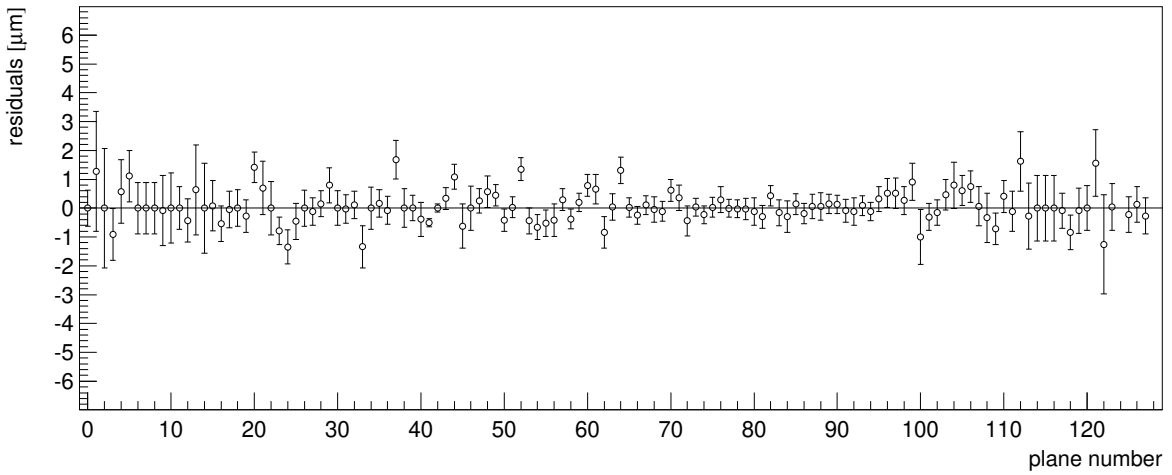

Figure 42: *Residuals of track penetration points for each plane, if the plane under study is not used for tracking.*

Tracks are reconstructed without the use of the plane under study and then the mean of the residuals is a measure of misalignments. Fig. 42 shows that the residuals scatter within ± 2 μm about zero.

2.3.3 Radiation Damage

The innermost edges of the silicon microstrip detectors are expected to experience a fluence of $3 \cdot 10^{14}$ minimum ionizing particles per cm^2 (or 100 kGy) during one year (10^7 s) of nominal operation after which they will be replaced. The results of dedicated irradiation studies [55] with single-sided p on n detector modules indicate acceptable detector performance up to the expected maximum fluence: the irradiated detectors can be biased beyond 500 V, and for detectors with polysilicon bias resistors the increase of the noise is consistent with the increase of the bulk leakage current. Using the full HERA-B readout chain and operating the detector at 8^o C, a clear separation of signal and noise was observed even at maximum fluence, and the corresponding S/N value was 14.

In the year 2000, the radiation load at HERA-B was about one order of magnitude lower than during nominal running conditions (see Table 19). Thus, no conclusions on the ultimate radiation tolerance of the installed detector modules are possible. The measured doses, as well as the moderate increase of leakage currents, show no significant deviations from the expectation.

Table 19: *Increase of leakage currents in detectors of superlayers 6 and 8 during the two indicated run periods in 2000. The accumulated number of interactions (#int.) is also shown as a fraction of interactions (#int_n) for one year (10^7 s) of nominal HERA-B running at 40 MHz. Quoted doses have been measured with glass dosimeters directly behind the exit window of the VDS vessel at a radial distance of 35 mm from the beam axis.*

run period	#int.	#int_n	dose(35 mm)	ΔI(SL6, 0°C)	ΔI(SL8, 20°C)
Mar 3 - Jun 06	2.2·10e13	5.5%	110 Gy	6 μA	12 μA
Jun 7 - Aug 28	1.8·10e13	4.5%	96 Gy	3 μA	8 μA

2.3.4 Material Budget

Fig. 43 shows that muons from J/Ψ decays cross, on average, 7% of a radiation length (RL) in the VDS. The distribution in Fig. 43 is rather similar to that shown in the Design Report (see Fig. 114 therein) for the 'thick' quadrant version with 1.2% RL in the detector planes and 1.6% RL in the support arms. The slight shift to somewhat larger values is in part due to the RL in the support arms, which is actually larger ($\approx$2.2%). The tail of the distribution extending beyond 10% RL is mostly due to the four ceramic hybrids carrying the readout chips; the Design Report did not take into account their contributions, which amounts to about 4% RL in an area of 73×42 mm^2.

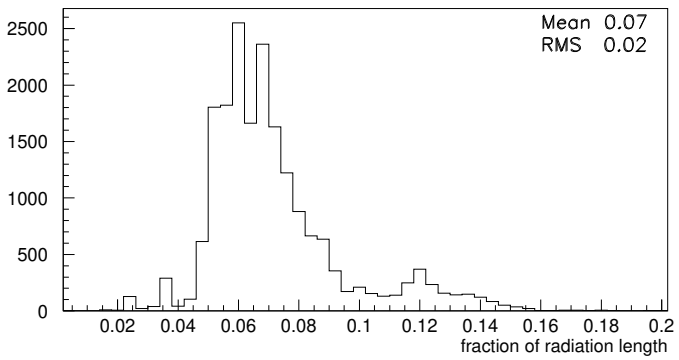

Figure 43: *Distribution of radiation lengths crossed by J/Ψ muons in the present VDS installation.*

2.3.5 Improvements

During the luminosity shutdown the VDS group is planning to implement the improvements listed below.

RF shield

The present RF-shield consists of four 5 μm thick and 12.7 mm wide stainless steel bands which surround - at square cross section - the proton beam axis inside the VDS vessel on a length of 2 m. During injection, the distance of the bands to the beam axis is 20 mm; for nominal running, the bands have to be pushed to 7 mm. Thus there is a safety margin of only 0.65 mm on each side of each band which cannot be visually inspected when the vessel is evacuated. Since a rupture of any band could immediately stop the HERA operation, and since the exchange of a broken band would take almost one week, we have so far avoided moving the bands to radial distances lower than 9 mm.

To safely safely reach the design value of 7 mm, we plan to install bands with a reduced width of 7 mm which have been manufactured for us on special request. With these narrower bands, the tolerances of the RF shielding mechanics are much more relaxed, and the amount of shielding material is reduced by almost 50%. As in the present installation, the bands will be coated with aluminum in order to increase their electrical conductivitiy.

Shielding Caps

In each Roman pot the installed detector modules are covered by a 150 μm thick aluminium cap which serves to protect the modules against RF pick-up and to separate the secondary vacuum in the pot from the primary vacuum of the storage ring. Caps of optimized shapes are produced as single seamless pieces by galvanic deposition of aluminium on (re-usable) stainless steel form pieces. Depending on the module lengths, the cap lengths range from about 90 to 430 mm. For the very long caps it turned out to be impossible to remove the Al-deposit without damage from the steel nucleus. Thus the 430 mm long caps were produced by welding a shorter cap on top of a cylindrical tube. This solution represented a viable backup alternative, at the expense of a non-optimized shape at the transition between cylinder and elliptical cap base.

The problem of removing the Al deposit from the form piece would be trivial if the form piece could be dissolved or melted without affecting the Al coating. Continued test series have shown that tin might be a suitable material for this purpose due to its low melting point and its mechanical properties which allow production of a polished form piece in the institute's workshop at reasonable effort. Coating of two tin form pieces for very long caps is now in progress, and we expect the samples back by the end of September.

Modules and HELIX Readout Chips

In the current installation, all quadrants of superlayers 1,2 and 3 are instrumented with pairs of single- and double-sided silicon detectors. For the next instrumentation only double-sided detectors will be used. In order to accomplish this, the mechanics of the modules for these superlayers has been improved.

All new modules will use the new version 3.1 or 3.1a of the HELIX readout chip which is available since July 2000, and which has successfully passed all tests so far. Compared to the installed version 2.2, both new versions feature (i) an improved control logic including (ii) a modified reset scheme for the pipeline amplifier to avoid drifts of the baseline, (iii) a modified bias current generator to fix the 'wake-up' problem of version 2.2, and (iv) a modified guard-ring structure to minimize crosstalk between comparators and pre-amplifiers. Many of these changes were already present in version 3.0. Version 3.1a has, in addition, a modified current source which no longer exhibits any oscillations, a

feature that is most relevant for the Inner Tracker application.

Cooling

While the detectors in the VDS vessel are operated at about 0° C, the operation temperature of detectors in SL 8 - being installed in a box after the exit window - could not be reduced below 20° C so far. We plan to improve the gas cooling such that this temperature can be lowered by at least 5° C.

Flux Monitoring

So far, dosimeters attached to SL8 have been used to monitor the integral radiation load of the detector modules. We plan to build and install a low-mass counter array at the exit window of the VDS vessel which will allow the time-resolved monitoring of interaction and/or background rates.

2.3.6 Module Production and Installation Plan for the Year 2001

It is planned to produce a complete set of new modules by the middle of 2001. The silicon detectors and first samples of the new HELIX-3.1 readout chips ($\approx$400) are available; the mechanical parts are either on hand or have been ordered.

The production of the VDS-modules proceeds in steps. The last step is the attachment of the electronics hybrids and their bonding. All modules will be prepared for this step by the end of October 2000. At that time, all ceramic hybrids will be loaded with passive components, and about one third of them will be already equipped with readout chips. The production of complete modules will thus start in November, and all modules should be finished by June 2001.

During the shutdown we will repair the bad Helix-2.2 modules in SL 8 and replace the modules in the 3 o'clock quadrants of SLs 1 to 3, that is in Roman pot 103, by 3 pairs of double-sided Helix-3.1 modules. Apart from these changes, we will resume the VDS operation in 2001 with the Helix-2.2 detector modules from 2000, which have experienced negligible radiation damage so far (see section 2.3.3). The date for the replacement of these 'old' Helix-2.2 modules has still to be determined; a possible time slot could be the shutdown at the end of 2001.

2.4 Inner Tracking

The inner tracking system covers the area around the beam pipe up to distances of 25 cm. It has to cope with particle rates up to $2 \star 10^4$ mm^{-2}s^{-1}. Its purpose is twofold: It delivers tracking at small radii delivering coordinates for about 40% of all tracks from B-decays. In addition it is expected to provide input for the first level trigger using four trigger stations.
The inner tracking uses MSGC/GEM detectors — in total 184 with 768 anode strips each — organized in 10 tracking stations along the beam line as shown in Fig. 44.

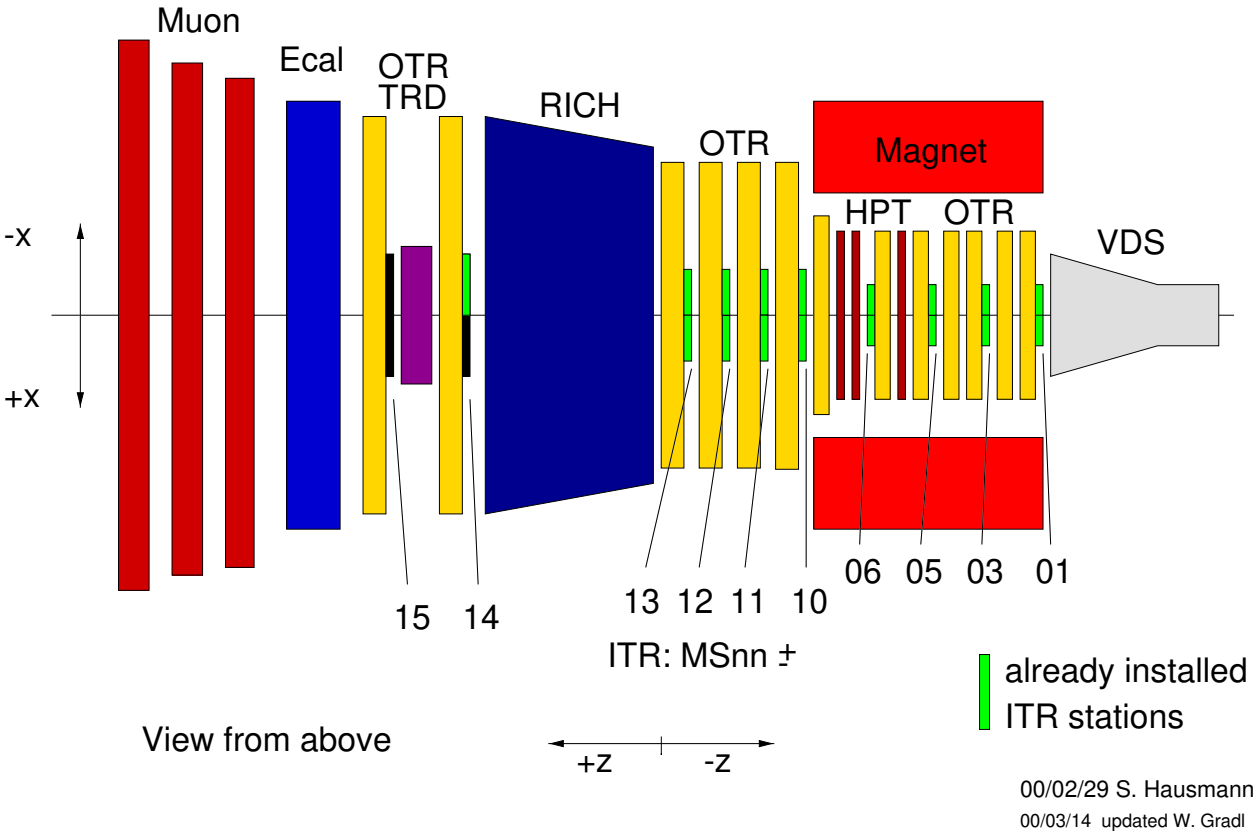

Figure 44: *Geometry of HERA – B tracking. The inner tracking stations which were installed during the run 2000 are indicated.*

2.4.1 Status of Installation and Subsystems

In the course of the year 2000 we have installed and commissioned all stations except the last two trigger stations behind the RICH detector with a total of 138 MSGC/GEM detectors. The detector does not deliver useful trigger information at present because of too high trigger thresholds (see below). This is the reason why the last two stations have not been installed. The detectors are in regular operation and included in data taking.

Detector status:

In general the detectors are working well and show stable operation. In the course of commissioning a certain number of defects have however shown up.

- One detector has developed a GEM short which was irrecoverable and two other detectors have massive damages on the cathode side leading to a complete loss of these detectors. Three more detectors show too large GEM spark rates and can therefore be operated only at reduced GEM voltages and therefore lower efficiency.

- In total we have observed 70 cathode shorts but at most 2 within one detector. Without further intervention a cathode short prevents the operation of 16 neighboring anodes, which are protected by a common HV resistor. These cathode shorts occurred during the initial commissioning phase of the detectors and must be regarded as 'infant mortality' due to faults in the substrates or dirt. This corresponds to a loss of 1.1% of strips.

- About 0.7% of individual anodes are broken or not connected. Most of them are production failures during lithography.

- At present 9 additional detectors cannot be operated because of HV problems like broken HV connections. These are recoverable once we have access and can be avoided in future.

The observed problems are summarized in Table 20. All broken detectors will be replaced resp. repaired during the shutdown. In addition we will cut the individual anodes which produce the cathode shorts. This will reduce the fraction of missing or broken anodes to a total of about 0.8% of isolated strips.

Table 20: *Problems observed during ITR operation.*

Problem	**Consequence**
1 GEM short	1 chamber off
2 severe MSGC defects	2 chambers off
3 GEMs sparking	3 chambers with reduced eff.
70 cathode shorts	efficiency reduced by 1.1 %
7 % interupted anodes	efficiency reduced by 0.3 %
9 HV problems	9 chambers off

The detector readout shows some additional failures which could not be repaired during the run because there was not sufficient access. Possible error sources are failure of interfaces for control signals or readout, broken components on the front end electronics or problems with the low voltage power supplies. All errors have occurred stochastically. In most cases the error rate could be reduced by system improvements. Towards the end of the run 5 detectors could not be read out at all, in addition 4 detectors showed one front end card with two HELIX chips (1/3 of a detector) which delivered no readout.

The readout clock is operated at 10 MHz. We plan to increase the rate to 20 MHz which has been demonstrated to work for all but 2 half stations. Because priority was given to physics data taking the collaboration decided to stay with 10 MHz during the year 2000 run and solve the remaining problems afterwards.

The gas system works very reliably controlling the gas pressure relative to the ambient pressure to better than 20 μbar.

The HV system including slow control works reliably and allows routine automatic ramping of the detectors and continuous control of all currents and voltages including several hardware protection features against discharges. It also counts GEM sparks and includes automatic recovery from them.

Summary: The detectors have shown stable running for several months. The fraction of broken strips as well as the number of cathode shorts is tolerable. Some basic weaknesses of the HV cabling and protection have led to 9 detectors which cannot be operated at present. The origin of these problems is known, they can easily be repaired outside of the pit and the problems can be avoided in future. The fraction of chambers which cannot be operated in the long run is therefore expected to be tolerable.

2.4.2 Detector Operation

All detectors needed consequent training during target operation. The drift and then the GEM voltages were raised slowly during operation over a period of typically one week. This led to a continuous reduction of the number of GEM sparks and automatic shutdowns of detectors due to high currents. All detectors, which are operated with an $Ar : CO_2$ 70:30 gas mixture, were first operated with a cathode voltage of 510 V and a GEM voltage of 420 V. With these conditions (same voltages for all detectors) the detector pulse height and correspondingly the gas gain varies by up to a factor 2.5 between different detectors. This is due to fluctuations of the GEM gain. The gain, however, does not vary over the area of individual detectors. Inspection of a sample of GEMs indicated a slight miss-alignment of the upper and lower copper holes for some GEMs and variations in the Kapton hole diameter. The latter is very sensitive to the parameters of the etching process. In a next step the gas gains were therefore adjusted by raising the GEM voltages individually. The variation of pulse heights for different detectors is now reduced to about 60%.

The GEM spark rate is continuously measured and recorded. It is proportional to the target rate and increases with gas gain. The measured GEM spark rate at a target rate of 10 MHz is about 1/day/detector in average. This is an acceptable value which does not affect the detector performance.

Summary: The detectors are routinely operated and work reliably after training and individual adjustments.

2.4.3 Tracking

The cluster analysis for the inner tracking detectors is done online by the level 2 trigger processors. The average noise per channel is determined for each run and cluster finding is based on a combined cut in signal over noise first for the strip charge and subsequently for the cluster charge of neighboring strips. This sparsification process is controlled by an online monitoring program which also logs relevant information into a database for each run.

The raw cluster charge distributions show a large number of hits with low pulse height which are not connected to particle tracks. For hits associated to tracks, Fig. 45 shows the cluster charge, the signal/noise distribution and the strip multiplicity for a typical detector with average gas gain.

The efficiency of the tracking detectors can be determined only after track reconstruction. This requires external detector information from the vertex detector or the outer tracking system. Tracks which are reconstructed in the vertex detector system and which pass through the active area of the MSGC/GEM detectors of the first tracking station (MS01) have been used to determine the absolute efficiency of these detectors. The result is shown in Fig. 46 for 7 detectors of this station as a function of the GEM voltage. Results for the other stations should be similar since the operating conditions are the same as for station 1. Precise results will be available soon. They rely on the

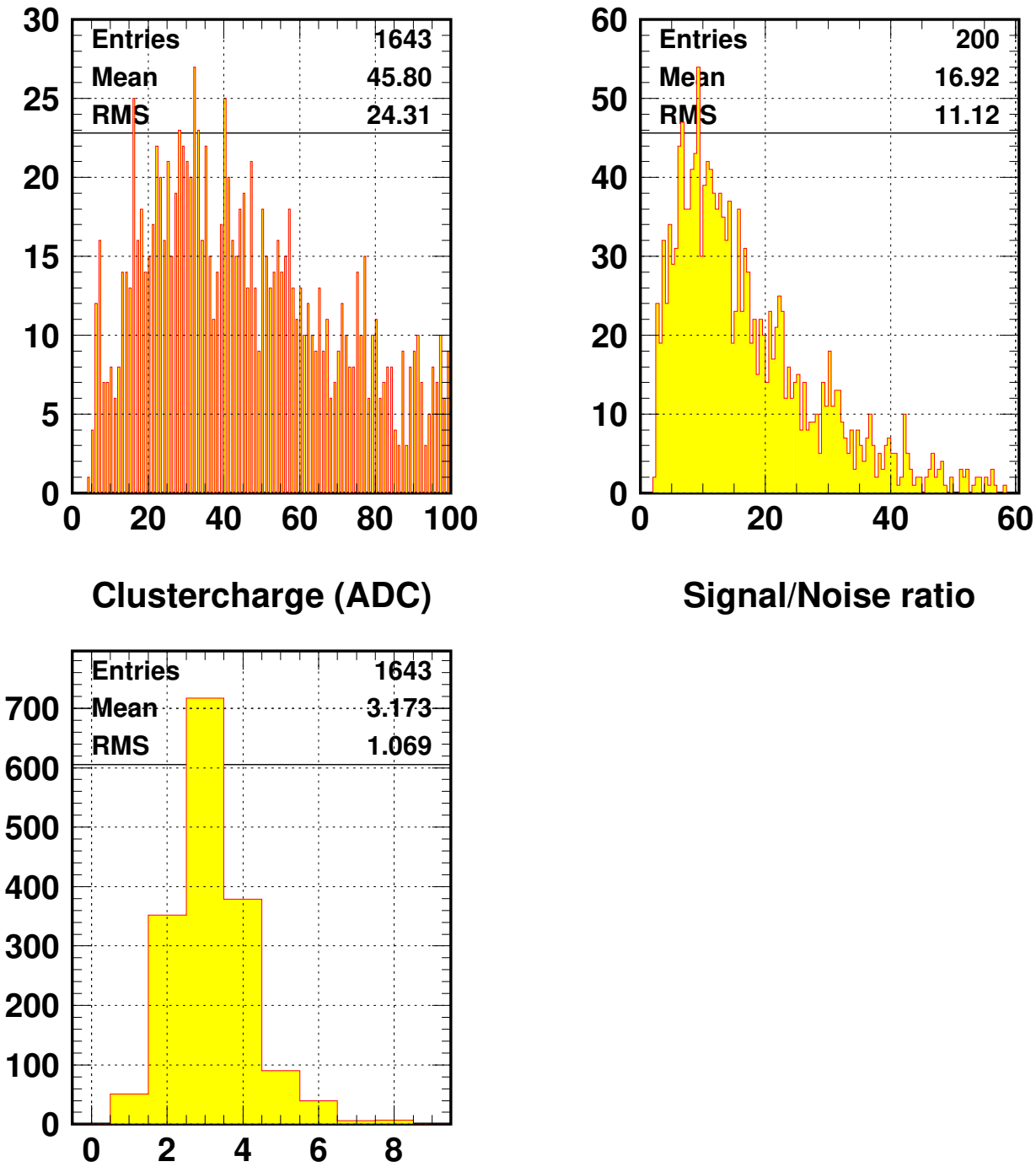

Figure 45: *Distribution of the cluster charge, the signal/noise ratio and the strip multiplicity for hits associated to a track for the detector* M01 + −4 + 0K359 *which shows average efficiency.*

ongoing improvement of the tracking software including the OTR.

It can be seen that the observed difference in efficiency shrinks from about 25% before the adjustment of the GEM voltages to less than 5% at the final settings (filled symbols). The global

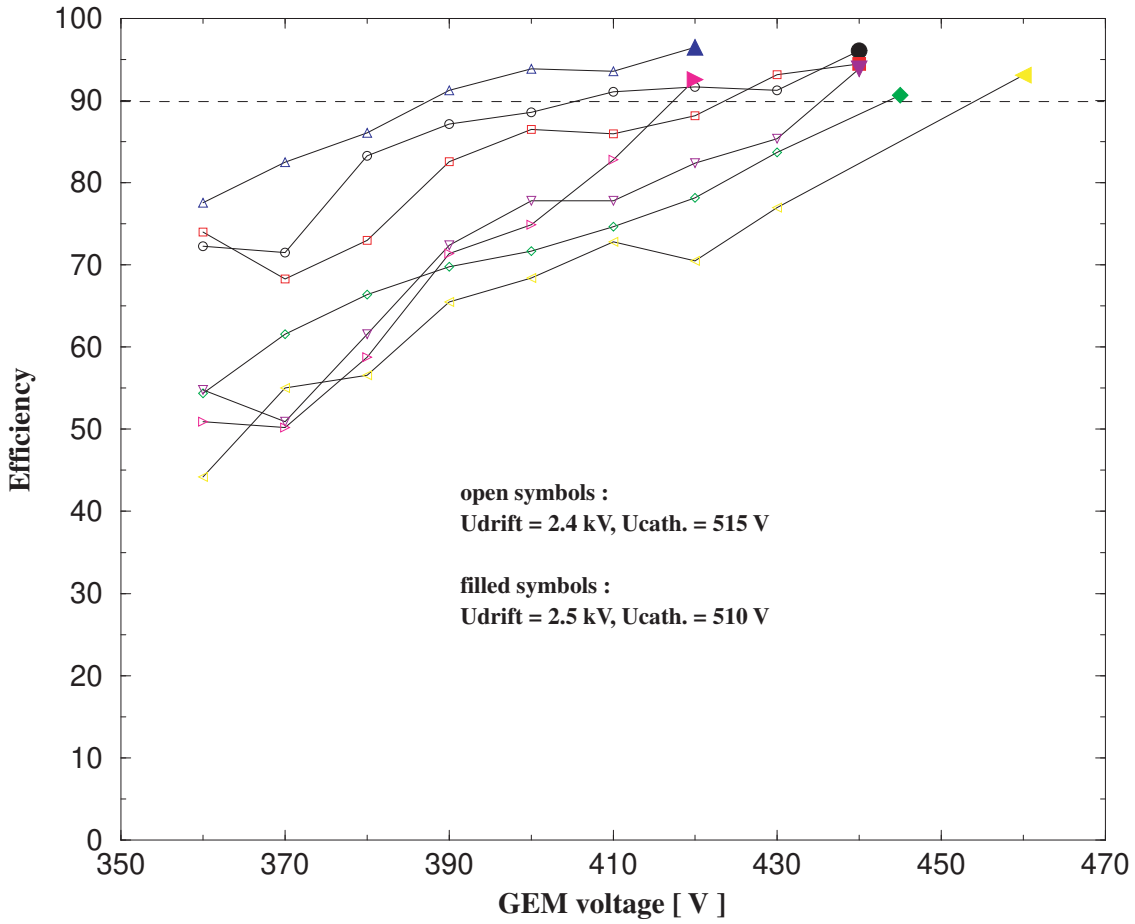

Figure 46: *Efficiency of detectors of station MS01 versus GEM voltage for fixed cathode and drift voltages. The filled symbols show the efficiencies for the current voltage settings after individual gain adjustments.*

efficiency as determined with external tracks saturates between 91% and 97% and does not further increase with cathode or GEM voltage despite the fact that signal/noise increases. We conclude that the detectors have sufficient gas gain for full hit efficiency. The saturation at this level is not fully understood and presently under study.

External tracks are also being used to align the detectors individually with respect to each other and the rest of HERA – B. Detectors within one half station which are mounted on the same support structure are aligned to better than 100 μm. At present, detectors of different stations are aligned to better than 200 μm. A significant improvement of the alignment using the global HERA – B tracking is currently being worked on.

The inner tracking clusters are fed into the offline reconstruction program to find tracks in the inner tracker system alone using stations MS10 to MS13 and common tracks with the outer tracking and the vertex detector. Figure 47 shows a typical event with tracks from outer and inner tracking.
.

The first results look promising, more work is however needed to tune the parameters for track finding and to determine the overall track efficiency for the inner tracking system. We are confident however that the inner tracking system will contribute adequately to the track reconstruction for

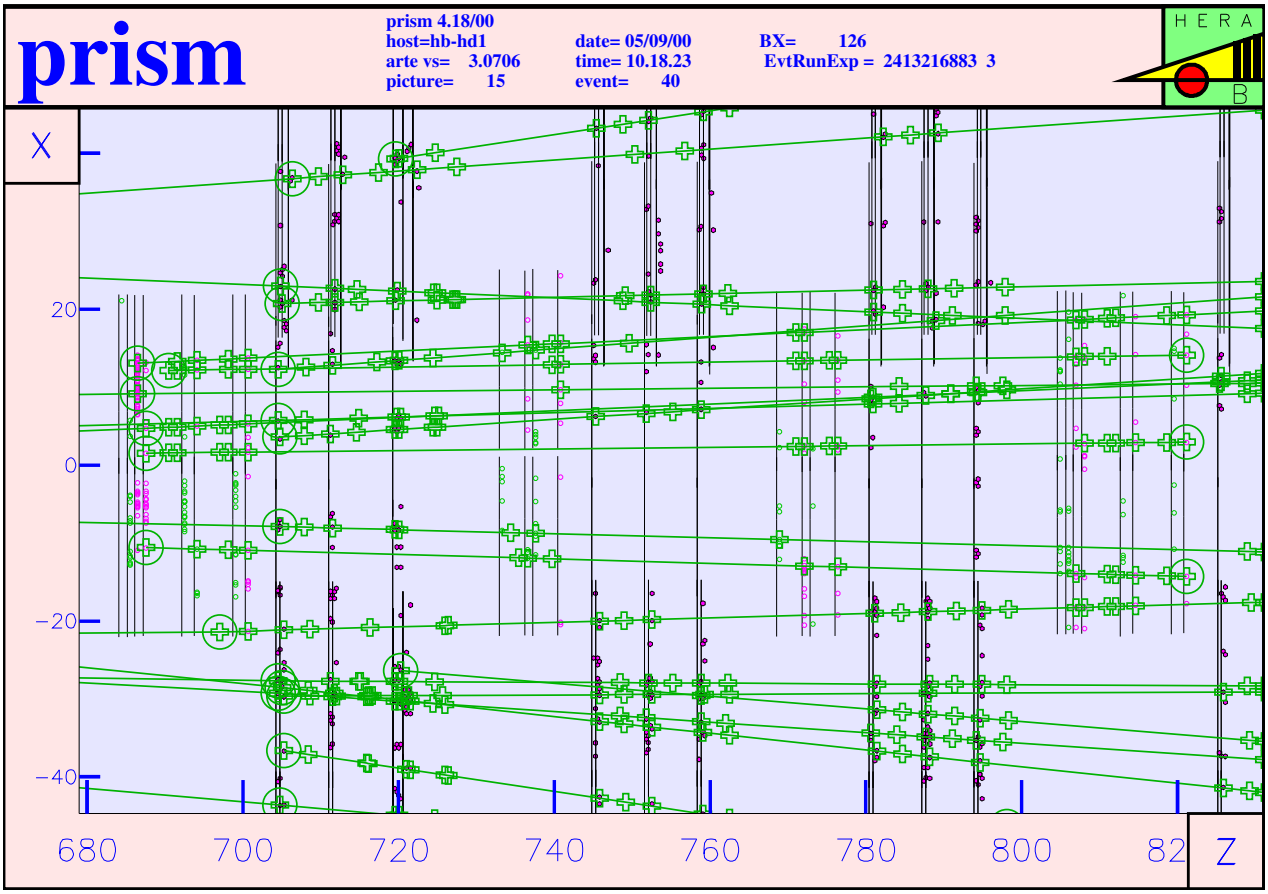

Figure 47: *Data event display showing the tracking area of stations MS10 to MS13 with hits and reconstructed track segments in the inner and part of the outer tracking system.*

the physics data which has been recorded in 2000 once the fine tuning has been finished.

2.4.4 Trigger Signals

First level trigger signals are delivered by 4 trigger stations, two in front of the RICH and two behind. The trigger is derived on the HELIX128 chip by discriminating the analog signal for each strip and a subsequent OR of the trigger signals of 4 neighboring strips. Each chip therefore delivers 32 trigger signals for each bunch crossing. In order to guarantee high efficiency each trigger station is build using double layers of MSGC/GEM detectors with identical strip orientation. The trigger signals of the two layers are ORed on the front end. In total there are 96 detectors used in the trigger of which 48 behind the RICH have not been installed for the run 2000.

The present trigger installation works technically, it does however not give high enough efficiency because the trigger threshold for the discrimination of the strip charges cannot be lowered below a signal corresponding to about 25000 electrons. Below this threshold the trigger outputs of the chips start to oscillate because the output signals of the trigger drivers are coupled back weakly to the analog input of the chips via power lines and printed circuit board. Since this problem could not be solved in time it was decided to concentrate on the tracking performance of the inner tracking system for the year 2000. In the meantime substantial progress has been made. Main improvements

come from two sources: 1) The voltage swing of the trigger output drivers was reduced from ± 2 V to ± 0.3 V thus reducing the primary source of the problem. 2) The grounding concept of the detectors and the chips was significantly improved. This has the consequence that new trigger driver electronics is needed. These improvements allow to reduce the trigger threshold to an equivalent of about 7000 electrons, limited by noise. Three double layers of trigger detectors with different combinations of these improvements were operated in HERA – B in August. Systematic test runs show an efficiency of double layers compatible with full efficiency but certainly higher than 90%.

2.4.5 Improvements of the Inner Tracking Detector during Shutdown

Major improvements are planned for the shutdown period.

- All detector stations will be taken out from the experiment to replace resp. repair broken chambers.
- The improved grounding scheme will be applied for all detectors. This includes the replacement of all HV cables on the stations with improved RF filtering.
- The two trigger stations after the RICH will be completed and installed.
- All front end cards for the detectors used in the trigger will be replaced using a new chip version. This is the biggest change which is necessary because the analog pipeline of the present chips is too short by five columns (500 ns).
- The trigger driver front end cards will be replaced by new ones adapted to the low voltage swing of the trigger outputs.
- We intend to test new gas mixtures like $Kr : CO_2$ or $Ne : CO_2$ to increase the signal.
- The available data taken under various conditions will allow to study in detail the reason for the observed saturation of the efficiency at too low values. The software, i. e. cluster finding and tracking will be improved.

These measures are well prepared and planned. Material needed has been ordered and will be available in time.

2.4.6 Summary

The inner tracking system based on MSGC/GEM detectors has overcome many major problems. During the last months there has been considerable progress. The system is quite vulnerable and not very robust in the intense hadronic environment, since the detectors have to be operated near the discharge limit to get acceptable efficiency. The problem of gas aging prevents the use of organic gases which have much better quenching properties.

Nevertheless the detector system was shown to allow routine operation with high reliability and good efficiency over long periods. A substantial improvement is still possible during the shutdown to further eliminate weak points. The system will be able to contribute to the first level trigger after the shutdown improving the overall trigger acceptance of the experiment by about 30%.

We are confident that we will have a reliable inner tracking system with the expected tracking and trigger performance at the restart of the running.

2.5 Outer Tracker

2.5.1 Hardware Status

Compared to the Technical Design Report the Outer Tracker (OTR) has undergone various stages of development. An overview of the final design and the operation parameters can be found e.g. in [56]. In the following we report the current status of the OTR and summarize some activities during the installation and commissioning phase (1999 – 2000) as far as it helps in understanding the still existing problems.

Chamber Assembly and Installation: The installation of the Outer Tracker chambers was carried through in parallel to the module production and the chamber assembly. The mechanical installation as well as the electrical connection of the super-layers was achieved mainly during monthly mini-shutdowns of 3 days length. This was possible since the readout and auxiliary electronics which are attached to the super-layer frames had been assembled and electrically tested before or during the chamber assembly outside the experimental area. By January 2000 all OTR super-layers had been installed.

The time schedule for OTR module production, chamber assembly, and installation did not allow for building a full-size prototype of a large chamber. Certain problems encountered during the assembly of the first chambers required some ad hoc modifications of the module design and of the assembly and installation procedures. The most important addition to the module production procedure, as described in the Module Production Guide [57], was the mechanical reinforcement by means of carbon-fiber (CF) rods. As a consequence, the chambers which were installed first show some deviations from the otherwise uniform OTR design:

MC2– : Prototype modules with graphite-coated Pokalon foil.
PC1– : Some modules without reinforcement.
PC4– : Many modules without reinforcement.
TC1– : Most modules without reinforcement.

The chamber TC2– originally contained no reinforced modules at all. This was changed in a major overhaul operation during December 1999 (see below: 'High Voltage Stability').

It is noteworthy that the caps of the two super-layer halves, although rather complicated, fit perfectly and did not cause problems when closing both halves. However, the installation of the modules inside the caps had in some cases problems because of too tight dimensions. For the modules above and below the beam pipe which are mechanically only attached at one end, the mechanical reinforcement was particularly important.

Readout Electronics: The electrical readout of the Outer Tracker [60] consists of the amplifier-shaper-discriminator boards (ASD-8) plugged to the signal feed-through connections on the gas-box, the TDC boards residing in crates mounted at the chamber frames, and the Second Level Buffer (SLB) boards situated in the electronics trailer. Trigger link boards provide the optical connections to the First Level Trigger (FLT) electronics. They are connected by cables to the hit-out connectors of the TDC boards.

Table 21 summarizes the installed components of the readout electronics and the failures observed during the first year of operation.

Table 21: *Components of the readout electronics and the failures observed during the first year of operation.*

Boards	amount	failures
ASD-8	7200	14[a]
LV distribution boards	212	4
TDC	955	3
TDC crates (power supplies)	99	3
SHARC SLB boards	34	1
Triggerlink boards		see below

[a]Additional 138 ASD8 boards delivered no signals for unknown reasons (possibly bad connections)

ASD-8 Threshold and Noise Behavior: Before installation all ASD-8 boards have been tested and classified according to their efficiency and noise behavior [60]: The boards are sorted into 4 categories with different gain, each subdivided in 3 sub-categories with different signal-to-noise distance. For each of the 12 classes a so called "noise reference threshold" U_{ref} was determined. This is the threshold value at which the ASD-8 board starts to show noise in the laboratory (> 2 kHz). It is used as reference value for the ASD-8 operation at the chambers.

During the assembly of the chambers grounding and shielding was improved until the noise occupancy of all channels was smaller than 10^{-2} at a threshold value of $U_{th} = U_{ref} + 200$ mV. The increase of the threshold by ΔU_{th} with respect to the value determined in the laboratory test is attributed to the operation inside a large system (system effects).

After the installation in Hall West the noise behavior of the chamber test was reproduced and no noise degradation was observed. The situation changed for the trigger layers when the trigger link-boards were installed.

TDC System: The TDC readout (955 TDC boards) was in general operated under stable conditions. At high trigger rates (> 1 kHz) approximately 1.5 % of the boards showed readout problems which have been traced to either connection problems of the SHARC cables to the SLB boards or problems of the transmission of the FCS signals. The FCS problems observed initially have been fixed by improving the termination of the backplane of the central FCS crate. The connections of SHARC cables will be systematically tested and improved during the shutdown.

Noise generated by the TDC–TLB connection: The hit outputs of the TDC boards are connected by 17-pair flat cables (length between 1 and 4 m) to the Trigger Link Boards (TLB). The hit outputs are single-line TTL signals. Every signal cable comprises 32 signal lines and 2 ground lines. The cables act as antennas and emit high-frequency electromagnetic noise, most likely generated by the fast TTL drivers on the TDC boards. The noise is transmitted to all signal (ASD8-to-TDC) cables in the neighbourhood of the trigger link cables. The electromagnetic noise travels along the signal cables and triggers oscillations of the corresponding amplifier boards making the operation of the chamber impossible. The effect occurs as soon as cables are connected to the hit-out of the TDC. It does not depend on the termination of the trigger link cables or whether they are connected to a TLB or not. The cable routing as well as the distance to the signal cables play an important role.

The following measures to reduce the emission of electromagnetic noise by the trigger-link cables have been tried with very little or no success:

- different shieldings of the trigger-link cables,
- increase of the number of ground lines (1 ground-line per signal-line),
- conversion of the single-line TTL outputs to differential LVDS signals.

The only measure which showed at least in the laboratory a significant improvement was the installation of commercial noise filters (ferrite rings) around the trigger-link cables directly at the output of the TDC board. In situ the installation of 4 such rings per cable was necessary to allow for an operation of the trigger chambers at least with an increased threshold value.

Figure 48 shows the noise occupancy versus the threshold increase ΔU_{th} for 8 super-layers of the –x side: MC1–, MC2–, PC2–, PC3– (not trigger layers), PC1–, PC4–, TC1–, TC2– (trigger layers). The noise rates are taken without beam. Under beam conditions the thresholds have to be increased by about 100 mV above the point of stable operation suggested by this measurement (for yet unknown reasons this increase has to be much higher for TC2–). The final threshold values ΔU_{th} at which the chambers have been operated are listed in Table 22. Values of ΔU_{th} of 500 mV and larger are cutting into the cell efficiency of the corresponding layers (see also section 2.5.3).

Trigger Link Boards (TLB): The Trigger Linkboards (TLB) have been available only in late fall 1999 and therefore had to be installed in situ. As the boards were missing during assembly time several problems of the entire system were identified very late.

All problems related to the TLB itself could be solved by now. Two problems remain in the transmission to the TFU's of the FLT: Failures of the Autobahn chips and instabilities in the optical transmitter-receiver system, due to sensitivities to the operating temperature and to the duty cycle of the data stream. A repair/upgrade program for the shutdown is described in section 2.5.4.

Detector Operation: Besides the below mentioned HV problems the operation of the Outer Tracker chambers did not cause any problems: The detector is fully integrated into the central Slow Control System (an exception is the gas monitoring), a calibration process running on the SLT farm evaluates the channel status, calculates the t_0, and updates the databases if necessary. The calibration process also provides data quality histograms at the hit level. Higher level monitoring of the reconstruction and the track quality is not yet available and will be developed during the shutdown.

Gas System: The gas system of the OTR produces the desired gas mixture (standard mix is Ar 65% CF_4 30% CO_2 5%) and circulates the counting gas through the detector. It controls the flows and regulates the pressures in all 26 OTR half–super-layers, purifies the gas upon return from the detector, and automatically performs a quantitative analysis of main and trace (O_2, N_2, H_2O) gas components for the common input and the outputs of all half–super-layers.

The system has been supplying all OTR chambers with gas since the beginning of the HERA-B run in January 2000. In February the flow reached the design value of 1 vol/h in all MC chambers and PC2, PC3 chambers; the flow in the large trigger layers is currently limited to 0.8 vol/h; it is planned to remove this restriction during the luminosity shutdown. For most of the running period the detector has been operating with a total flow of $\approx$ 18 m^3/h which corresponds to a totally circulated volume of $\approx$ 80000 m^3 over the year 2000 run period. Fresh gas has been continuously added at rates of 0.5–2%/h by the mixing station. The monthly gas consumption of CF_4 – by far the most expensive gas component at about 70 DM/kg – was about 400 kg/month. Even though the

Table 22: *Operation thresholds of the Super-layers.*

Super-layer	MC1–	MC2–	MC3–	MC4–	MC5–	MC6–	MC8–
ΔU_{th} [mV]	200	200	200	200	200	200	200
Super-layer	MC1+	MC2+	MC3+	MC4+	MC5+	MC6+	MC8+
ΔU_{th} [mV]	200	200	200	200	200	200	200
Super-layer	PC1–	PC2–	PC3–	PC4–	TC1–	TC2–	
ΔU_{th} [mV]	600	500	400	500	600	600	
Super-layer	PC1+	PC2+	PC3+	PC4+	TC1+	TC2+	
ΔU_{th} [mV]	600	500	400	600	500	500	

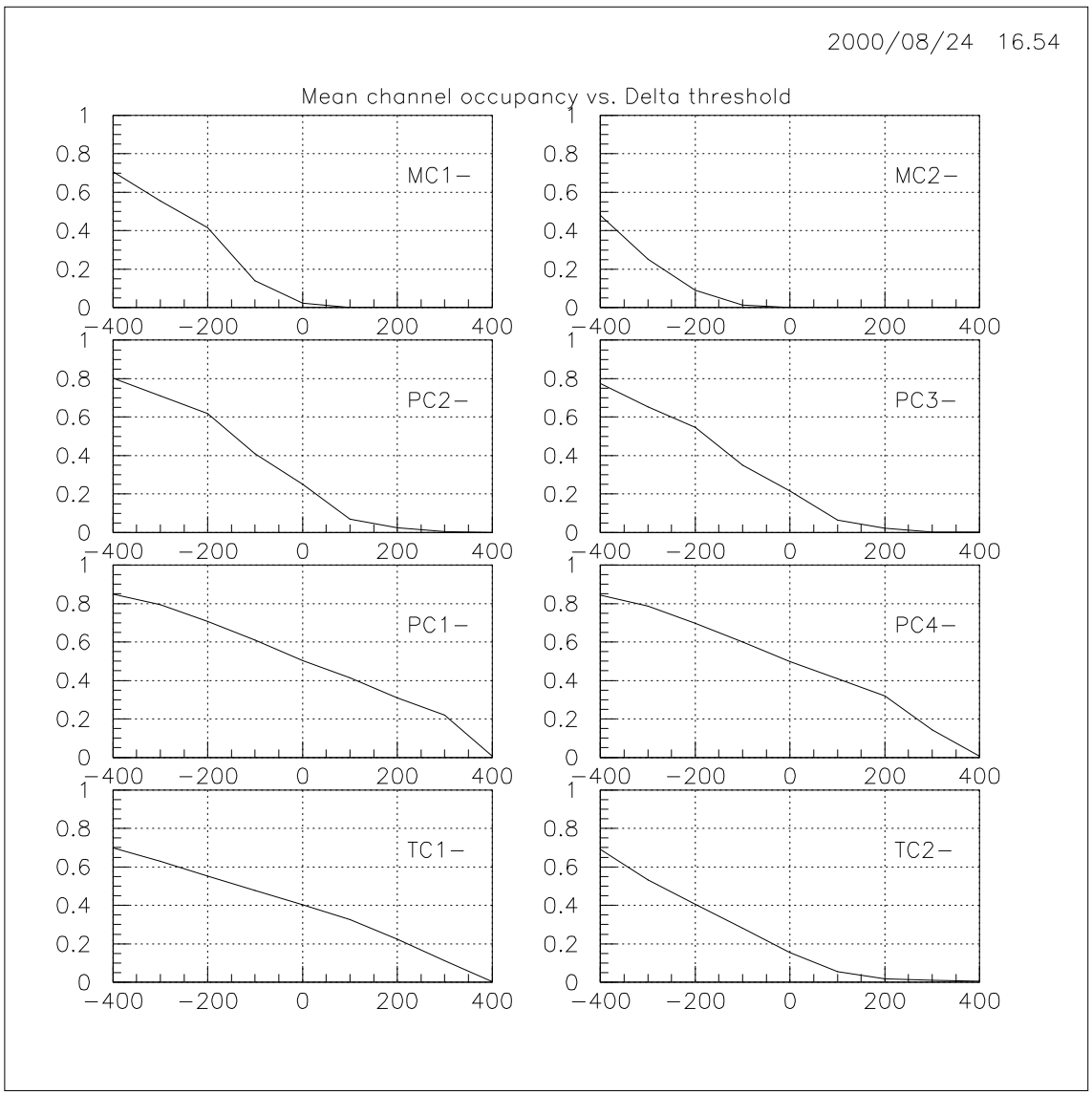

Figure 48: *Noise occupancy versus threshold increase* ΔU_{th} *for 8 super-layers of the –x side (5 mm cells).* ΔU_{th}*=0 corresponds to the noise level reached in the laboratory tests. The increased noise level in the trigger layers PC1,4 and TC1,2 is clearly visible.*

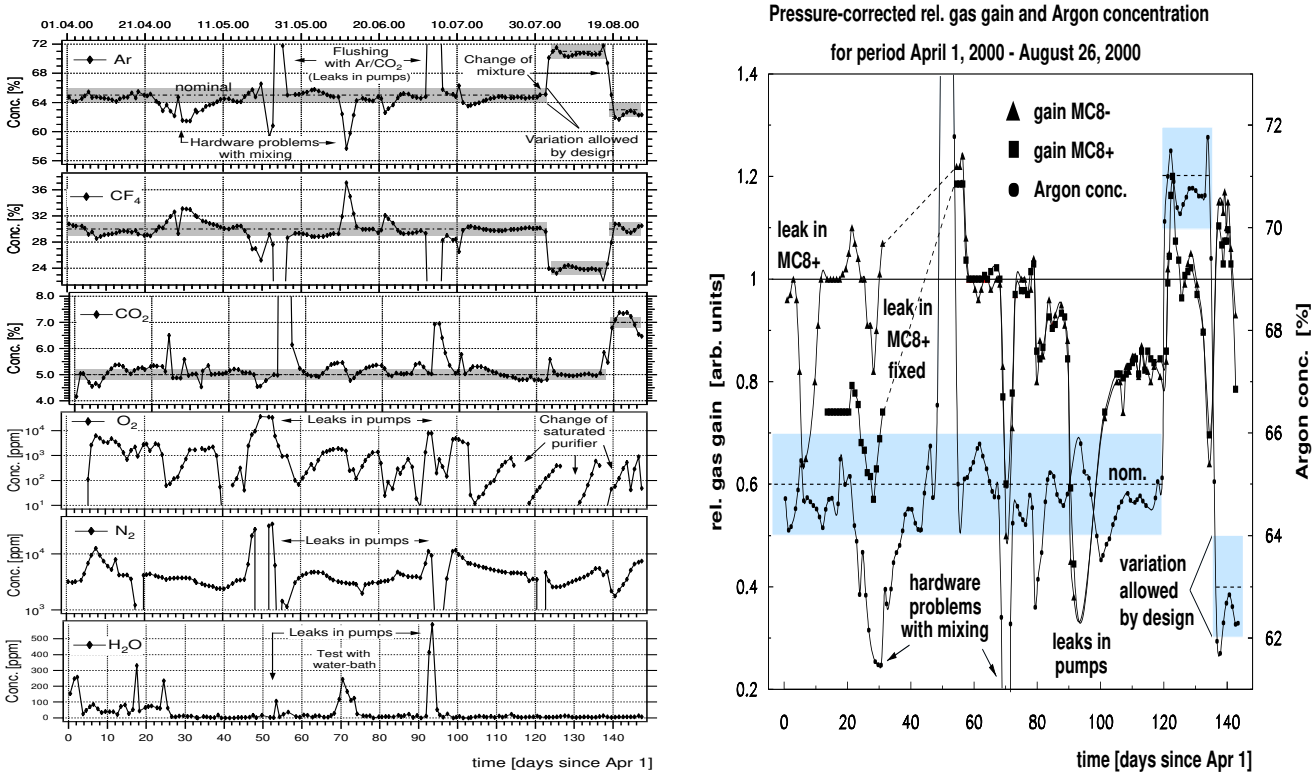

Figure 49: *Left: Concentrations of main and trace components in the OTR counting gas measured at the common input. Right: Gas gain measured in MC8 and Argon concentration.*

total amount of gas ordered for the 1999 run proved to be sufficient also for the run in 2000, serious problems with CF_4 supply were encountered because the main vendor Air Products was repeatedly incapable to deliver CF_4 bundles on time. Operations could only continue because additional CF_4 bottles were purchased from another vendor on short notice and because the fresh gas consumption was lowered to a uncomfortably low level. It is recommended to consider switching to a new supplier in the future and to negotiate appropriate penalties for delivery delays in any new contract with CF_4 suppliers.

The pressure regulation of the chambers worked well keeping them at slight overpressures of 0.3-0.6 mbar relative to ambient air pressure. A system of safety valves successfully prevented all chambers from becoming dangerously over- or underpressurized while preventing air from entering the chambers during pressure alarms.

The purification system for removal of oxygen and water was commissioned by mid-April. During commissioning it was observed that the oxygen purifier capable of regeneration absorbs not only oxygen, but also significant amounts of CO_2 and water. Appropriate CO_2 conditioning procedures after regeneration were successfully established to ensure a stable CO_2 concentration in the counting gas. Due to the water absorption by the oxygen purifier the detector was operated with very dry gas ($c(H_2O) < 20$ ppm) for most of the 2000 run even after the water purifier had been excluded from the system (see Figure 49 (left)). With several leaks fixed in early July one regenerated purifier could keep the oxygen content at levels below 200 ppm for about 10 days giving the gas crew considerably more than the needed minimum of 3 days to regenerate the second oxygen purifier in parallel.

The gas system caused a total OTR downtime of about two weeks in 2000. This time was mostly needed to find leaks that had developed in the system. Leaks occurred in the bellows of 4 of the 14

metal bellows pumps that circulate the gas. The leakage is most likely due to metal shavings and/or dust getting wedged in the outside of the moving bellows and finally causing a rupture. In order to prevent further leaks, 5 pumps were lifted up from the floor of the pump house and an air filter was installed. During the shutdown it is planned to install a leak detection system for the pumps using an oxygen meter and valve system (cost $\approx$ 25 kDM) to pinpoint any future pump leaks very quickly; this should drastically reduce the downtime caused by leak hunts for faulty pumps. Further leaks were caused by fittings that had loosened, most likely due to vibrations on the gas trailer. As a preventive measure the gas crew now regularly tightens all fittings in the underpressure part of the system.

Figure 49 (left) shows that for most of the run period the gas system was able to keep the variation of the main gas concentrations within the range allowed by design: (65$\pm$1)% for Argon, (30$\pm$1)% for CF_4, and (5$\pm$0.2)% for CO_2. A variation of Argon concentration by 1% corresponds to a change in gas gain of $\approx$15% under nominal operating conditions. However, a loose cable in the mixing system caused temporary deviations of several percent from the nominal Argon content, which corresponded to a measured gain drop of about 50% as shown in Figure 49 (right). In addition, unavoidable air pressure changes and correlated variations of the absolute chamber pressure of up to 40 mbar can produce gain changes of up to 25%.

The variations in gas concentrations were reduced by improving the corresponding monitoring and alarm system. However, there are indications that the losses of wires in the OTR are correlated with high gas gain. Consequently, the gas gain must be better regulated in the future. It is planned to build a feedback system based on gain measurements in 5 mm and 10 mm honeycomb monitor chambers that regulates the HV for the OTR (see section 2.5.4).

High Voltage Stability: From the very beginning of OTR operation in July 1999 it was observed that HV groups occasionally failed. The average long term rate of these failures was one HV group per 5 hours up-time of the Outer Tracker, but there were strong fluctuations. Since a HV group combines 16 readout channels, the failure of a single channel causes a loss rate which is a factor 16 higher.

The failure rate was especially high in TC2–, the first assembled and installed large chamber. Here it was suspected that this was caused by mechanical instabilities of the modules, none of which was reinforced with CF rods. The complete overhaul of TC2– in December 1999 comprised the following steps:

1. The gas box was opened in situ, i.e. the chamber was retracted from its beam position but not removed from the detector. Then the modules were removed layer by layer, put into boxes, and transported to the repair area.

2. All modules were reinforced with six 4 m long CF rods each.

3. All reinforced modules were subjected to a rigorous HV test in air. With reference to a flat table, the module was bent with a sagitta of 8 mm, a condition similar to what was observed on modules installed in TC2– during the first assembly. All wires which then showed shorts or excessive dark currents were disabled. Compared to the original test procedure which only checked perfectly flat modules, the number of eliminated wires roughly doubled, raising the fraction from 0.6 to 1.3 %.

4. The repaired and tested modules were reinstalled in the gas box which then was closed and sealed again.

During the 8 months of running time after this repair only 16 of 606 HV groups in TC2– showed problems, compared to 115 groups during the 5 months before the repair. While this is a remarkable improvement, it is not a complete cure of the problem which shows that a full understanding of the OTR HV stability problem is still lacking.

As of mid August 2000 there were 499 defect HV groups in the whole Outer Tracker. Table 23 shows their distribution over the 13 super-layers, together with the corresponding percentages of damage.

Table 23: *Distribution of defect HV groups in the Outer Tracker.*

	$-x$			$+x$			both x		
SL	total	bad	%	total	bad	%	total	bad	%
MC1	78	1	1.3	60	1	1.7	138	2	1.4
MC2	84			66	2	3.0	150	2	1.3
MC3	108	1	0.9	90	8	8.9	198	9	4.5
MC4	114	12	10.5	96	11	11.5	210	23	11.0
MC5	44	1	2.3	41	2	4.9	85	3	3.5
MC6	120	1	0.8	102			222	1	0.5
MC8	126	9	7.1	136			262	9	3.4
PC1	621	30	4.8	496	44	8.9	1117	74	6.6
PC2	415	47	11.3	337	27	8.0	752	74	9.8
PC3	415	29	7.0	337	18	5.3	752	47	6.3
PC4	625	26	4.2	500	47	9.4	1125	73	6.5
TC1	584	53	9.1	498	48	9.6	1082	101	9.3
TC2	606	16	2.6	520	65	12.5	1126	81	7.2
Sum	3940	226	5.7	3279	273	8.3	7219	499	6.9

A statistical analysis of the faulty groups yielded the following results:

- Modules with 5 mm cells are more affected than modules with 10 mm cells. This indicates that mechanical imperfections which are much more critical in 5 mm than in 10 mm cells may contribute to the problem. Modules in the spatially tight region of the overlap caps have failed more often than others. Apart from that the faults do not concentrate in particular module types or module regions. Particularly high loss rates in certain super-layers, e.g. MC4, could not be traced back to any specialties of production, assembly etc.
- The repaired chamber TC2– has a significantly smaller fault rate than all other large chambers with reinforced modules. This indicates that not only the module reinforcement but also the more rigorous module testing are necessary for enhancing the HV stability. Another possibly relevant difference of TC2– and all other large chambers is that about 30 % of its modules are equipped with "old" type HV boards.
- It may be interesting to note that MC2–, the only chamber with graphite coated modules, had no losses despite being operated from the very beginning. Although this observation is not statistically significant, one may speculate that the higher surface resistance of the graphite compared to the gold coating is limiting discharges. In this chamber all modules are equipped with "old" HV boards.

In addition a series of other tests was performed. The results can be summarized as follows:

- The measured Ohmic resistances of the broken HV groups show a broad distribution between 200 kΩ and 20 MΩ, with a sharp peak at 1.1 MΩ. The peak is created by shorted drift cells and accounts for less than 10 % of the faulty HV groups. This indicates that broken wires or otherwise shorted drift cells cannot be the major source of the OTR HV problems.

- HV groups continue to fail even without beam. Due to the limited time of this test the failure rate could not be significantly distinguished from the one observed with beam.

- There are no obvious correlations with environmental conditions (air pressure, chamber temperature) or gas quality (fraction of contaminants).

- Increasing the argon fraction of the gas at the expense of the quenching components (CF_4 and CO_2) significantly raises the fault rate. Tests with decreased argon fraction were terminated by the end of the 2000 run, within the limited statistics there are only indications that the HV fault rate is slightly smaller than with the original gas. This will be investigated in more detail during the shutdown 2000/2001.

- Increasing the resistance in the common supply line of a HV group (serving 16 wires) from 0.1 to 1.1 MΩ prevents the group from failing. During the last months of running, this modification was made to about 20 % of the OTR HV groups and none of them failed afterwards while in the same time 80 failures occurred in the unmodified part of the detector. Simulations using SPICE have shown that with the lower resistance the time between an initial (presumably non-destructive) breakdown of a drift cell and the return of the high voltage to its nominal value is very short (around 1 ms, depending on some assumptions). This possibly is too short for the charged remnants of a discharge to disappear from the affected cell region, thus creating the conditions for repetitive and finally destructive discharges.

All these external observations did not provide sufficient evidence to draw final conclusions about the reason for failing HV groups in the Outer Tracker. There only were strong indications that discharges and mechanical module imperfections are important ingredients.

The inspection of damaged modules from the chamber PC1+ at the beginning of the 2000/2001 shutdown revealed a somewhat unexpected major source of the OTR HV problems: In 39 out of 49 cases the "short" was caused by a burnt-in carbon trace of varying resistance across either of two capacitors on the bottom side of the HV board. In no case any of the 15 top side capacitors caused the problem. This systematic difference probably has to do with the differing mounting techniques used for top and bottom side components, investigations are ongoing. Only two of the 49 faulty HV groups (and of 496 groups in total) are related to shorted drift cells. This count does not include the four cases of obvious mechanical module damage.

We are currently trying to understand the experimental findings from the above list in terms of this new situation. In particular there are no convincing models yet for the different behavior of 5 and 10 mm cells and for the effectiveness of the increased resistance in the common supply line of a HV group.

Dead and Noisy Channels: The number of dead OTR channels in the HERA-B data at any point in time is strongly determined by the organization of the HV distribution. Each of the 160 HV sources on the supply unit in the electronics trailer serves up to 6 cables. Each of these cables serves up to 16 HV groups on the detector, and each HV group supplies 16 wires. As soon as a single wire develops a short, it shuts down its serving HV source. This disables up to $6 \times 16 \times 16 = 1536$ wires, about 1.4 % of the OTR channels. Disconnection of the proper cable to the detector reduces

this number to 256 wires or 0.2 % of the OTR. A further reduction to the 16 wires of the failing HV group requires access to the detector which is possible once per month, sometimes more often. Elimination of the failing wire needs extraction of the module from the detector which requires a major shutdown.

Depending on the cable and HV group disconnection status the number of dead channels in the OTR varies between 5 and 15 %. As can be seen from table 23, towards the end of the 2000 run disconnected HV groups accounted for 6.9 % dead channels. Wires which were cut during module testing prior to installation contribute less than 1 %, the same is true for bad HV connections inside the gas boxes. Problems in the readout electronics contribute another 2 % of dead channels (see table 21).

Assuming that in general only one broken wire is responsible for a failing HV group, a module repair by bad wire disconnection reduces the number of dead channels by a factor 16. If all defect OTR modules could be repaired during the 2000/2001 shutdown a base contribution of about 2 % dead channels from single disconnected wires would remain.

During the 2000 run about 5 % of all ASD-8 channels were marked as noisy on the basis of their large occupancy and/or bad TDC spectrum shape. It should be possible to considerably reduce this rate by the noise reduction measures scheduled for the shutdown (see section 2.5.4).

2.5.2 Track Reconstruction Software

Status of Reconstruction with Ranger: The general concept of track reconstruction in the Main Tracker is described in [58]. The first step is to find track segments in the pattern tracker (PC area). Track segments found in the pattern tracker are propagated through the magnet, determining the particle's momentum, an estimate of which is already given by the track deflection relative to the direction to the target. In a subsequent step, these track candidates will have to be matched to the track segments in the silicon vertex detector. The resulting tracks are then continued downstream to the lepton identification devices. As an additional tool, the use of external seeds for track reconstruction is foreseen. External seeds could be track segments in the VDS (downstream propagation) or seeds generated on the basis of information from the ECAL, RICH, MUON detectors (upstream propagation). All described features are implemented in a software package called *ranger* [59] which consists of a set of procedures for pattern recognition in the Main Tracker and track parameter reconstruction (fitting) in the full HERA-B detector. The reconstruction software is fully commissioned on simulated and real data. It is available for online and offline analysis.

Efficiencies are calculated for reference tracks which are a track class defined by both the geometrical acceptance and the physics interest of the experiment. A reference track in the pattern tracker is required to cross at least 18 layers of the tracker. A track candidate is regarded to properly reconstruct a particle if at least 70% of the hits where caused by this particle. The performance of the reconstruction program was studied using samples of simulated golden B decays and unbiased inelastic interactions passed through the full HERA-B detector simulation procedure. To take into account the OTR performance, mask files with the description of not working cells were used. The efficiency to reconstruct a muon from a golden B decay for different performances of the trackers is shown in Fig. 50a. The reconstruction efficiency depends only weakly on the target rate (see Fig. 50b).

The computing time shown in Fig. 50c increases only slightly faster than linear as function of the number of interactions. The different steps of the reconstruction share this time quite unequally: For the combined OTR and ITR reconstruction and for 5 inelastic interactions the tracking in the

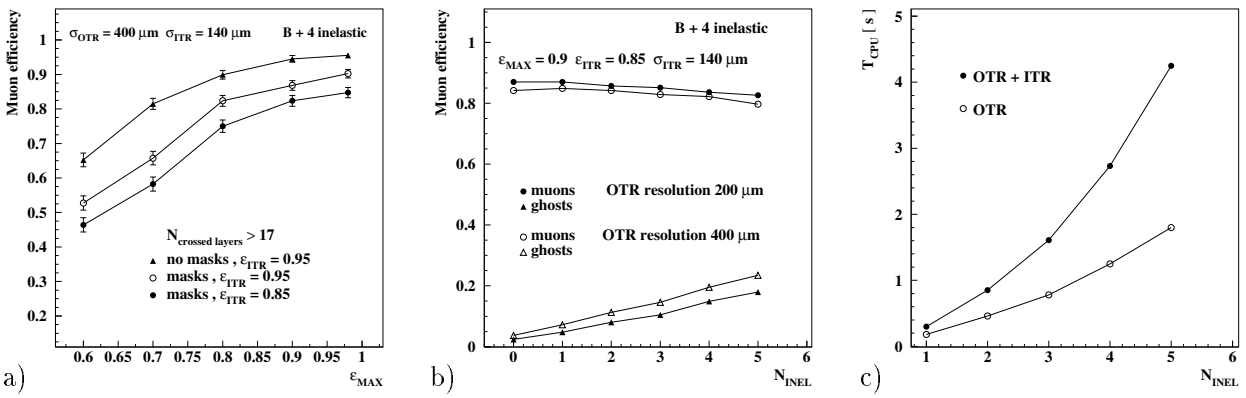

Figure 50: *a) Efficiency of muon reconstruction as function of OTR cell efficiency. b) Efficiency of muon reconstruction as function of the number of superimposed inelastic interactions. c) Computing time of combined pattern and magnet tracker analysis as function of the number of inelastic interactions.*

PC area takes 85% of the time, the magnet propagation 13%, and the propagation in the TC area 2%. Improvements of the first step will be worked on in the future.

A comparison of the computing time for reconstruction of real and simulated events shows that tracking for real data is still a factor of about 1.7 longer. Only part of it can be explained by a higher occupancy for real data (factor 1.4). These differences have to be further studied.

Tracker Alignment: The OTR consists of 978 modules. Each module is divided into up to 4 active areas. Each of these areas is represented within the geometry description as a so called GEDE table. These GEDE volumes are considered as the basic alignment units and treated as rigid bodies. The alignment data structures allow in general for 3 rotations and 3 translations although only 3 of these transformations are assumed to be dominant (du: direction perpendicular to the wire and the z-axis, dz: along the z-axis and $d\alpha$: stereo angle correction).

At present only du and the z-position of a whole layer are taken into account by the alignment procedure. The procedure is based on tracks given by the reconstruction program *ranger*. The Kalman filter algorithm of *ranger* has been proven to be robust enough to do tracking even in a situation with large misalignment (i.e. in the order of several millimeters). Therefore the alignment parameters can be determined by an iterative approach. The largest disadvantage of such a method is the necessary computing time. At present the processing time per event is of the order of half a second and the number of events to be processed for the OTR alignment is about 400k. Therefore one iteration needs about 50 hours CPU time.

Within a super-layer the spread around the nominal position has been found to be approximately 1 mm. Larger deviations are observed for special modules (e.g. above the beam pipe) or between the 5 mm and 10 mm modules which have different mounting plates.

The alignment has been tested mainly for the linear tracking region (PC and TC) and residuals with external tracks show a clear improvement in width. Also the studies on the efficiencies of the OTR (see below, Fig. 52a) give as a by-product an upper limit on the precision of the alignment in the PC region. In the study the rms spread of the cell position averaged over one module is about 100 μm for the 5 mm modules in PC– and about 250 μm for PC+.

For the magnet chambers work is in progress. Unfortunately due to frequent accesses in the magnet area the chamber positions are changing and – contrary to the PC and TC chambers – there exists no mechanism for a precise re-positioning of the super-layers. Therefore different sets of alignment constants are needed for short periods of runs.

The internal module alignment has been studied by analyzing average shifts of the wire positions between two mono-layers within a single module. By considering the difference between residuals in different mono-layers the result is independent of the (inter) module alignment. The observed shifts are in general smaller than about 60 μm and thus confirm the design goal of 100 μm for the relative cell alignment within one module.

Individual module alignment in z position and stereo angle and also a possible online alignment are still open questions. Although none of these is expected to be a problem in principle, detailed work will be necessary. Furthermore any alignment algorithm will benefit if the time consumption of track reconstruction can be reduced.

Tracker Calibration: The Outer Tracker reconstruction uses as input the wire positions, the measured drift distances and the corresponding errors of a set of hits. As the detector measures a TDC value and not a distance, a calibration procedure is required.

Calibration of the TDC Offset: The TDC value that is output from the front-end electronics can be translated into a drift time by subtraction of a channel dependent TDC offset t_0. The TDC is synchronized to the bunch clock. Substantial evidence is found that the t_0 calibration must be performed for every channel separately to reach the required precision.

Different methods have been developed to determine the t_0 from a TDC spectrum only. The systematic uncertainty (among others due to differences in wire length) is estimated to be of the order of 100 μm.

Methods to improve the t_0 calibration are under development. A correction for the signal propagation time in the wire by using the y coordinate information of the reconstructed track is expected to provide a better correspondence between TDC spectra from sectors with a different wire length. The ultimate precision might be obtained by using residuals from track fitting. However, since the number of degrees of freedom is enormous, it is not evident that such a procedure will converge.

Calibration of the Drift Time Space Relation: The drift time obtained after subtraction of the TDC offset is translated into an estimate for the distance-of-closest-approach and a corresponding error. These two relations are called the drift time space relation or rt-relation $r(t)$ and the resolution function $\sigma(t)$.

The relations are determined from reconstruction of real data by requiring that for every 'drift time bin' the distribution of normalized residuals[36] is centered around zero and has unity width.[37] In order to obtain smooth functions, the relations are parameterized in terms of polynomial B-splines. An iterative method has been developed that performs an 'unbinned' calibration in order to fully use the available statistics.

It is assumed that only a small number of rt-relations is required to calibrate the detector. In particular there is only one such relation for all 5 mm cells in the field free region of the detector. In the magnetic field region, the rt-relation significantly depends on the strength of the field. An effort

[36] The normalized residual is the residual divided by the estimated error.

[37] As the residual distributions are rather non-Gaussian, the width is iteratively determined in terms of the root-mean-square within 3 sigma of the average of the distribution.

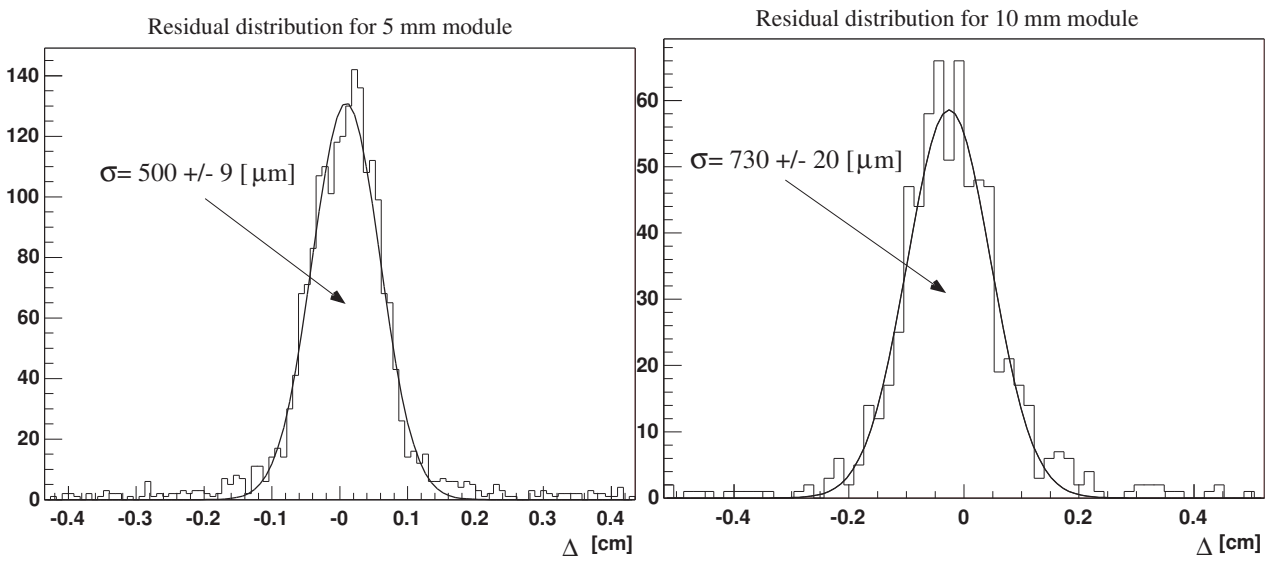

Figure 51: *Residual distribution of a typical 5 mm module (left) and 10 mm module (right) in the PC area.*

Table 24: *Conditions for runs used for the efficiency analysis. The "new" threshold values for the PC super-layers are given in Table 22. In run 14577 the "old" threshold was 100 mV higher for super-layers PC1+, PC2+, PC3–, PC3+, PC4–. The gain is given relative to a nominal gain.*

Nr	Run	date	rate [MHz]	$Ar/CF_4/CO_2$	Threshold	HV [V]	Gain
1	14577	12.04.00	4.9	65/30/5	old	1700/1900	1.13
2	16990	11.08.00	5.0	70/25/5	new	1650/1850	1.02
3	17255	25.08.00	2.0	63/30/7	"	1715/1915	1.17
4	17254	25.08.00	1.8	"	"	1785/1985	1.46

to calibrate the detector in the magnetic field is under way.

Figure 51 shows the observed residual distribution of two typical modules in the PC area. The current estimate of the average resolution for 5 mm and 10 mm cells is 600 ± 50 μm and 700 ± 50 μm, respectively.

2.5.3 Detector Performance

Cell and Track Efficiencies: The outer tracker cell efficiencies were estimated for super-layers PC1, PC2, PC3, PC4 which are used for pattern recognition and in case of PC1 and PC4 for triggering. Four runs taken between beginning of April and end of August 2000 (Table 24) have been analyzed and compared.

Taking run 17255 as an example the cell efficiency as a function of the distance from the wire is shown in Fig. 52a for the upper long wire part (sector 1) of a standard module of super-layer PC1–. From the fitted curve the efficiency in the plateau was determined to be 0.93. This region has a radius of about 2 mm around the wire. In the region outside of the plateau which corresponds to the edges of the hexagonal cell, the efficiency drops to zero. The efficiencies of the 128 cells of the

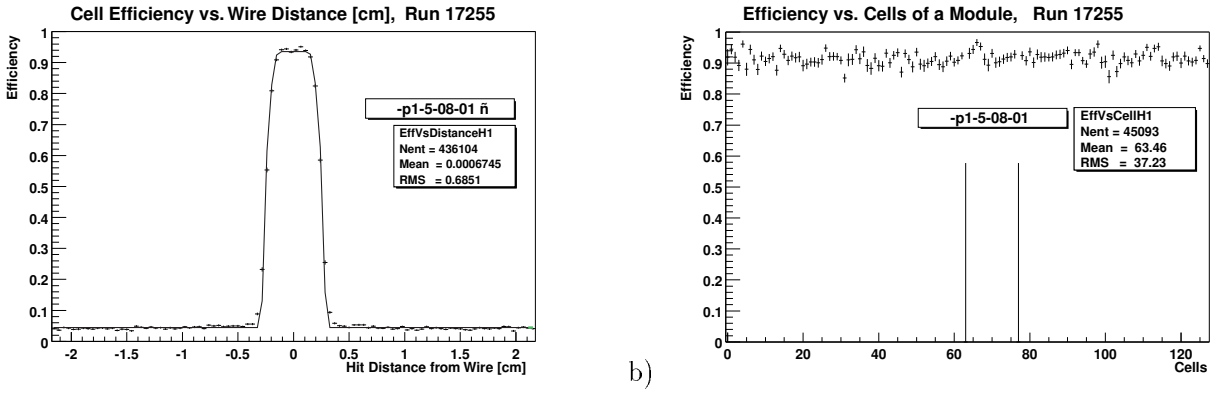

Figure 52: *a) Dependence of the cell efficiency on the distance from the anode wire (5 mm cell) for module 8 in sector 1 in stereo layer 5 of super-layer PC1–. b) Efficiency of the 128 cells of the same module.*

same module sector given in Fig. 52b are rather constant and mainly above 0.90.

The fitted plateau efficiencies of all 5 mm module sectors of super-layer PC4– are plotted in Fig. 53 for the four runs. A clear gain dependence is observed comparing the runs 17255 (gain 1.17) and 17254 (gain 1.46) which were taken on the same day with the same gas mixture and air pressure values. The corresponding results for the 10 mm modules can be found in Fig. 54. A small number of modules with efficiencies below 0.7, mainly caused by low statistics or a large number of disconnected HV groups, have been excluded. The resulting super-layer efficiency is the mean of the distribution which is still influenced by the tail of bad modules. Most of the distributions peak around or well above 0.90.

This analysis was performed for a total of about 1000 module sectors in all eight super-layers halfs PC1– to PC4+. The mean values are distributed in Fig. 55 as a function of the threshold for runs 14577 and 16990. For both, 5 mm and 10 mm modules, there is a clear threshold dependence. A more detailed comparison of both runs is difficult since several parameters as threshold, gas mixture and high voltage were changed.

The runs 17255 and 17254 differ in the high voltage settings only which results in different gains of 1.17 and 1.46, respectively. The values in Fig. 56 show therefore not only the threshold dependence but also a significant gain dependence. The gain values were measured with radiated cells of super-layer MC8 (see also Fig. 49 (right)).

Summarizing the results of the preliminary efficiency analysis, it can be stated that there is a clear dependence on the threshold and the gain. The 5 mm modules of super-layers with the smallest threshold have efficiencies above 0.90. The efficiency for 10 mm modules is with one exception larger than for 5 mm modules. A fair comparison between runs 14577, 16990 and runs 17254, 17255 is not possible since the number of dead HV groups has increased considerably over the running time. More detailed studies will be performed with the existing data to estimate the inefficiencies due to the wire strips within the module. Furthermore, the analysis will be extended to the TC and MC super-layers.

Resolution and Alignment Results: In the previous section the spatial resolutions of OTR hits have been shown (Figure 51). The resulting estimates of the average resolutions are 600 $\pm$ 50 μm

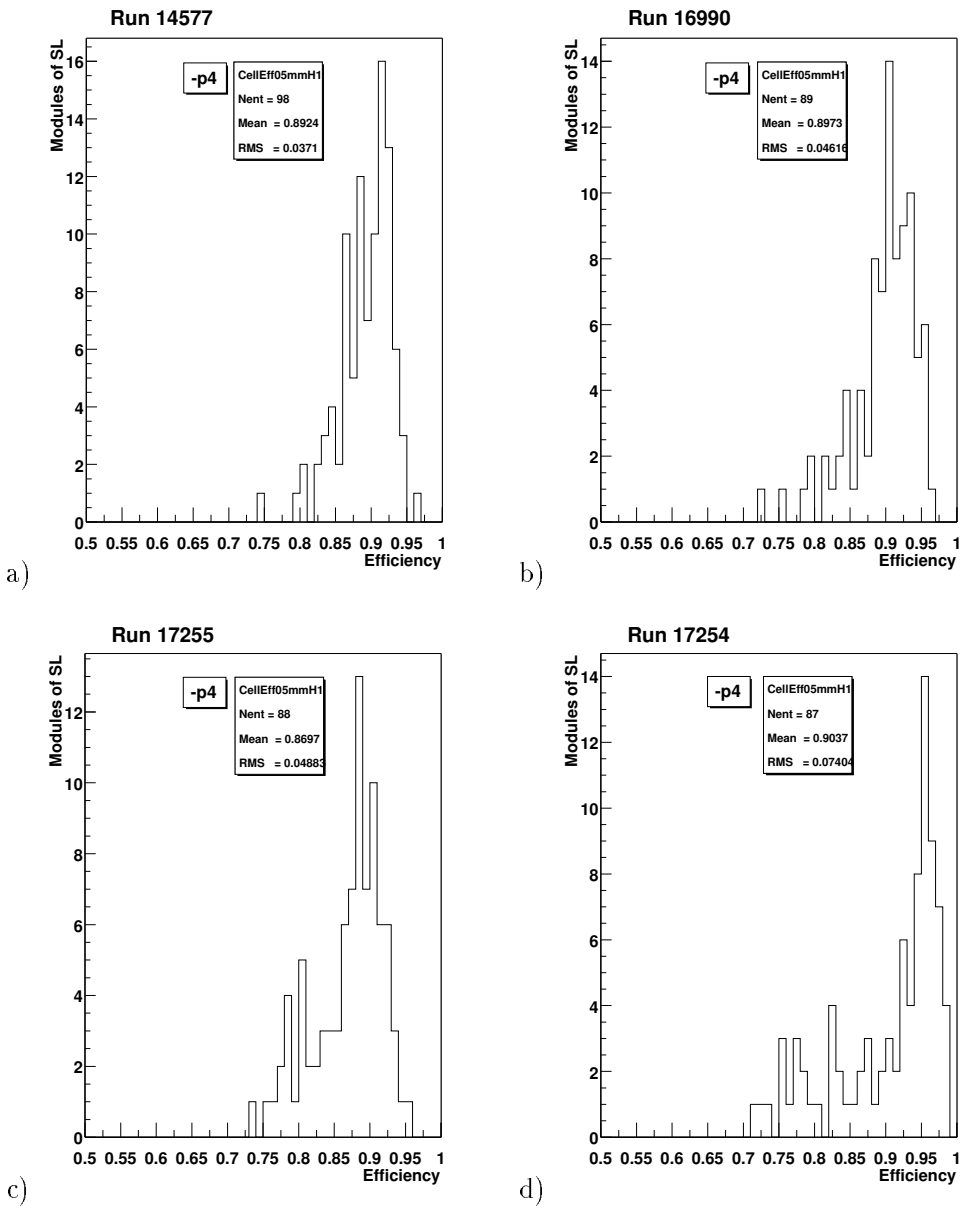

Figure 53: *Efficiency of 5 mm modules of super-layer PC4– for four different runs. a) run 14577, b) run 16990, c) run 17255, d) run 17254.*

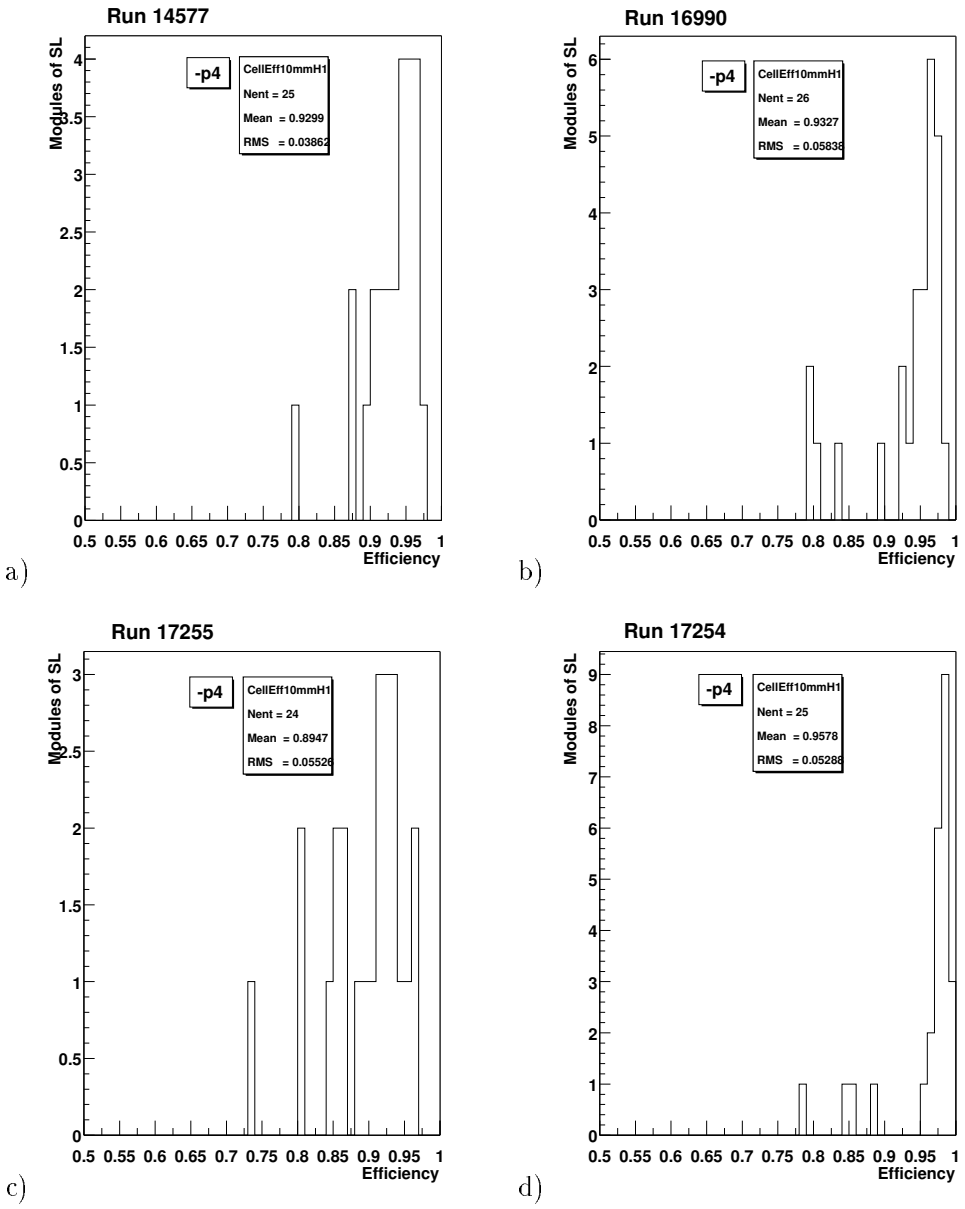

Figure 54: *Efficiency of 10 mm modules of super-layer PC4– for four different runs. a) run 14577, b) run 16990, c) run 17255, d) run 17254.*

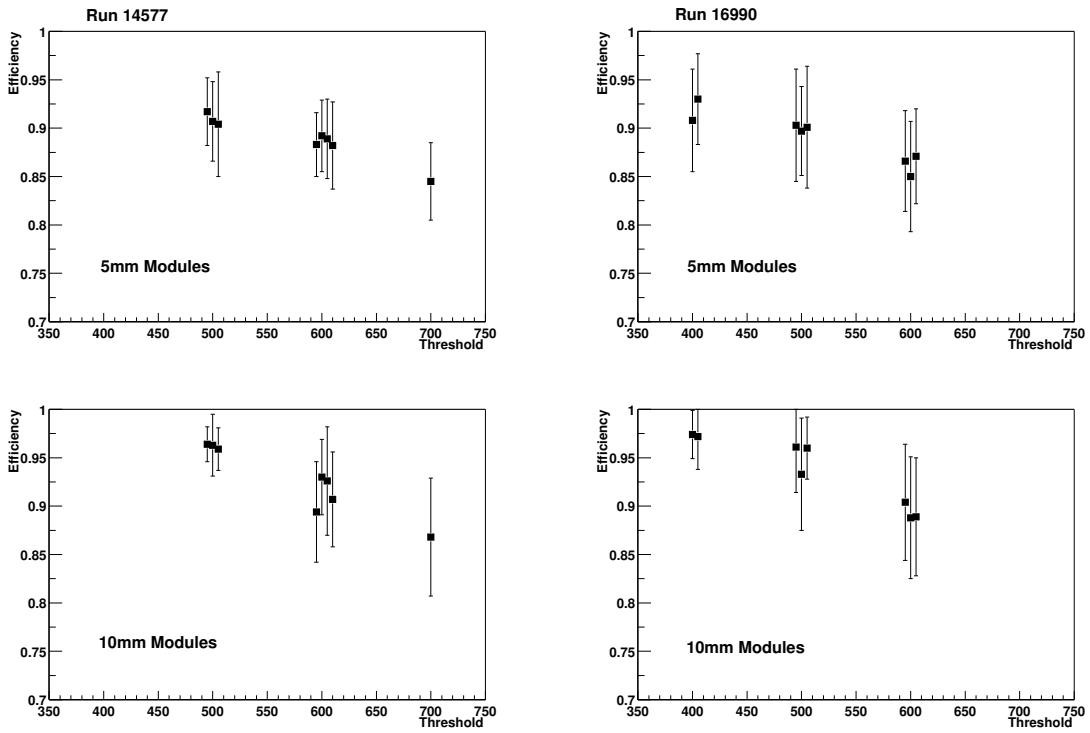

Figure 55: *Average efficiency of the PC super-layer halfs for runs 14577 and 16990 taken under different conditions (see tab. 24). The error bars are the rms values of the distributions.*

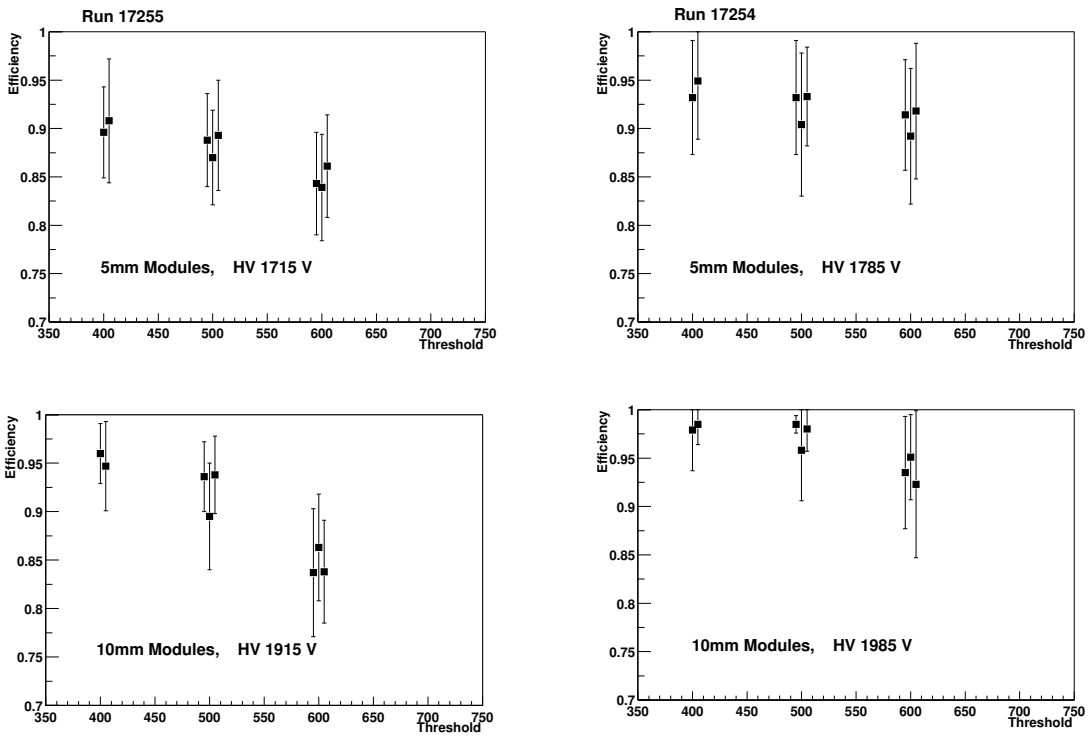

Figure 56: *Average efficiency of the PC super-layer halfs for runs 17255 and 17254 taken under identical conditions, except the high voltage. The corresponding gains are 1.17 and 1.46.*

and 700 ± 50 μm for 5 mm and 10 mm cells, respectively. This is much larger than the 200 μm which had been assumed in the design phase of the detector and verified in test measurements.

The procedure to determine the resolution from residuals of reconstructed tracks yields a result which reflects both the intrinsic resolution of the wire chambers and the remaining errors in the calibration and alignment. In order to understand the resolution it is essential to disentangle these effects.

If a charged particle creates more than one hit within a certain module, the correlation between the drift times of those hits can be used to obtain an estimate of the resolution relatively independent of the module alignment. Following this analysis the current estimate of the intrinsic resolution of a 5 mm cell is 350 ± 50 μm. This value sets the landmark for the calibration and alignment of the whole detector.

Still, the 350 μm is substantially larger than the 200-300 μm that has been observed in test measurements. This can be explained by the fact that the ASD-8 amplifiers have to be operated at higher thresholds and lower gas gain than used for the test measurements, due to the HV and noise problems (see the discussion in section 2.5.1).

The remaining difference between the observed average resolution of 600 μ, the internal resolution of 350 μ and the alignment errors of 100 to 250 μ can probably be attributed to the degrees of freedom that are not yet considered in the alignment procedure, i.e. dz and stereo angle corrections. Different aproaches to include these into the alignment procedure are under consideration.

Concluding remarks on the OTR Performance Studies: The presented studies on efficiencies, alignment and resoltion are still very preliminary and incomplete. We are well aware that not all quoted results are consistent and that more detailed studies are necessary. For example, the hit resolution obtained from fitted tracks of about 500 to 1000 μm, the internal resolution of 350 μm and the observed alignment errors between about 100 and 250 μm seem to be inconsistent.

Concerning the efficiency studies, the results have to be compared to the expected geometrical acceptance, sorted according to module qualities and interpreted in terms of tracking and triggering efficiencies.

The hope is also that the repair and upgrade programm for the OTR during the shutdown will improve the performance considerably. The run 17254 with the gain increased by 1.46 gives a guide line of what could be expected.

2.5.4 Repairs and Upgrades During the Shutdown

General Plan: The HERA shutdown 2000/2001 will be used to fix problems which have been encountered in the OTR during installation, commissioning, and first running experience. The major observed draw backs are (see section 2.5.1):

- high voltage instabilities of the modules which cause shorts in the HV groups;
- noise induced by the signal cables connecting the TDCs of the trigger layers to the TLBs;
- instabilities of the optical links between TLB and FLT.

Solutions for these problems are considered vital for the operation of the OTR after the shutdown. The actions which will be taken during the shutdown are explained below.

Apart from working on these major problems, some maintenance and upgrade work will be done, both on hardware and software:

- Improvement of the cabling of the TDC system to the SLB boards and the FCS system;
- improvement of gas gain monitoring and installation of an automatic gain steering;
- installation of a leak control system for the gas system;
- improvement of calibration and alignment, implementation of dedicated fast tracking, integration into the online system;
- improvement of reproducibility of the positions of the magnet chambers;
- improvement of tracking, like ghost rate reduction and implementation of external seeds;
- studies of chamber performance, tracking efficiencies.

Module Improvements: The major OTR activity scheduled for the 2000/2001 shutdown is a substantial reduction of the dead channel count by repairing as many modules as possible. This requires the gas boxes of the super-layers to be opened, followed by extraction, repair, test and re-installation of the modules. In addition two working places for module production have been set up and production materials have been provided, just to be prepared to replace strongly damaged modules by new ones.

This is a major logistics and manpower effort. A detailed time schedule and manpower distribution until the end of this year exists. The operation has started with the treatment of the most crucial trigger layers which will last until about February 2001. Dependent on the experience the remaining PC layers will be repaired during spring 2001. It is currently unlikely that MC chambers can be repaired.

The following investigation and repair activities are foreseen:

- All bottom side capacitors on the HV boards (not only the damaged ones) will be exchanged using a clean soldering technique which avoids any adhesive and uncontrolled disposal of soldering fluid. This technique has already been established. For the whole OTR this means the exchange of 14 500 SMD capacitors, for the trigger layers PC1, PC4, TC1, and TC2 only 9 000 are enough.
- All modules without reinforcement will be reinforced with CF rods. This mainly affects the chambers TC1– and PC4–. Minor mechanical damages will be repaired, severely damaged modules have to be rebuilt.
- All repaired modules will be subjected to a rigorous HV test, which identifies short and hot wires, while mechanically exercising the module. All bad wires will be disconnected from the HV board. Experience with TC2– shows that this procedure doubles the bad wire count compared to testing the module in a perfectly flat state. The expected total cut rate is 1.5%. If the total dark current of a module cannot be substantially reduced by disconnecting a few wires (< 5 by previous experience), the module should be rebuilt.

- After installation of each module layer in the gas box the capacitances at various points of the HV system will be measured. Various error conditions (unplugged HV cables, unplugged ASD-8 boards etc.) are characterized by typical values of the capacitance w.r.t. ground. For each installed layer there will be a final HV test.
- The modifications of the HV circuitry resulting from the investigations described below will be implemented for the whole Outer Tracker.
- Even though the main source of HV trouble in the Outer Tracker has been identified by now, it is still foreseen to thoroughly investigate a small number of damaged modules. However, the priority of these activities has decreased a bit:
  - In order to better understand what causes the breakdown of wires, a few selected modules will be carefully dissected and later be subjected to a materials analysis. Even if the scope of the broken wire problem has shrunk a lot, it is still important to understand the reason for this to happen.
  - For another damaged module the pulse heights along the wire will be measured for all drift cells. These measurements will be repeated for different module deformations. This serves a better understanding of the influence of the unavoidable module deformations on the performance of the Outer Tracker.

With these modifications it should be possible to safely operate the Outer Tracker at a higher gain than in the 2000 run.

Drift Gas Studies: As discussed in section 2.5.1 (High Voltage Stability) there are indications that the HV failures are caused by discharges in a cell. It is therefore important to investigate whether the quenching properties of the drift gas, mainly determined by the CO_2 and CF_4 content, are sufficient. Depending on the observations made on the opened drift cells, in particular if we can identify the location of discharges (e.g. on the strips?) we consider a detailed investigation of the influence of CO_2 and CF_4 on discharges.

As we know from various laboratory tests, the water content in the drift gas is another important parameter. In the closed gas system with active purifiers (operating since April 2000) the drift gas was particularly dry, below about 20 ppm (Fig. 49). At such a low water content anode etching was observed in laboratory tests (note that there the irradiation level was much higher than expected in HERA-B). On the other side, a water content above about 1000 ppm was observed to make the strips conductive. As a compromise between these boundaries the OTR group has earlier decided to run at about 200 to 300 ppm of water. To maintain this level while running the purification system turned out to be difficult. A system for controlled water injection has meanwhile been developed and is currently tested in a limited part of the OTR (superlayers PC2 and PC3).

Review of the HV Protection System: The positive results obtained by adding a protective resistor into the common supply line of HV groups (see section 2.5.1, 'HV Stability') suggest to review the whole HV protection scheme of the OTR. This includes the scheme of current limitation and tripping of the HV supplies as well as the protection resistors in the HV circuitry.

In the circuit successfully tested in the OTR an additional resistor of 1 MΩ was added in the supply line of a HV group. However, this is not optimal since at the highest anticipated currents per HV group the voltage drop would be about 35 V. This would cause too high a dependence of the

gain on the interaction rate. Currently different schemes to obtain a constant HV up to a certain threshold current are investigated.

Noise Reduction: In order to increase the single cell efficiency, further measures to decrease the noise must be taken during the shutdown. A possible re-routing of the trigger link cables for PC1+ (ΔU_{th}=600 mV, see table 22) should decrease the noise for this chamber to the level of the other PC superlayers.

Further noise reduction is only possible by eliminating/attenuating the source of the noise on the TDC board: Currently the effect of the fast TTL driver is studied. Possibilities are investigated to remove the drivers from the TDC boards. A replacement of these drivers by differential low voltage drivers (LVDS) is considered and will be tested. However, an implementation of differential cables would require substantial modifications on both the TDC and the TLB side.

If the tests are successful at least some trigger chambers could be improved during the shutdown. A treatment of all trigger layers seems difficult given the time the electronics will be accessible during the shutdown.

Triggerlink Boards: The current quality of the optical link between TLB and TFU is judged to be insufficient to fulfill the requirements by the FLT (see section 2.5.1). Therefore it is planned to rebuild, at least partially, the transmitters on the TLBs. The possible changes are:

1. The offset and modulation currents of the laser diodes on the optical transmitter become remotely programmable.
2. Use nowadays commercially available integrated drivers for the laser diodes.
3. The boards will be tested more rigorously before installation.
4. In order to avoid FLT inefficiencies, signals from broken OTR wires should be turned on permanently in the wire memory of the FLT. A serial interface using FCS strobe signals is foreseen to set bits to 1.
5. The cooling of the boards has to be improved.

Automatic Gas Gain Control: Because of the observed gain dependence of HV failures it was decided to improve the gain monitoring and to develop an automatic gain steering. The monitoring is currently done with special monitor chambers in the gas input and output and in addition by 4 channels dedicated analog readout of Fe-55 spectra in both MC8 super-layer halves. During the shutdown the 'intra-super-layer monitoring' will be extended to include a PC and a TC chamber. The input for the automatic gain steering will be provided by a special chamber ('Karlsruhe type') in the input flow (outside the HERA radiation).

2.5.5 Outer Tracker Summary

The Outer Tracker sub-detector was ready for data taking by the beginning of this year. After the installation of the last super-layer in January the commissioning of the readout electronics, the slow control and the gas system was successfully completed around April, when routine data taking started. The detector is since then smoothly running. Tracking, alignment and calibration

are well advanced and continuously improving. Efficiency and resolution studies have led to a good understanding of the detector properties and of possible improvements.

The major worry during running in 2000 was the progressive HV instability which in the end left almost 7% of the OTR channels dead. Meanwhile the major source of this trouble has been identified and corrective action has been initiated. There exists a detailed plan of shutdown activities to repair the Outer Tracker modules. The confidence that the planned measures will be successful is based on three observations: First, the HV instability problem has changed its character from fundamental to mostly technological. Second, the treatment of TC2– in December 1999 led to a very low loss rate in this super-layer. And third, there is a highly significant lack of any failures in super-layers equipped with additional protective resistors.

The other major worries are the noise induced into the trigger layers by the TDC-to-TLB connection and transfer instabilities of the optical link to the FLT. These effects cause a decreased efficiency for the tracking and the trigger. Both problems will be worked on as well during the shutdown.

Apart from these problems the Outer Tracker is running well suggesting that the design is in principle sound. The problems encountered can mainly be traced back to the time pressure during the detector development and a missing full-scale prototyping.

2.6 Status of the High-p_T Trigger

2.6.1 Overview

The concept of the high-p_T trigger is as follows: tracking chambers with a pad-type readout are placed within the spectrometer magnet. Pad hits are input to dedicated processors, and high-p_T tracks are selected based on the hit patterns. Such tracks tend to bend little or make larger angles with respect to the beam, and their hit-patterns are distinct from those caused by minimum bias tracks.

The tracking chambers with pad readout come in two types: gas-pixel chambers for the region nearest the beam, and straw-tube chambers with "pickup-pads" for the larger outer region. Both types of chambers required extensive research and development [61, 62]. The gas-pixel chambers use short anode wires oriented parallel to the beam. The pad is formed by four potential wires in the corners and one signal wire in the center. The tracks going from the main vertex to the inner high-p_T chambers are almost parallel to the wires. They pass through about 3.5 cm of gas so that the amount of primary ionization is large; moreover, the drift times for these electrons are almost the same (for the central region of the chamber where gas amplification is maximal) and there are no boundary effects. Thus the signal has a fast rise-time and the fraction of total charge collected during the integration time of the ASD-8 is substantial. The signal wires are connected to the ASD-8 cards (located outside the acceptance) via twisted pair cables having a diameter of only 50 μm/conductor and a length of about 1.4 m.

The straw tube chambers utilize straw tubes against which are positioned printed circuits consisting of a pad pattern. These pads are positioned very close to, or in contact with, the outer surface of the straw tubes; the distance of separation is $\lesssim 300$ μm. A gas avalanche occuring at an anode wire then induces an image charge on the pad directly above the avalanche. The pads connect to traces which bring the signals out to ASD-8 cards located outside the acceptance. No signal is read from the anode wires directly, and the inner surface of the straw tubes (which constitute the cathode) must be resistive instead of conductive (metallized) –as is typically found on straw tubes– in order for a substantial signal to be induced on the pads. The induced signal is $\sim 1/3$ of that collected by the anode wire.

There are a total of 12 chambers for the high-p_T system: six gas-pixel chambers for the inner region and six straw tube chambers for the outer region. Half of the chambers are located on the $+x$ side of the proton beam and half on the $-x$ side. For each side the six chambers are positioned at three different distances from the target: $z \simeq 450$ cm (the PT1 station), 570 cm (PT2 station), and 610 cm (PT3 station). The inner region chambers have a total of 11960 channels and cover the angular ranges $10 < \theta_x < 58$ mrad and $10 < \theta_y < 44$ mrad; the outer region chambers have a total of 6240 channels and cover the ranges $38 < \theta_x < 250$ mrad and $44 < \theta_y < 143$ mrad. The amount of material comprised by these chambers is listed in Table 25; the total amount is 2.6% of a radiation length for all three inner chambers traversed by a particle, and 3.9% for all three outer chambers.

The inner gas pixel chambers were constructed at ITEP, Moscow and were completed in October, 1999. The outer straw tube chambers were constructed at the University of Cincinnati and Princeton University and were completed in June, 2000. All inner chambers and 4 of 6 outer chambers were installed during the 2000 running period. The final chamber configuration is shown in Fig. 57.

Due to their positions within the magnet and the high interaction rate and track multiplicity of HERA – B , the high-p_T chambers are subjected to a substantial amount of ionizing radiation. Such ionization can polymerize impurities in the gas volume, and such polymers can subsequently coat the

Table 25: *Material constituting an inner and outer high-p_T chamber.*

Chamber	Material	Depth (mm)	Rad. lengths (%)
Inner	G10 plates	0.20	0.21
	stainless steel field wires, $\phi = 300$ μm	35	0.20
	Solder		0.12
	Twisted-pair cable, $\phi = 50$ μm		0.07
	Gas	35	0.03
	Miscellaneous		0.25
	Total $\times$ 3 chambers:		**2.6**
Outer	straw tubes	0.060 (wall)	0.084
	tungsten anode wires, $\phi = 20$ μm	$0.020 \times (\pi/4)$	0.004
	carbon fiber support tubes	0.89 (wall)	0.16
	silver thread	0.5	0.093
	honeycomb support panels (G10 faces)	1.0	0.048
	honeycomb circuit panel (G10 faces)	1.0	0.52
	aluminum foil (ground)	0.025	0.029
	kapton insulator	0.025	0.009
	pad circuit (G10 substrate)	0.20	0.103
	pad circuit (Cu traces + pads)	0.025	0.174
	carbon fiber plates	1.6	0.042
	G10 strips	1.6	0.027
	Total $\times$ 3 chambers:		**3.9**

anode wires. To minimize aging effects, we use counting gases with very small or negligible amounts of a quenching hydrocarbon component such as CH_4. The mixture for the gas pixel chambers is $Ar/CF_4/CH_4$ 68/30/2, and the mixture for the straw tube chambers is Ar/CO_2 80/20. The large fraction of CF_4 used in the gas pixel chambers is believed to be beneficial for aging. The mixture for the straw tube chambers has been measured to give minimal or negligible aging at high dose rates [63].

2.6.2 Performance of Inner Chambers during the 2000 Run

All six chambers were operational at a voltage setting at least 50 V above the value corresponding to the beginning of the efficiency plateau. During the last month of data taking, the chambers were operated routinely along with the rest of the HERA – B detector. The number of dead channels is relatively small: out of 11 960 channels, 18 are dead due to missing wires or disconnected cables and 12 have lost one wire (from two in the cell) resulting in an efficiency loss of about 30%. An attempt will be made to repair these channels during the Lumi shutdown. There were 227 channels dead due to bad ASD-8 cards (which we believe can be recovered), and 61 channels dead for unknown reasons. There were 593 noisy channels with an occupancy greater than 20% (the real occupancy in minimum bias events is less than a few percent). The majority of these can be made quiet by increasing the ASD-8 discriminator threshold; this results in a small loss ($\sim$20%) in cell efficiency. There were 73 channels which remained noisy even at high threshold settings. We believe that better shielding may further reduce the number of noisy channels. A typical hit map for PT1 (two chambers, one for $+x$ and one for $-x$) is shown in Fig. 58. The chamber performance achieved during the 2000 run and

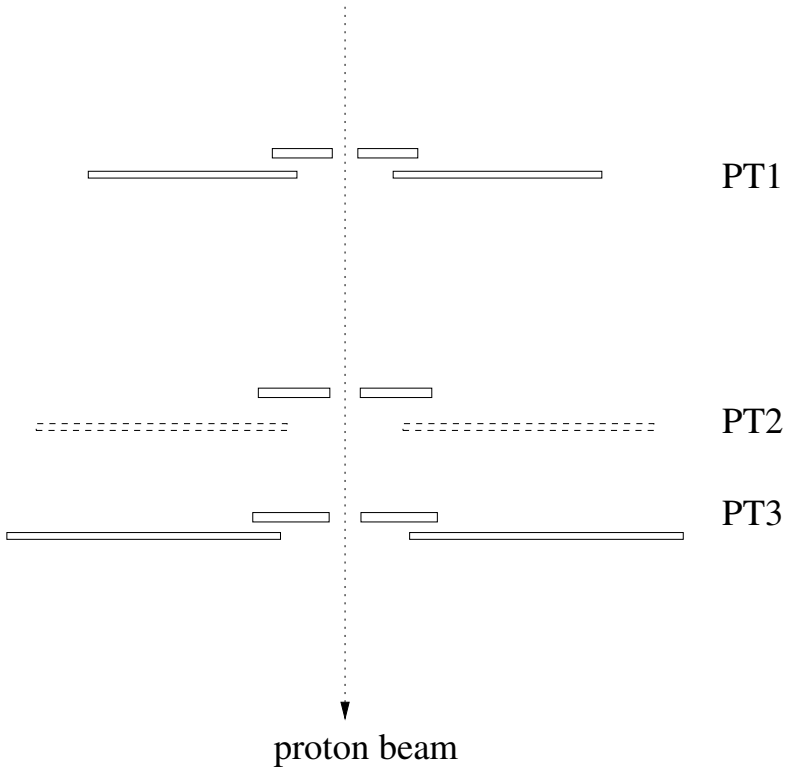

Figure 57: *The configuration of high-p_T chambers for the 2000 run. The outer PT2 chambers (shown dashed) were not installed due to the very limited access to the detector.*

that expected for the 2001 running period are summarized in Table 26.

Table 26: *Inner chamber performance achieved during the 2000 run and that expected for the 2001 running period.*

	Present	**2001**
Number of dead wires	30 (0.25%)	$< 30 (< 0.25\%)$
Number of channels dead for unknown reason	61 (0.5%)	$< 20 (< 0.2\%)$
Number of bad ASD-8 channels	227 (1.9%)	$\sim$ 8 ($< 0.1\%$)
Number of very noisy channels	73 (0.6%)	a few
Number of noisy channels requiring higher threshold	520 (4.3%×20%=0.86%)	$< 0.2\%$
Overall inefficiency	4.1%	$\lesssim 1\%$

The single-cell efficiency was determined using tracks defined by matching VDS, ECAL, and RICH segments. In order to reduce the ghost rate, a coincidence was required with two other high-

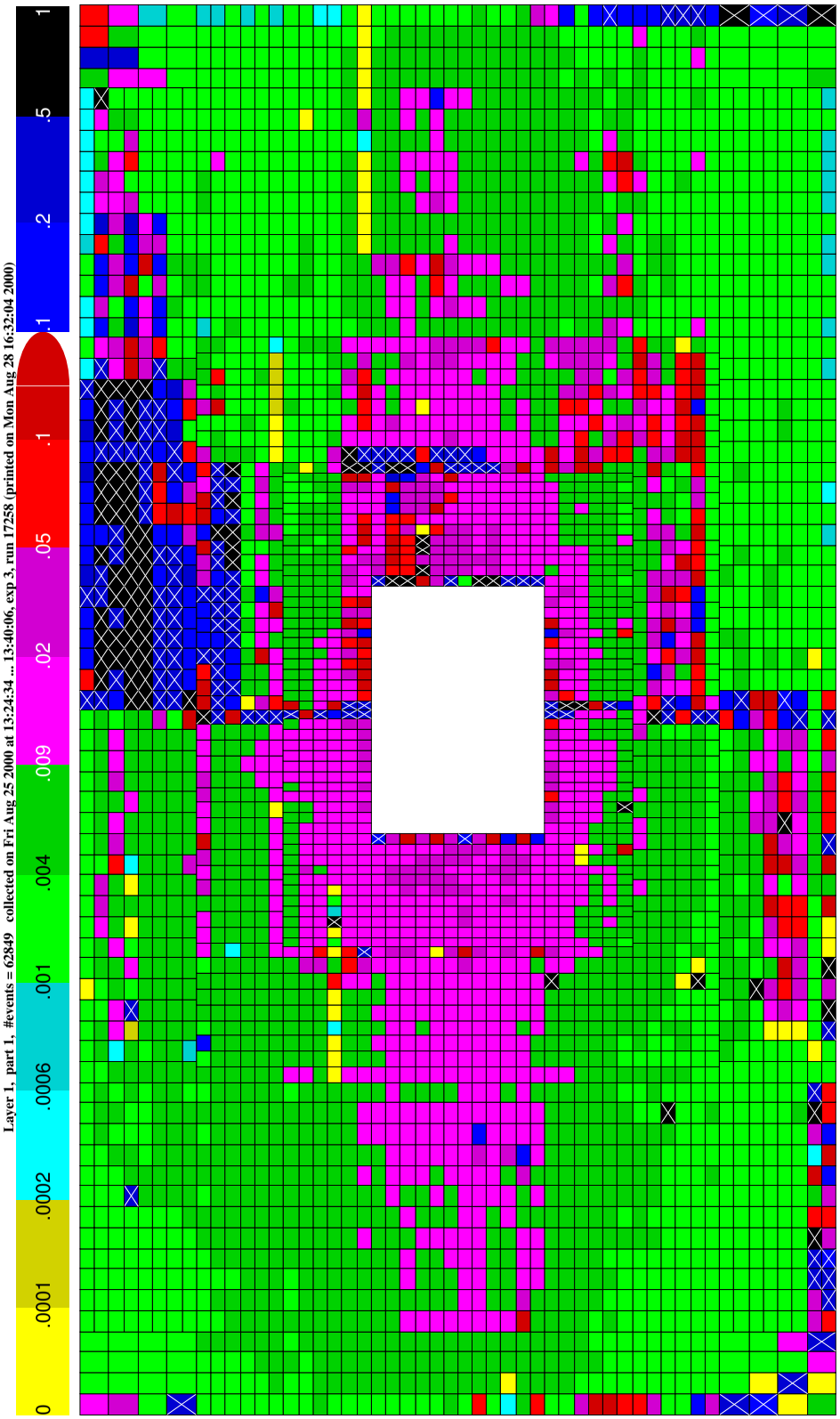

Figure 58: *Hit map of PT1 inner chambers during 2000 run. Cells with crosses were masked out (not used) for pretrigger studies.*

p_T stations (e.g., PT1 and PT3). All known dead and hot channels were excluded. The efficiencies obtained for different chambers and cell sizes are shown in Fig. 59.

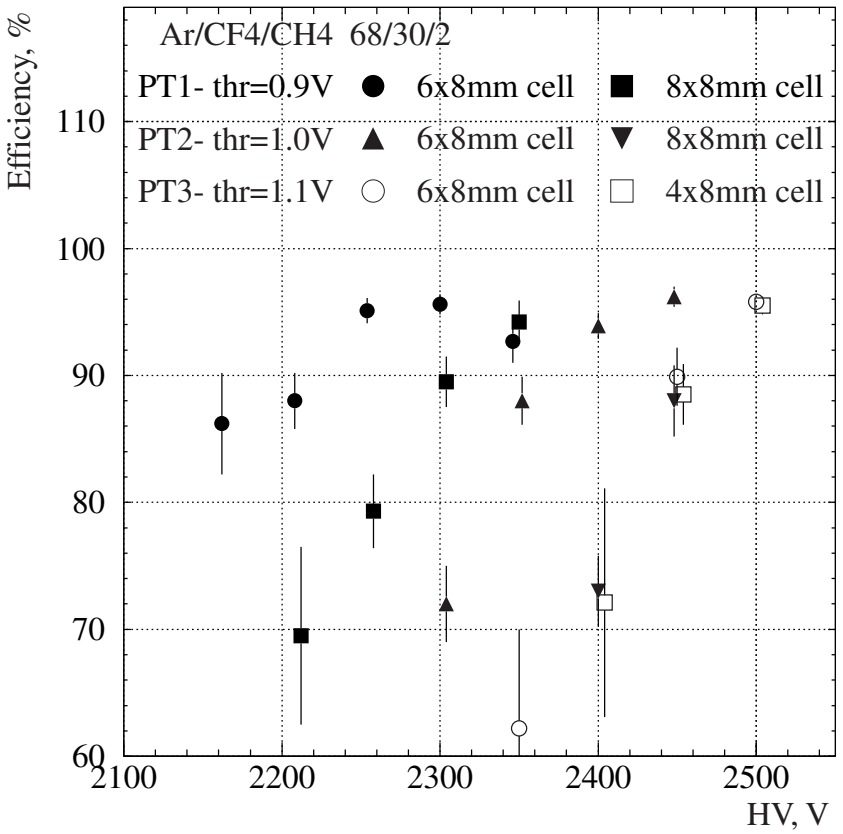

Figure 59: *Efficiencies measured for inner high-p_T chambers during the 2000 run using VDS-ECAL-RICH tracks.*

The PT2 and PT3 chambers have larger cell sizes than PT1 and thus require higher HV settings. The efficiency measured reaches a plateau of about 96% and does not increase further. This could indicate that some fraction of the reference tracks are ghosts or come from the coasting beam; alternatively, there may exist a timing problem or an electronics inefficiency with large signals. The timing of signal readout from the the front-end electronics was achieved using the leading edge of signals arriving after an empty bunch. The timing accuracy obtained was better than 5 ns. Previous tests at the ITEP synchrotron yielded a single-cell efficiency higher than 99% for fluxes up to about 5×10^5 particles/cm^2-s. These measurements, however, were performed without a magnetic field.

The inner chambers have been aligned using VDS-OTR-RICH tracks. The precision achieved is better than 0.2 mm in the y-direction and better than 1.3 mm in the x-direction –with one exception: the PT1+x chamber was erroneously raised by 1.3 mm in y when it should have been lowered. We have not corrected for rotations, which Fig. 60 implies are at the level of $\lesssim$2.5 mrad; this level of chamber rotation has negligible impact upon pretrigger efficiency. The achieved accuracy in y alignment is within our requirements, and we expect to obtain improved precision in x with subsequent iterations of the chamber alignment procedure.

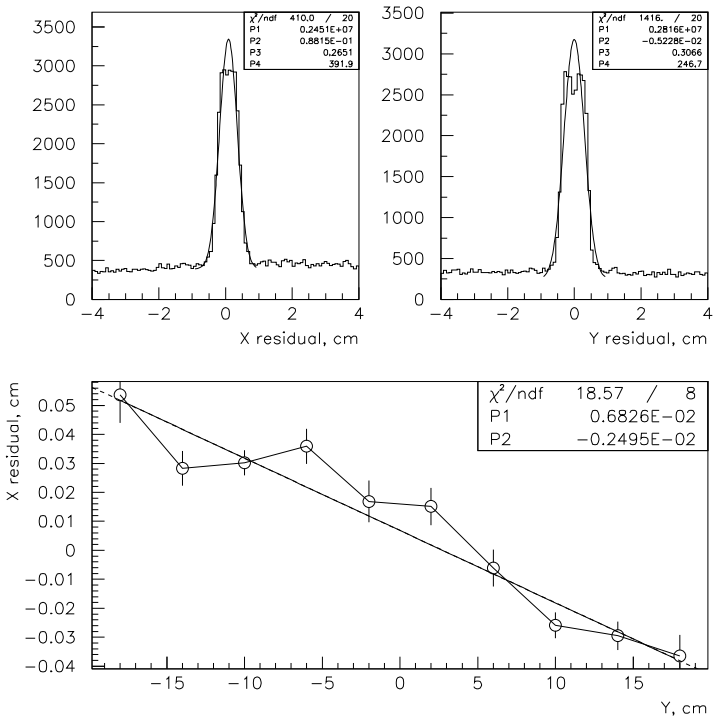

Figure 60: *Alignment achieved for inner high-p_T chambers.*

The pretrigger rate as a function of interaction rate is shown in Fig. 61 (for inner chambers only). All channels with occupancy larger than 20% have been masked out and not considered. The average number of pretriggers is 0.18/BX at an interaction rate of 5 MHz; this is about 60% larger than the Monte Carlo prediction of 0.11/BX. The contributions from the $+x$ and $-x$ sides are equal. The pretrigger rate drops if one makes more stringent cuts on noisy channels. The pretrigger rate is 1.06/BX at an interaction rate of 20 MHz, again somewhat larger than the Monte Carlo prediction of 0.61/BX. The rate of the high-p_T pretriggers in coincidence with the electron (muon) FLT-SLT trigger with $p_t > 1.5$ (1.0) GeV/c is 0.82/BX at 2 MHz. This is a factor of two larger than the Monte Carlo prediction. The distribution of pretriggers among cells of the inner PT1 chambers is shown in Fig. 62.

In summary, the inner high-p_T chambers have been commissioned. The overall chamber efficiencies were found to be 92%, which takes into account the single cell efficiency (96%, Fig. 59) and the percentage of bad channels (4%, Table 26). This provides an overall efficiency of $(0.92)^3 = 0.78$ for the high-p_T hadron-lepton trigger and $(0.78)^2 = 0.61$ for the high-p_T trigger with two hadrons. The pretrigger rate is within a factor of two of Monte Carlo predictions and thus we expect to obtain a rejection factor similar to that given in the TDR. However, there still remain several concerns:

- The sources of noise have not been identified and may change in an uncontrollable way. The level of noise may increase.
- In order to minimize the amount of material in the chambers, the anode wires were soldered on the HV side of the chamber at one point only. Unfortunately this has resulted in the loss of 17 wires. It is not known how this process will develop in time, although most of the wires were lost at the beginning of the run and no new problems arose during the last month of running.

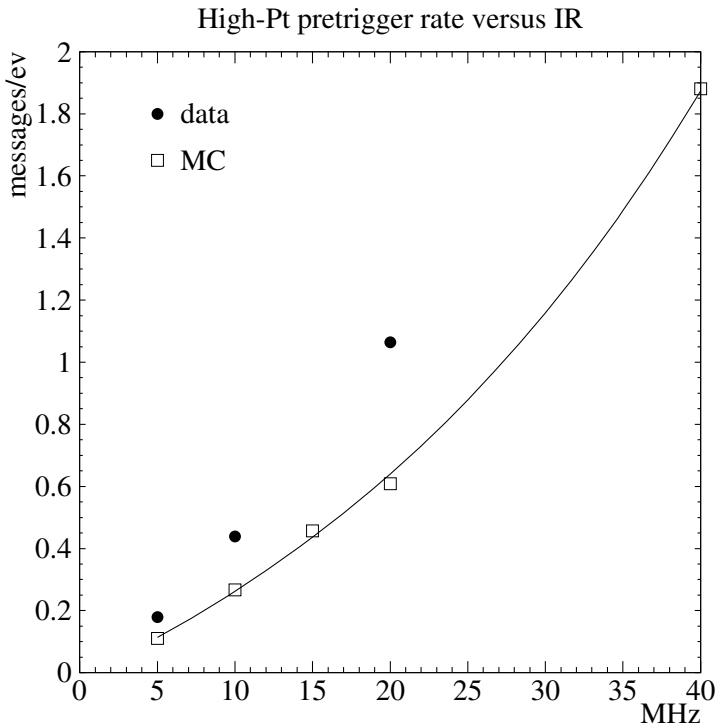

Figure 61: *Pretrigger rate as a function of interaction rate.*

- The expected amount of collected charge is about 0.6 C/(cm-year) at an interaction rate of 20 MHz, but aging of the chambers has been studied in the HERA – B environment for only a small fraction of this amount. We have tested our gas mixture in HERA – B using a muon tube chamber, and no aging was observed at the nominal gas gain of the inner high-p_T chambers. At larger gas gain, however (a factor of five higher), aging occurred very quickly.

Our plans for the Lumi shutdown are as follows:

1. noise studies, tests of ASD BLR;
2. shielding of chambers;
3. repair of wires;
4. modification of the cable support to make them movable together with the chambers;
5. upgrade of the gas quality control system;
6. automatic HV adjustment to compensate changes in the gas gain due to pressure variations;
7. production of spare chambers;
8. production of spare electronic modules (FE and FED);
9. studies of pretrigger and trigger rates, chamber efficiencies, etc. using collected data.

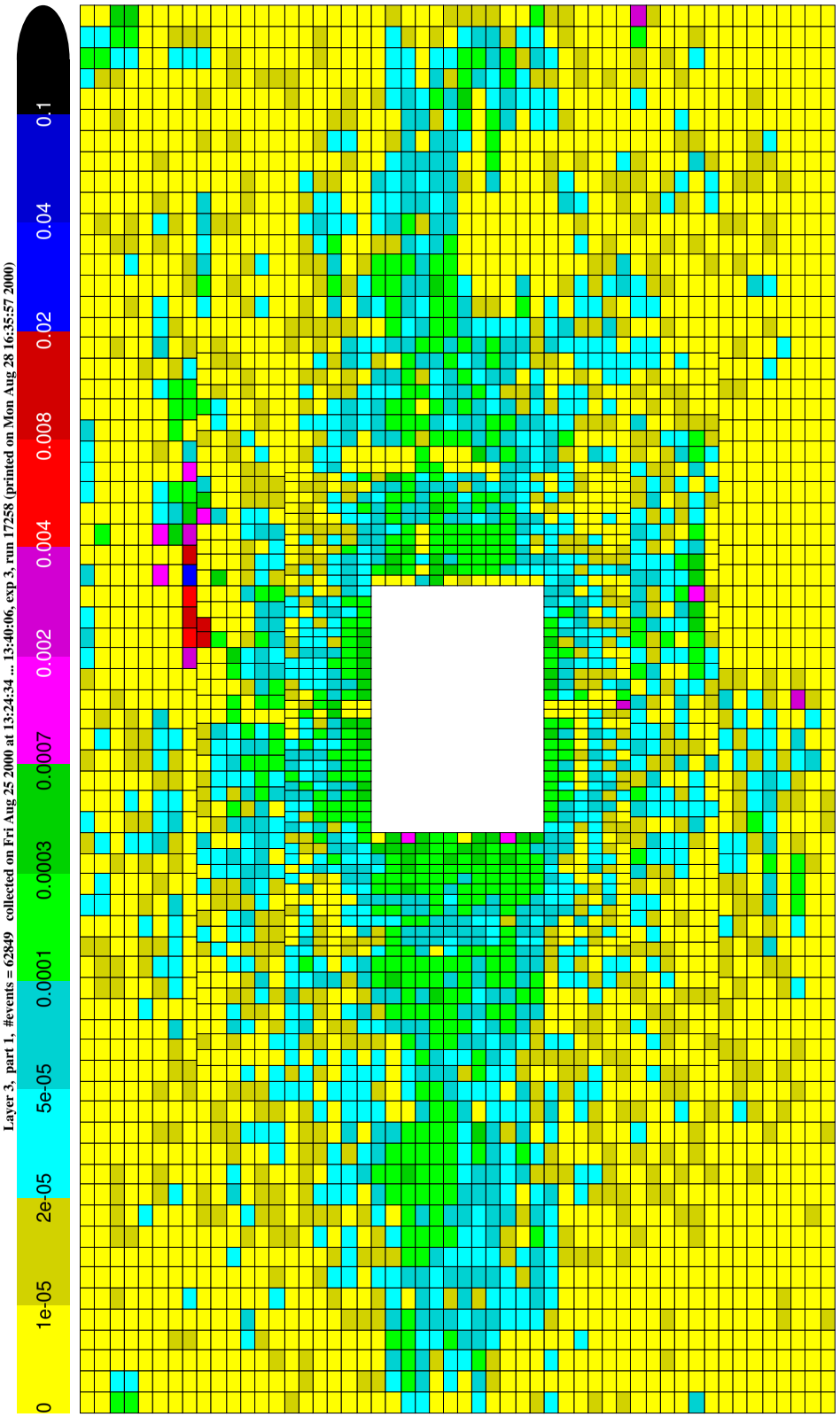

Figure 62: *Distribution of pretriggers among cells of the inner PT1 chambers.*

2.6.3 Status of Outer Chambers during the 2000 Run

During the 2000 running period, four of six outer high-p_T chambers were installed in the experiment and run regularly at nominal high voltage. The very limited access to the detector (one scheduled day per month) precluded installation of the remaining two chambers. The chambers that were installed were partially instrumented with front-end ASD-8 cards and read out. The cards were fully operational and we had no difficulties setting threshold values (via a DAC) for the ASD-8 discriminators. All straw tubes except two out of 1488 were active. We were encouraged by the fact that after all chambers had undergone final adjustments, there were no high voltage problems for the remainder of the run ($\gtrsim$ 4 weeks), which included 1-2 hours running at an interaction rate of 10 MHz. We observed no dark currents or drop in chamber currents over time (for fixed interaction rate), as is symptomatic of radiation damage and wire chamber aging.

Unfortunately we observed a substantial amount of noise and oscillations on the ASD-8 cards. After applying additional shielding to the chambers (consisting of aluminized mylar having thickness of 70 μm) and reconfiguring the grounding scheme of the ASD-8's, the noise was substantially reduced. However, we did not have time to sufficiently study the oscillations and understand their sources. At various times the oscillations disappeared and the readout appeared satisfactory; in one instance during an access we observed clean signals from cosmic rays on a digital oscilloscope. However, the intermittent nature of the oscillations/noise prevented us from measuring chamber efficiencies or inputting meaningful signals to the pretrigger electronics. Fig. 63 shows pad occupancy as a function of threshold setting of the ASD-8 discriminator. The figure displays eight channels of an ASD-8 for a PT3 chamber. The open circles were more typically observed, and illustrate unphysically large occupancy even up to high threshold settings (the occupancy from real particles was at most a few percent). This behavior is characteristic of oscillations in the electronics. The dark squares show the same channels during a different time period when the electronics were quieter. The horizontal scale is in DAC counts; a value of 170 corresponds to about 1.6 V. For this threshold the chambers should be $\gtrsim$99% efficient (based on testbeam data).

Our plans for the Lumi shutdown are as follows:

1. study and understand sources of noise and how to shield from them;
2. study and understand oscillations, improve grounding scheme to prevent them;
3. install last two (PT2) chambers;
4. install all ASD-8 cards and cables;
5. complete installation and cabling of all front-end readout crates;
6. replace fuses in some low voltage distribution boards.

2.6.4 Status of Pretrigger Electronics

After several modifications of the link and pretrigger boards, a solution was found that provides a relatively stable operation of the optical links. Six modified link boards and four modified pretrigger boards were installed in the experiment and worked essentially error-free during periods without target operation when the number of hits was small (i.e., re-initialization was required once every 10 minutes). During data taking, errors in the bunch number transmission occurred occasionally, presumably due to the larger number of hits in the data streams. This may imply that the DC

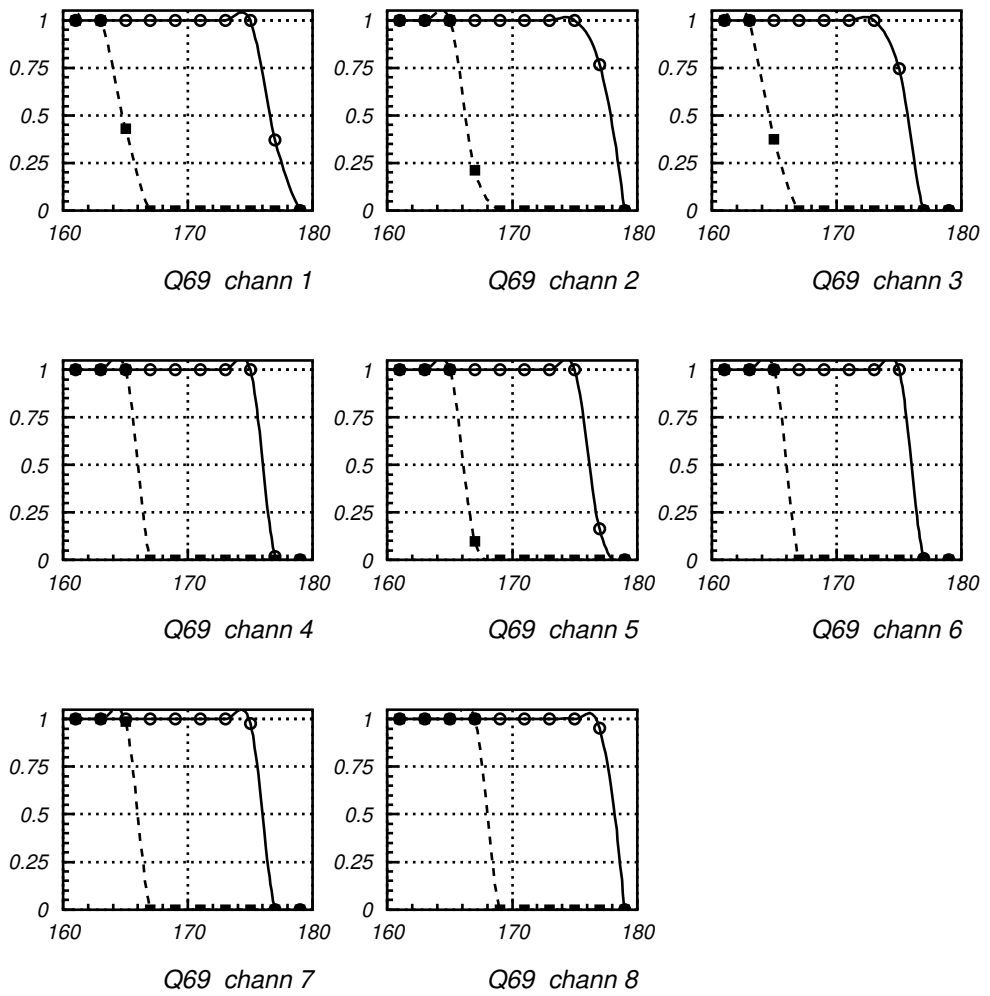

Figure 63: *The measured occupancy of eight ASD-8 channels for an outer PT3 chamber as a function of threshold setting of the ASD-8. The high occupancy represented by open circles indicates oscillations. The data represented by dark squares was obtained during a period when the chambers were quieter. The horizontal scale is in DAC counts; a value of 170 is equivalent to about 1.6 V.*

offset for the optical receivers should be increased at higher interaction rates. This can be achieved by adding DACs to the optical receivers of all pretrigger boards, which we plan to implement. The problem will be studied during the Lumi shutdown.

A slice test using 12 rows of pads in the inner chambers with the FLT in transparent mode has been performed. Data is transferred from the link boards to the pretrigger boards in two cycles per bunch crossing. It was found that the first data transmission cycle gives an incorrect bunch number distribution; this problem is under investigation. In the second transmission cycle there is agreement between the FLT record and the DAQ data 93% of the time. Fig. 64 shows the x distribution in PT1 for tracks causing a pretrigger, as obtained from the FLT record and from the DAQ data.

One serious concern we have is whether the present optical link can provide the required stability over an extended period of time. Thus we are considering whether it worthwhile to develop a new, more reliable optical link for the experiment. For example, one improvement would be to provide

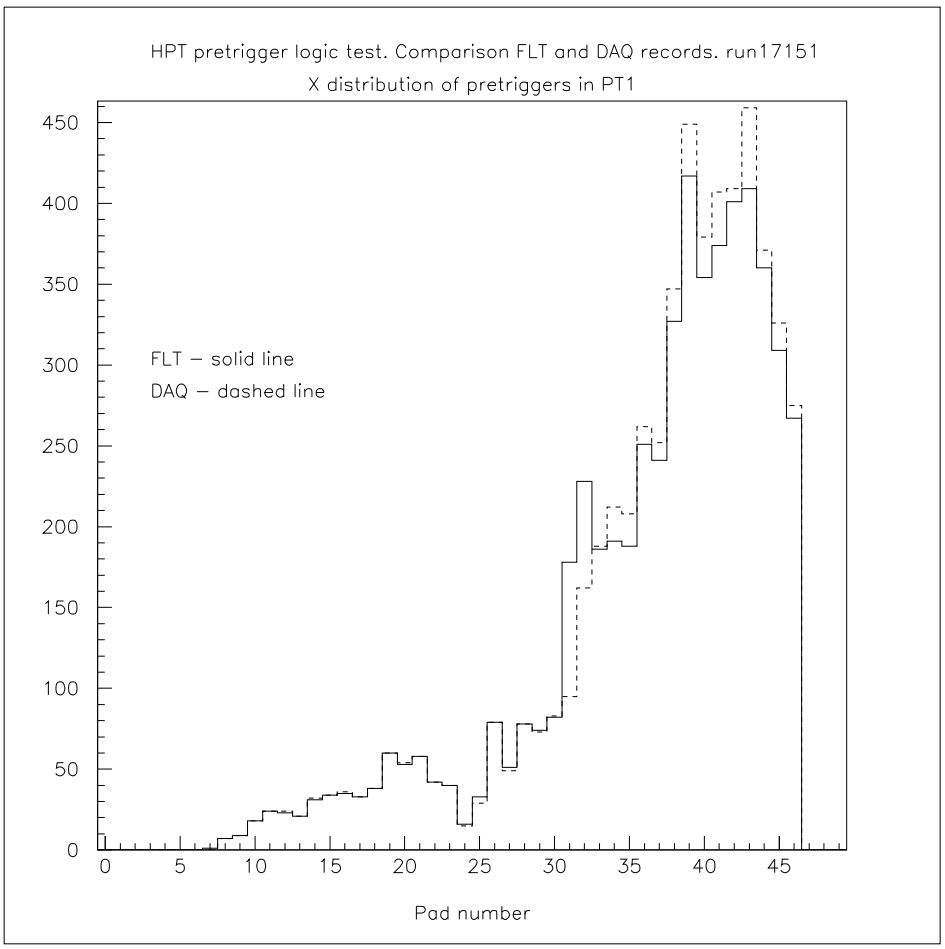

Figure 64: *The x distribution in PT1 of tracks causing a pretrigger.*

DACs for remote adjustment of the receivers. The plans for the pretrigger electronics during the Lumi shutdown are as follows:

1. study the pretrigger electronics using test signals;
2. upgrade of pretrigger electronics;
3. installation and commissioning of the pretrigger electronics;
4. debugging of the pretrigger-FLT chain.

The costs associated with upgrading the pretrigger electronics (item 2 above) are listed in Table 27.

Table 27: *Costs for upgrading the pretrigger electronics during the Lumi shutdown.*

Activity	**Estimated Cost (kDM)**
Modification of 44 pretrigger boards	
(i.e., change to Autobahn handshake)	0
Equipment of 44 pretrigger boards with 12-fold DAC's	3
VME control of 11 Front End Crates	
1 VME board (+ 1 spare)	2
11 Front-end receivers (+ 2 spare)	12
100 m cable + connectors	1
Equipment of 70 link boards (type BCD)	
with 12-fold DAC's (optional)	5
Equipment of 18 link boards (type A)	
with 16-fold DAC's (optional)	2
Additional components (to replace bad ones):	
160 ptical transmitters	0
100 optical receivers	0
50 Autobahn chips	0
Total:	25.0

2.7 The HERA – B RICH

The HERA – B Ring Imaging Čerenkov detector (RICH) is used for identifying and tracking charged particles. Čerenkov rings formed on the focal surface of the RICH provide information about the velocity $\beta = v/c$ and the direction of a charged particle passing the radiator. The particle's velocity is related to the Čerenkov angle by the Čerenkov law, $\cos\theta_C = 1/n\beta$ (where n is the refractive index of the radiator). Čerenkov angles are determined by measuring the radii of Čerenkov rings detected with the RICH. The track direction is found from the location of the center of the Čerenkov ring on the focal surface and can be used to improve the tracking capabilities of a spectrometer by directly providing precise direction information which can be used, among other things, to determine the particle's momentum. The measured velocity and momentum p together determine the mass m of the particle. In the small angle approximation the Čerenkov angle relation can be rewritten as:

$$\theta_C^2 = \theta_0^2 - \frac{m^2}{p^2} \tag{8}$$

where $\cos\theta_0 = 1/n$. This relation can be illustrated as in Fig. 65, where the square of the Čerenkov angle is plotted against $1/p^2$. Particles of a given mass belong to linear bands with a slope of $-m^2$.

The HERA-B RICH detector was installed in Spring 1998, and has been in stable operation over the last two years. Following commissioning, the performance of the HERA – B RICH was found to meet design expectations. Event analysis tools which enable both a stand-alone search/measurement of individual rings and analysis of events based on the information from tracking systems have been developed. In what follows we shall report on performance studies and the stand-alone ring search and particle identification capabilities of this device.

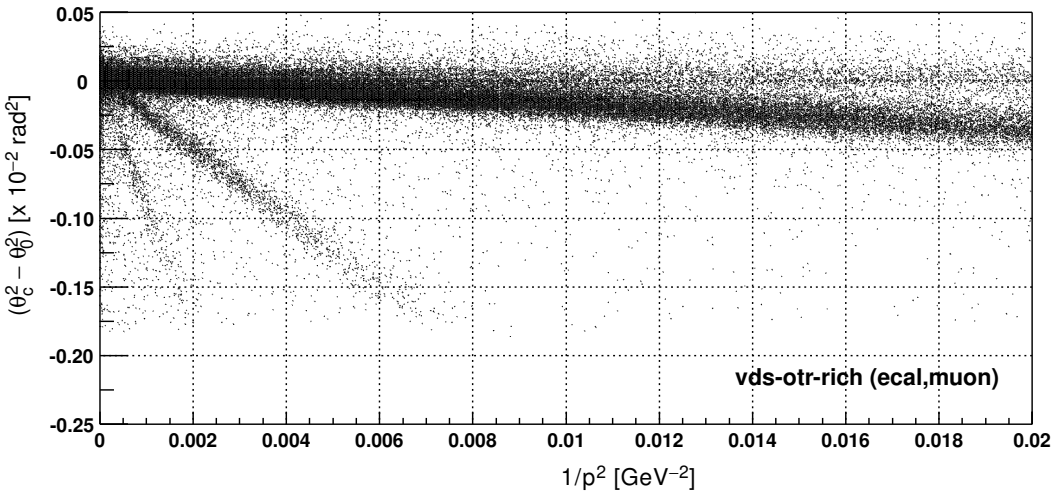

Figure 65: *r2p2 plot: the difference of squares of the measured and the maximal value of Čerenkov angle, $\theta_c^2 - \theta_0^2$, is plotted as a function of $1/p^2$ to find the particle identity through association with a particular band corresponding to a stable charged particle. Bands for electrons, pions, kaons, and protons can be clearly seen.*

2.7.1 Expected Performance

The performance characteristics of a RICH detector for particle identification and tracking are governed in large part by two critical parameters, the angular resolution for individual photons σ_θ,

and the mean number of detected Čerenkov photons N_γ. In HERA – B RICH design studies it was determined that an angular resolution of $\sigma = 0.7$ mrad is needed in the central region and that more than 20 photons must be detected on average per $\beta = 1$ track [26].

For reasons of detector occupancy, angular resolution, quantum efficiency and costs, Hamamatsu M16 and M4 PMTs were chosen for the RICH photon detectors. The expected single photon resolution is 0.7 mrad and 1 mrad for the regions occupied by M16 and M4 PMTs, respectively.

The yield of Čerenkov photons depends on Čerenkov angle θ_C and radiator length L according to $N_\gamma = N_0 L \sin^2 \theta_C^2$, where N_0 is a figure-of-merit reflecting the quantum efficiency and optical efficiency of the RICH system. From the data available on quantum efficiency, mirror reflectivities, window and optical system transmissions of the components we have employed in the HERA – B RICH, one calculates the HERA – B RICH ($L = 2.75$ m) merit factor to be $N_0 = 43$/cm, which gives the the mean number of photons expected for particles approaching the velocity of light $N(\beta = 1)_\gamma = 32$ and the limiting Čerenkov angle $\theta(\beta = 1)_0 = 52.3$ mrad.

2.7.2 Measured Single-photon Angular Resolution

The RMS spread in Čerenkov angles for single photons can be estimated taking the mean of the hit residuals σ_θ for each single ring. To reconstruct the rings, a stand-alone RICH pattern recognition algorithm (RISE) is used followed by a ring fit with the center and the radius as free parameters. The values of σ_θ are displayed in Fig. 66. The distribution is a convolution of the contributions of the M16 and the M4 PMTs, but is dominated by the considerably larger number of M16 channels. The measured resolution is consistent with the expectations as noted above. This result is in agreement with an independent check, where we have used the data collected in the absence of magnetic field. In this case straight tracks, defined by a high energy cluster in the calorimeter and the position of the target wire, were used to determine the Čerenkov angle for each individual hit on the photon detector [67]. The resulting resolution is 0.7 mrad for the finer granularity (M16) cells, and 1.0 mrad for the coarser (M4) ones.

2.7.3 Measured Photon Yield

We have sought to understand the photon yield using several approaches [64, 65]. In every instance, the results are consistent with the expected yield estimates. For all rings found by the stand-alone ring-finding algorithm, the number of photons can be determined. From this, the raw photon yield can be calculated [64] and is histogrammed in Fig. 67. This distribution includes all rings found without corrections for acceptance losses such as shadowing due to the beam pipe. The width of the observed distribution is explained by Poisson statistics. The mean value corresponds to a figure of merit $N_0 = 44$/cm. The result of a "hand-scan" analysis [65] of events with isolated rings is shown in Fig. 67. The analysis determined $N_0 = 43 \pm 4$/cm.

From these studies we conclude that the observed photon yield $N_0 = 43 \pm 4$/cm is completely consistent with expectations. The resulting number of detected Čerenkov photons per $\beta = 1$ track is $N_\gamma = 32 \pm 3$, well above the minimum value required for efficient particle identification.

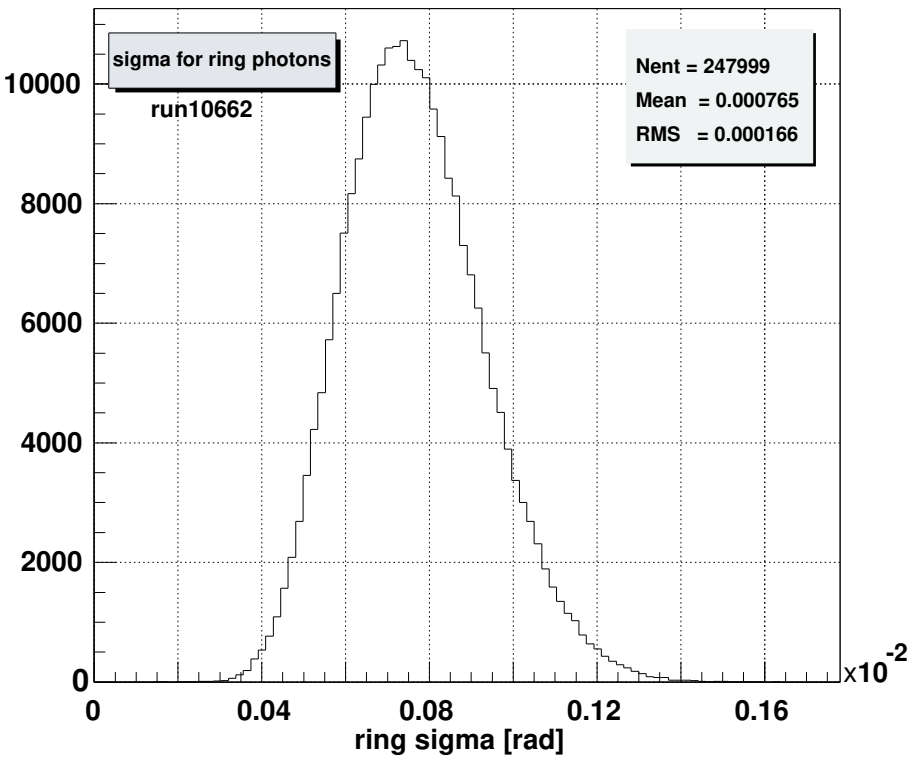

Figure 66: *Single photon resolution*

2.7.4 Stability of Operation

The photon detector has been stably operated since summer 1998. The number of hot channels was reduced to about 25 well identified individual channels, and has remained at that level (Fig. 68) throughout the run. The number of dead channels is, on the other hand, mainly related to missing PMTs which we expect to install during the shut-down. Even now, the detector has only about 2% faulty (dead or noisy) channels. Further, we have observed no changes in the alignment of the optical system.

2.7.5 Tracking Capabilities

Using the RICH in conjunction with other detector sub-systems [70] to measure momentum is an unexpected benefit, in particular for the period when no or little tracking system was available. From the rings found on the photon detector, track directions are deduced and matched in the non-bending plane with the track candidates from the silicon vertex detector. From the deflection in the bending plane the momentum of the particle is then determined.

The high accuracy of the track angle measurement can be checked by comparing the vertex detector track direction with the one measured with the RICH. This is possible in the non-bending plane only, and the result is shown in Fig. 69 as a function of momentum. We also note that this angular resolution is better than the present accuracy of the main tracking system (Fig. 73).

The momentum resolution can be estimated by analyzing the width of the bands of a "r2p2" plot

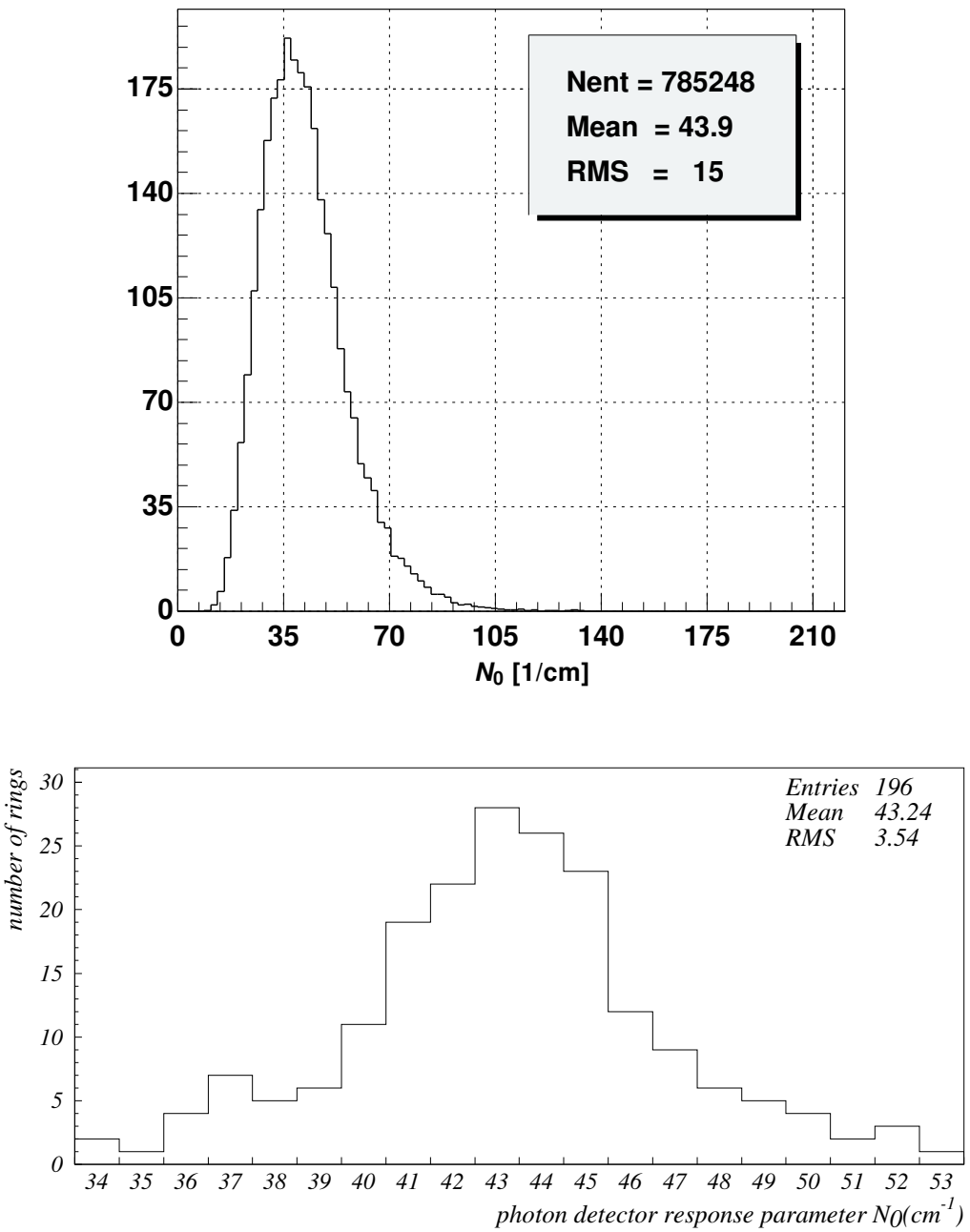

Figure 67: *The figure-of-merit N_0 as found by the stand-alone ring-finding algorithm (top) and by analyzing well isolated tracks in an event scan (bottom).*

(Fig. 65). When momentum is determined only with the vertex detector and RICH [64], we find:

$$\left(\frac{\sigma_p}{p}\right)^2 = \left(1.6 \cdot 10^{-2}\right)^2 + \left(0.15 \cdot 10^{-2}/(\mathrm{GeV/c})\right)^2 p^2 \quad . \tag{9}$$

The resolution is worse than that expected from the measured single-photon yield and angular resolution, taking multiple-coulomb scattering into account. Here the total radiation length was taken from the GEANT detector simulation. Better agreement is achieved, if the constant term is increased by approximately a factor 1.5, which implies a larger multiple-scattering contribution.

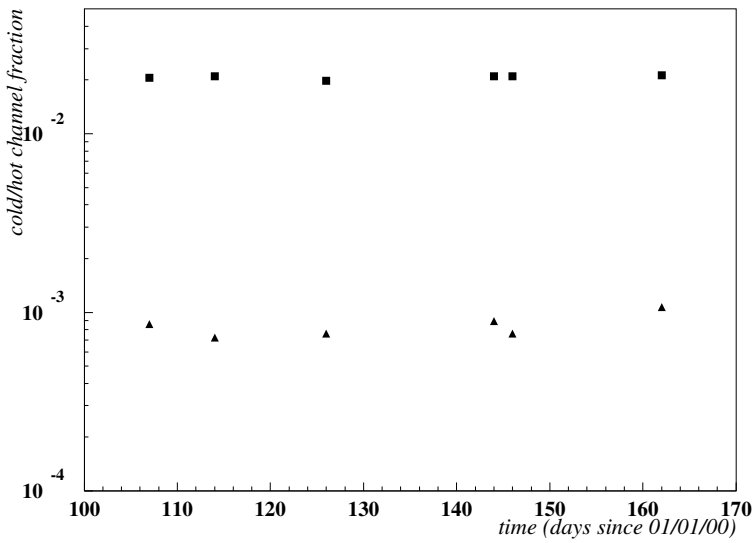

Figure 68: *Variation in time of the fraction of hot (triangles) and cold (squares) channels of the photon detector.*

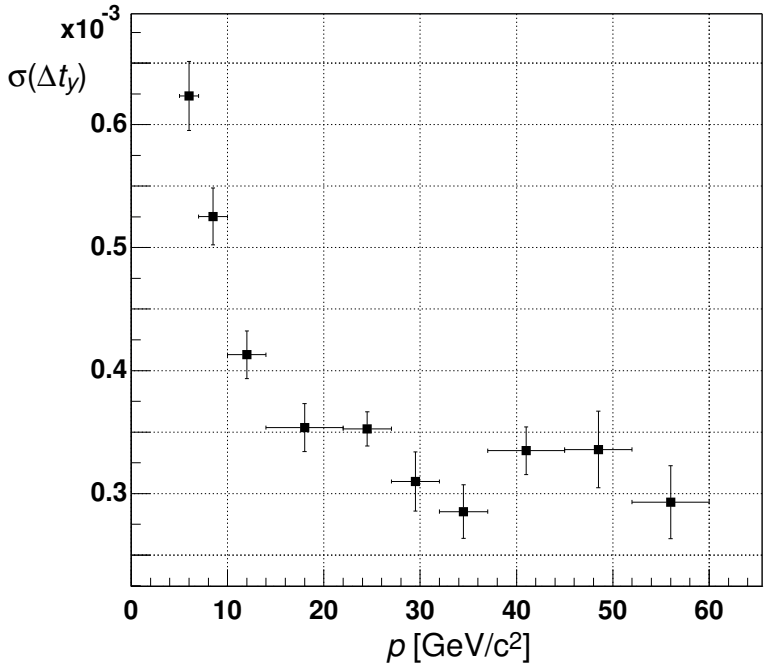

Figure 69: *Resolution in vertical angle difference for pion track matched by the VDS and RICH. To clean the track sample, it was required that the track be associated with the π-band of the "r2p2"-plot (Fig. 65).*

The momentum resolution of this rudimentary spectrometer is sufficient to reconstruct particle decays such as K^0_S in the pion-pion invariant mass spectrum (Fig. 70). A clear K^0_S signal is present

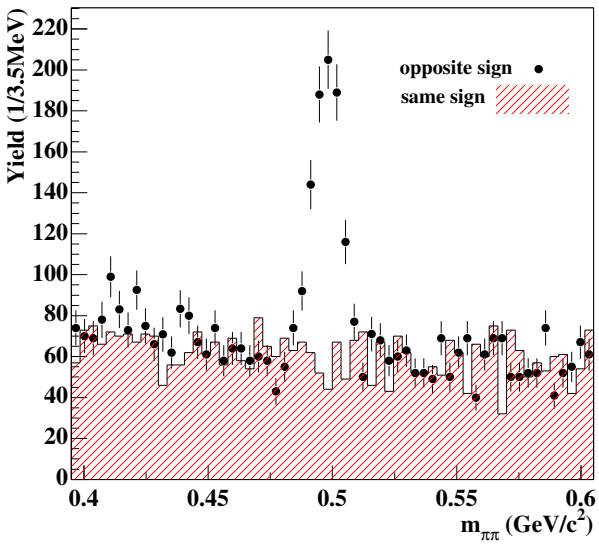

Figure 70: *Invariant mass for pion pairs reconstructed using the VDS and RICH for momentum measurement. Data indicated by points are for opposite sign charges; shaded histogram indicates the corresponding distribution for same-sign charges. Pairs are required to have a vertex downstream of the target wire. Pairs that form a vertex at a target wire show no K^0_S peak.*

for opposite-sign pairs with vertices downstream of the target wires. The RMS width of the peak is 5.7 ± 0.4 MeV/c^2, well centered on the K^0_S mass, which implies an average momentum resolution of $2.0 \pm 0.2\%$. This, in turn, is in reasonable agreement with the momentum resolution quoted above for the tracks making up this peak which have typical momenta in the range from 10 to 15 GeV/c.

The efficiency of the stand-alone ring-finding algorithm depends sensitively on the quality of the detected ring, which is related to the number of photons S attributed to the ring and the background hits B under the ring, estimated using the side bands. We define the significance of the ring detection to be $S/\sqrt{B}$; to keep the number of ghosts at a reasonable level (around 10% in MC simulated 1+4 interactions), a minimal significance of three is required. The efficiency of finding a ring which can be associated with a charged particle track, is shown in Fig. 71; the efficiency reaches values above 90%. The drop at low momenta is caused by the small number of photons in these rings. To determine the efficiency, VDS-OTR matched tracks were used, for which it was checked whether they can be associated with a ring or not. The result was cross-checked using a K^0_S sample reconstructed without the any requirements on RICH information. To further illustrate the capability of the stand-alone ring search, we plot in Fig. 72 invariant mass spectra for two-body final states πp, KK and πp.

2.7.6 Particle Identification Capabilities

The particle identification capabilities of a RICH are exploited by comparing the measured values of the particle momentum p, Čerenkov angle and/or number of detected photons N_γ with the expected values for a given particle hypothesis.

Analysis methods

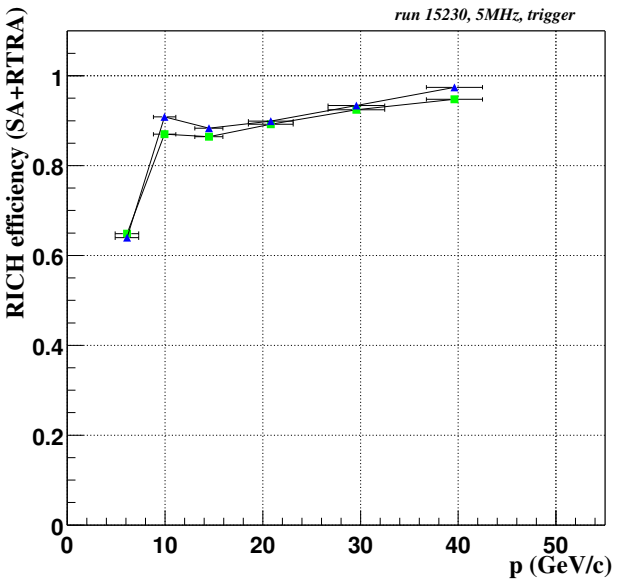

Figure 71: *Efficiency for finding a ring related to a track found in the tracking system, as a function of particle momentum. The efficiency of the stand-alone search (lower curve) increases slightly if for the remaining tracks the track direction is used as a seed for the ring search (upper curve).*

Two analysis methods were employed as particle-identification tools. In the stand-alone ring-finding algorithm (RISE) a ring-fitting procedure (RIFIT) is used to determine the radius and center location of the ring. From the value of the ring radius the Čerenkov angle is deduced. In this case, the particle identification capability can be visualized by plotting the measured values of in θ_c^2 versus $1/p^2$ (Fig. 65). The bands formed by electrons, pions, kaons and protons are clearly visible. The momentum ranges over which a good particle identification—defined as a four-sigma separation of the bands—is possible are given in Table 28.

Table 28: *Momentum range where "2+2 sigma" particle identification with the RIFIT algorithm is possible.*

Band	Momentum Range
$e - \pi$	3.4 – 15 GeV/c
$\pi - K$	12 – 54 GeV/c
$K - p$	23 – 85 GeV/c

A likelihood for each particle hypothesis can be calculated through the deviation of the measured Čerenkov angle from the one expected at a given momentum, relative to the RMS widths of the bands on the r2p2 plot.

The second particle identification method (RIRE/RITER algorithms) relies on the use of the track parameters as supplied by the tracking system to determine the Čerenkov angle for each individual detected Čerenkov photon [26, 71, 72]. For each of the hypotheses the likelihood can then be calculated, based on individual Čerenkov photons.

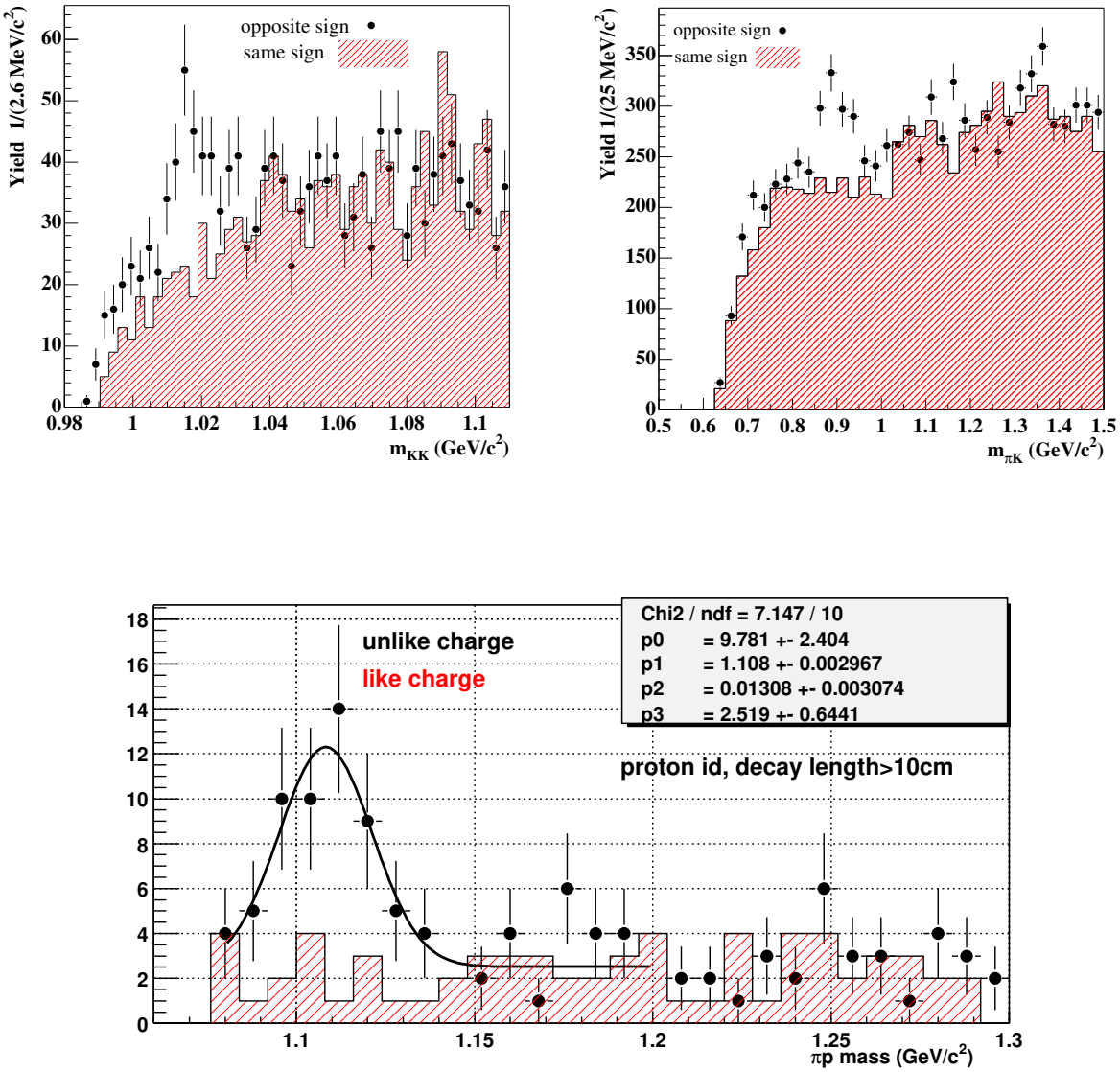

Figure 72: *Invariant mass for kaon pairs (top, left), pion-kaon pairs (top, right), and for pion-proton pairs (bottom) reconstructed using the VDS and RICH for momentum determination.*

This allows also the identification of particles close to or below the Čerenkov threshold, where there are few or no detected photons. Note, that in this case, the measured track direction enters directly into the likelihood calculation, so that it is essential that the tracking system is well aligned and that the direction errors are well understood. The relative alignment of the OTR and RICH was determined from the data, an example of which can be seen in Fig. 73. We note that the error in direction determination (around 1.2 mrad), seen in Fig. 73, is larger than the single-photon resolution (0.7 mrad), and, therefore, degrades the particle-identification performance of the track-based methods.

Identification efficiency

To determine the identification efficiency of the algorithms employed, we have performed an

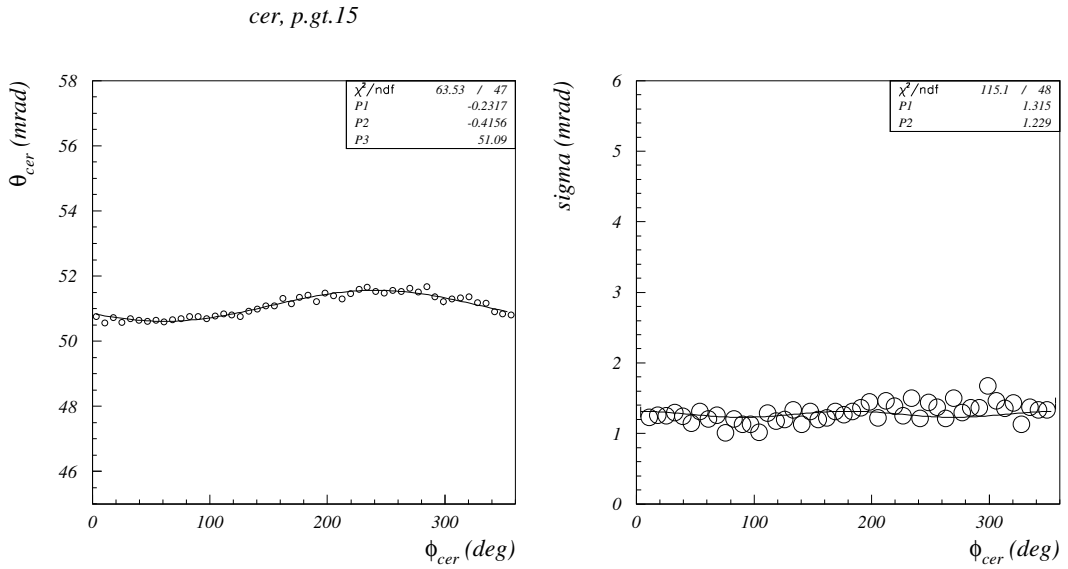

Figure 73: *Relative alignment of the RICH and the OTR: the variation of the mean Čerenkov angle (left) and the error in the track direction as given by the tracking system (right), both as a function of azimuthal angle around track direction. A misalignment of a few tenths of mrad shows up as a sine-modulated mean Čerenkov angle.*

analysis of well defined final states. In particular, particles which originate from reconstructed secondary vertices of K^0_S (Fig. 74) and Λ (Fig. 78) decays and which have a matched OTR segment, were used in the study. The momentum distribution of pions in the sample, collected from the minimum bias run 14577, is shown in Fig. 76.

In Fig. 75, the efficiency and the misidentification probability of the ring-fitting algorithm (RIFIT) are shown for pions with momenta between 14 and 35 GeV/c as a function of the likelihood cut. The low misidentification rate is explained by the large separation of the kaon band from other bands in the selected momentum region. In Fig. 76, the efficiency is plotted as a function of momentum. The efficiency reaches a value of 0.9 for momenta around 20 GeV/c. As expected, the efficiency follows the variation of the mean number of detected photons.

In Fig. 77, the efficiencies and fake probabilities are shown for the track-based algorithm. The efficiency is high (0.8 - 0.9) in the momentum region close to the threshold, and starts decreasing at higher momenta. This behavior is understood: the efficiency at higher momenta is dominated by the present alignment accuracy of the tracking system. In Fig. 78, yet another proof is given of the identification abilities of the HERA-B RICH near threshold using pions and protons from Λ decays. In this case most pions have momenta slightly above threshold, between 5 and 10 GeV/c, and almost all protons are below threshold.

The performance at high momenta was explored by using the decays $J/\psi \to \mu^+\mu^-$ in the data recorded with the trigger requiring two muons with high transverse momenta. The resulting efficiency plot is shown in Fig. 80.

To summarize we note that the two analysis methods, if properly combined, look very promising

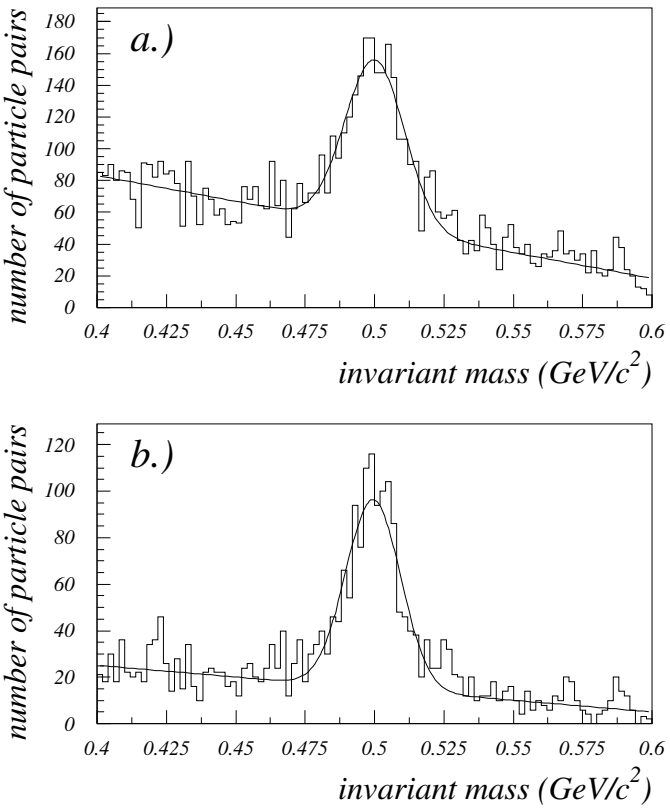

Figure 74: *Two pion invariant mass plot for tracks with detached vertices without and with a requirement that both particles are pions.*

for an efficient particle identification. Due to the excellent angular resolution and the high photon yield of the HERA-B RICH, the ring fit method promises the most accurate determination of the Čerenkov radius. The performance suffers from rings with low significance (small number of photons or high background level), where it becomes more difficult to determine all ring parameters simultaneously. In the track-based algorithm, the ring center and the radius are fixed and, therefore, an efficient identification near the Čerenkov threshold is possible. It is worth noting that the performance of the HERA – B RICH, in particular the identification efficiency at high momenta and at high track densities, will benefit considerably from improvements in the alignment of the tracking system.

We illustrate the performance of a combination of the two identification methods on an example of the analysis of $D^0 \to \pi^+ K^-$ and $D^+ \to \pi^+\pi^+ K^-$ final states, where a clear charm signal can be observed (Fig. 81).

2.7.7 Plans for the Shut-down

Photon detector

In addition to the about 25 faulty PMTs, most of which are expected to be replaced by the

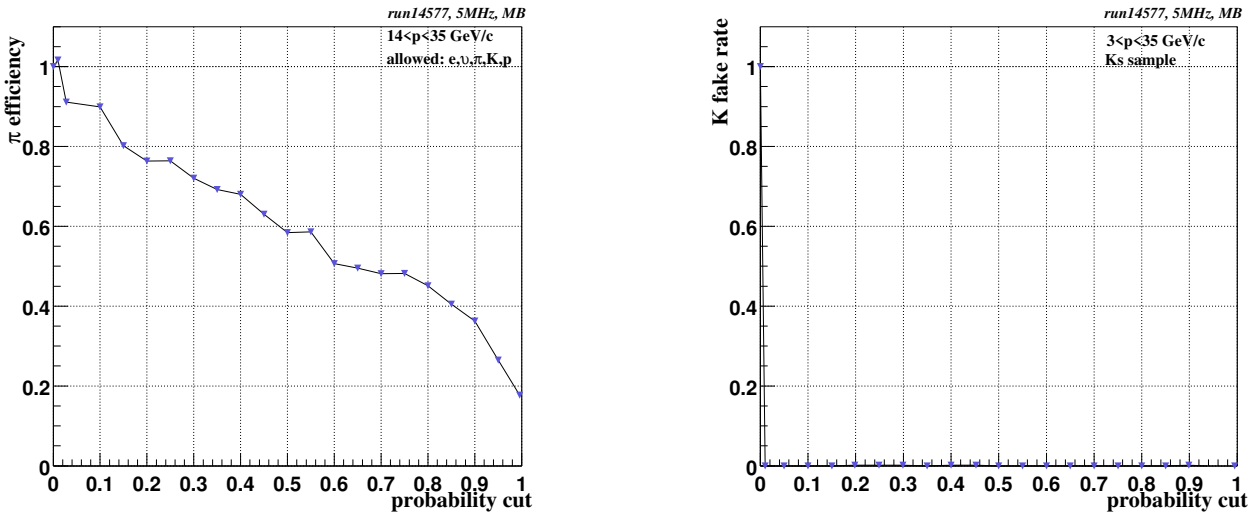

Figure 75: *Stand-alone identification efficiency as determined by using tracks from the K^0_S decays in minimum bias events: probability that the particle was identified as a pion (left) or misidentified as a kaon (right), for pions with momentum between 14 and 35 GeV/c.*

,

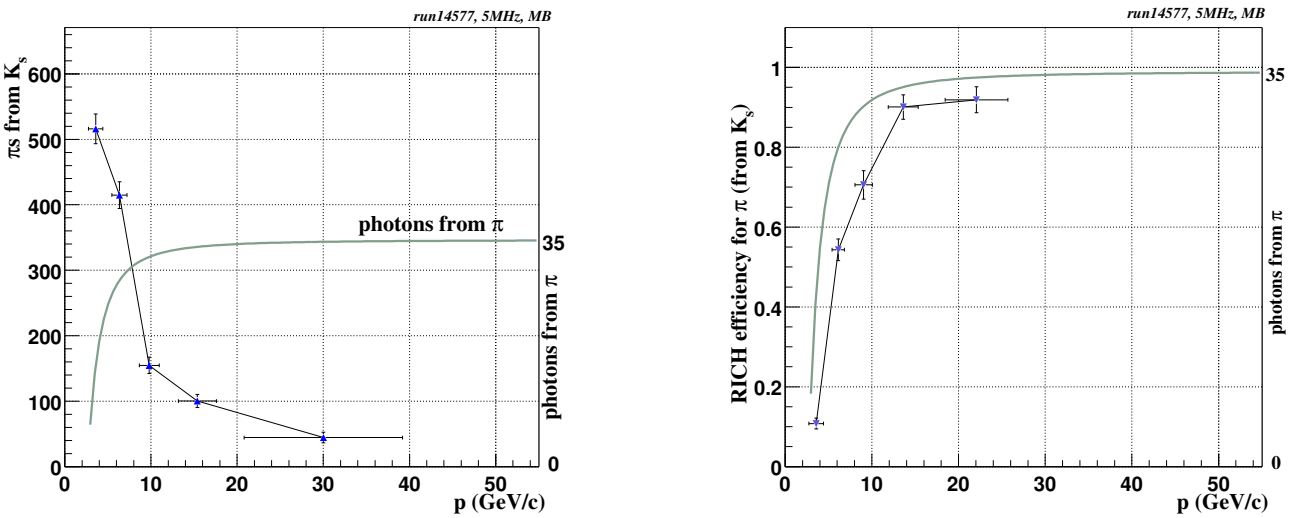

Figure 76: *a) Momentum distribution of pions from reconstructed $K^0_S \to \pi^+\pi^-$ decays. b) Stand-alone identification efficiency as a function of momentum, as deduced from K^0_S decays in minimum bias events.*

manufacturer, an additional set of 10 have been ordered. With these, we expect to fill all empty PMT slots on the detector, which will then remove most of the dead channels. We will have a few spare pieces left and do not foresee any danger, however, since our past experience shows that we have a vanishingly small PMT failure rate.

Gas system

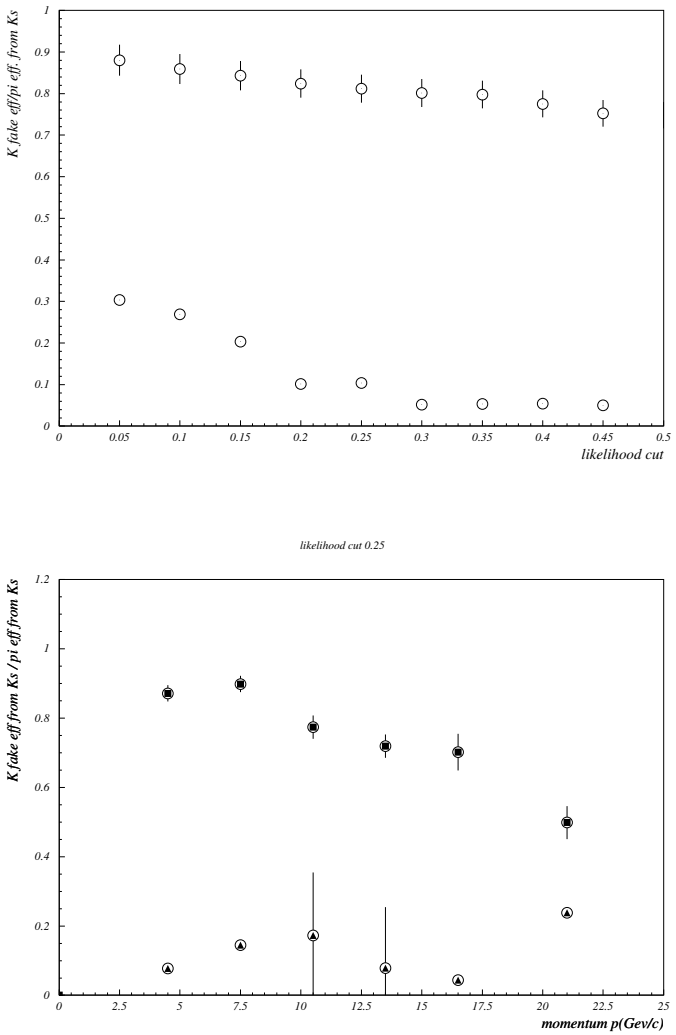

Figure 77: *Track based identification efficiency as deduced from $K^0_S \to \pi^+\pi^-$ decays in minimum bias events. Above: probability that the particle was identified as a pion (open circles with error bars) and kaon (open circles) as a function of the likelihood cut. Below: momentum dependence of the efficiency (full circles) and fake probability (open circles with triangles) at a fixed likelihood cut of 0.25.*

A few upgrades to the RICH gas system have been suggested to improve operations. In fact, almost all expert interaction with the gas system could eventually be eliminated. Most of the operations difficulty with the gas system was due to the lack of C_4F_{10} reserve. However, it is clear that understanding the different flow rates of gas in the various stages of the system would make possible the automatic regulation of the manual valves, including the back-pressure regulator and the throttle valve.

Flow Sensor and Regulation: A measurement of the flow into the vessel is possibly interesting. However, since most flow sensors are force sensors, the mass of the medium changes the response. During changing mixtures, a reasonably priced sensor will give an ambiguous response. For stable mixtures, the relative response can be tuned. The total flow into the vessel can be regulated from

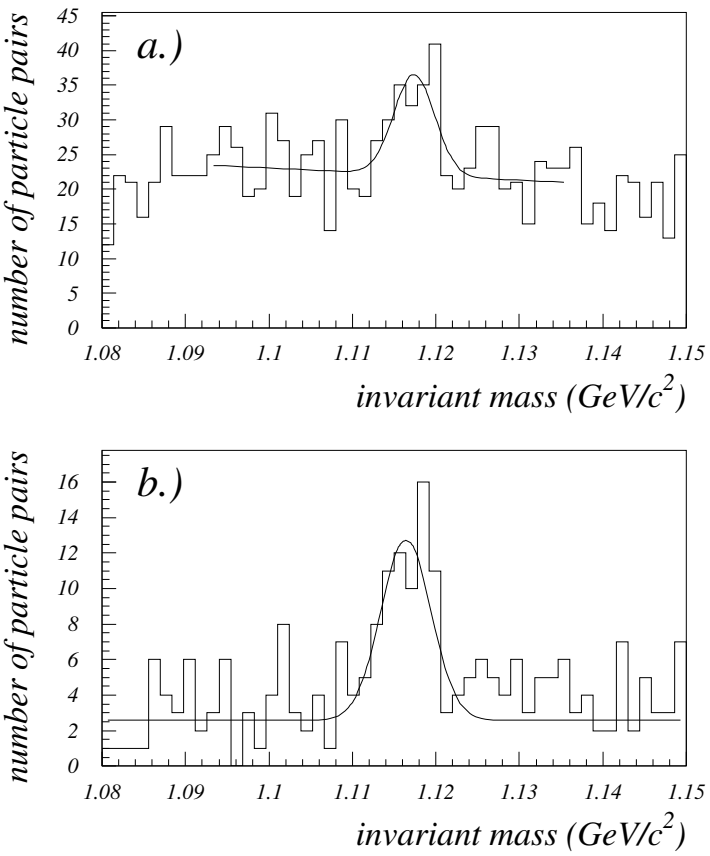

Figure 78: *Pion-proton invariant mass plot for tracks with detached vertices without and with a requirement that the positive particle is a proton and the negative one is a* π.

the process controller with the replacement of the manual throttle valve with an electronic stepping valve (valve body with stepping motor attachment). As input, the process controller will take the compressor speed and possibly check this against the measured flow rate.

Back-pressure Regulation: The total flow into the vessel is the combined flow of gas through the back-pressure regulator and the evaporated C_4F_{10} from the liquid buffer volume. The back pressure regulator may be fitted with a stepping motor and driven by the process controller based on pressure readout. Here we need only an appropriate stepping motor and a replacement of at least one analog manometer.

Distillation: One other possible upgrade would be to replace the heat exchangers in the distillation process. However, the current set up is clearly limited by temperature and not the efficiency of the heat exchangers. This would only be a viable upgrade if it can be shown that a different arrangement of heat exchangers would give the same or better distillation performance while making a better match to the power requirements of the installed cooling compressor.

To conclude we note that several possible upgrades exist. Certainly we should pursue those that can safely remove what little manual intervention is currently needed. Possible improvements to the distillation process should be critically studied.

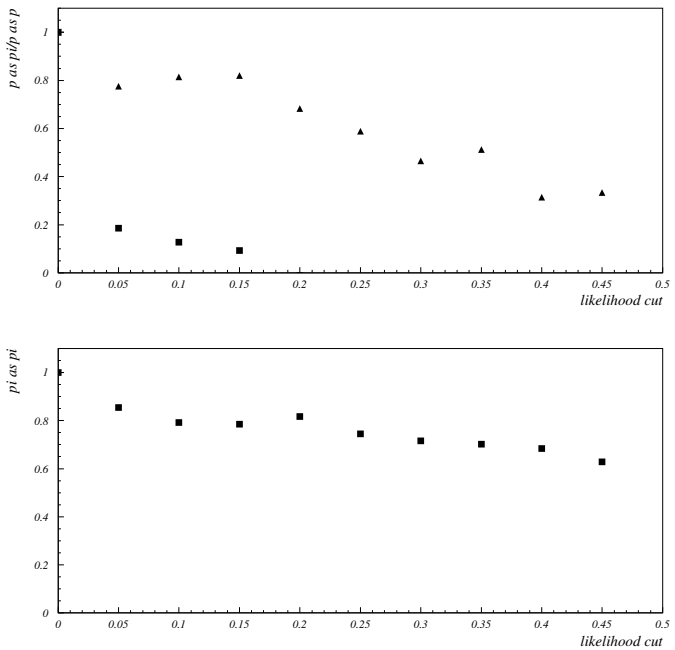

Figure 79: *Track based PID efficiency for the decay products of* Λ *in minimum bias events: positive particle identified as a proton (above, triangles) and pion (above, squares), and negative particle identified as a pion (below).*

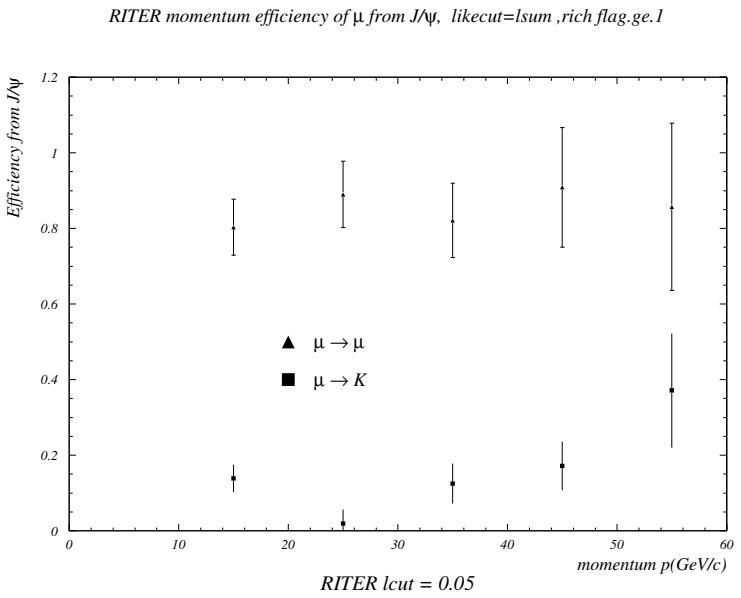

Figure 80: *Track based identification efficiency as deduced from* $J/\psi \to \mu^+\mu^-$ *decays in triggered data: a very preliminary result on the momentum dependence of the efficiency (triangles) and fake probability (squares) at a fixed likelihood cut of 0.05. Note that the highest momentum bin refers to all tracks above 50 GeV/c.*

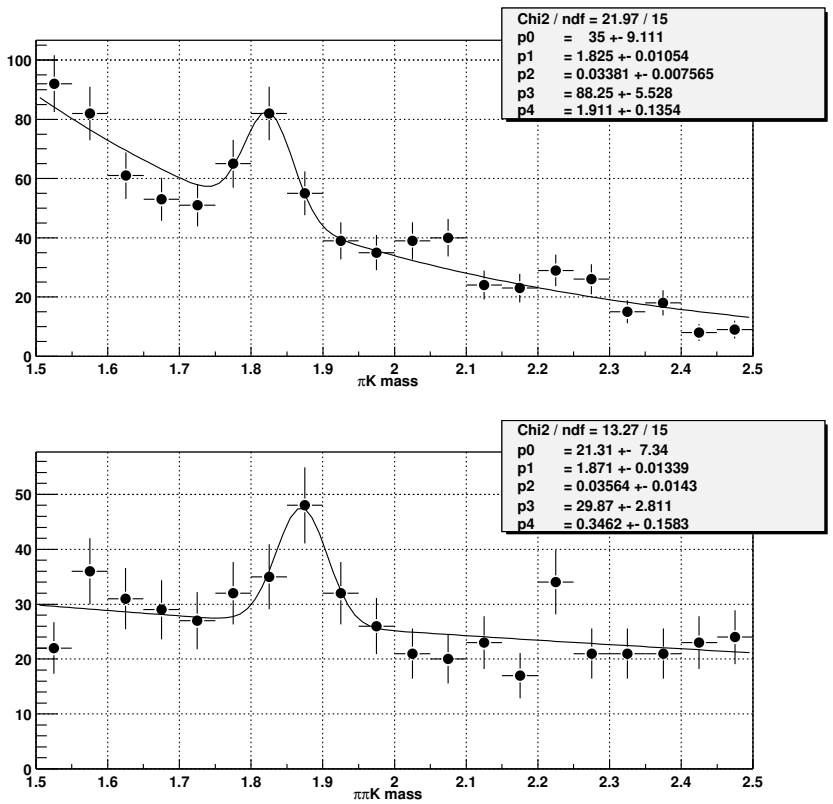

Figure 81: *Invariant mass distribution for π^+K^- (top) and $\pi^+\pi^+K^-$ (bottom). Tracks were required to have matched OTR and VDS segments, and to have a common vertex which should not be part of the primary vertex. The π/K identification was based on the higher likelihood value from both types of identification algorithms.*

2.8 Transition Radiation Detector

The Transition Radiation Detector (TRD) is part of the electron identification system of the HERA – B experiment. The major role of the TRD is the efficient detection of electrons and the rejection of hadrons at the level of less 10% in the inner region of the Electromagnetic Calorimeter where the angular density of secondaries and occupancies is very high.

The TRD has also good pattern recognition and tracking capability due to the multi-hit (15-20 hits/track) detection of each track, so called "continuous tracking". The pattern recognition of the electron track is very straight forward and efficient due to the detection of the TR X-ray energy deposition.

The main concept of the TRD is based on a fine grained structure [73] of the TR radiator (polypropylene fibers) and the sensitive elements (straw proportional tubes), where track position and transition photon measurements are taken. Good electron/hadron separation is possible in the energy interval of 1-2 GeV (threshold of TR) to about 100 GeV when hadrons start to radiate.

The hadron rejection by the TRD is achieved by counting the number of TR-hits, i.e. the hits with energy deposit more than E_{thr} inside the straw drift tubes, which are the main detecting element of the TRD.

For E_{thr} above a few KeV the hits from the hadron track originate mostly from energetic knock-on electrons, while for high momentum electron tracks a large proportion of such hits are produced via the absorption of TR photons in Xe with is the main component of the gas mixture.

The Transition Radiation Detector [74] consists of 2 super-layers with straw planes tilted by ∓ 30 degrees relative to the horizontal axes. Each super-layer contain 16 planes of straws interlayered with the radiator layers.

The radiator consists of polypropylene fibers with a diameter of 20 μm resulting in a total radiator thickness of 1.6 cm per layer. As beam test performed at DESY have shown, the efficiency of a radiator made from fibers is about 20% better than the efficiency of traditionally used transition radiators.

The active detector elements of the TRD are constructed from thin multilayer (Kapton + carbonload Kapton + Al) cylindrical drift tubes. Straws of two different lengths (65 and 135 cm) with a diameter of 6 mm are used. The detector is operated with a gas mixture of Xe:CF_4:CO_2 70:20:10 at a gas gain of 2.5×10^4. This mixture combines the advantages of efficient TR-absorption with short total drift time and stability with respect to discharge [17]. The total drift time for 6 mm straws is 64 ns.

The straw Transition Radiation Detector concept has been developed during the last several years within the framework of the RD-6 program of the ATLAS experiment at LHC [75].

2.8.1 Status

The Transition Radiation Detector was installed in HERA – B during the summer of 1999 and tested during run 99 and run 00. The high voltage system has been implemented in the HERA – B slow control system. For the last two years, a temporary gas system using premixed gases was used.

Signal processing and readout electronics The front-end electronics of the TRD was developed on the basis of the ASDBLR front-end chip [76]. It is an 8 channel bipolar integrated circuit designed for use in straw - based tracking and Transition Radiation Detectors. It's specifications are:

- A shaping time of 8 ns at the discriminator level of inputs signal. Selectable ion tail cancelation for two gas options: fast gas mixture (tracking) and Xe-based gas mixture (TRD);
- The baseline restoration breaks the DC path with non linear (diode based) recovery elements. The recovery time is less than 90 ns for a 100 fC signal;
- Stable threshold operation at rates of up to 20 MHz. Low Level Discriminator (tracking) up to 20 fC (10 uA/fC), high Level (PID) Discriminator up to 200 fC (1 uA/fC);

The front-end electronics based on the ASDBLR chip are completely compatible with the HERA-B front end drivers and can provide different type of connections for particle identification and tracking modes.

The TRD connection to HERA – B readout system is via the standard Front End Drivers FED TDChit boards, where the the hit information is used for particle identification and tracking. Testing of the readout chain with a complete ASDBLR front-end, FED TDC with drift time measurement and standard connection to HERA – B DAQ, is now finished.

The current Fast Control System of the TRD is now the final version and connected to FCS HERA – B .

Slow Control of TRD is implemented in the Common HERA – B Slow Control System.

The critical point of the TRD is the production of the Front-End Drivers TDChitboards which is planned for the beginning of 2001.

2.8.2 Detector Performance

During the data taking periods 1999 and 2000 the TRD was tested with the available electronics in the common frame readout of HERA – B . In addition, an aging test was done on an alpha-beam (Karlsruhe).

Results of the aging test:

- No variation in the signal amplitude due to space charge effects up to rates of 4.5×10^5 per one cm of the anode wire, five times above the highest particle density at HERA – B .
- The anode wires have collected an integrated charge up to 2 C/cm, corresponding to three years of HERA – B TRD running. No aging or etching was observed.

The detector performance together with specially developed front-end electronics (base on ASDBLR) has been tested at the HERA – B spectrometer with target rates of up to 30 MHz.

Fig. 82 shows a TRD drift time spectrum measured at HERA – B . Fig. 83 shows the HERA bunch structure measured by the TRD and shows the synchronization of the TRD readout with the common DAQ. The structure of the HERA beam can be clearly seen in comparison with a random signals which was used for the trigger. Fig. 84 shows the stand-alone reconstruction of tracks in

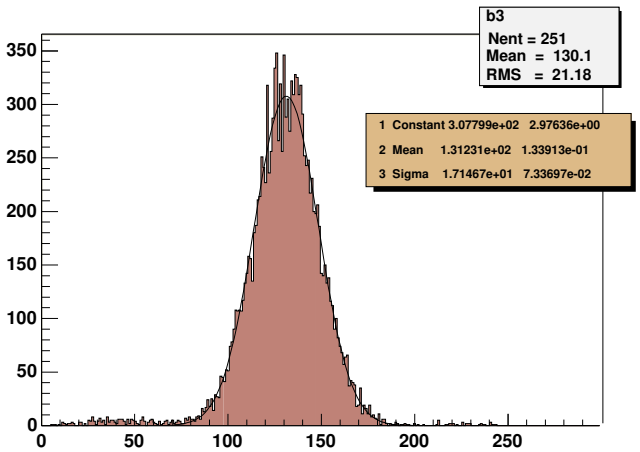

Figure 82: *Drift time spectra for TRD ASDBLR front-end electronics*

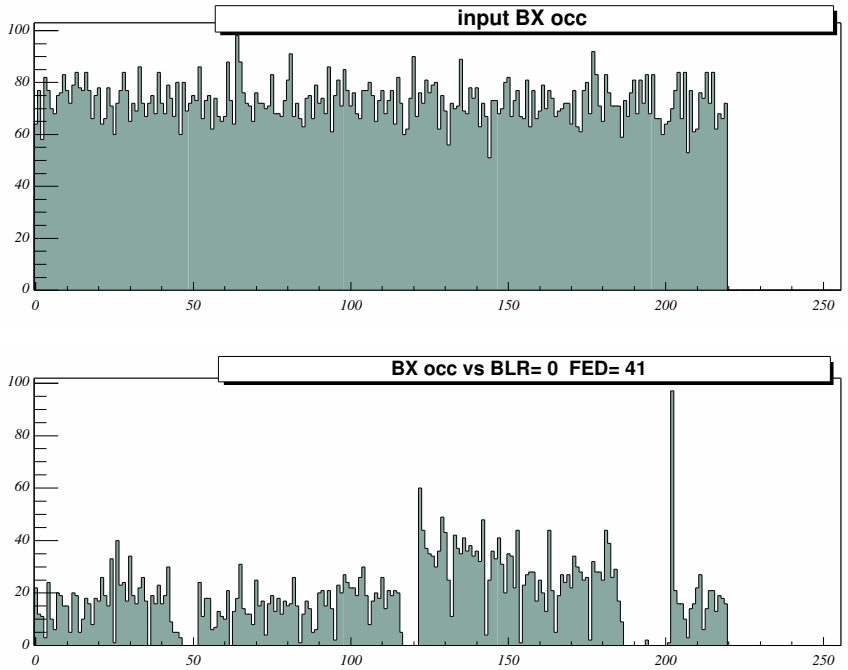

Figure 83: *Bunch structure of HERA as measured by the TRD in a minimum bias run*

TRD by using 5 layers of straws planes. This presents the reconstructed angle of tracks in the area of the TRD and shows the tracking capability of the TRD. Fig. 85 shows the correlations between ECAL reconstructed clusters and reconstructed tracks (planes)in the TRD. The plot shows the distance between the nearest ECAL clusters and planes reconstructed in the TRD. This plot shows the experimental data without alignment.

2.8.3 Shutdown Plans 2000-2001

- As mentioned above the main task of 2000-2001 shutdown is the production and installation of Front End Drivers based on TDChit boards, this will give the possibility of using the full scale

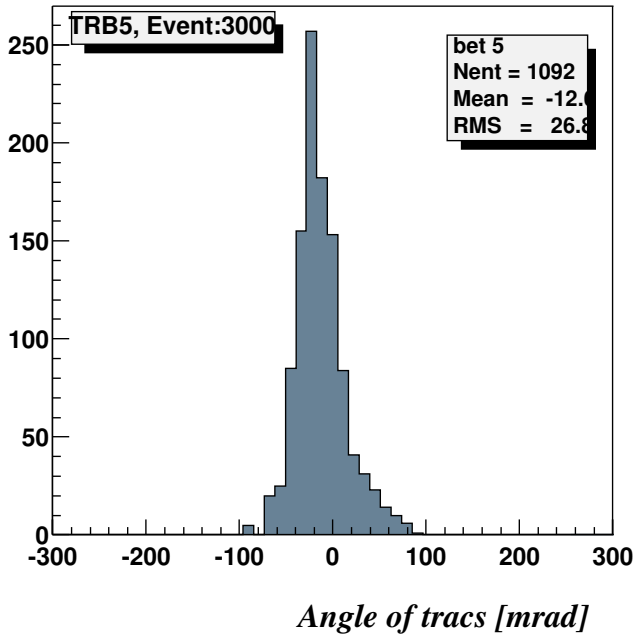

Figure 84: *Standalone reconstructed tracks direction of the TRD (5 layers)*

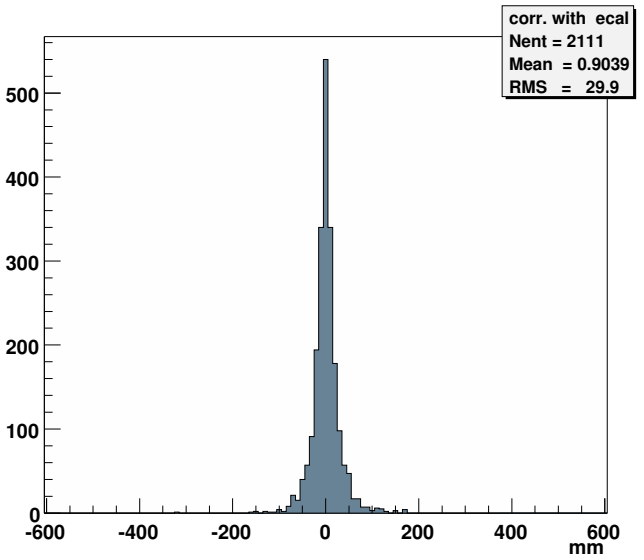

Figure 85: *Distance between clusters of the ECal and reconstructed track planes of the TRD*

TRD for particle identification and tracking in the inner area of HERA – B spectrometer.

- Assembling the closed loop gas system with purification element.
- Improvement of the reconstruction and particle identification software of the TRD.

2.9 Electromagnetic Calorimeter

2.9.1 General Remarks

The HERA – B Electromagnetic Calorimeter had been assembled in autumn 1997, and equipped with photomultipliers/bases, a test LED system and cabled during winter shut-down 1997/1998. At that time the installation of readout electronics also had been started. First data were taken in spring 1998, when HERA – B magnet was switched off. Initial calibration of R/O equipped part had been done assuming an azimuthal symmetry of ECAL occupancy. The first π^0 signal was observed soon and the measured invariant mass of π^0 peak was used for an absolute calibration of the calorimeter. With increasing statistics other particles decaying into $\gamma\,'s$ were observed (like η and ω) also. During the year 1998 the installation of the pretrigger electronics started. Analyzing the data taken with ECAL pretrigger in 2-cluster mode with high E_T threshold (to match DAQ bandwidth) allowed to extract clear $J/\Psi \to e^+e^-$ signal [77]. In summer 2000 the installation of readout and pretrigger electronics had been completed and ECAL acceptance reached its designed value.

In the following sections the main problems observed during ECAL operation will be considered. Proposed solutions together with financial issues will be addressed in the upgrade/repair plan section.

2.9.2 Radiation Hardness

Materials chosen for the construction of the modules were tested for radiation damage up to doses corresponding to more than a year of HERA – B operation at full luminosity ($\sim 5 Mrad$ at showermax position for those ECAL cells which are closest to the beam). Integrated luminosity collected during previous HERA – B operation now achieved $\sim 40\%$ of designed HERA – B annual dose. No radiation damage of the modules had been observed. As stated in [1], annual replacement of innermost ECAL modules had been foreseen, but for the moment there is no sign of necessity of such an operation. Moreover, in order to measure radiation damage in realistic HERA – B conditions, it seems reasonable to postpone the module replacement until 2001/2002 shut-down (see plans). Estimated light yield of the most damaged modules will not degrade more than $\sim 30\%$ which is acceptable from the point of view of ECAL performance (few percent degradation of energy and spatial resolution). In contrast to this, the active Cockroft-Walton showed significant radiation damage already after 25% of designed annual dose. The problem was traced to the damage of DAC chip MAX515CPA used for HV control. The solution of the problem had been found soon after occurring of the first base failures. It required the redesign and replacement of ECAL CW control boards located under ECAL and minor changes of existing CW bases (just removal of the chip, cabling was not changed). The corresponding upgrade of the innermost ECAL part had been done very quickly, so the problem practically had no influence on ECAL data quality. It was decided to upgrade the remaining part of Inner ECAL to the radiation hard version during the lumi shut-down (see plans). As Middle (and Outer) ECAL are concerned, the expected dose for bases there is small enough to leave the present design without modifications. Other components that are used for C-W base construction, proved to be radiation hard to survive at least one year of HERA – B operation at full luminosity. In order to have enough spare bases for the replacement and further improve radiation hardness, the production of new set of Inner bases (fully SMD based, compatible with old design) is foreseen.

2.9.3 Noise Problem

ECAL readout suffers from significant pick-up noise. The origin of the noise is still not fully understood, most probably there are several noise sources. The level of the noise is correlated with the operation of other power-consuming electronics located nearby to ECAL readout electronics at the electronic hut (like FLT crates). The distribution of the noise over ECAL clearly follows R/O board structure (or coaxial signal cable grouping done by the same scheme). Several measures taken like changing of R/O crates grounding scheme, improving input connector contacts and so on decreased the level of the noise, but further reduction of an order of magnitude is still needed. One should emphasize that the noise is seen by readout ADC's due to the 50-Ohm termination of signal cables from both sides. There is a possibility to redistribute noise and decrease its level at ADC input by increasing the output impedance of PM bases. This solution was tested for different PM types used in HERA – B ECAL as well as AC coupling for bases with preamplifiers. Simultaneously with noise reduction it leads to increasing of the signal amplitude by a factor of 2 that further improves signal-to-noise ratio. The drawback of such a solution are base line shifts caused by signals from previous bunch crossings (at level of 1 % of previous BX signal amplitude). In turn it leads to an average base line shift which is automatically taken into account by ADC pedestal measurements simultaneously with data taking and variations of the base line due to short term "memory" of 40 meter coaxial cables (4 previous BX's). It is equivalent to a pile-up with ~ 0.2 "smoothed" interactions in addition to an average of 4 interactions per BX at HERA – B , which seems to be negligible. Nevertheless a detailed MC study of such an effect is foreseen.

2.9.4 Readout Electronics

During the last period of data taking the remaining part of the Outer ECAL readout and pretrigger boards have been installed. The whole readout and pretrigger system is now completed and the shutdown period will be focused on the improvement of performances of the two systems based on the past experience. Main efforts will concentrate on the noise reduction and improvement of the reliability of data transmission both to pretrigger and to *SHARC* 's.

Analog circuits:

As it was discussed above the planned modification of the bases will cause an increase of the analog signals by a factor of 2. The gain of amplifiers on the readout boards side should accordingly been decreased to keep the optimal PM dynamic range. This implies the modification of few components in the analog cards sitting in the readout boards. Analog cards with nonlinear transfer function (HAMAMATSU region) will be replaced with linear ADC cards that show better signal/noise performance.

Digital part:

Data transmission from Readout boards to *SHARC* boards came out to be a very critical point due mainly to the connector being used. We have already a design of an interface piggy back to be mounted on the existing connector on the readout board. The connection should be more stable since we will use standard flat cable connectors. The mechanics of the interface is such to minimize problems coming out by the added connection.

2.9.5 Slow Control

Presently ECAL slow control consists out of the following parts:

- PM HV control - allows to set, monitor and keep history of individual high voltage channels. Using LED pulses and feedback from DAQ, system is able to adjust HV of individual channels to get desirable PM gain variation. The system includes a hardware protection against overcurrent for groups of bases. The status of HV protection and recovery procedure are software controlled.
- LED control system - to set any desirable pattern of LEDs to be fired by test pulse system and to vary the amplitude of LEDs pulses. At present the last option is not available due to frequent failures of the regulated voltage power supplies. A solution exists and will be implemented during shut-down.
- Test pulse system - to issue LED ignition pulses, FCS external triggers and test trigger pulses to ECAL readout / pretrigger. The First BX signal (prescaled and delayed) is used to initiate the sequence. Prescale factor, individual delays, enable/disable of pulses are software controlled. Being connected to ECAL trigger inhibit system allows also to inhibit pretriggers during particular bunch crossings. The last option is not tested yet.
- Crate control - the part of common HERA – B crate control system. Requires some minor modifications - in particular moving of control software from VME computer sitting in the crate controlled by this software.

In addition there is a set of various tools for different test purposes. Most of them are using direct access to ECAL electronics via VME, alternative to the main data taking path.

Two additional systems are going to be built:

- Low Voltage control system to monitor ECAL LV status directly. There are two options: to built the system based on old VME-based multichannel ADC available at Bologna group, or built a new one based on commercial slow control ADC's.
- Timing Control System (TCS) to monitor the adjustment of FCS and test pulse system timing. Because of many common features of TCS for different subdetectors its design should be done in a centralized way.

2.9.6 Calibration

Up to now the calibration of the calorimeter is based on information provided by ECAL itself [78]. Basic assumption is that the occupancy in minimum bias data is a smooth function of ECAL coordinates. Absolute calibration is done using the measured position of π^0 peak in two-cluster invariant mass spectrum. Having enough statistics the calibration of individual ECAL cells using π^0 method becomes possible. To provide such a statistics, a so-called on-line calibration method [79] is used - information is processed at the 2-nd Level Processing where rates of several kHz are available. Usually statistics of about several tens of millions events is collected in 2-3 hours of HERA – B operation. In this case the precision of the calibration is estimated to be about $2-3\%$. Few months ago an improved version was implemented - now calibration data are collected at the 2-nd Level continuously during any data taking using ECAL, thus avoiding the loss of valuable beam time for special ECAL calibration runs.

A complementary calibration method using E/P information (cluster energy, measured by ECAL is compared with matching track momentum and electron peak is searched) from runs with Outer Tracker was developed recently. It works at the 4-th Level Farm, where OTR reconstructed tracks are available. Results are promising, but require more detailed study, both on Monte-Carlo and real data.

Another method is under development - calibration using MIP signals - which also works at the 4-th Level Farm. This method is expected to be rather fast but is very sensitive to the actual noise level. Therefore is was not used up to now.

2.9.7 Monitoring

The operation of the calorimeter is monitored at several levels [78]. There is a special monitoring node at the 2-nd Level, where the ECAL response to LED pulses + randomly triggered data are analyzed. This level periodically provides an information concerning pedestals and status of individual ECAL channels being used for control, data reconstruction and trigger programming. Information at the 4-th Level is controlled by the global Data Quality control system. The experience of the last year showed that the system is reliable and convenient. Upgrade wish is to replace 2-nd Level monitoring node (hb-cr17) with double-processor computer like 4-LT nodes - it will improve the performance by a factor of 2.

2.9.8 Performance

Data collected during HERA – B operation are still under processing. Results presented in this paper could be considered as an example to illustrate ECAL performance. They are based on the analysis of about 1.2 million of events. The used set-up included about 80% of the Inner and Middle sections of ECAL instrumented with readout electronics. About 10% of ECAL pretrigger boards were installed. Trigger conditions were the following: at least one ECAL cell with a transverse energy E_T greater than 1 GeV in the equipped pretrigger region and at least two clusters on ECAL with $E_T \geq 1.1\,GeV$ and with invariant mass above 2.2 GeV/c^2.

The two-cluster invariant mass distribution is shown in the Fig. 86, where each cluster had E_T above 0.3 GeV. A clear π^0 peak with the width of $\sigma(m)/m \sim 7\%$ is seen.

When events with two clusters with $E_T \geq 0.6\ GeV$ are selected (Fig. 87, additional cuts are: distance between clusters above 4 ECAL cells, E_T of clusters pair is above 2 GeV), a very clear η peak can be seen. In this case the mass resolution is about $\sigma(m)/m \sim 5\%$ which is better than for π^0 as expected.

Fitting the π^0 mass peak allowed to extract information on energy (Fig. 88) and position resolutions. As shown in [80] energy resolution was estimated to be $\sigma(E)/E = (22.5 \pm 0.5)\%/\sqrt{E} \bigoplus (1.7 \pm 0.3)\%$ in the region $12 - 60\ GeV$ what is close to design values. Spatial resolution was estimated to be $\sigma_{x,y} = 0.2\ cm$ and linearity better than 0.5% in $12 - 80\ GeV$ range.

It should be mentioned that the above analysis was done for an ECAL region with relatively low noise level. It provides the confidence that ECAL performance can achieve designed values after the reduction of noise.

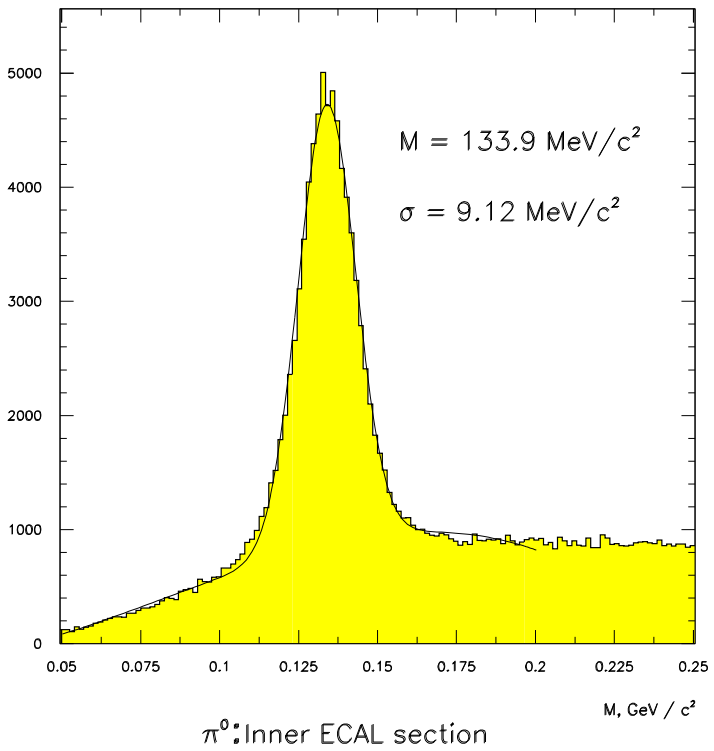

Figure 86: π^0 *signal in two-cluster invariant mass spectrum, Inner ECAL.*

2.9.9 Upgrade/Repair Plans

Innermost ECAL modules:

The module replacement procedure had been described in [1], but had never been tested in reality. Important is to prove such a procedure even if there is no actual need to replace working modules. The plan is to take out one of the innermost modules and temporary replace it with a dummy module (to be made). The irradiated module together with a new module will be tested at DESY test beam with the same set of photomultipliers in order to measure directly the effect of radiation damage. Test includes light yield measurement, transverse and longitudinal scan and energy scan to get energy resolution. After beam tests the module will be installed back to ECAL.

Test beam will be available at the second week of January 2001, requested beam time - 1 week, manpower - 2 people (taken into account in visits plan).

For the module replacement in future (16 Inner modules equipped with HAMAMATSU PMs) we are planning to produce necessary module components during lumi shutdown. Production of spare scintillator tiles had been started at Moscow (should be covered by ITEP financing), KURARAY WLS fibres had been ordered in the beginning of June 2000 (cost is 8.3 kDM, reserved in ECAL financial plan). Reassembly of the modules may require the production of some additional tools,

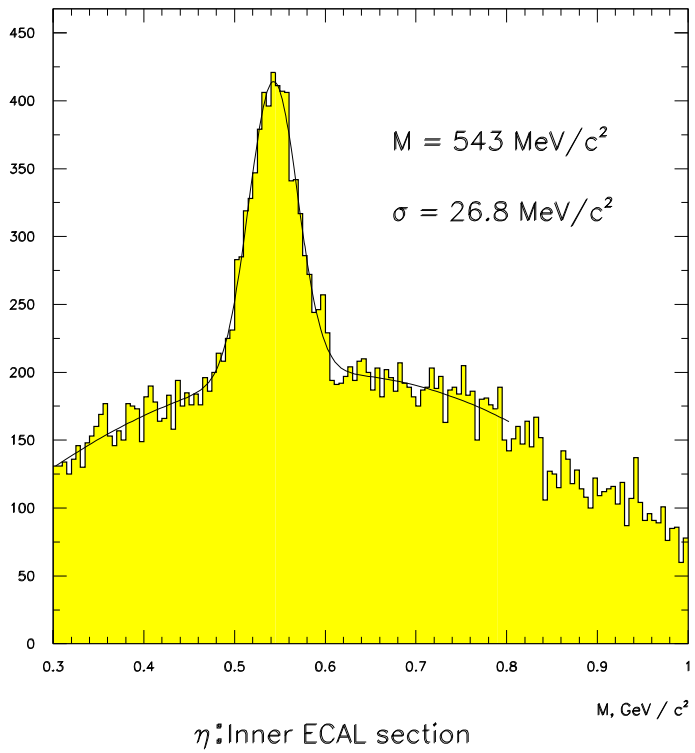

Figure 87: *Inner ECAL, two-cluster invariant mass at η mass region.*

that is mainly foreseen to be done at ITEP, but some reserve at DESY (about 5 kDM) would be necessary for year 2001.

Upgrade of Inner HV system:

As it was observed earlier, the DAC chip MAX515 used for the HV control at Cockroft-Walton bases proved to be not radiation hard. Innermost section of ECAL (HAMAMATSU equipped region) was upgraded last year to a new control scheme with remote voltage control. These scheme had been proven during last months experience. To provide safe and stable operation of ECAL in future, it is necessary to upgrade the rest of Inner ECAL to a new control scheme. 20 control boards and 70 on-module distributor PCB's are produced, components had been ordered and partly arrived. Last delivery (quad DAC chips MAX5250) is expected by December 2000.

Total cost of such a production is 20 kDM, money reserved and partially spent.

Low voltage power supplies, misc.:

The purchase of 3 LV power supplies (type EWS-300-6) had been foreseen. Ordered in June, received in August. Cost - 3 kDM. Front panels and cable support for C-W distributors should be produced and installed. Estimated cost - 2.5 kDM

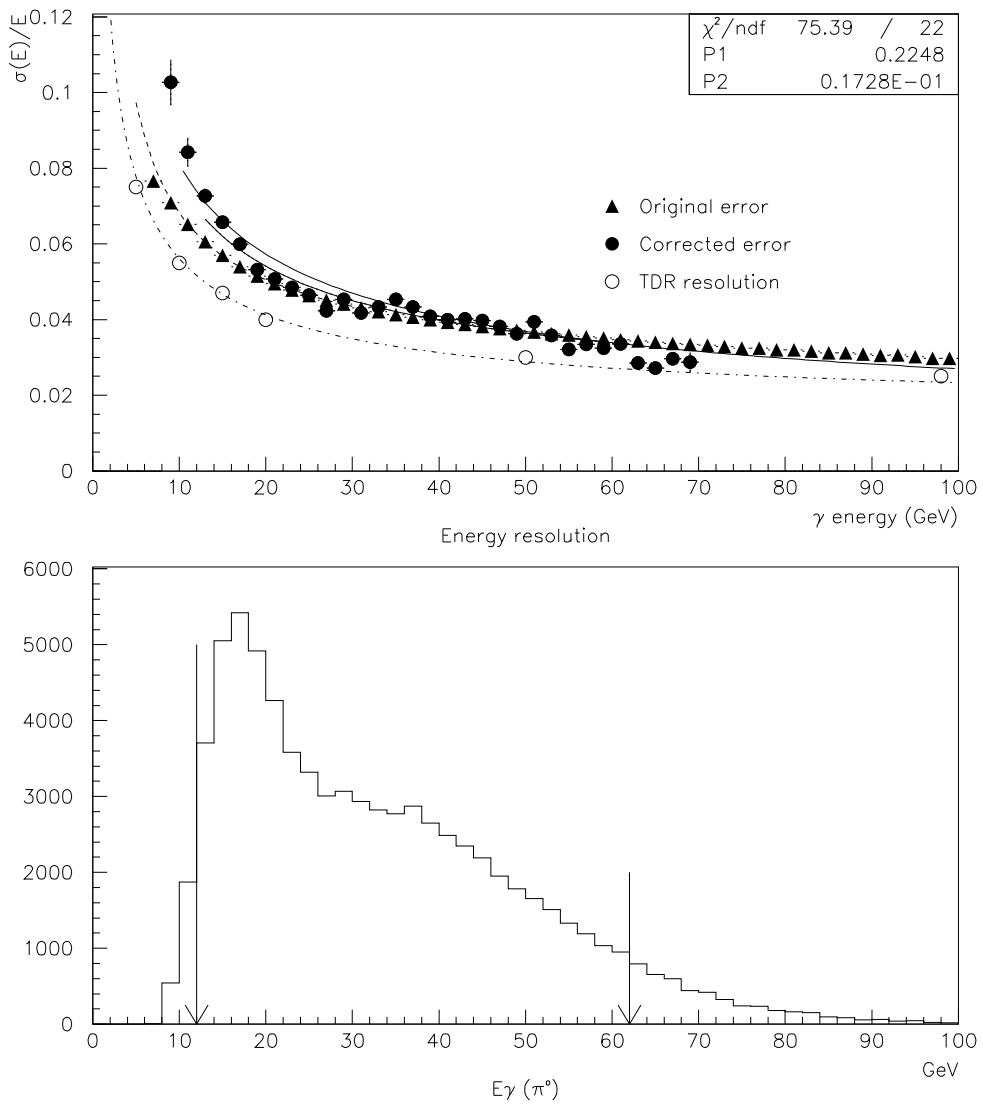

Figure 88: *Inner ECAL energy resolution.*

Replacement/repair of cables:

During last year some control cables were damaged and need to be repaired. In addition some of twisted-pair control cables for the Inner ECAL are of the old type and need to be replaced by standard cables. To improve the reliability of HV control and provide better ground connection between ECAL channels the replacement of Middle/Outer chip-select cables is also foreseen. Overall cost of cables/connectors estimated to be 5 kDM. Will be ordered soon (delivery estimated to be fast).

Modification of CW bases (noise reduction):

At present ECAL suffers from significant noise. In addition to improvement of grounding scheme

(isolation between R/O crates and racks, disconnecting extra power grounding), the modification of all CW bases (6000 pieces) is foreseen. For Innner FEU-68 bases AC coupling together with decreasing of output impedance should significantly reduce the noise and increase 2 times signal amplitude. For Middle/Outer FEU-84 simple exchange of 1 resistor per base (50 Ohm to 1 KOhm) should give the same result. Complementary modification of input ADC circuits at the R/O boards will decrease the noise factor of 2 in addition. Unfortunately the final test of proposed changes had not been done (FCS system is not able to acquire consecutive triggers), so the solution is based only on calculations and LED signal measurements.

Cost of components - negligible. Manpower - at the low limit (1 technician for 5 months)

Production of spare Inner CW bases:

In order to improve the reliability of the system it was decided to produce a spare set of inner CW bases (upgraded version, fully compatible with the present one). PCB design is almost finished, ordering of components is in progress. Main problem - very long delivery time (for example chip capacitors could be delivered by SIEMENS only in 15 months !). Cost estimate 65 kDM, manpower also at the low limit.

Table 29: *ECAL request for lumi shut-down.*

Item	Cost	Status
WLS fibres	8.5 kDM	ordered
Tools	5 kDM	reserve
Inner HV upgrade	20 kDM	partially ready
Spare power supplies	3 kDM	received
Front panels etc.	2.5 kDM	not ready
Cable replacement	5 kDM	not ready
New HV bases	65 kDM	ordering started
Total:	109 kDM	

Readout Electronics:

Upgrade of Readout Electronics includes modification of the analog ADC cards (change of amplifiers gain, see section 2.9.3), and improvement of R/O to $SHARC$ connection reliability.

FCS system:

One of the crucial point as far stability of operation is concerned is the necessity to monitor the stability of the gate delivered by the FCS system. For this aim we are going to build a slow control system based on standard VME TDC's. This system could come out to be of general interest also for other subsystems. We will discuss it with the collaboration.

High and Low Voltage monitor system:

One of the item not implemented in the actual slow control was the monitor of the status of the ECAL High- and Low- voltage system. We have already a design for this based on standard ADC

VME modules. We will implement it during the shutdown period.

Pretrigger rate monitor:

One of the most important figure of the stability of the pretrigger operation is the measurement of the rate of candidates delivered to the FLT. We are going to improve the already used system (based on obsolete VME scaler) with a new one based on commercially available VME scalers.

Energy Inhibit card:

It is already available a new version of the card that should represent the final version of this item . The card is under test but unfortunately we were not able to test it on beam. During the shutdown period we will work in order to have it available and properly working for the start of the run in the year 2001.

Funding and manpower:

The Bologna group is issuing a request to INFN to provide the money needed for the development and installation (with the associated manpower) of the last 5 of above mentioned items.

2.10 Muon System

2.10.1 Status of Muon System Hardware

The Muon system hardware is essentially complete.

All 342 tube chambers, 132 pad chambers, and 16 pixel chambers are installed and running in HERA – B. In addition, two spare pixel chambers exist, of the type used in super-layers 1, 2, and 3. Chamber operation has been smooth and reliable.

The chambers are supplied high voltage from a CAEN HV mainframe. The output channels of the unit are split to provide 522 separate HV cables to the detector. The high voltage is computer controlled using standard HERA – B software. Voltage ramp-up and ramp-down are performed automatically within the HERA – B DAQ framework. And, as done for several other systems in HERA – B, a beam-dump inhibit signal is generated when the HV is on.

The gas system has been in continuous operation since April. Gas pressures and flows are continuously monitored and alarms are produced when any of the parameters is outside the normal operating range. A few *accidental* tests of the monitor and alarm system were made while doing minor work on the system. Serious gas problems will trip a HV interlock, shutting down the chamber HV.

All readout electronics are installed and operating. The readout system consists of the front end readout (ASD-8 based cards mounted directly on the chambers), front end drivers (the first level buffer, located in special crates near the detector), and trigger link boards (located in the front end driver crates). In addition, the pad readout has pre-amplifiers to drive the signal from the pad through ~ 3 m of cable to the ASD card located at the end of the chamber, and pixel mapping boards to re-organize the trigger signals for the pixel chambers to the format required by the pretrigger and FLT. The Muon system has 15,232 instrumented tube wires, 8,308 instrumented cathode pads, and 5,304 instrumented pixels, for a total of 28,844 instrumented channels of which 11,020 are used by the pretrigger, and 13,704 are used by the FLT.

The trigger links are covered in the pretrigger and FLT sections.

The front end readout is based on the ASD-8 chip [81]. Uniquely in HERA – B, the Muon electronics is designed to provide separate threshold settings for each ASD-8 channel [82]. In principle, this allows for the optimization of each channel for maximum efficiency. Each threshold level is generated by digital-to-analog converter (DAC).

To control 28,844 DAC channels, we use 72 embedded controllers to which we communicate via 8 RS485 serial links from a VME CPU. The controllers serve a dual purpose by locally monitoring the voltages, currents, and temperatures in the readout system. Both functions have worked out well. Though not used to the fullest extent possible, thresholds are adjusted individually to suppress non-functioning channels, and to quiet isolated noisy channels.

The front end drivers (FED's) are similar in design to those of the outer tracker, high-p_{T}, and RICH detectors. The front end drivers receive timing signals from the fast control system, and detector signals from the front end readout. Detector signals are assigned to the bunch crossing in which they are received, and buffered for up to 128 bunch crossings while awaiting a first level trigger decision. The signals are also routed via trigger links to the pretrigger and first level trigger system.

2.10.2 Performance and Running Experience

The muon detector has been in continuous operation since April 2000 when the recirculating gas system began operation. Detector operation is controlled by the shift crew.

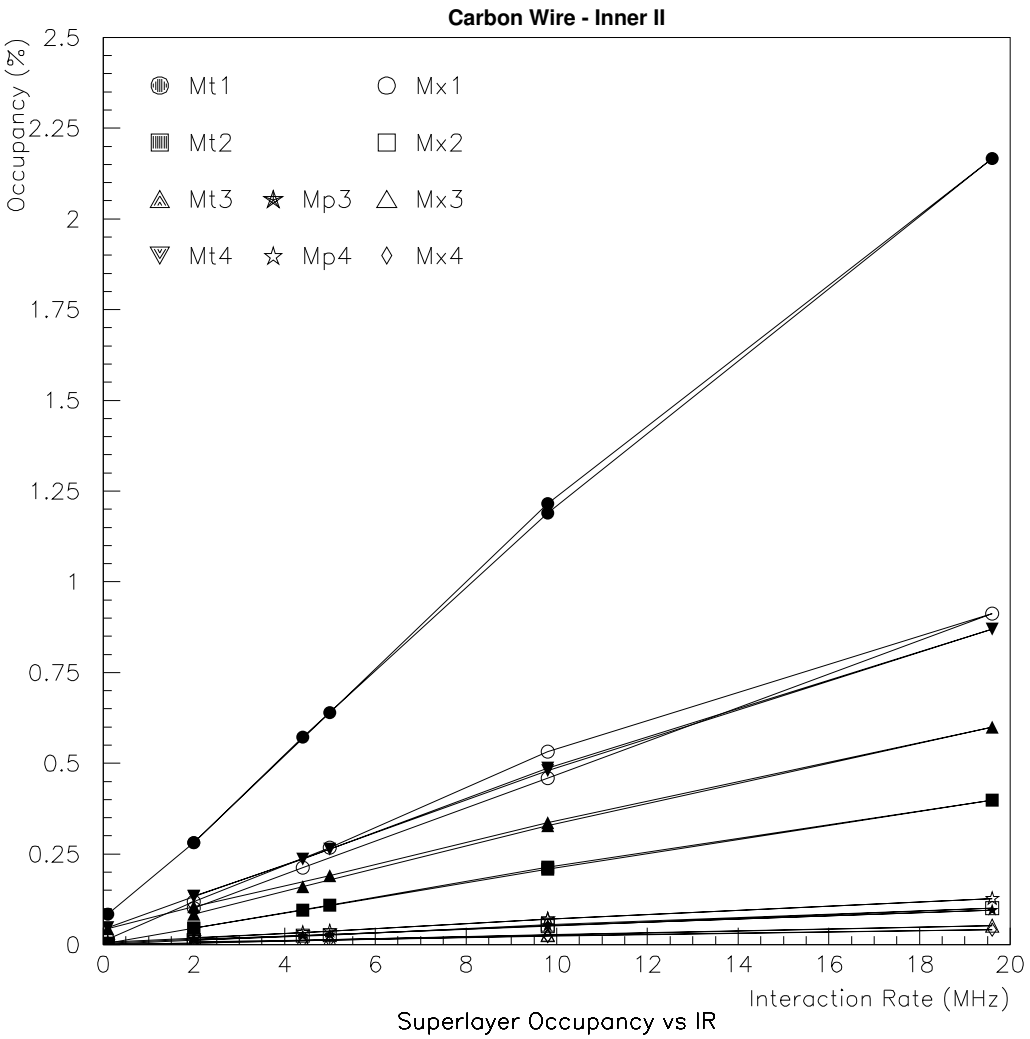

Figure 89: *Occupancies as a function of target rate for different parts of the Muon system.*

We made a number of checks of system performance. The occupancies and track rates are seen to scale linearly with target rate (Fig. 89). The small deviations from linearity are expected since we are using the target rate settings rather than the measured target rates.

The occupancy distributions are displayed in the compact set of plots in Figs. 90 and 91. Some observations on the occupancy distributions:

- There is evidence for backscattering into MU4, but, since augmenting the shielding behind MU4 in fall 1999, the amount doesn't pose any problems for detector operation or Physics.
- The highest occupancies are in MU1, as expected, and don't exceed 10% at 40 MHz target rate.

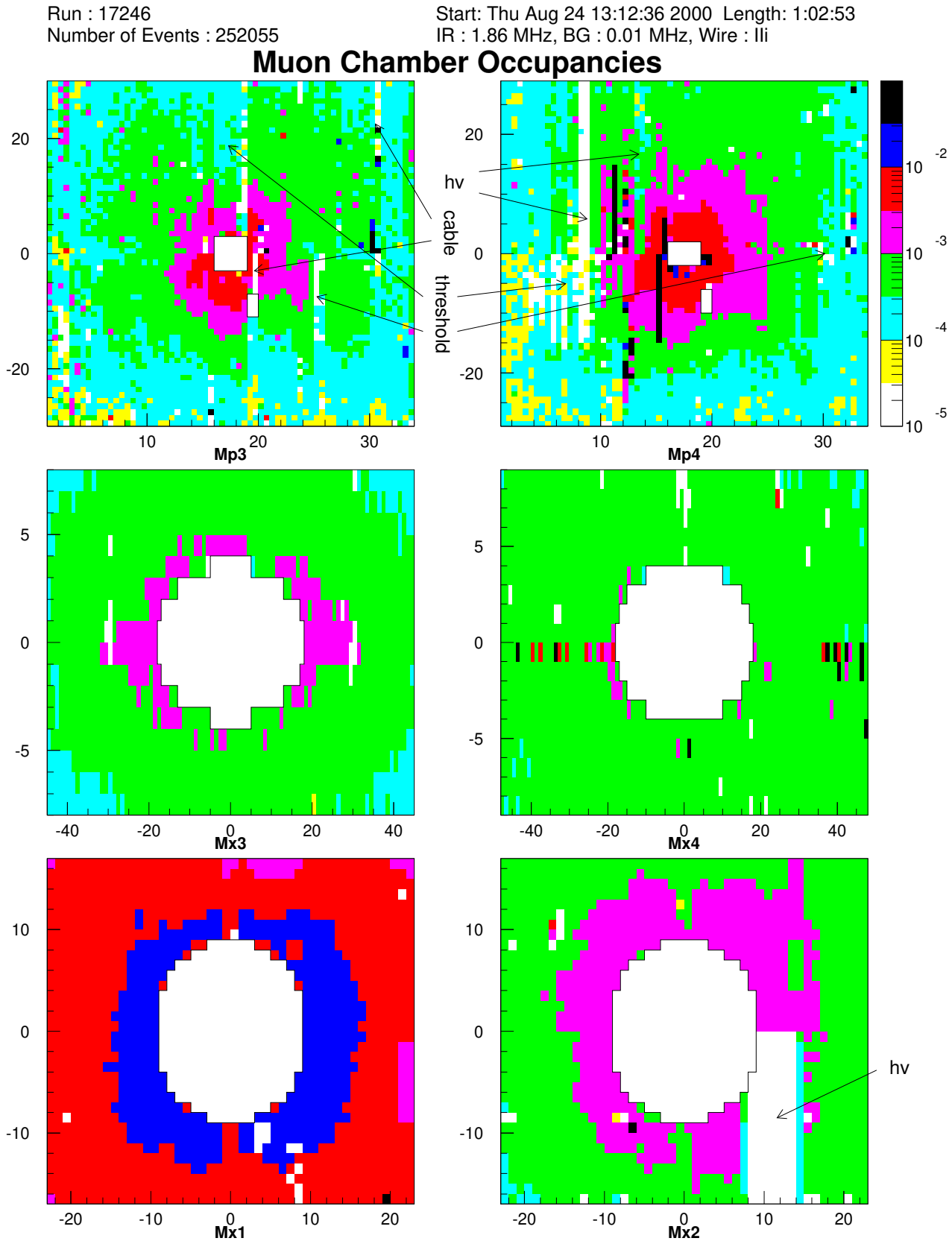

Figure 90: *Occupancies in the pad and pixel channels. The term "cable" refers to a suspected problem with a signal cable. "Threshold" refers to a high threshold value set to suppress noise and resulting in decreased readout efficiency. The term "hv" refers to a problem in applying the high voltage bias.*

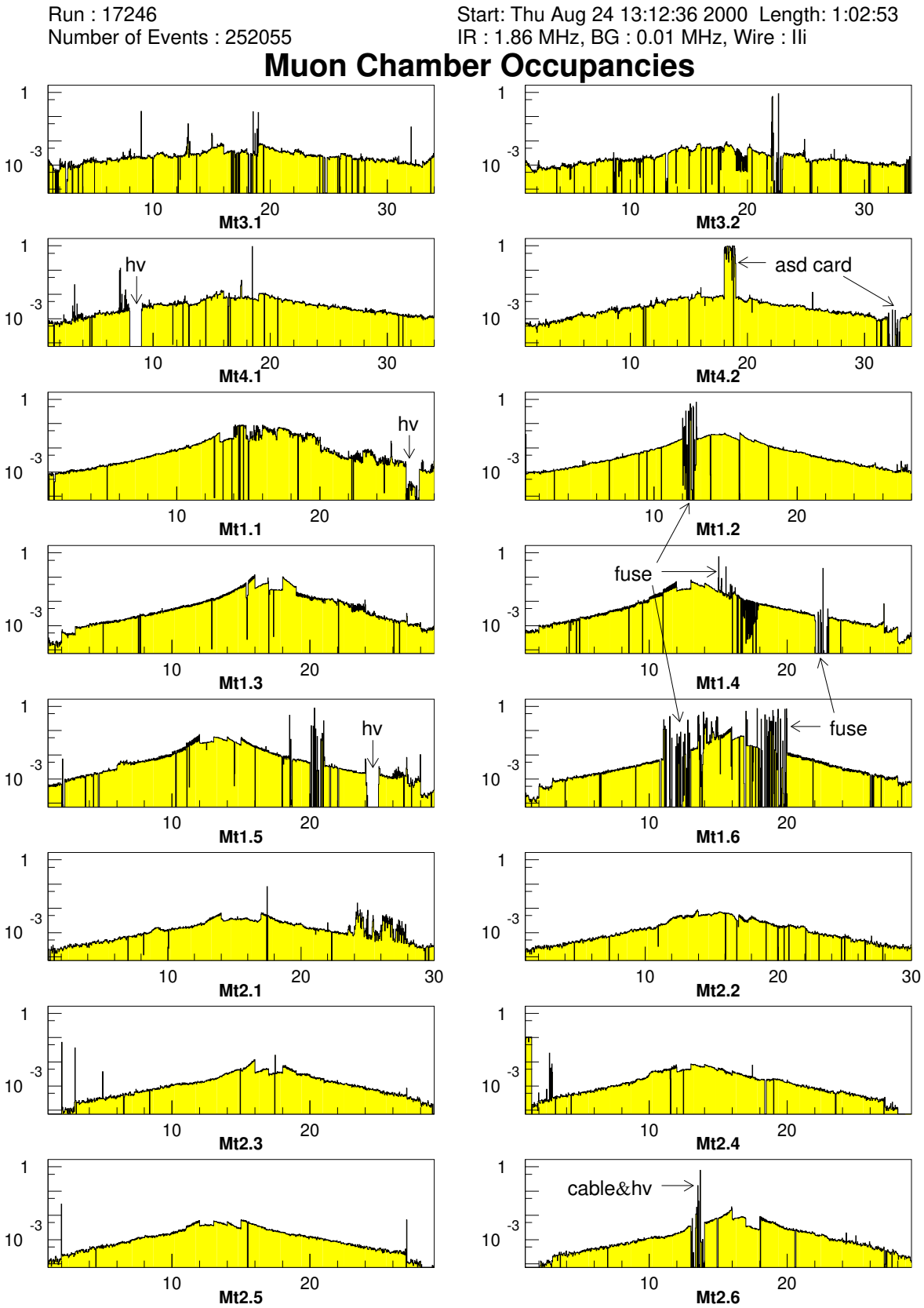

Figure 91: *Occupancies in the tube channels. The term "asd card" indicates that the thresholds could not be set on the asd card. "Fuse" means that a power fuse blew on a power distribution card which supplies the indicated chamber. The other terms are explained in the previous figure caption.*

Again, this isn't expected to pose any problems.

- The occupancy distributions are smooth, except for known chamber or readout problems, and across boundaries between chambers of different sizes.

The cause for each region of bad channels is indicated on the occupancy distribution plots of Figures 90 and 91. The types of problems, explained in the figure captions, will be repaired during the 2000-2001 shutdown.

The ultimate measure of system performance is the tracking efficiency, especially for high momentum muons. Unfortunately, a source of high momentum muons is not readily available, so we use the plentiful muons from π and K decays. These are less desirable because their momentum spectrum peaks near the threshold energy for muons. These low energy muons will suffer more from scattering effects, resulting in an underestimate of the efficiency.

Table 30: *Efficiencies measured for the Muon detector. Efficiencies for Monte Carlo data incorporating only geometric effects are shown for comparison to data, where available. "Single" means the single layer efficiency of a double layer chamber, and "double" means the double layer efficiency – pads are double layer only, and pixels are single layer only. Due to the tracking algorithm used, it was not possible to determine the double layer efficiency of the MU3 and MU4 0° wires. The efficiencies listed in the "all regions" include all regions of a layer and hence take into account the effect of non-working channels.*

region	MC data		real data good regions		real data all regions	
	single	double	single	double	single	double
MU1 0°	93.5%	99.8%	85.3%	96.6%		89.4%
MU1 +20°	92.2%	99.5%	85.4%	97.8%		95.0%
MU1 20°	92.1%	99.6%	84.8%	97.5%		76.2%
MU2 0°	91.5%	99.6%	82.5%	97.4%		97.3%
MU2 +20°	91.1%	99.3%	82.2%	98.3%		97.9%
MU2 −20°	91.1%	99.0%	84.2%	98.3%		95.5%
MU3 0°	89.6%		84.4%		83.2%	
MU4 0°	89.3%		84.0%		83.9%	
MU3 pads						75%
MU4 pads						68%
MU1 pixels			85%			
MU2 pixels			85%			
MU3 pixels			91%			
MU4 pixels			85%			

The efficiency measurements are displayed in Table 30. The tube chamber efficiencies are determined by modifying the stand-alone track finding code such that hits in a particular sub-layer are not required, then taking the ratio of tracks with hits in that sub-layer to the total number of tracks found (the tracks must extrapolate into or through the layer in question). Each tube sub-layer is composed of a double layer of tubes offset by half a cell, so we quote the efficiency for a single layer of tubes and the double layer, where a hit can be registered in either or both layers. The efficiencies in the tube chambers are lower in the data than in the Monte Carlo, especially the single layer

efficiencies. This Monte Carlo incorporates only geometric effects (size of cell and aluminum walls in the chambers) and thus the difference with data is due to the intrinsic efficiency of the detector.

The calculation of the pad efficiency is a bit more difficult because the stand-alone tracking algorithm can't be used – the tracking algorithm starts from pad coincidences. A special algorithm was developed to determine the pad efficiency. Using hits in the 0° tube chambers, a MU1 hit is paired with all MU2 hits within an acceptance angle, designed to enhance the sample with good tracks with $p > 10\,\mathrm{GeV/c}$. The line formed by these hits is extrapolated to MU3 and MU4, and the residuals to nearby hits determined. If a MU3 (MU4) hit residual is less than 10 cm, then the smallest residual in MU4 (MU3) is histogrammed. A second histogram is made for the case that a pad hit is coincident with the wire hit. The resulting histograms have signal to background ranging from 10 : 1 to 1 : 1, so background subtraction is done using sidebands. Finally, the pad efficiency is calculated as the ratio of the wire + pad signal to the wire signal.

The pad efficiency numbers should be treated with some care. Although the statistical errors are a couple of percent, variations between runs with similar conditions are about 20%. These systematic variations are not understood; it is suggested that they may arise from the process of determining the background subtracted signal from the residual histograms. This question is currently under study. The cause of the low pad efficiency is discussed further below.

A preliminary calculation of the pixel efficiency is shown for completeness. These numbers are a first try at determining the pixel efficiency and the algorithm is still being tuned. The basic idea is to make use of the fact that small angle muons tend to have rather high momenta, so the tracks point back to the target. The calculation starts by forming clusters from hits in the pixel detectors. Then, starting from two super-layers, pairs of clusters that point back to the target are chosen. A cluster on a third super-layer is required to lie within 5 cm of the line to the target. The residuals of clusters in the remaining layer are histogrammed, and the number of entries in the signal peak is determined – background subtraction is important mostly for MU1. Finally, the efficiency is determined from the ratio of the signal entries to all the candidate lines with clusters in the other layers.

It is not understood why the measured pixel efficiencies are more than a few per cent lower than 100%. Additional data analysis is planned in which the inner tracker information will be used to confirm muon tracks. Also, a program is planned to measure the efficiencies of the pixel chambers in a test beam or with cosmic rays.

We made efficiency measurements in the test beam to benchmark the tube and pad chamber performance. Figure 92 shows the test beam results for the tube chamber efficiency using three different gas mixtures. Last year we operated the muon chambers with the $Ar/CF_4/CO_2$ gas mixture at a voltage of 2400 V.

In Fig. 93 we display measurements of the pad efficiency (circles) along with the tube efficiency for the corresponding conditions. Note that the pad readout efficiency lags the tube efficiency by about 150 V. This measurement lead to a decision in June to raise the operating voltage to 2450 V and eventually 2500 V. The immediate effect was a dramatic rise in the pad efficiencies and the first observation of a J/ψ mass peak in real time.

At the end of the year 2000 run, the preamp voltages were set to about 3.8 volts. Unfortunately, even at 2500 volt chamber bias, the operating point is just at the knee of the plateau curve. The result was that even for chambers with good values of ASD threshold (0.9 volts or below), the best readout efficiency was in the range 85% to 90%. In the subsequent section on Shutdown plans, we discuss ways to improve the efficiency.

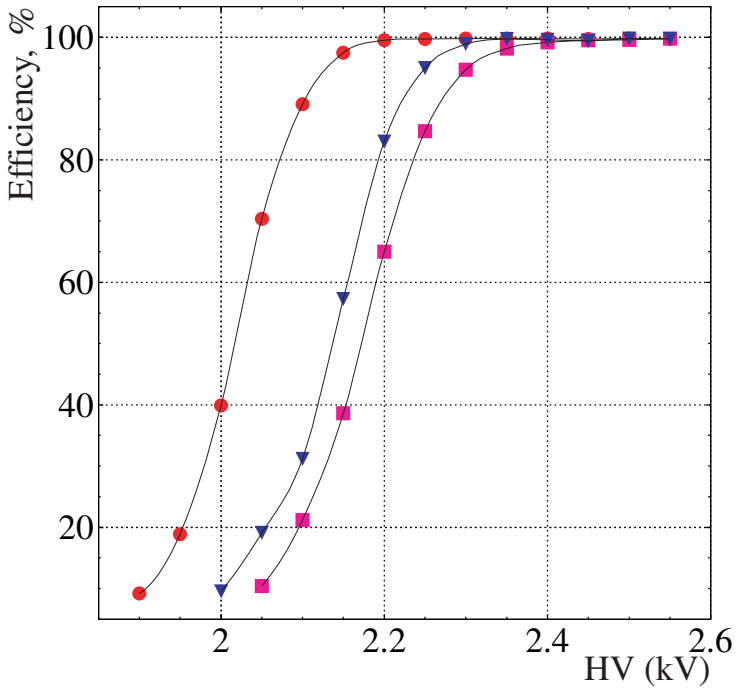

Figure 92: *Efficiency of a tube chamber double layer as a function of high voltage from test beam measurements. All measurements are taken with an ASD threshold of* 0.9 V *and a* 96 nsec *time window. The curves are for the gas mixtures* $Ar/CF_4/CH_4$ *(74:20:6) (circles),* $Ar/CF_4/CO_2$ *(65:30:5) (triangles), and* $Ar/CF_4/CH_4$ *(67:30:3) (squares).*

2.10.3 Chamber Aging Studies

Irradiation with a ^{106}Ru source showed that tube chambers filled with $Ar/CF_4/CH_4$ (67:30:3) and $Ar/CF_4/CO_2$ (65:30:5) mixtures are able to tolerate doses up to 2 C/cm per year without visible aging effects. Since it is not clear how to extrapolate aging results from small to large areas of irradiation, we have carried out the aging tests with large area tube chambers in the high-rate hadronic HERA – B environment.

We placed test chambers between the ECAL and the first muon absorber, where the particle flux is extremely high. The chambers were subdivided to allow groups of anode wires to be operated at different gas gains. Our results showed that aging in the case of the gas mixture $Ar/CF_4/CH_4$(67:30:3)+ 500 ppm H_2O depends on the gas amplification factor and area of irradiation. Electron microscopic analysis of irradiated anode wires operated at a gas gain of $\sim 10^5$ revealed deposits containing carbon and fluorine as the only detectable elements (hydrogen is not detectable). At the same time, irradiated wires operated at smaller gas gains of $\sim 2 \times 10^4$ showed no aging effects up to an accumulated charge of 0.8 C/cm.

Using the gas mixture $Ar/CF_4/CO_2$(65:30:5) + 1000 ppm H_2O no aging effects were observed up to a total charge of 0.8 C/cm when operated at gas gains up to $\sim 2 \times 10^5$. This is the gas mixture that we currently use.

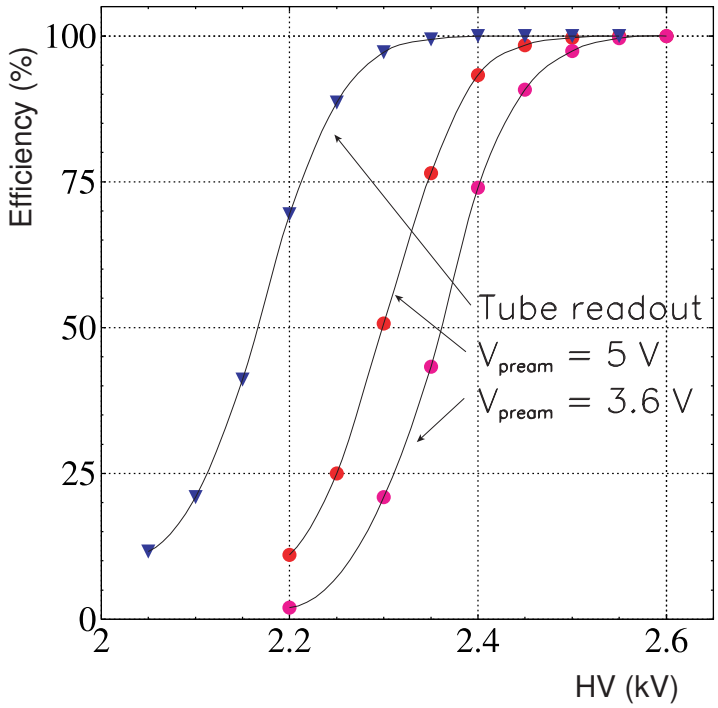

Figure 93: *Efficiency of the tube (triangles) and pad (circles) readout of a pad chamber as a function of high voltage from test beam measurements. The pad measurements are for a single layer, with a tube hit required in triggering. Data are shown with preamplifier bias of* 3.6 V *and* 5.0 V. *The ASD threshold is* 0.9 V *and the timing gate width is 400 ns.*

2.10.4 Shutdown Plans

The main goals during the shutdown are to improve the efficiency of the pad system, to repair chambers and readout electronics and to be ready for data taking in 2001.

One factor affecting the pad efficiency is illustrated in Figure 94 which shows the average ASD threshold for the half of each pad chamber closest to the beam (see [83]). Some chambers did not have an internal grounding modification (due to the tight time schedule for installation). These chambers are identified as "no pad ground" in the figure and were responsible for the bulk of the pad channels with high thresholds and hence low efficiency. During the 2000-2001 shutdown, these chambers will be modified.

Pad chambers with good threshold values, when operated at 2500 volts in the 2000 run, achieved efficiencies of about 85-90%. With the modification just mentioned, repair of some chambers and some other modifications under consideration (see below), the pad system as a whole should be able to operate with efficiencies of $\sim 90\%$ for the 2001 run.

One of the pad plateau curves shown in Figure 93 is for a pad preamp bias voltage of 5 volts. (In the 2000 run, a bias of 3.5 volts was used.) The higher electronic gain with 5 volts bias results in a plateau curve shifted to lower HV values and hence higher efficiency at a given HV value. It is currently not possible to operate the pad preamps beyond a bias of about 4 volts because the noise rate becomes too large. We are investigating ways to further reduce the noise. Preliminary

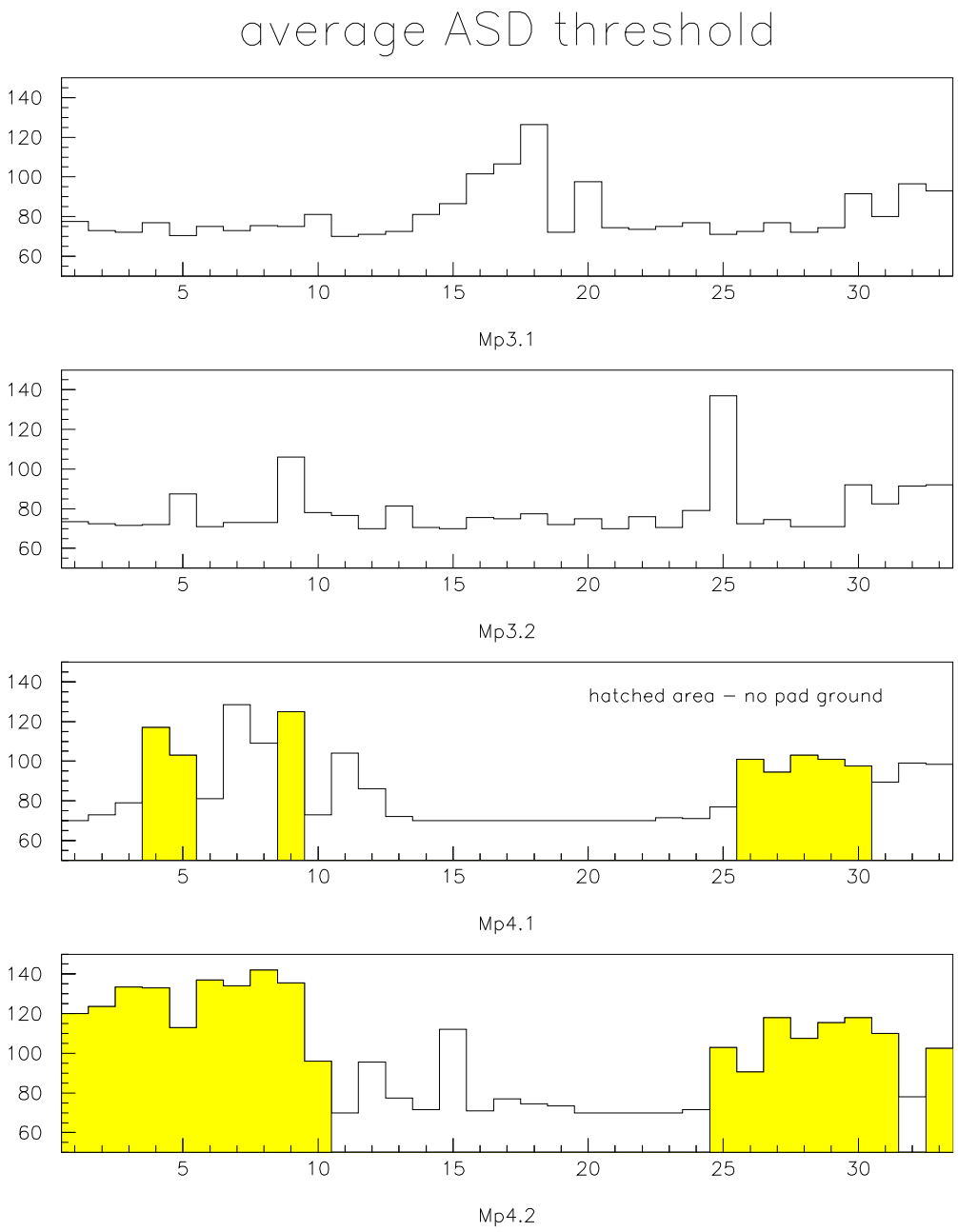

Figure 94: *Average per half chamber nearest the beam of ASD threshold in millivolts. Some chambers did not have an internal grounding modification (due to the tight time schedule for installation). These chambers are identified as "no pad ground" in the figure and were responsible for the bulk of the pad channels with high thresholds and hence low efficiency. During the 2000-2001 shutdown, these chambers will be modified.*

measurements with a single pad layer have identified some promising modifications which include

- installation of additional filter capacitors on the preamp power bus, and
- replacement of cable termination resistors on the ASD card with capacitors to better match the cable impedance.

Tests with full chambers will be necessary to assess the effectiveness of these modifications. Furthermore, it is not realistic to assume that all pad chambers could be removed, modified, and reinstalled before the tunnel closure in the summer of 2001.

Further improvement in efficiency is possible with chamber bias at 2550 volts. However, this is near to the minimum voltage for streamer formation of about 2600 volts. Safe maximum interaction rate would have to be determined for operation at 2550 volts.

A modification that could be implemented on a longer time scale is to replace the existing ASD readout cards with a modified design. The idea is to increase the shaping time of the amplifier used before the discriminator stage. The ASD-8 chip has a shaping time of about 6 ns, but the rise time of the pad pulse is about 25 ns. Thus, the ASD-8 responds to only a small fraction of the pad signal. An amplifier stage with a longer shaping time could operate at higher charge thresholds and lower noise compared to the ASD-8. Furthermore, the larger signal available at the input to the comparator would result in high efficiency.

To implement the replacement of ASD cards for the pad channels would require design of a new circuit, prototype testing, large scale production and installation in the West Hall. It is unlikely to replace all ASD cards before the tunnel closure in 2001 because all top pad chambers have to be dismounted be access the lower ones. The muon group will prepare a cost and time estimate.

The other items to work on are much more routine. We will repair some detectable gas leaks in pad chambers and make repairs to some chambers and components that are not easily accessible. Additionally, we have been asked to complete the removal of some foam material that fails to meet safety standards.

Some power distribution boxes on the MU1 frame are in inaccessible locations are will be moved. Also, we will consider using resettable fuses to reduce the recovery time time after a fuse trips. A few chambers with broken anode wires or other HV problems such as cables will be repaired.

The gas leaks that we want to repair are detectable, but not serious enough to interfere with the 2000 run. The necessary manpower is already arranged and a work schedule is being developed. The most serious problem is that the majority of the chambers that need to be removed are on the platform that will sit between the tram bridge and the West Hall crane shaft. We will probably have to arrange to access these chambers during weekends when crews are not at work.

Some aspects of the gas system need to be completed. Gas quality monitors will be installed. These are small drift tubes with readout to monitor the gas gain and purity. A gas purification system will be installed that is a small copy of the outer tracker system. The slow control software will be upgraded to allow for automatic adjustment of chamber HV bias to compensate for changes in atmospheric pressure.

Finally, we note that pixel chamber MX2 needs repair of one HV section and correction of a cable mapping problem for two cables. As mentioned earlier, work must be done to understand the efficiency of the pixel chambers.